

ČESKÉ VYSOKÉ UČENÍ TECHNICKÉ V PRAZE

Fakulta jaderná a fyzikálně inženýrská

DISERTAČNÍ PRÁCE

**A Study of Open Charm Production
in $p+p$ Collisions at STAR**

Posluchač: Ing. David Tlustý

Školitel: Mgr. Jaroslav Bielčík PhD.

b

Dedication

To my parents, for your outstanding support and selfless generosity. You have been friends and role models.

Acknowledgements

I would like to thank Nuclear Physics Institute (NPI) and Faculty of Nuclear Sciences and Physical Engineering (FNSPE) of CTU Prague for their full-time support throughout my graduate research. They provided me with the opportunity to join the STAR Collaboration and supported my travel to meetings and conferences around USA, Europe and India. I would like also to thank Lawrence Berkeley National Laboratory (LBNL) and Brookhaven National Laboratory (BNL) for their co-sponsoring of my stays at LBNL and BNL which significantly contributed to results presented in this thesis. I owe enormous gratitude towards my supervisor Jaroslav Bielik, who has encouraged me to be thoughtful, critical, and actively involved. For the tremendous amount of advice, I would like to thank particularly to Xin Dong, Lijuan Ruan, Jamie Dunlop, Bill Christie, Daniel Kikola, Yifei Zhang, Alex Schmah, Jan Kapitan, Petr Chaloupka, and Pavol Federic. There are many members of the STAR collaboration employed at NPI, FNSPE, LBNL, and BNL whose support has been essential, namely Jana Bielikova, Michal Sumbera, Hans-Georg Ritter, Zhanbu Xu, and the former STAR spokesperson Nu Xu. Thanks to Jerome Lauret and Lydia Didenko for their endless computing support and encouragement. I could not have done this without the support and patience of my family.

Abstract

The Standard Model of particle physics has successfully described discoveries of the charm, bottom, and top quarks, and the Z, W^\pm , and Higgs bosons. Heavy Ion Collisions has been a unique experimental tool to create a matter of deconfined quarks and gluons called Quark Gluon Plasma (QGP). The Relativistic Heavy Ion Collider (RHIC) was built to achieve temperature and energy density high enough to create the QGP and the experiments at RHIC, STAR and PHENIX, were designed to test the predictions of QCD and understand the properties of the deconfined matter.

Heavy quarks are expected to be created from initial hard scatterings in the heavy ion collisions. Their large masses are not easily affected by the strong interaction with QCD medium, thus they carry clean information from the system at an early stage. The interaction between heavy quarks and the medium is sensitive to the medium dynamics, therefore heavy quarks are suggested as an ideal probe to quantify the properties of the strongly interacting QCD matter. The measurement of charm production total cross section in p+p and Au+Au collisions is important to understand both open charm and charmonium production mechanisms in the nuclear matter. Many charm measurements at RHIC are indirect based on non-photonic electrons from semileptonic decays of heavy flavor mesons. These measurements doesn't provide a direct access to charm quarks kinematics and they include contribution from bottom hadron decays.

This thesis presents measurements of D^0 and $D^{*\pm}$ mesons production at mid-rapidity in p+p collisions at $\sqrt{s} = 200$ and 500 GeV at RHIC. The measurements were done by STAR experiment. These open charm mesons were reconstructed directly via hadronic decay channels with daughter particles identified by STAR Time Projection Chamber and Time Of Flight detectors. With the knowledge of the charm quark fragmentation ratios, both p_T -differential and p_T -integrated invariant cross sections of charm-anticharm quark pair production at mid-rapidity were calculated and total charm-anticharm quark pair cross section was estimated using QCD based models. The p_T -differential invariant cross section of charm-anticharm quark pair production at mid-rapidity was measured at $0.6 < p_T < 6$ GeV/ c in p+p collisions at $\sqrt{s} = 200$ GeV from events triggered by minimum bias trigger, at $1 < p_T < 6.5$ GeV/ c in p+p collisions at $\sqrt{s} = 500$ GeV from events triggered by minimum bias trigger, and at $5 < p_T < 18$ GeV/ c in p+p collisions at $\sqrt{s} = 500$ GeV from events triggered by high E_T trigger. The p_T -integrated invariant cross section of charm-anticharm quark pair production at mid-rapidity was measured to be $170 \pm 45(\text{stat})_{-59}^{+38}(\text{sys}) \mu\text{b}$ in p+p collisions at $\sqrt{s} = 200$ GeV and $225 \pm 38(\text{stat}) \pm 19(\text{sys}) \pm 26(\text{norm}) \mu\text{b}$ in p+p collisions at $\sqrt{s} = 500$ GeV. The total charm-anticharm quark pair production cross section was estimated to be $797 \pm 210(\text{stat})_{-295}^{+208}(\text{sys}) \mu\text{b}$ in p+p collisions at $\sqrt{s} = 200$ GeV and $1260 \pm 211(\text{stat}) \pm 109(\text{sys}) \pm 146(\text{norm}) \mu\text{b}$ in p+p collisions at $\sqrt{s} = 500$ GeV. All these measurements are compared to theoretical model calculations and physics implications are discussed.

Author's Contribution

I have been employed by the Nuclear Physics Institute of the Academy of Sciences Czech Republic since January 2008 where I have been an active member of the Nuclear Spectroscopy group. I have become also a member of the STAR collaboration at the Relativistic Heavy Ion Collider, where I have made a number of contributions to the running of the experiment, data calibration and analysis, and presenting new results at conferences.

Service Work

I joined the STAR collaboration with primary interest in heavy flavor physics under supervision of Dr. Jaroslav Bielcik. The first work I have done for STAR was a service work for Research and Development project “Muon Telescope Detector (MTD) for STAR”. During my 3 months stay in the year 2008 at BNL, I have worked on data analysis of test beam data in order to optimize voltage upon the electrode. I found that optimal voltage was 6.3 kV, upon which detector performs with time resolution of 58.5 ps and the spatial resolution along the direction of the read-out strips of 0.5 cm. The final conclusion of this work was that the prototype satisfied the STAR requirements.

Simulation and Analysis

In 2009, I simulated the response of newly installed Time-Of-Flight detector on the D^0 meson hadronic daughter particles (pions and kaons) in order to estimate the significance of the D^0 invariant mass peak from expected 300M minimum bias events of the Run 2009. In addition, I calibrated the detector response using the small sample of the year 2009 data. The simulations had shown that the reconstruction of D^0 meson in hadronic channel from 200 GeV p+p collisions (Run 2009) data could be possible with significance to be around 4 for 100M events, which was confirmed in 2010, when myself and Prof. Yifei Zhang presented two independent analyses to STAR collaboration. This was the first reconstruction of D^0 meson in hadronic channel in 200 GeV p+p collisions data at RHIC. I am a primary author of the paper Phys. Rev. D **86**, 072013 that included these results. Results have shown a very good agreement with FONLL prediction and have provided a key baseline for further measurements in Au+Au collisions. My analysis is presented in this thesis. In 2010, I was a member of the team awarded with the Prize of the Rector of the Czech Technical University for contribution to STAR program.

In 2011 and 2012, I analyzed D^0 and D^* production in p+p collision at 500 GeV (Run 2011). Preliminary results are perfectly consistent with FONLL prediction and open charm total cross section matches the improved NLO calculation providing an important intermediate point between already published result at 200 GeV and LHC results of 2.76 TeV and 7 TeV. This analysis is also presented in this thesis. Run 2011 contains integrated luminosity = 22 pb⁻¹ data triggered by a high E_T trigger having allowed us to extend the open charm invariant cross section p_T range up to 18 GeV. I have adopted the technique of requirement the pion from D^* decay to be the triggering particle, which eliminates the trigger bias. The analysis from high E_T triggered events is briefly discussed and its preliminary results presented in the last two paragraphs of chapter 6. This technique will be also used in both p+p 200 GeV and AuAu 200 GeV allowing us to further extend the $D^0 R_{AA}$ measurement, which already reveals strong suppression for $p_T > 3$ GeV.

Published Papers With Author's Primary Contribution

1. L. Adamczyk *et al.* (STAR Collaboration), Phys. Rev. D **86**, 072013 (2012).
2. D. Thusty *et al.* (STAR Collaboration), J. Phys. Conf. Ser. **509**, 012078 (2014).
3. D. Thusty *et al.* (STAR Collaboration), PoS(EPS-HEP 2013)197.
4. D. Thusty *et al.* (STAR Collaboration), Nucl. Phys. **A904-905**, 639c (2013).
5. D. Thusty *et al.* (STAR Collaboration), Nucl. Phys. **A910-911**, 289-292 (2013).
6. D. Thusty *et al.* (STAR Collaboration), J. Phys. Conf. Ser. **389**, 012024 (2012).
7. D. Thusty *et al.* (STAR Collaboration), Nucl. Phys. **A862-863**, 328 (2011).

These papers are included in this thesis in chapter C.3.

Contents

Dedication	i
Acknowledgements	iii
Abstract	v
Author's Contribution	vii
1 Introduction	1
1.1 Quantum Chromodynamics	2
1.1.1 Strongly Interacting Particles	3
1.1.2 Asymptotic Freedom	4
1.1.3 The QCD Running Coupling Constant	5
1.1.4 Confinement, Deconfinement and Bag Model	6
1.2 Lagrangian QCD and Chiral Symmetry	7
1.2.1 Spontaneous Breaking of Chiral Symmetry	8
1.2.2 Restoration of Chiral Symmetry and Quark Gluon Plasma	9
1.3 Heavy Ion Collisions	9
1.3.1 Space-time Evolution	11
1.3.2 Initial Energy Density - Bjorken Formula	12
1.3.3 Partonic Collectivity	13
1.3.4 Energy Loss and Suppression	14
1.4 Heavy Quark Production	15
1.5 A Selection of Current Experimental Results	17
1.5.1 Invariant Cross Section of Non-photonic Electrons Produced in p+p Collisions	19
1.5.2 Invariant Cross Section of D^0 Mesons in p+p and Au+Au Collisions at $\sqrt{s_{\text{NN}}} = 200$ GeV	21
1.5.3 Nuclear Modification Factor of D^0 production at RHIC	22

1.5.4	Nuclear Modification Factor of D^0 production at LHC	25
1.6	Thesis Outline	26
2	Experimental Setup	27
2.1	The Relativistic Heavy Ion Collider	27
2.2	The Solenoidal Tracker at RHIC	29
2.3	Trigger	32
2.4	Time Projection Chamber	33
2.4.1	Tracking	37
2.4.2	Particle Identification	38
2.5	Time of Flight Detector	41
2.5.1	Barrel Time of Flight	41
2.5.2	The Vertex Position Detector	42
2.5.3	Particle Identification by TOF	43
2.6	Barrel Electromagnetic Calorimeter	45
3	Analysis Of the Experimental Data	47
3.1	Event Selection	49
3.2	Particle Selection	53
3.2.1	Track Quality Cuts	53
3.2.2	Particle identification	56
3.3	D^0 reconstruction	62
3.4	D^* reconstruction	71
4	Efficiency and Acceptance Correction	77
4.1	Track Reconstruction Efficiency ε_R	78
4.2	Matching Efficiency, ε_M	80
4.3	Particle Identification Efficiency, ε_{PID}	88
4.4	Kinematical cuts efficiency	89
4.5	Trigger bias correction	93
4.5.1	Trigger Bias Correction in Run9 pp200 Analysis	96
5	Systematic Errors Evaluation	99
5.1	Uncertainty on the Raw Yield Determination	99
5.1.1	Double counting	101
5.2	Uncertainty on the Efficiency Determination	103
6	Results	107
7	Discussion and Outlook	123
A	Differential Invariant Cross Section	127
A.1	As a Hagedorn Shape Function	127
A.2	As a Lévy Function	128

B	D^* Decay Kinematics	131
B.1	General Relations	131
B.2	Monte-Carlo Toy Model	134
C	Treatment of Errors	137
C.1	Treatment of Errors in Efficiency Calculations	137
C.2	Treatment of Systematic Errors	139
C.3	Treatment of Correlated Errors	141
	Bibliography	143
	Published Papers	149

List of Figures

1.1	Quarkonic and gluonic loops between gluonic propagators.	4
1.2	The strong coupling constant α_S as a function of the energy scale Q . The respective degree of QCD perturbation theory used in the extraction of α_S is indicated in brackets (NLO: next-to-leading order; NNLO: next-to-next-to leading order; res. NNLO: NNLO matched with resummed next-to-leading logs; N ³ LO: next-to-NNLO). Figure taken from Ref. [4].	5
1.3	Quark masses in the QCD vacuum and the Higgs vacuum. Figure taken from Ref. [17].	10
1.4	The space-time evolution of a heavy ion collision. Figure taken from Ref. [19].	11
1.5	Non-central collision. Participant nucleons in the almond-shaped overlap region experience a force from the pressure gradient. Figure taken from Ref. [23].	13

1.6	The basic Feynman diagrams for charm quark pair production at the Leading Order (LO) level.	16
1.7	Charm quark fragmentation to D^0 and two main D^0 decay channels. . . .	18
1.8	Invariant cross section of electrons from bottom (upper left) and charm meson (upper right) decay, together with the ratio of the corresponding measurements to the FONLL predictions for bottom (lower left) and charm electrons (lower right). The solid circles are experimental measurements. The error bars and the boxes are, respectively, the statistical and systematic uncertainties. The solid and dotted curves are the FONLL predictions and their uncertainties. The dashed and dot-dashed curves are the FONLL prediction for $B \rightarrow D \rightarrow e$	20
1.9	Charm quark pair cross section as a function of the number of binary collisions N_{bin} . Circles represent measurement in p+p collisions carried out in years 2009 (run9) and 2012 (run12), artificially nudged aside of each other for better clarity, and squares represent measurement in Au+Au collisions for various centralities. The asterix denotes the measurement in AuAu collisions all centralities combined.	21
1.10	The p_T -differential D^0 invariant yield in Au+Au collisions at $\sqrt{s} = 200$ GeV for various centralities (subfigure a) and the D^0 meson nuclear modification factor (subfigure b). Figures taken from Ref. [39].	23
1.11	Nuclear modification factor in Pb+Pb collisions at $\sqrt{s_{NN}} = 2.76$ TeV. . . .	25
2.1	The RHIC accelerator scheme. Figure taken from Ref. [58].	28
2.2	The Artistic view of the STAR detector.	31

2.3	The STAR Trigger.	33
2.4	The STAR Time Projection Chamber.	34
2.5	The 1/12th of the base of the TPC instrumented by MWPC split in an inner and outer sector. Figure taken from Ref. [61].	36
2.6	An illustration on how an artificial track can be formed from neighboring hits. Figure taken from Ref. [65].	37
2.7	An illustration of the procedure of getting an enriched sample of kaons (top row) and a pure sample sample of protons (middle row) and pions (bottom row). The left column illustrates topological cuts on daughter particle tracks, the middle column shows reconstructed invariant mass and the right column shows dE/dx values of rich (pure) sample of the daughter particles after the cuts on invariant masses together with dE/dx mean values and their predictions from Bichsel functions.	40
2.8	Barrel Time Of Flight geometry.	42
2.9	Start Time.	43
2.10	Particle Identification by STAR TOF.	45
2.11	Placement of BEMC in STAR. Figure taken from Ref. [76].	46
3.1	Event from a p+p collision reconstructed in TPC. Yellow and Green lines represent tracks and Red box represent z -position of vertex calculated by (2.4). Blue short thick lines represent matched hits in TOF and green short thick lines represent matched hits in BEMC.	49

-
- 3.2 Correlation between z-position of the first TPC vertex and z-position of the VPD vertex from VPDMB trigger before (Panel a) and after (Panel b) 2x matching in Fast cut is applied. Panel c): Vertex z-position difference between the TPC vertex and the VPD vertex. The blue vertical lines indicate the cut window used to select the triggered events. 51
- 3.3 Number of events that passed cuts in the event chain. The left panel shows Run11 pp500 statistics while the right panel Run9 pp200 statistics. 52
- 3.4 Pion multiplicity as a function of the BBC Coincidence Rate for tracks with matching in fast detectors and for all TPC primary tracks. 55
- 3.5 Time of Flight over the Run9 pp200 data taking period. 57
- 3.6 Results of Time of Flight 25ns shift correction. 58
- 3.7 The scatter plot depicts $n\sigma_K^{1/\beta}$ as a function of the track momentum whose slices were projected along Y-axis and fitted by gaussian distributions. The red open circles represent second moments (σ) of those distributions that are fitted by power-law function f_{Res} and the dashed curve in the scatter plot is the power-law function f_{Pos} fit the first moments (μ) of the gaussian distributions. The grey curves in the scatter plot represent PID cuts used to select kaons. 60
- 3.8 $n\sigma_\pi^{1/\beta}$ as a function of the track momentum. The black lines depict the TOF PID cut for pions. $1/\beta$ of pions is affected by Coulomb re-scatterings at lower momenta so I used a wider range according to (3.6). 62

- 3.9 Upper Panel: Opposite-charged $K\pi$ invariant mass with the combinatorial background reconstructed by Like-Sign and Rotated Momentum techniques for all $K\pi$ pairs within $(1.0 < p_T < 2.0 \text{ GeV}/c)$ and $|y(K\pi)| < 1$. The gray rectangle illustrates the zoom to D^0 mass window. Lower left panel: Opposite-charged $K\pi$ pairs invariant mass after Like-Sign background subtracted. Lower right panel: Opposite-charged $K\pi$ pairs invariant mass after Rotated-Momentum background subtracted. 65
- 3.10 Upper Panel: Opposite-charged $K\pi$ invariant mass with the combinatorial background reconstructed by Like-Sign and Rotated Momentum techniques for all $K\pi$ pairs within $(0.9 < p_T < 1.5 \text{ GeV}/c)$ and $|y(K\pi)| < 1$. The gray rectangle illustrates the zoom to D^0 mass window. Lower left panel: Opposite-charged $K\pi$ pairs invariant mass after Like-Sign background subtracted. Lower right panel: Opposite-charged $K\pi$ pairs invariant mass after Rotated-Momentum background subtracted. 66
- 3.11 Upper Panel: Opposite-charged $K\pi$ invariant mass with the combinatorial background reconstructed by Like-Sign and Rotated Momentum techniques for all $K\pi$ pairs within $(1.5 < p_T < 2.0 \text{ GeV}/c)$ and $|y(K\pi)| < 1$. The gray rectangle illustrates the zoom to D^0 mass window. Lower left panel: Opposite-charged $K\pi$ pairs invariant mass after Like-Sign background subtracted. Lower right panel: Opposite-charged $K\pi$ pairs invariant mass after Rotated-Momentum background subtracted. 67
- 3.12 Invariant mass spectrum of oppositely charged kaon-pion pairs. Kaons pions came from D^0 hadronic decay generated by PYTHIA and their momenta were randomly smeared by gaussian functions with widths equal to known p_T resolution values. 70
- 3.13 $\cos(\theta^*)$ of the kaon in the CMS of the $K\pi$ pair. 72

- 3.14 Upper panel: ΔM spectrum with combinatorial backgrounds reconstructed by Side-band and Wrong-sign technique. Green stars and the black line represent the ΔM with Side-band background subtracted and the gaussian fit to it respectively in the range from 0.14 to 0.16 GeV/ c^2 . Lower panel: ΔM with Wrong-sign background subtracted and the gaussian fit to it in the range from 0.14 to 0.16 GeV/ c^2 . The width of the gaussian function is fixed to be the same as in the case of the Side-band background subtracted. 74
- 3.15 ΔM spectra with combinatorial backgrounds reconstructed by Side-band and Wrong-sign techniques in $K^\mp \pi^\pm \pi^\pm p_T$ bins. 75
- 4.1 π^+, π^-, K^+, K^- track reconstruction efficiency. Errors are depicted by contours. 79
- 4.2 TOF Matching efficiency as a function of the track p_T . Open red (closed blue) circles depict the efficiency calculated according to (4.3) from the production P11id for pions (kaons). The pp2pp data were analyzed 1) by the same way with results depicted as green closed squares (kaons) and black thick dots (pions) 2) according to (4.4) with results depicted as dark red crosses (kaons) and dark blue (pions) asterisks. 81
- 4.3 BEMC Matching efficiency as a function of the track p_T . Open (closed) black circles depict the efficiency calculated according to (4.3) from the production P11id for pions (kaons). The pp2pp_Production2009 trigger set was analyzed 1) by the same way with results depicted as red closed asterisks (kaons) and blue open asterisks (pions) 2) according to (4.4) with results depicted as brown closed asterisks (kaons) and green open stars (pions) asterisks. 83

4.4	The degree of correlation between phenomena T and B calculated according to (4.5). Red color is dedicated to pions while the black represents kaons.	84
4.5	The degree of correlation between phenomena B and T calculated according to (4.5). Red color is dedicated to pions while the black represents kaons. .	84
4.6	The TOF and BEMC matching efficiency separately.	85
4.7	TOF and BEMC matching efficiency combined. Kaons with no TOF information and $p_T < 1.3 \text{ GeV}/c$ were rejected (see subsection 3.2.2 , so that $\varepsilon_M = \varrho_T \varepsilon_T$ for kaons up to $p_T < 1.3 \text{ GeV}/c$	85
4.8	D^0 meson reconstruction efficiency as a fuction of PYTHIA generated D^0 meson p_T	88
4.9	p_T resolution kaons and pion by TPC.	90
4.10	Surface plot of D^* transverse momentum t and reconstructed D^0 invariant mass M^{RC}	92
4.11	Projections $\int_a^b g^{\text{RC}}(t, \cos(\theta^*)) dt$. The drop at $\cos(\theta^*)$ close to -1 is the result of the kaon momentum at D^0 rest going against the D^0 momentum direction resulting in a much smaller momentum in the lab frame, thus lower reconstruction efficiency.	93
4.12	Event counter for general events denoted as "MB" and events containing D^* mesons denoted as "Charmed". "fireBBC" and "FireVPD" columns represent events that initialized BBC and VPD trigger respectively. "good Vz" denotes events from which vertices with positive ranking were sucessfully reconstructed.	95
4.13	Trigger, Vertex reconstruction efficiency and Trigger Bias.	96

4.14	The $\beta(t)$ for events containing the D^0 and events containing the D^* mesons. Figure taken from Ref. [28].	97
5.1	Probability of a particle being in overlapping PID region.	102
5.2	Left panel: Reconstructed invariant mass of D^0 meson where both daughter particles were misidentified so that the kaon was assigned the pion mass and vice versa, i. e. $g^{\text{RC}}(t, M^{\text{Mis}})$. Right panel: Reconstructed invariant mass of D^0 meson with correct daughter particle identification, i. e. $g^{\text{RC}}(t, M^{\text{RC}})$	102
5.3	The fraction of the over counting in the Wrong-sign background.	103
5.4	Systematic discrepancy between the data and the embedding.	104
6.1	Charm quark production cross section as inferred from D^0 and D^* production in p+p collisions at $\sqrt{s}=500$ GeV compared with FONLL predictions. The D^0 and D^* data points were divided by the charm quark fragmentation ratios $f_c = 0.565$ and $f_c = 0.224$ respectively. FONLL calculations [83] used $\mu_R = \mu_F = m_c$ where μ_R is the renormalization scale, μ_F is the factorization scale and m_c is the charm quark mass. "m = 1.5" in the legend denotes $m_c = 1.5 \text{ GeV}/c^2$ and "m = 1.27" denotes $m_c = 1.27 \text{ GeV}/c^2$. Data points are already corrected on bin widths and fitted by Hagedorn Power-law function (A.2).	112

- 6.2 Charm quark production cross section as inferred from D^0 and D^* production in p+p collisions at $\sqrt{s}=500$ GeV compared with FONLL prediction. The D^0 and D^* data points were divided by the charm quark fragmentation ratios $f_c = 0.565$ and $f_c = 0.224$ respectively. FONLL prediction [83] used $\mu_R = \mu_F = m_c = 1.5$ GeV/ c^2 where μ_R is the renormalization scale, μ_F is the factorization scale and m_c is the charm quark mass. Data points are already corrected on bin widths and fitted by Lévy Power-law function (A.4) with m_0 chosen to be 1.5 GeV/ c^2 113
- 6.3 Charm quark production cross section as inferred from D^0 and D^* production in p+p collisions at $\sqrt{s}=500$ GeV compared with FONLL prediction. The D^0 and D^* data points were divided by the charm quark fragmentation ratios $f_c = 0.565$ and $f_c = 0.224$ respectively. FONLL prediction [83] used $\mu_R = \mu_F = m_c = 1.27$ GeV/ c^2 where μ_R is the renormalization scale, μ_F is the factorization scale and m_c is the charm quark mass. Data points are already corrected on bin widths and fitted by Lévy Power-law function (A.4) with m_0 chosen to be 1.27 GeV/ c^2 114
- 6.4 Charm quark production cross section as inferred from D^0 and D^* production in p+p collisions at $\sqrt{s}=200$ GeV compared with FONLL calculation [26]. The D^0 and D^* data points were divided by the charm quark fragmentation ratios $f_c = 0.565$ and $f_c = 0.224$ respectively. D^0 data points from this analysis are shown as green triangles, compared with results from [28] having the tag "(Published)" in the legend. Data points are already corrected on bin widths and fitted by Hagedorn Power-law function (A.2). 118
- 6.5 Total Charm quark production cross section as a function of Centre-of-mass collision energy \sqrt{s} 119

6.6	Charm quark production cross section as inferred from D^0 and D^* production in p+p collisions at $\sqrt{s}=500$ GeV compared with FONLL prediction [83]. The D^0 and D^* data points were divided by the charm quark fragmentation ratios $f_c = 0.565$ and $f_c = 0.224$ respectively. Data points are already corrected on bin widths and fitted by Lévy Power-law function (A.4) with m_0 chosen to be $1.5 \text{ GeV}/c^2$. D^* data points came from datasets triggered by minimum bias trigger (open black squares) and BHT1 trigger (closed red circles).	122
7.1	The Artistic view of the STAR detector with two new upgrades, the Heavy Flavor Tracker (HFT) and Muon Telescope Detector (MTD).	125
B.1	Kinematically possible values of the soft pion transverse momentum from the $D^* \rightarrow D^0 \pi_S$ decay.	133
B.2	D^0 decay kinematics $g(t, p_T)$.	135
B.3	D^* decay kinematics $g(t, p_T)$.	136

List of Tables

1.1	Basic properties of quarks [4].	3
3.1	Run11 pp500 results in p_T bins.	68
3.2	The results of the χ^2 test of two hypothesis, one assuming no signal in the sample and the other gaussian signal in the same sample. It shows p -values of the linear function and linear+gaussian function fits to data in critical region of the invariant mass between 1.72 and 2.1 GeV/ c^2	69
3.3	Results in p_T bins from Run9 pp200 analysis. If the $\chi^2/\text{n.d.f.}$ is greater than 1 the contribution to averaged raw yield is scaled by.	71
3.4	D^* raw yield results in p_T bins.	73

- 4.1 Track reconstruction ε_R and matching efficiency ε_M for daughter particles from D^0 (first row) or D^* (second to last row) decay. D^0/D^* transverse momentum bins (a, b) correspond to the bins in the analysis of experimental data. Column $G^{(a,b)}(p_T)$ shows p_T profiles of the daughter particles in (a, b) . Let's note that $\xi^{D^0} = \xi^K \times \xi^\pi$ and $\xi^{D^*} = \xi^K \times \xi^\pi \times \xi^{\pi_S} \dots \dots \dots$ 87
- 4.2 The kinematical cut efficiency on D^0 candidates's mass $\varepsilon_{\text{Mass}}$ and on $\cos(\theta^*)\varepsilon_\theta$ in D^* transverse momentum bins (a, b) correspond to the bins in the analysis of experimental data. 91
- 4.3 Trigger Bias $\beta(t)$ in D^0/D^* transverse momentum bins (a, b) 94
- 5.1 Discrepancy Δ between signals obtained by subtraction of backgrounds reconstructed by different methods in D^0/D^* transverse momentum bins (a, b) and discrepancy δ between bin counting and gaussian fit to the signal in D^* transverse momentum bins (a, b) 100
- 5.2 Systematic errors from discrepancy between embedded and experimental data. First column presents D^0/D^* transverse momentum bins (a, b) and the last column corresponding systematic uncertainty obtained from values shown in middle columns by (5.7). 105
- 6.1 Final results from Run9 pp200 analysis. Table show values of all variables in equation (6.1). Some variables don't depend on reconstructed D^0 p_T so they are displayed in cells stretched over more columns. Let's note those results are not corrected on bin widths. 109

6.2	Final results from Run11 pp500 analysis. Table show values of all variables in equation (6.1). Some variables don't depend on reconstructed D^0/D^* p_T so they are displayed in cells stretched over more columns. Let's note those results are not corrected on bin widths.	110
6.3	The results after bin width correction having used three differential cross section parametrization: 1) Hagedorn parametrization where $f(p_T) = (A.2)$; 2) Lévy parametrization where $f(p_T) = (A.4)$ with $m_0 = 1.5 \text{ GeV}/c^2$; 3) Lévy parametrization where $f(p_T) = (A.4)$ with $m_0 = 1.27 \text{ GeV}/c^2$. $p_T^{(6)}$ is in units GeV/c	111
6.4	The results of fits.	115

CHAPTER 1

Introduction

The idea of matter consisting of discrete components appeared in many ancient cultures such as Greece and India. It went together with the idea that there had to exist a fundamental component which was further indivisible. Ancient Greeks called such component *Atom* derived from the word *Atomos*, i.e. indivisible. In the early 1800s, John Dalton used the concept of atoms to explain why elements always react in ratios of small whole numbers (the law of multiple proportions). The idea of atoms has become widely accepted in chemistry and further verified by botanist Robert Brown ("Brownian motion" 1827), and physicist Jean Perrin. J. J. Thomson concluded from his experiments with cathode rays that each atom contains an electron and found that atoms are further divisible. With the discoveries of atomic nucleus and its components during the first half of 20th century the whole new area of physics, the physics of micro-world, has been developed.

Following the discovery of the pion in 1947, there was a dramatic increase in the discovery of new particles with the invention of the bubble chamber in 1952 by Donald Glaser, and the development of particle accelerators. The quark model, proposed by Gell-Mann and

George Zweig in 1964, hypothesized that these particles were not elementary, but rather were composed of constituent particles named *quarks*. Their existence was confirmed in 1968 from deep inelastic scattering (DIS) experiments of leptons on hadrons [1], [2]. The existence of charm quark was proved by discovery of J/Ψ meson in 1974, followed by the bottom quark in 1977 when Υ meson was discovered. Finally, the top quark's invariant mass peak was reconstructed in 1995 in Wb decay channel [3].

In recent days, the state-of-art theory describing electromagnetic, weak, and strong interactions, and elementary particles that can interact through the interactions is called The Standard Model. It separates elementary particles into two groups according to whether they follow the Pauli exclusion principle (PEP); half-integer spin particles, known as *fermions* do follow the PEP, whereas gauge *bosons*, mediators of the fundamental interactions, don't follow the PEP and have integer spin. Fermions are classified by how they interact, and separated into six leptons interacting weakly and, if charged, electromagnetically, and six quarks interacting furthermore strongly. The gauge bosons are the force carriers that mediate the interactions and the number of gauge bosons in each interaction is determined by the dimension of their gauge group. The mediator of the electromagnetic force is the photon γ , which is a massless and chargeless particle that couples to electric charge and is well described by Quantum Electrodynamics (QED). The mediators of the weak force are the material neutral Z^0 boson, and charged W^\pm bosons. The strong force mediators are the gluons which are massless and interact with the color charge of quarks. There are eight types of gauge gluons.

1.1 Quantum Chromodynamics

Quantum Chromodynamics (QCD) is a gauge theory explaining strong interaction as an exchange of intermediate bosons (gluons) between particles with color charge. Gluons in QCD play the same role as photons in Quantum Electrodynamics. On contrary to

Flavor	Charge	Isospin	Mass [GeV/ c^2]
u	2/3	1/2	$2.3_{-0.5}^{+0.7} \times 10^{-3}$
d	-1/3	-1/2	$4.8_{-0.3}^{+0.7} \times 10^{-3}$
c	2/3	0	1.275 ± 0.025
s	-1/3	0	0.095 ± 0.005
t	2/3	0	$173.5 \pm 0.6 \pm 0.8$
b	-1/3	0	4.18 ± 0.03

Table 1.1: Basic properties of quarks [4].

photons, gluons carry color charge, thus they interact among themselves. It implies two essential properties. Colored system is weakly coupled on short distances (or equivalently at high momenta) while very strongly coupled on longer distances. These properties are called *asymptotic freedom*, and *confinement* respectively.

1.1.1 Strongly Interacting Particles

The Standard Model (SM) of particle physics recognizes two types of fundamental fermions: leptons and quarks. Both carry spin $1/2\hbar$, their dynamics is described by Dirac equation, but they differ on how they interact. While leptons are subject to electromagnetic (if they carry electric charge) and weak interactions, quarks in addition undergo strong interactions. Furthermore, quarks have smaller electric charge in comparison with leptons, it's relative values are $\pm\frac{1}{3}e$ and $\pm\frac{2}{3}e$. Known quarks are listed in the Table 1.1 together with their basic properties [4].

There are three color charges a quark can possess, *red* (r), *green* (g), and *blue* (b), and three corresponding anti-colors (\bar{r} , \bar{g} , and \bar{b}) for the anti-quarks. Quarks bind together through the strong interaction to form color-neutral bound-states of a dimension about 1 fm, known as *hadrons*, through the combination of a quark and anti-quark, known as

a *meson*, or through the combination of three quarks or anti-quarks each with different color, known as a *baryon*. However, the LHCb Collaboration at LHC recently confirmed [5] the existence of the state $Z(4430)^-$ as a particle whose minimal quark content is $c\bar{c}d\bar{u}$ [6]. This is the first unambiguous evidence for the existence of mesons beyond the traditional $q\bar{q}$ model [7].

1.1.2 Asymptotic Freedom

The nucleon structure mentioned in previous paragraphs reveals during deep inelastic scattering [1], [2]. Quarks used to act as point-like free particles. This feature called *asymptotic freedom* can be explained by the assumption of the self-interacting gluon field leading to creation of the bosonic loops between bosonic propagators (see Figure 1.1).

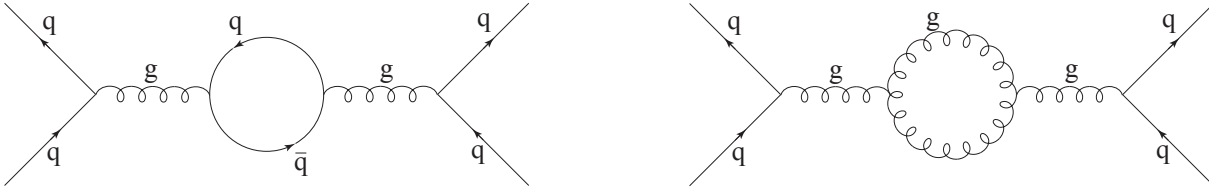


Figure 1.1: Quarkonic and gluonic loops between gluonic propagators.

The effect of vacuum polarization in QED (fermionic loops) implies the shadowing of the electric charge among interacting particles. At large momentum transfers Q , the particles penetrate through the cloud of virtual e^+e^- pairs, whereby they get a higher effective charge and the strength of the interaction increases. Quarkonic loops in QCD has the same effect, but gluons unlike photons can also create virtual loops because they carry a color charge. Since there are more types of virtual gluons than quarks the gluonic loops contribute to the interaction constant α_S more than quarkonic loops. And because the contributions from gluonic loops have negative signs in QCD the α_S dwindles with decreasing distance (i.e. increase of the momentum transfer), as illustrated in Fig 1.2. Under extreme conditions, $\alpha_S \rightarrow 0$ and asymptotic freedom is achieved, whereby quarks and gluons behave like quasi-free particles.

1.1.3 The QCD Running Coupling Constant

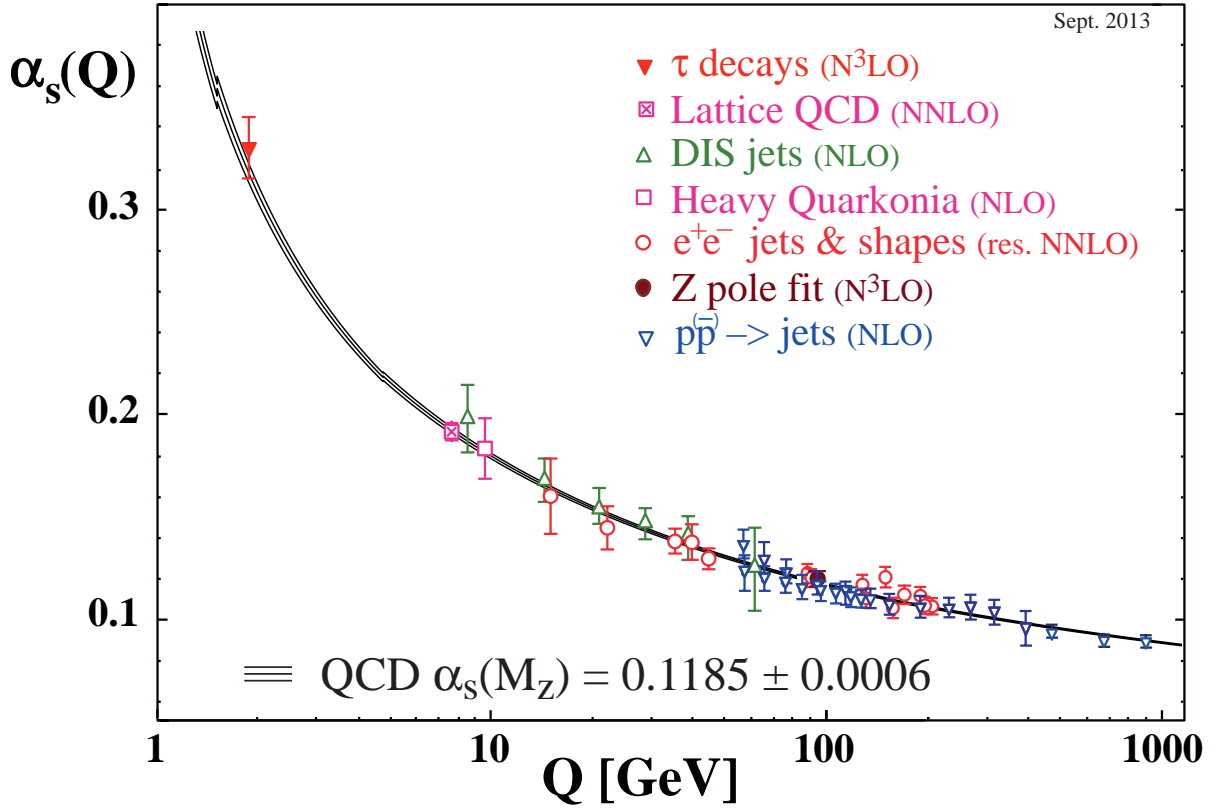


Figure 1.2: The strong coupling constant α_S as a function of the energy scale Q . The respective degree of QCD perturbation theory used in the extraction of α_S is indicated in brackets (NLO: next-to-leading order; NNLO: next-to-next-to leading order; res. NNLO: NNLO matched with resummed next-to-leading logs; N³LO: next-to-NNLO). Figure taken from Ref. [4].

The value of α_S , at a given energy or momentum transfer scale Q , can't be predicted by QCD and must be obtained from experiment. However, QCD predicts the functional form of the energy dependence of α_S in its simplest form [9] as

$$\alpha_S(Q^2) = \frac{12\pi}{(33 - 2N_f) \ln \frac{Q^2}{\Lambda^2}} \quad (1.1)$$

where N_f is the number of active quark flavors at the energy scale Q and Λ is the only dimensional parameter of pure QCD (pure means without extra matter). It replaces the

dimensionless α_S by a process called dimensional transmutation. Because α_S depends on the scale, it is pretty much true that every value of α_S is realized for some value of Q . Instead of talking about the values of $\alpha_S(Q)$, one may talk about the value of Q where α_S gets as big as one, and this value of Q is known as Λ_{QCD} .

Measurements of α_S are shown in Fig. 1.2 for a range of energy scales from $Q = 1.78$ GeV to $Q = 1$ TeV. The world average value of the strong coupling constant is evaluated at the mass of the Z boson, and is calculated as $\alpha_S(M_Z) = 0.1185 \pm 0.0006$ [4].

At energy scales above 1 GeV where $\alpha_S < 1$, QCD can be calculated perturbatively (pQCD), i.e. by usage of a truncated expansion of physical quantities in powers of α_S [10].

1.1.4 Confinement, Deconfinement and Bag Model

When α_S approaches unity, pQCD fails and QCD equations became hardly solvable. Low energy scale interactions, such as the fragmentation of quarks and gluons into colorless hadrons (*hadronization*) can be studied using numerical methods like *Lattice Gauge Theory* (lQCD) [11]. By using lattice QCD, the QCD potential can be approximately estimated as

$$V(r) \approx \lambda r. \quad (1.2)$$

Fermionic loops in QED shield the electric charge, hence the electromagnetic force dwindles at increasing distances. But, gluonic loops amplify the color charge making the interaction constant surge at increasing distances. The connection between the two quarks becomes like a color flux. When enough energy is stored in the flux tube, colorless $q\bar{q}$ pairs can be formed quantum-mechanically out of the vacuum. This process is called *string fragmentation*. String fragmentation makes it impossible to extract an individual quark from a hadron unless the magnitude of the strong coupling is significantly reduced. There-

fore, quarks are typically confined within hadrons. Under extreme conditions, quarks can indeed become deconfined and exists as free particles. Recent lattice QCD calculations estimate that this can happen at the so called *critical temperature* $T_c = 162$ MeV [12] which corresponds according to Maxwell-Boltzmann distribution to 1.9×10^{12} Kelvins. This theoretical phase of matter is called *quark-gluon plasma* (QGP).

The mechanism of such deconfinement can be described by the so called *bag model*; If there is a system of quarks and gluons bound into a hadron, then the color fields create region of positive energy density, called a *bag*, which contains all the partons within a hadron [13]. The boundary of the bag exerts an inward pressure which keeps the quarks confined. If the temperature is forced to increase, then the volume of the bags must increase to compensate. If the temperature is high enough, the bags will start to overlap and merge. At this point, the system is best described as one big bag containing all of the partons. This represents deconfined matter. Likewise, if the bags are forced into a small volume they will also overlap and merge.

1.2 Lagrangian QCD and Chiral Symmetry

QCD is described by a Lagrangian and its symmetries which corresponds to conservation laws (according to the Noether's theorem) of currents and charges. The QCD Lagrangian density is given by

$$\mathcal{L} = \overline{\psi}_q(x)[i\gamma^\mu D_\mu - m_q]\psi_q(x) - \frac{1}{4}G_{\mu\nu}^a G^{a\mu\nu} \quad (1.3)$$

where ψ_q is quark field, γ_μ Dirac matrices, and $G_{\mu\nu}^a$ gluonic tensor

$$G_{\mu\nu}^a(x) = \partial_\mu A_\nu^a(x) - \partial_\nu A_\mu^a(x) + gf^{abc}A_\mu^b(x)A_\nu^c(x)$$

The $D_\mu \equiv \partial_\mu - ig\frac{\lambda^a}{2}A_\mu^a(x)$ is covariant derivative responsible for the interaction between quarks and calibrating potential $A_\mu^a(x)$, g interaction constant, λ_a Gell-Mann matrices, and f^{abc} structural constant of the group SU(3).

\mathcal{L} has several global symmetries as well as the local SU(3) color gauge symmetry. The relevant symmetry here is chirality, which can be manifested by rewriting \mathcal{L} in terms of left- and right-handed quark fields. The handed-ness is defined as

$$\psi_L \equiv \frac{1}{2}(1 - \gamma^5)\psi \quad \psi_R \equiv \frac{1}{2}(1 + \gamma^5)\psi \quad (1.4)$$

so that L and R correspond to helicity -1 and $+1$ in the limit of quark masses equal to zero. For small quark masses compared to the Λ introduced in (1.1) with value around 200 MeV, we can neglect the mass terms and \mathcal{L} becomes invariant under $SU(3)_R \times SU(3)_L$. These symmetries are called chiral symmetries because they conserve quark handedness (chirality).

1.2.1 Spontaneous Breaking of Chiral Symmetry

While \mathcal{L} has chiral symmetry, the vacuum state does not share this symmetry [14], so the Chiral Symmetry is spontaneously broken. In 1961 (before the Goldstone theorem or even quarks themselves were introduced) Nambu and Jona-Lasinio suggested that this is because of a nonzero vacuum expectation value (VEV) of $\psi\bar{\psi}$ condensation [15]. The idea came from the analogy with the theory of superconductivity.

Imagine a traveling quark ψ_L collides with $\psi_R\bar{\psi}_L$, which fills the QCD vacuum, and annihilates the $\bar{\psi}_L$ in the pair freeing the ψ_R which continues to propagate. The ψ_R carries the same momentum and quantum numbers except for chirality. This is Yukawa coupling which could be written in the Lagrangian and serve as a mass term for quarks. This term also does not explicitly break chiral symmetry of the Lagrangian. This mass generating mechanism is similar to the Higgs-Kibble mechanism except the mass generating field is the $\psi_R\bar{\psi}_L$ field instead of the Higgs field. One has to note also, that the Chiral Symmetry is not a perfect symmetry of QCD, but only an approximate one as far as the pions as the Goldstone bosons have a finite even if small (compared to all other hadrons) mass. Thus the mass of quarks confined in hadrons have two components, the component generated

by the interaction with the Higgs field and explicitly breaking the chiral symmetry of QCD Lagrangian, and the component generated by the interaction with $\psi_R \bar{\psi}_L$ and spontaneously breaking the QCD Lagrangian. Let's call those masses *Higgs quark mass* and *QCD quark mass* respectively.

1.2.2 Restoration of Chiral Symmetry and Quark Gluon Plasma

According to thermal quantum field theory, the spontaneously broken chiral symmetry can be restored at high temperature [16] created in high energy heavy ion collisions. At high temperatures, due to kinematical energy, the pair production energy increases. If it exceeds the binding energy of $\psi_R \bar{\psi}_L$ pairs, there is no more condensation and chiral symmetry is restored. QCD predicts that hadronic matter undergoes a phase transition to QGP where quarks and gluons are deconfined from bound states of hadrons.

As mentioned in previous paragraphs, quarks are confined inside hadrons while their mass is dominantly generated by Yukawa's coupling to QCD vacuum. However, this is valid only in the case of light quarks u and d , partially in case of strange quarks. The masses of Heavy quarks (c, b, t) are almost exclusively generated through their coupling to the Higgs field, as shown in Figure 1.3. In a QGP, where chiral symmetry might be restored, light quarks are left with their bare current masses while heavy quarks's masses remain unchanged [17].

1.3 Heavy Ion Collisions

Experimental physicists have developed excellent facilities called heavy ion colliders which are capable to bring up conditions required for QGP formation. One of the colliders called The Relativistic Heavy Ion Collider (RHIC) located at the Brookhaven National

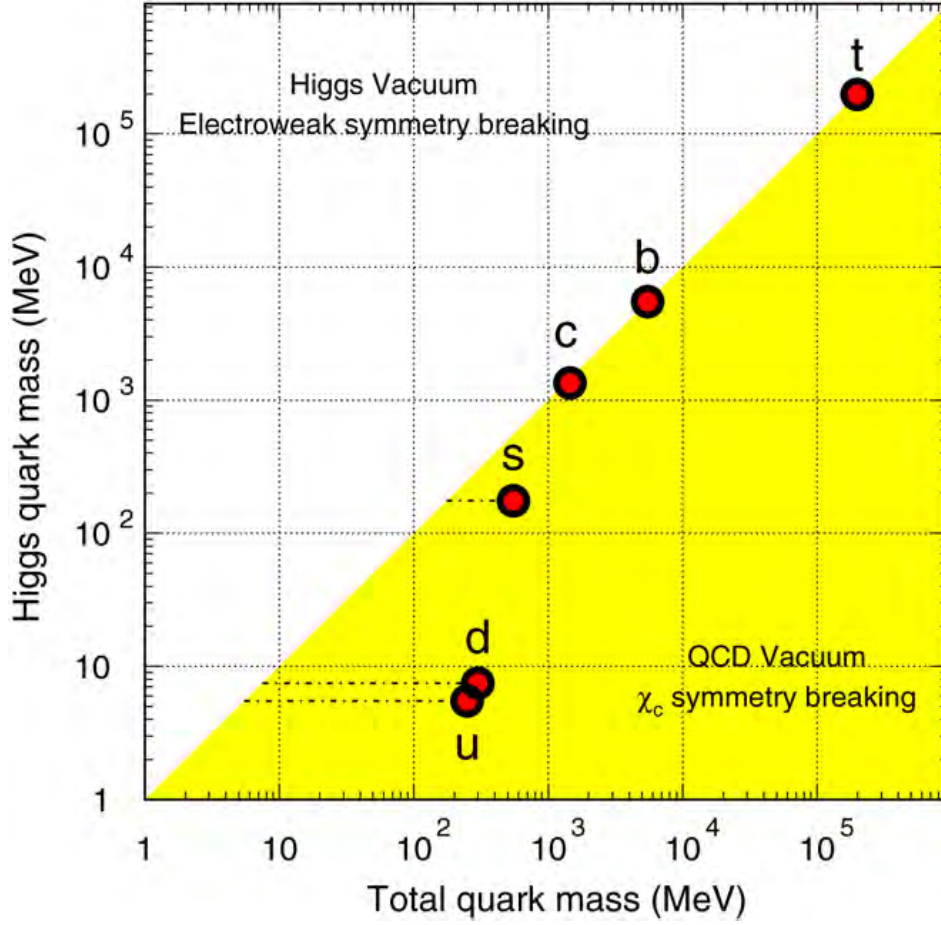


Figure 1.3: Quark masses in the QCD vacuum and the Higgs vacuum. Figure taken from Ref. [17].

Laboratory (BNL) in Long Island, state New York, was particularly designed to form QGP by colliding Au nuclei at $\sqrt{s} = 200$ GeV per nucleon. The experimental layout of this facility is described in Section 2.1 and a description of the space-time evolution, energy density, and freeze-out conditions are discussed in this section. This is followed by a description of several signatures for the existence of a QGP in heavy ion collisions. This section only defines a comments those signatures, the experimental results confirming the existence of QGP is described in section 1.5.

1.3.1 Space-time Evolution

The space-time evolution of a heavy ion collision is shown in Fig. 1.4 assuming that QGP is formed. The figure is asymmetrically divided into narrow column on the left depicting schematically various stages of the collision rotated by 90 degrees and wide space-time graph roughly showing the corresponding stages of the matter on the right. τ and T denote the proper time of the evolving system $\tau = \sqrt{t^2 - z^2}$ (τ as the variable and T as a value).

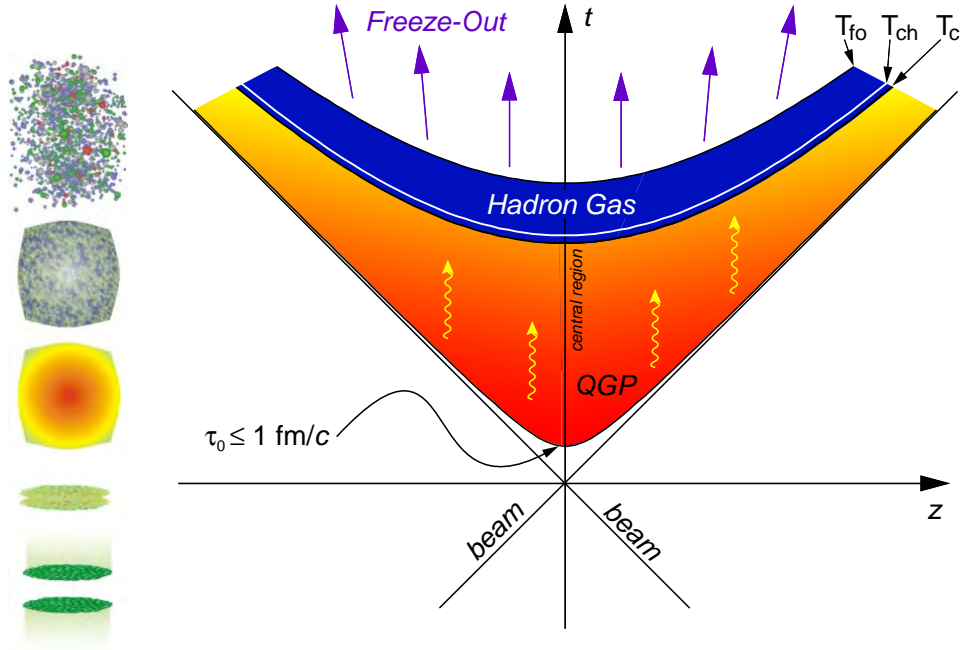


Figure 1.4: The space-time evolution of a heavy ion collision. Figure taken from Ref. [19].

The incoming nuclei moving at relativistic speeds are Lorentz contracted in the direction of motion, appearing as thin disks to an observer at rest. As the nuclei collide, the partons experience hard interactions from which heavy quarks and high- p_T jets are formed. As the nuclei traverse each other, they create an area in which the temperature and density increase and more quark anti-quark pairs are created. This area is called fireball. As the energy density reaches the critical value, quarks become deconfined, the chiral

symmetry is restored and the nuclear matter transits into QGP. The QGP is in the thermal equilibrium, the pressure of the system causes the fireball to expand, and temperatures and densities begin to decrease until the critical temperature T_c (see the graph on Figure 1.4) is reached again, the matter transits from QGP and hadronization occurs, i.e. quarks become confined in hadrons again and chiral symmetry spontaneously break. Those newly created hadrons are still close to each other so that inelastic collisions are dominant. The system expands and cools until it reaches the chemical freeze-out temperature (T_{ch}), after which only elastic collisions can frequently occur so particle ratios become fixed, because hadrons can no longer be destroyed. After further expansion and cooling, the average distance between the hadrons is longer than the strong interaction range so that even the particle momenta can't be changed. This stage is called the kinetic freeze-out (T_{fo}).

QGP cannot be directly observed, because the deconfined state occurs during the time of units of fm/c (the exact time depends on the initial energy density, the volume of the of the fireball and the precise value is unknown; some values will be discussed in the next subsection). Strong experimental arguments indicate that the transition to a QGP has indeed occurred [18]. Those arguments are called QGP signatures and some of them are discussed in further in this section.

1.3.2 Initial Energy Density - Bjorken Formula

The energy density necessary to form QGP has been expected to be $\mathcal{E}_c \sim 1 \text{ GeV/fm}^3$ [21]. The Bjorken energy density [20] is used in measurements of the peak energy density in heavy ion collisions, and is defined as

$$\mathcal{E}_{\text{Bj}}(\tau) = \frac{1}{\tau_0 S_T} \frac{dE_T}{dy}, \quad (1.5)$$

where τ_0 is the formation time of the medium, S_T is the transverse area overlap of the

colliding nuclei, and dE_T/dy is the transverse energy density per unit rapidity which is usually measured. The value at RHIC for $\sqrt{s_{NN}} = 200$ GeV was measured to be 5.4 GeV/fm³ in the most central collisions (all nucleons participate in collision) [22]. The Bjorken model requires a small crossing time for the nuclei ($\tau < 2R/\gamma = 0.13$ in Au+Au collisions at $\sqrt{s_{NN}} = 200$ GeV) and the calculation in [22] assumes $\tau_0 = 1$ fm/c.

1.3.3 Partonic Collectivity

In the heavy ion collisions which are not central, the fireball has an almond shape which is spatially anisotropic. This initial spatial anisotropy transforms into a momentum anisotropy due to the different pressure gradients in the expanding fireball, shown in Figure 1.5 as the red area. This boosts momenta of particles in the direction of the pressure gradient.

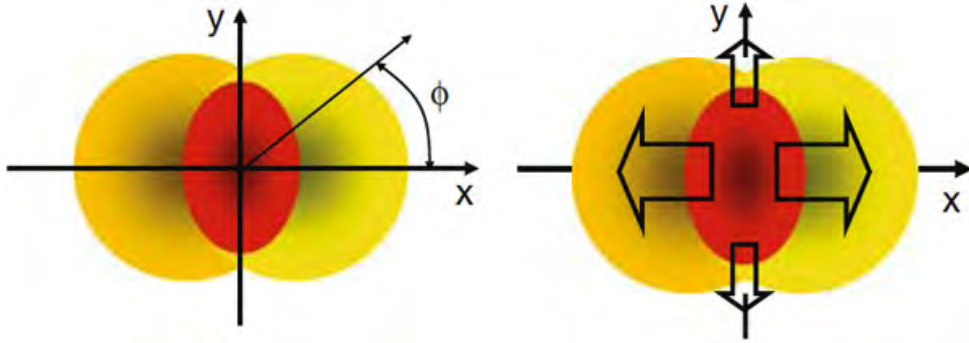


Figure 1.5: Non-central collision. Participant nucleons in the almond-shaped overlap region experience a force from the pressure gradient. Figure taken from Ref. [23].

The momentum anisotropy called *flow* is determined by decomposing the observed final-state particle distribution into a Fourier expansion, i.e.

$$E \frac{d^3 N}{dp^3} = \frac{d^2 N}{2\pi p_T dp_T dy} \left(1 + \sum_{n=1}^{\infty} 2v_n \cos[n(\phi - \phi_{RP})] \right), \quad (1.6)$$

where ϕ_{RP} is the reaction plane angle (Figure 1.5 depicts the case when $\phi_{\text{RP}} = 0$) and the coefficients

$$v_n = \langle \cos[n(\phi - \phi_{\text{RP}})] \rangle \quad (1.7)$$

represent the flow. v_1 is called *radial flow*, v_2 *elliptical flow*, v_3 *triangular flow*, etc. The elliptic flow is the most interesting observable, because it's the largest at mid-rapidity which makes it very sensitive QGP signature providing the degree of thermalization.

1.3.4 Energy Loss and Suppression

Another QGP signature is the suppression of particle production in heavy ion collisions. The suppression is represented by observable called the *nuclear modification factor* R_{AB} in the collision system $A + B$ with respect to a reference measurement, generally obtained from p+p collisions at the same energy:

$$R_{AB} \equiv \frac{1}{N_{\text{bin}}} \frac{\frac{d^2 N_{AB}(p_T)}{dp_T dy}}{\frac{d^2 N_{p+p}(p_T)}{dp_T dy}}, \quad (1.8)$$

where N_{bin} is average number of binary (nucleon on nucleon) collisions in the $A+B$ system, $d^2 N_{AB}(p_T)/(dp_T dy)$ differential invariant yield from the $A + B$ and $d^2 N_{p+p}(p_T)/(dp_T dy)$ from the p+p. N_{bin} as well as the centrality of the collision (sometimes called the number of participants) is calculated from particle multiplicity by using the Glauber model based fits into particle multiplicity distribution [24].

High-momentum partons are created in hard-scattering processes that occur in the early stage of an collision (either $A+B$, $p+A$, or p+p). Their production can be calculated using perturbative QCD. They subsequently traverse the hot QGP, losing energy as they interact with its constituents. This energy loss is expected to occur via inelastic processes (gluon radiation induced in the medium, or radiative energy loss, analogous to bremsstrahlung

in QED) and via elastic processes (collisional energy loss). Such energy loss would result in the p_T spectrum modification relative to the spectrum in p+p collisions where newly created particles travel through the QCD vacuum instead of the QGP. It is not possible to measure those high-momentum partons directly. One can either reconstruct clusters of correlated hadrons known as *jets* or reconstruct hadrons consisting of at least one heavy quark (charm or bottom). Energy loss would then result in the softening and broadening of the observed jet structure, known as *jet quenching*, or $R_{AB} < 1$ for high-momentum heavy quark hadrons respectively. The main disadvantage of studying the energy loss through jet quenching lies in the jet reconstruction, which depends on the used reconstruction algorithm, whereas the type of the parton traveling through QGP is known in the case of heavy quark hadrons reconstruction. The details about heavy quark production are discussed in the next section.

Heavy quarks are an excellent probe to study properties of QGP, because

- the formation time of heavy quarks is smaller than the formation of QGP,
- interactions with QGP don't change flavor identity,
- the temperature of QGP is lower than the minimum energy for the creation of heavy quark-antiquark pair, so they cannot be destroyed/created in the QGP and thus can penetrate through all stages of the system evolution.

1.4 Heavy Quark Production

The heavy quark production is dominated by initial gluon fusion at initial hard partonic collisions and can be described by perturbative QCD (pQCD) due to their large mass [27]. The minimum value of momentum transfer Q in the production of a heavy quark-antiquark pair is $2m_q$ where m_q is the heavy quark mass. So the space-time scale is in the

order of $1/2m_q \sim 0.1 \text{ fm}/c$ for charm and $\sim 0.02 \text{ fm}/c$ for bottom quark which is much lower than the expected lifetime of the QGP.

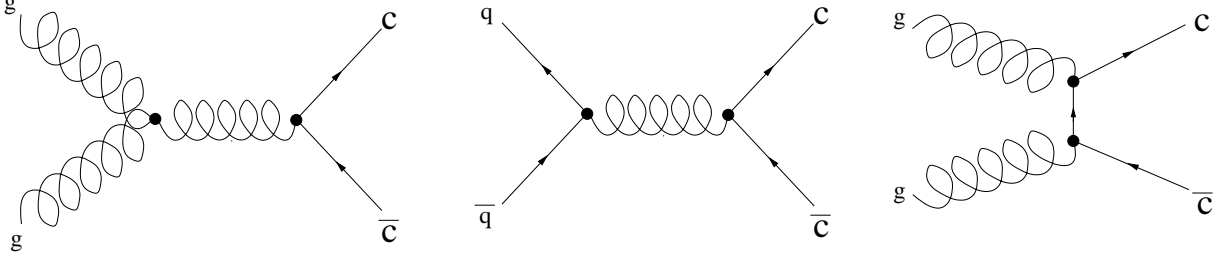


Figure 1.6: The basic Feynman diagrams for charm quark pair production at the Leading Order (LO) level.

The charm cross-section can be calculated from an amplitude which is found by summing up the terms of the Feynman diagrams. Three of the lowest order (Leading Order) diagrams for charm in 200 GeV collisions are shown in Figure 1.6. They have been evaluated at the Next-to-Leading Order (NLO) level [25] including diagrams of orders α_S^2 and α_S^3 . The renormalization scale has been chosen near or at the m_q . This calculation has been extended to the Fixed-Order Next-to-Leading-Log level (FONLL) by including terms of orders $\alpha_S^2 (\alpha_S \log(p_T/m_q))^k$ (Leading Log) and $\alpha_S^3 (\alpha_S \log(p_T/m_q))^k$ (Next-to-leading Log) owing to the rise of large logarithms of the ratio p_T/m_q to all orders in the perturbative expansion [26]. The results for p+p collisions at $\sqrt{s} = 200 \text{ GeV}$ using the FONLL approach were presented in [27] and confirmed by results presented in [28] based also on analysis discussed in this thesis. However, calculations of the charm cross section at low p_T ($< 1 \text{ GeV}/c$) become complicated because charm quarks cannot be treated as a massless flavor. Furthermore, in the low momentum transfer region there is a large uncertainty in the gluon density function, and the strong coupling constant increases dramatically. Thus, pQCD calculations have little predictive power for the total charm cross section in high-energy hadron-hadron collisions [29]. These theoretical issues further demonstrate the necessity of precise experimental measurements to provide constraints that improve theoretical calculations like the one published in [30].

1.5 A Selection of Current Experimental Results

This section will discuss a selection of experimental results relevant to the analysis described in this thesis in chapters 3, 4, 5, and 6. The first subsection will present a measurement in p+p collisions focused mainly on comparison with FONLL, whereas all other subsections will present measurements in the heavy ion collisions.

The state-of-art measurements of inclusive heavy quark production are carried out through two main approaches:

1. single leptons from heavy-flavor semi-leptonic decays
2. hadrons from hadronic decays

Both are drawn schematically in Figure 1.7 which depicts a created pair of charm quarks hadronizing into *open charm* mesons D^0 and \bar{D}^0 whose properties can be found in [4] where one can find also the probability of a charm quark hadronizing to D^0 meson being 56.5%. The term "open charm" emphasizes the fact that such particle consists of just one charm quark or antiquark. When it comes to bottom quarks, one can analogically use the term *open bottom*. The Figure further shows the D^0 undergoing a hadronic decay into negative kaon and positive pion with branching ratio of 3.87% and \bar{D}^0 undergoing a semi-leptonic decay into electron (or muon), corresponding neutrino and positive kaon. The branching ratio of such decay is 9.6%. All of those number are again taken from Ref. [4]. One advantage of the first method is that the electrons, called *non-photonic electrons* (NPE), coming from the semi-leptonic decay of the open charm or open bottom mesons are easy to be triggered by detectors and another advantage is relatively large branching ratio resulting in relatively large statistics. However, interpretations of the experimental results contain ambiguities because

- (a) electrons or muons are produced by various charmed and bottomed hadron decays, and

(b) heavy-flavor hadrons contributing to leptons at a certain p_T can come from a wide kinematic region due to the decay smearing. The second method suffers from a large combinatorial background particularly (signal to background ratio is on the order of 1/1000) in heavy-ion collisions.

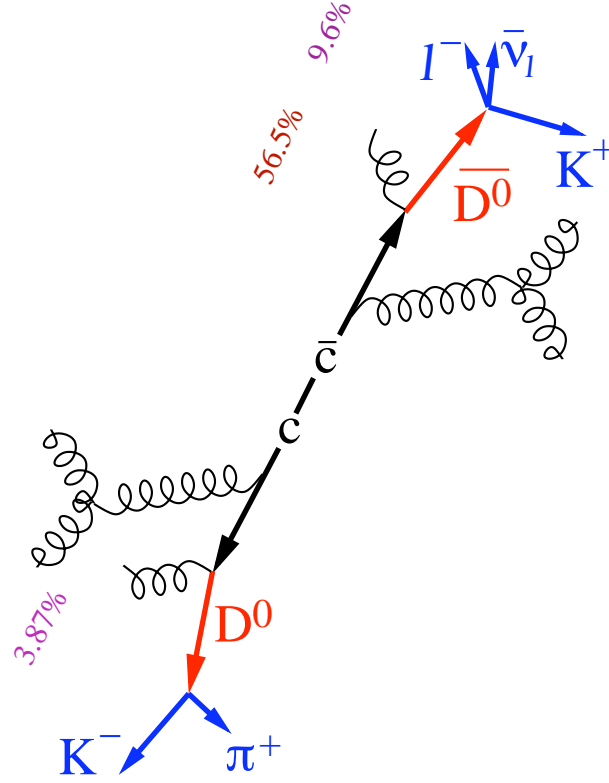


Figure 1.7: Charm quark fragmentation to D^0 and two main D^0 decay channels.

The long-term goal of the heavy flavor physics in the STAR Collaboration decadal plan [31] (STAR experiment is discussed in chapter 2) has been to give answers to questions:

- Are the interactions of energetic partons with QCD matter characterized by weak or strong coupling?
- What is the detailed mechanism for partonic energy loss?

Let's note that the term "weak coupling" has nothing to do with the weak interaction,

but it regards the QCD running coupling constant.

1.5.1 Invariant Cross Section of Non-photonic Electrons Produced in p+p Collisions

Electrons from bottom and charm meson decays are the two dominant components of the non-photonic electrons. Mostly due to the decay kinematics, the azimuthal correlations between the daughter electron and daughter hadron are different for bottom meson decays and charm meson decays. A study of these azimuthal correlations has been carried out on STAR data and is compared with a PYTHIA [32] simulation to obtain the ratio of the bottom electron yield to the heavy-flavor decay electron yield $\frac{e_b}{e_b+e_c}$ [33], where PYTHIA was tuned to reproduce STAR measurements of D mesons p_T spectra [34]. Using the measured $e_b/(e_b + e_c)$ together with the measured non-photonic electron cross section with the electrons from J/Ψ , Υ decay and Drell-Yan processes subtracted, these two components were disentangled. Figure 1.8 shows the invariant cross section of electrons $\left(\frac{e^++e^-}{2}\right)$ from bottom (upper left) and charm (upper right) mesons as a function of p_T and the corresponding FONLL predictions, along with the ratio of each measurement to the FONLL calculations (lower panels).

The integrated cross section of electrons $\left(\frac{e^++e^-}{2}\right)$ at $3 \text{ GeV}/c < p_T < 10 \text{ GeV}/c$ coming from open bottom, open charm were measured to be

$$\begin{aligned} \left. \frac{d\sigma_{(B \rightarrow e) + (B \rightarrow D \rightarrow e)}}{dy} \right|_{y_e=0} &= 4.0 \pm 0.5(\text{stat}) \pm 1.1(\text{syst})\text{nb}, \\ \left. \frac{d\sigma_{D \rightarrow e}}{dy} \right|_{y_e=0} &= 6.2 \pm 0.7(\text{stat}) \pm 1.5(\text{syst})\text{nb} \end{aligned}$$

respectively.

The FONLL prediction was successfully tested also at Tevatron [35] and LHC [36] energies as well as in this thesis for RHIC energies of $\sqrt{s} = 200$ and 500 GeV (see chapter 6).

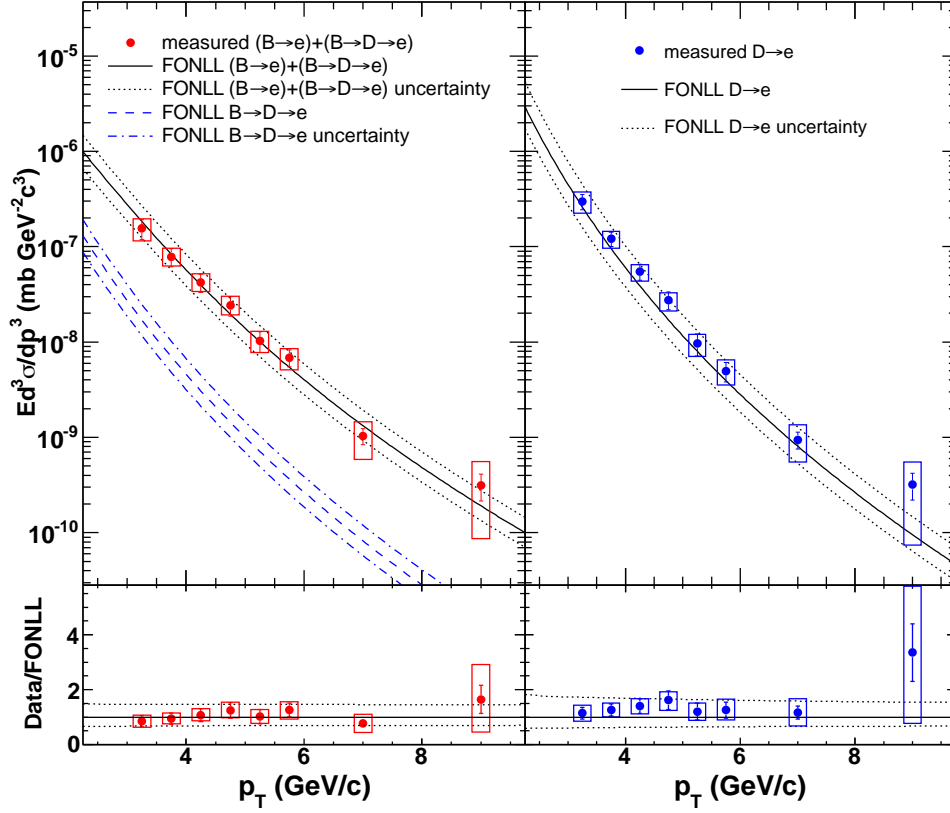


Figure 1.8: Invariant cross section of electrons from bottom (upper left) and charm meson (upper right) decay, together with the ratio of the corresponding measurements to the FONLL predictions for bottom (lower left) and charm electrons (lower right). The solid circles are experimental measurements. The error bars and the boxes are, respectively, the statistical and systematic uncertainties. The solid and dotted curves are the FONLL predictions and their uncertainties. The dashed and dot-dashed curves are the FONLL prediction for $B \rightarrow D \rightarrow e$.

1.5.2 Invariant Cross Section of D^0 Mesons in p+p and Au+Au Collisions at $\sqrt{s_{NN}} = 200$ GeV

A temperature of 300-600 MeV, which may have been reached in 200 GeV central Au+Au collisions of RHIC [37] is significantly lower than the threshold energy of charm-anticharm quark pair production, thus no thermal production of heavy flavor is expected to take place and therefore the initially produced heavy quarks experience the full collision history with the medium. The Figure 1.9 shows charm pair production cross section per one binary collision $\sigma_{c\bar{c}}^{NN}$ as a function of the number of binary collisions N_{bin} .

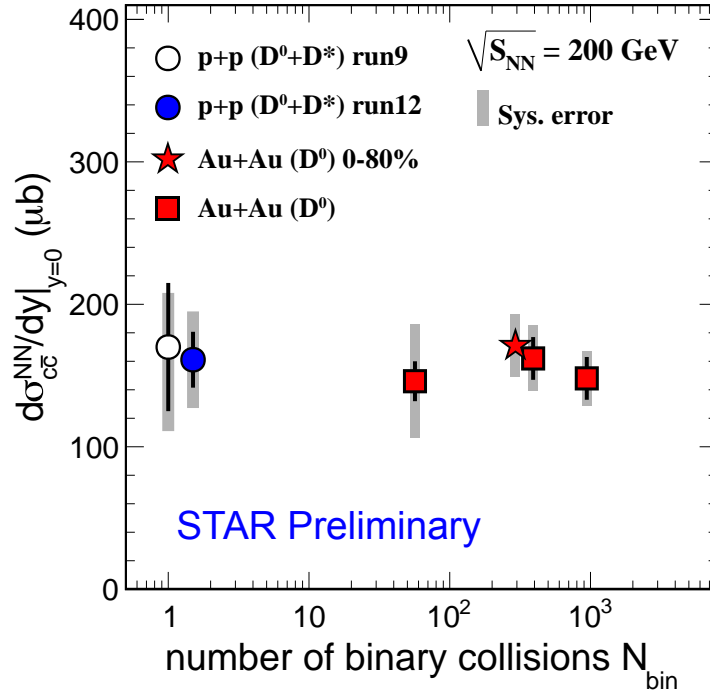


Figure 1.9: Charm quark pair cross section as a function of the number of binary collisions N_{bin} . Circles represent measurement in p+p collisions carried out in years 2009 (run9) and 2012 (run12), artificially nudged aside of each other for better clarity, and squares represent measurement in Au+Au collisions for various centralities. The asterisk denotes the measurement in AuAu collisions all centralities combined.

The integrated cross section (integrated over all p_T) scales with number of binary collision, which is consistent with the expectation of the charm quarks being produced in initial hard processes. It also might suggest that the nuclear shadowing¹ are not significant at $\sqrt{s_{NN}} = 200$ GeV, but it is necessary to have measurements in d+Au or p+Au collisions to be sure about such assumptions.

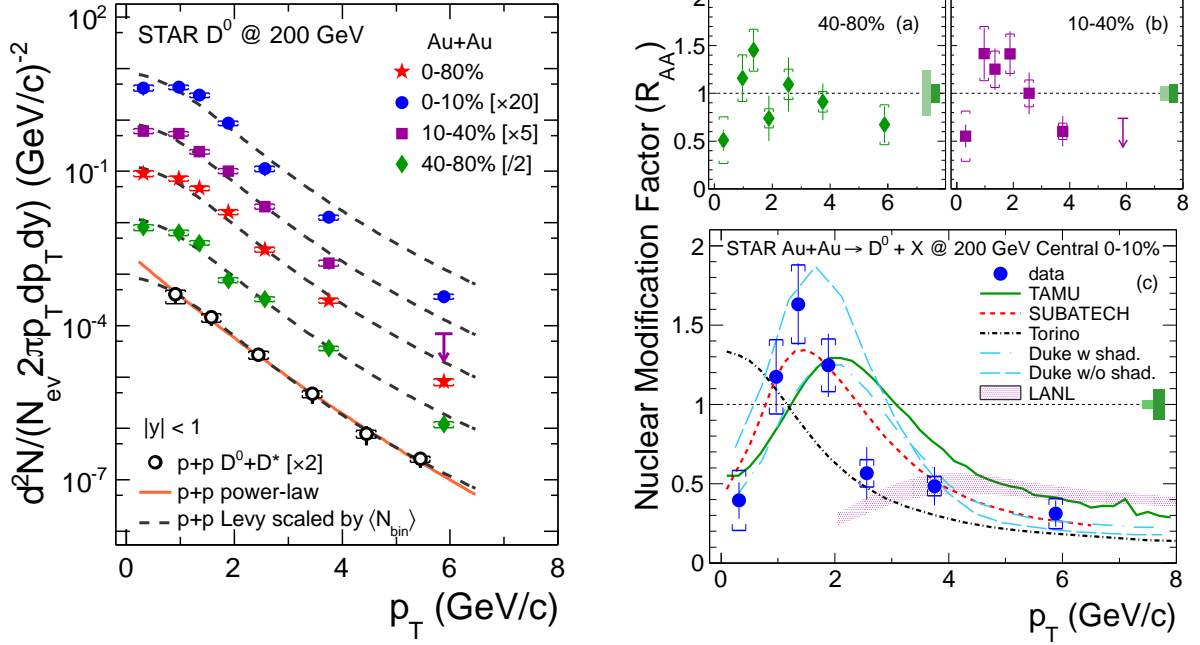
1.5.3 Nuclear Modification Factor of D^0 production at RHIC

Figure 1.10a reveals the experimental result on the modification of the D^0 differential invariant yield p_T spectra in Au+Au collisions at $\sqrt{s} = 200$ GeV from the STAR Collaboration. Figure 1.10b shows D^0 nuclear modification factor R_{AA} for the centrality bins of 40-80% (panel a), 10-40% (panel b) and 0-10% (panel c). The vertical bars around unity in Figure 1.10b from left to right represent the overall scaling uncertainties for N_{bin} in Au+Au collisions and cross-section in p+p collisions, respectively. Strong suppression is observed in the most central collisions for $p_T > 2.5$ GeV/ c , while no suppression is seen in peripheral collisions which is similar to the suppression of the light hadrons [38]. Figure 1.10b (panel c) also shows a comparison of the measured R_{AA} with several recent model calculations. The paper [39] provides a detailed discussion of the results. Let's summarize main findings in the next 3 paragraphs.

Energetic heavy quarks were predicted to lose less energy than light quarks via gluon radiation when they traverse the QGP [40]. In contrast, measurements of heavy flavor decay electrons at RHIC and charm hadrons at the LHC show significant suppression at high transverse momentum, p_T , in central Au+Au collisions, similar to that of light hadrons [41], [42], [43]. This has led to the reconsideration of the effect of heavy-quark collisional energy loss [44], [45]. A complete understanding of the partonic energy loss mechanisms in the QGP requires systematic and precise measurements of various hadrons

¹Parton distribution functions (PDF) of a single nucleon differ from PDF of a nucleon binded in nucleus, which can affect production cross sections in heavy ion collisions

carrying different quark flavors at RHIC and the LHC.



(a) Centrality dependence of the D^0 p_T differential invariant yield in Au+Au collisions (solid symbols). The curves are number-of-binary-collision-scaled Lévy functions from fit to the p+p result (open circles) [28]. The arrow denotes the upper limit with 90% confidence level of the last data point for 10-40% collisions.

(b) Panels (a)(b): D^0 R_{AA} for peripheral 40-80% and semi-central 10-40% collisions; Panel (c): D^0 R_{AA} for 0-10% most central events (blue circles) compared with model calculations. The vertical bars around unity denote the overall normalization uncertainties in the Au+Au and p+p data, respectively.

Figure 1.10: The p_T -differential D^0 invariant yield in Au+Au collisions at $\sqrt{s} = 200$ GeV for various centralities (subfigure a) and the D^0 meson nuclear modification factor (subfigure b). Figures taken from Ref. [39].

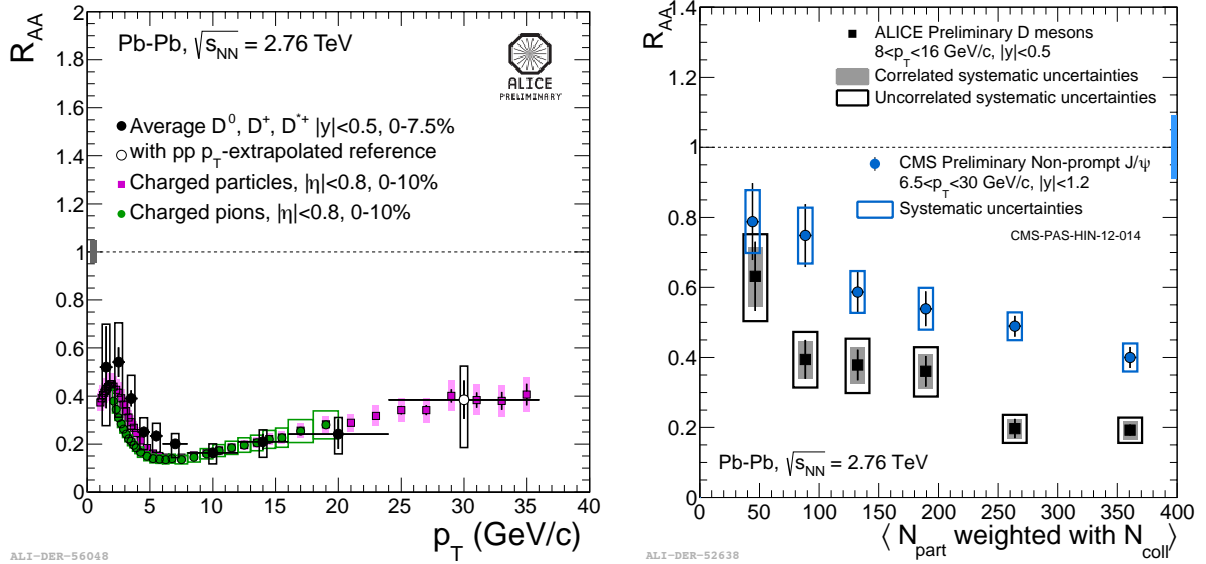
Heavy quarks are expected to hadronize in elementary collisions mainly through hard fragmentation. In high-energy heavy-ion collisions, the large charm-pair abundance could increase the coalescence probability, in particular for $p_T \lesssim 2$ GeV/c. The coalescence of charm with a light quark from the medium with a large radial flow may introduce a p_T -

dependent enhancement to the observed charmed hadron spectrum compared to that from fragmentation [46], [47]. Furthermore, this may lead to a baryon-to-meson enhancement for charmed hadrons similar to that observed for light-flavor hadrons [48], [38].

The TAMU group [46] used the Langevin approach to calculate heavy quark propagation in the medium, which was described by a (2+1)D ideal hydrodynamic model. The interaction strength between a charm quark and the medium is calculated using the T-Matrix dynamic method, including charmed resonance continuous regeneration and dissociation. While traversing through the medium, collisional energy loss and the hadronization including both fragmentation and coalescence mechanisms are considered for the charm quark. The SUBATECH group [47] used the Hard-Thermal-Loop (HTL) to calculate charm-medium interactions with both fragmentation and coalescence hadronization processes. It suggests that the radiative energy loss has a negligible impact on the final charmed hadron R_{AA} . The Torino group [49] directly applied the HTL calculation results to the charm-medium interaction strength from the SUBATECH group in their Langevin simulation. The medium was described via viscous hydrodynamics. But, they didn't include the charm-quark coalescence hadronization process. The Duke group calculation [50] used Langevin framework as TAMU, collisional plus radiative energy loss and hybrid fragmentation plus recombination or heavy quark coalescence with light quarks from the QGP. The recombination was calculated with and without nuclear shadowing effects highlighting the importance of Cold-nuclear-matter (CNM) effects. The maximum of R_{AA} around $p_T \simeq 1.5$ GeV/ c is consistent with the predictions of SUBATECH, Duke and TAMU groups whereas inconsistent with Torino prediction. SUBATECH explicitly suggests that the maximum is induced by the transverse flow picked up from the expanding medium through coalescence with light-quarks. This indicates that collisional energy loss alone can account for the large suppression in R_{AA} . A coalescence type mechanism is important in modeling charm-quark hadronization at low and intermediate p_T . CNM effects might play a role, but probably not as significant as Duke calculation has assumed.

1.5.4 Nuclear Modification Factor of D^0 production at LHC

Open Charm mesons R_{AA} has been measured by the ALICE Collaboration [51] at Large Hadron Collider (LHC) in Pb+Pb collision at $\sqrt{s_{NN}} = 2.76$ TeV. The results shown in Figure 1.11a reveals strong suppression of open charm mesons comparable (within errors) with light particles and consistent with the prediction of TAMU, SUBATECH, Torino and Duke models. However, the measurement is not precise enough to justify these models $p_T < 2$ GeV/ c . The radiative energy loss which might be negligible at low p_T should play a more significant role for heavy quarks with higher p_T which are likely to be produced at LHC. One then expects a hierarchy in the energy loss: $\Delta E_g > \Delta E_{u,d,s} > \Delta E_c > \Delta E_b$. Whether this will transform into $R_{AA}^\pi < R_{AA}^D < R_{AA}^B$, it still remains a question. However, CMS collaboration [52] analyzed production of the non-prompt J/ψ [53] which is exclusively a decay product of Open Bottom B mesons.



(a) R_{AA} of various open charm mesons, charged pions, and charged particles in most central Pb+Pb collisions.

(b) A comparison of the R_{AA} of charm and bottom production (through B meson decaying into J/ψ).

Figure 1.11: Nuclear modification factor in Pb+Pb collisions at $\sqrt{s_{NN}} = 2.76$ TeV.

Figure 1.11b shows R_{AA} as a function of centrality (proportional to number of binary collisions) of D mesons and non-prompt J/ψ . Rapidity ranges of those measurement slightly differ, but mean p_T is around 10 GeV/ c for both measurements. The comparison clearly indicates $R_{AA}^D < R_{AA}^B$ consistent with prediction [54]. The prediction includes mass-dependent radiative and collisional energy loss indicating $\Delta E_c > \Delta E_b$.

1.6 Thesis Outline

A brief overview of the Particle physics, Quantum Chromodynamics, and Heavy ion collisions together with the selection of experimental result has been presented in this chapter 1. Chapters 2-7 and appendices are dedicated to the analysis of D^0 and $D^{*\pm}$ meson production in p+p collisions at $\sqrt{s} = 200$ and 500 GeV at RHIC.

Chapter 2 describes briefly the accelerator RHIC and closely the experiment STAR at the configuration of the year 2011, i.e. the configuration which provided the data for the analysis described in this thesis. STAR experiment has been upgraded two new subsystems, Heavy Flavor Tracker and Muon Telescope Detector, which are covered in chapter 7. Chapter 3 describes the analysis of purely experimental data including some notes about the Time of Flight detector calibration, while chapter 4 describes a selection of experimental data enriched by simulated data whose purpose is to calculate detector efficiencies. Systematic errors have been always a know-how of experimental physicists hence chapter 5 is dedicated to them. The final results are presented in chapter 6 and their implications discussed in chapter 7 which also involves the discussion of the future of the open charm measurements at STAR.

The thesis headings have 4 levels, listed the highest to lowest level: chapter, section, subsection, and subsubsection.

CHAPTER 2

Experimental Setup

This chapter describes the experimental facility which provided data for the analysis discussed in chapters 3, 4, 5, and 6. The first section is about the accelerator, the second is the experiment overview and the following sections describe particular subsystems of the experiment.

2.1 The Relativistic Heavy Ion Collider

The Relativistic Heavy Ion Collider (RHIC) is experimental facility located at Brookhaven National Laboratory on Long Island, state New York. RHIC is also able to collide spin-polarized proton beams, and is still the most powerful polarized-proton collider. The scheme of the RHIC is depicted in Figure 2.1. The accelerator chain starts with an optically-pumped polarized H^- ion source [55] producing H^- ions at an energy of 35 keV to be accelerated to 200 MeV with a radio-frequency quadrupole and Linear Particle Accelerator (LINAC). The ions are then stripped of electrons by passage through a foil,

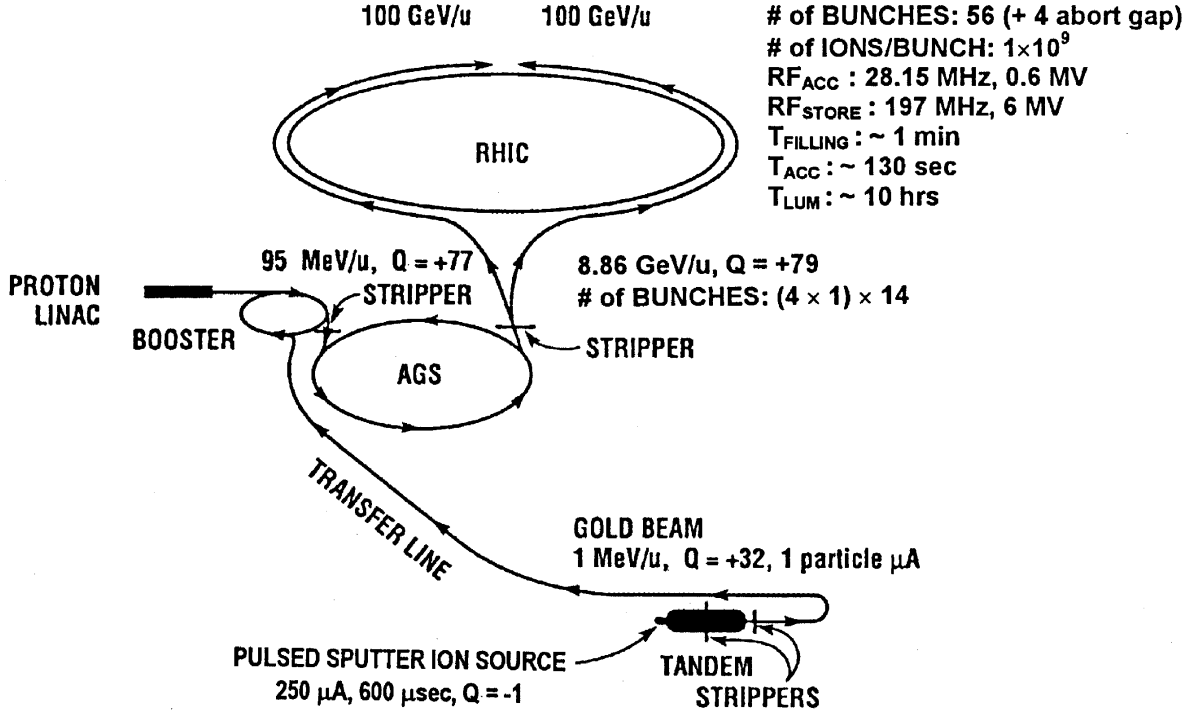


Figure 2.1: The RHIC accelerator scheme. Figure taken from Ref. [58].

creating a proton beam for injection into the Booster synchrotron [56] which further accelerates it to 2 GeV, and then to the Alternating Gradient Synchrotron (AGS) which boosts them to approximately 23 GeV. Finally the proton beam is split and injected into the RHIC rings where they are accelerated to the final energy 100 GeV or 250 GeV for collisions at center-of-mass energies of $\sqrt{s}=200$ GeV or 500 GeV [57].

The heavy ions to be collided originate from a pulsed sputter ion source [59] and they are then accelerated by a Tandem Van de Graaf accelerator to an energy of about 1 MeV/nucleon. The ions are then sent into the Booster synchrotron. After the Booster, ion beams are sent into the AGS to get to energies of 8.86 GeV/nucleon before injecting them into the RHIC ring. The maximum center-of-mass energy per nucleon RHIC can achieve with Au+Au collisions is 200 GeV and with U+U collisions it is 193 GeV.

Over the years, RHIC has collided p+p, Cu+Cu, Au+Au, U+U, using isotopes $^{63}_{29}\text{Cu}$,

$^{197}_{79}\text{Au}$, and $^{238}_{92}\text{U}$. There were also non-symmetric collisions of $\text{Cu}+\text{Au}$, $\text{He}+\text{Au}$, and $\text{d}+\text{Au}$. The $\text{d}+\text{Au}$ has particular importance in exploring the Cold nuclear matter effects. In 2015, RHIC will run 9 weeks of polarized $\text{p}+\text{p}$ collisions at $\sqrt{s} = 200$ GeV, 5 weeks of $\text{p}+\text{Au}$ collisions at $\sqrt{s_{NN}} = 200$ GeV with transverse polarization of the proton, and 2 weeks of $\text{p}+\text{Si}$ collisions $\sqrt{s_{NN}} = 200$ GeV with transverse polarization of the proton. In 2016, RHIC will run 10 weeks of $\text{Au}+\text{Au}$ collisions $\sqrt{s_{NN}} = 200$ GeV, 7 weeks of $\text{Au}+\text{Au}$ and $\text{p}+\text{p}$ collisions at $\sqrt{s_{NN}} = 62$ GeV, or 7 weeks of polarized $\text{p}+\text{p}$ collisions at 510 GeV.

2.2 The Solenoidal Tracker at RHIC

The Solenoidal Tracker At RHIC, summarily STAR, is named after room-temperature solenoid magnet which surrounds most of the detector subsystems. The STAR magnet can be run at either it's full field strength (0.5 T) or at half-full strength (0.25 T). The magnetic field is parallel to the beam axis, and is uniform within 0.0040 T [60]. The STAR detector [61] is a combination of 13 detector subsystems (see Figure 2.2 depicting 6 of them so that the end cap is pulled back allowing the internals of STAR to be viewed.) from which 6 are azimuthally symmetric about the beam pipe which run through the center of STAR and reciprocally homocentric covering the pseudorapidity range from -1 to 1 . Two of those five are newly installed Heavy Flavor Tracker (HFT) and Muon Telescope Detector. Both has not been available yet in 2011 and one is Barrel Shower-max Detector (BSMD) whose purpose is to measure detailed spatial shape of electromagnetic showers in order to separate showers caused by hadrons and by electrons. The rest three subsystems were used in this analysis, listed as follows

- Time Projection Chamber (TPC)
- Time Of Flight Detector(TOF)
- Barrel Electromagnetic Calorimeter (BEMC)

Then there are non-homocentric detectors, 2 are positioned in the forward rapidity region ($1.086 < \eta < 2$)

- Endcap Electromagnetic Calorimeter (EEMC)
- Forward GEM Tracker (FGT)

and 3 were paired coincidental fast triggering detectors

- Vertex Position Detector (VPD)
- Beam-beam Counter (BBC)
- Zero Degree Calorimeter (ZDC)

VPD has been the main triggering detector for p+p collisions since 2009 with the state of art time resolution around 80 ps, i.e. vertex z-position resolution < 2.5 cm. In AuAu collisions, the time resolution is outstanding 30 ps, thus it is also the best option for the TOF start time. BBC with its high efficiency (above 90%) provides the best estimation of event rate and ZDC (located 18 m down the beam line at the first bends of the beam pipe) is the most sensitive on any diffractive process that can occur being able to detect even singly diffractive processes. Finally, the remaining subsystem is Forward Muon Spectrometer (FMS).

Coordinates in STAR are often given in terms of the cartesian directions x , y , and z . These are defined such that the y -axis points up and the z -axis points along the beam line from the origin of the coordinate system ($x = y = z = 0$) at the geometric center of STAR towards forward rapidity detectors (FGT, EEMC). Angular coordinates such that θ is measured from the positive z -axis, and ϕ is measured from the positive y -axis. In practice, θ -angles are rarely used and angular coverage with respect to the z -axis is

Solenoidal Tracker At RHIC : $-1 < \eta < 1, 0 < \phi < 2\pi$

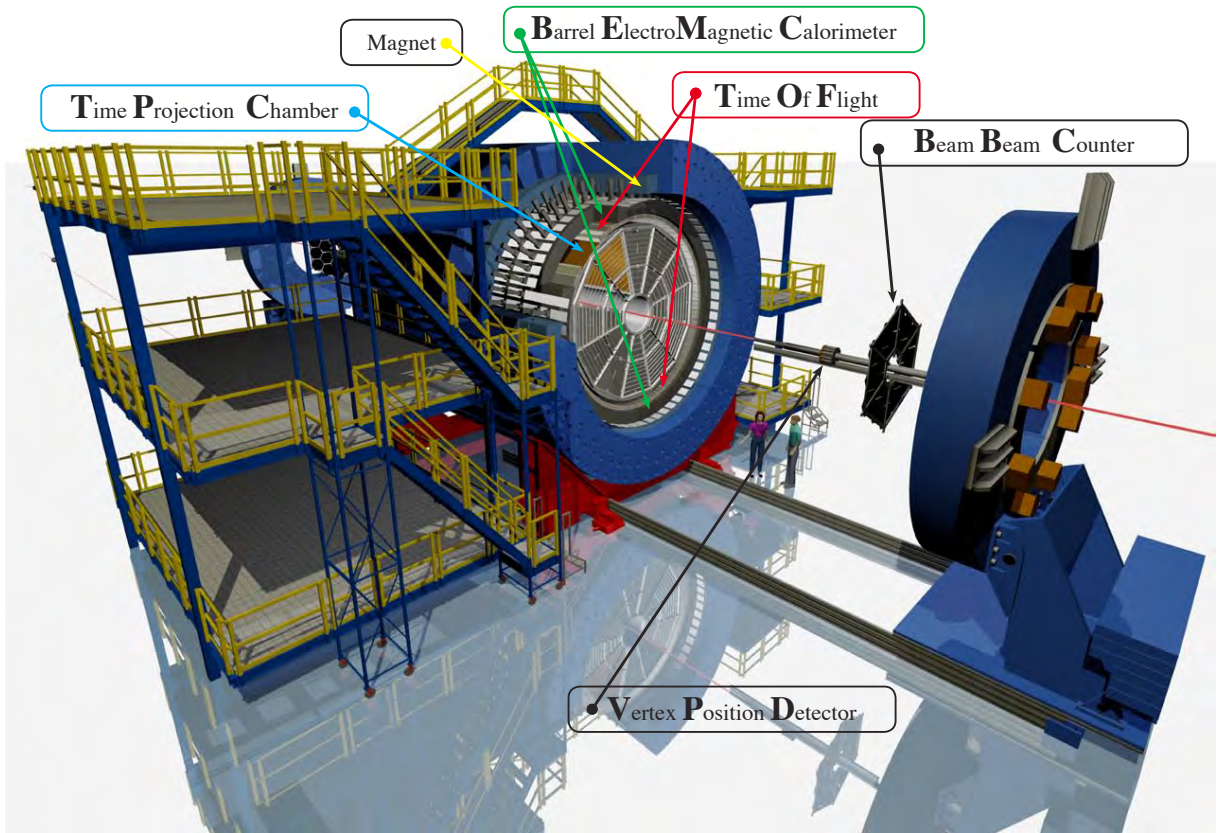


Figure 2.2: The Artistic view of the STAR detector.

usually given in terms of pseudorapidity, η , which is defined as:

$$\eta \equiv -\ln \left(\tan \frac{\theta}{2} \right). \quad (2.1)$$

2.3 Trigger

The STAR Trigger is a pipelined system in which digitized signals from the fast trigger detectors (VPD, ZDC, BBC, BEMC, EEMC, TOF) are examined at the bunch crossing rate ~ 10 MHz [62]. The scheme is depicted in Figure 2.3. The digitized signal from the detectors is fed into Data Storage and Manipulation (DSM) boards where it is analyzed and combined with the other signals in a 4-layer synchronous system based on custom VME modules. Each board receives new data every RHIC clock tick, performs a simple calculation (eg., a part of the sum), and passes the result to the next DSM board in the tree. The tree narrows to one DSM board, which passes the final results to the Trigger Control Unit (TCU) where it is combined with LIVE/BUSY status bits from the other detectors (non triggering detectors) to act as an 18-bit address for the 16-bit Trigger Word lookup table (LUT) whose output is used to classify the type of each interaction. The 16-bit Trigger Word is used as an address to access the pre-scale system and the Action Word look-up table. This DSM+TCU-based decision tree constitutes Level 0 of the trigger which is issued within $1.5 \mu\text{s}$ for each bunch crossing. The pre-scale system allows the TCU to select only a pre-determined fraction of each trigger type. The Action Word look-up table is loaded with a list of which detectors should be triggered for this Trigger Word and what action those detectors should take.

When an interaction is selected at Level 0, each STAR detector designated to participate in this type of event is notified using a 4-bit Trigger Command and told to identify this event with a 12-bit token. This token guarantees that the resources are available in the trigger system to complete a Level 2 decision to abort or to hand off the event to DAQ. All of the raw trigger detector data and the results from Level 2 analyses are packaged and

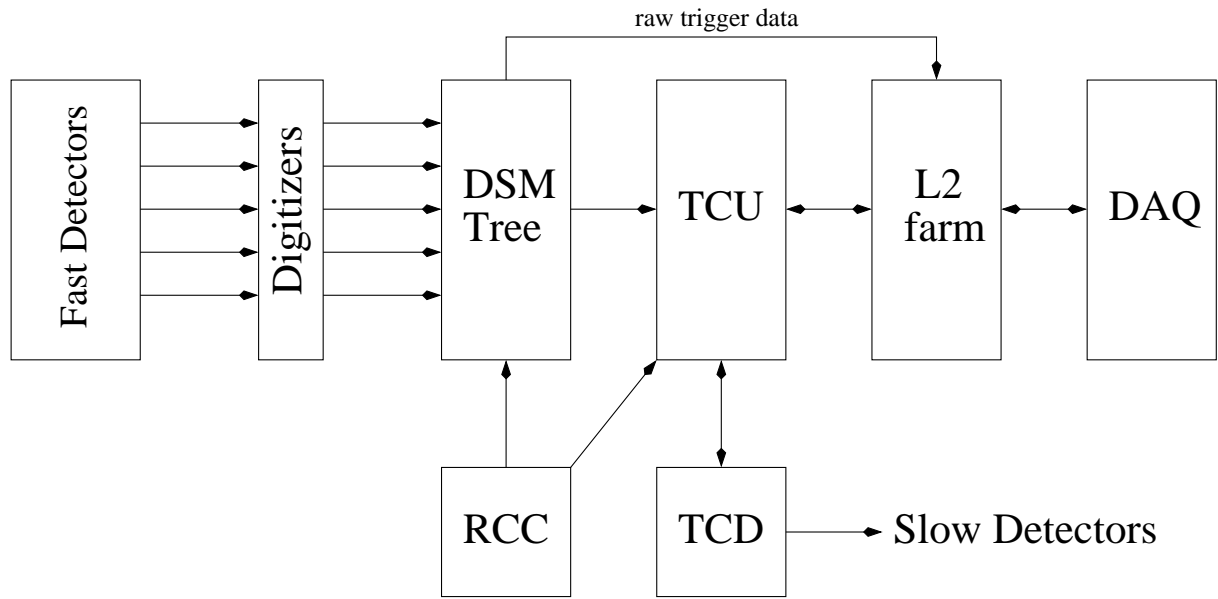


Figure 2.3: The STAR Trigger.

sent to DAQ with the token. The token stays with the event and is used as an identifier within DAQ to organize collection of all the fragments from each STAR detector. Once DAQ either accepts and stores the event or aborts it, the token is returned to the trigger and recycled.

The RHIC clock is received and distributed, with the correct phase, by Rhic Clock and Control (RCC) board to all DSMs and TCU. If the event is selected, then a trigger is issued. The Action Word, Trigger Word and token are passed to the Trigger Clock Distribution (TCD) crate for distribution to the detector subsystems.

2.4 Time Projection Chamber

One might say: "TPC is the STAR!". The Time Projection Chamber (TPC) covering an azimuthal angle of $0 < \phi < 2\pi$ is the main tracking sub-detector measuring the tracks of charged particles. It is a 4.2 m long cylinder with the inner radius of 0.5 m and the outer

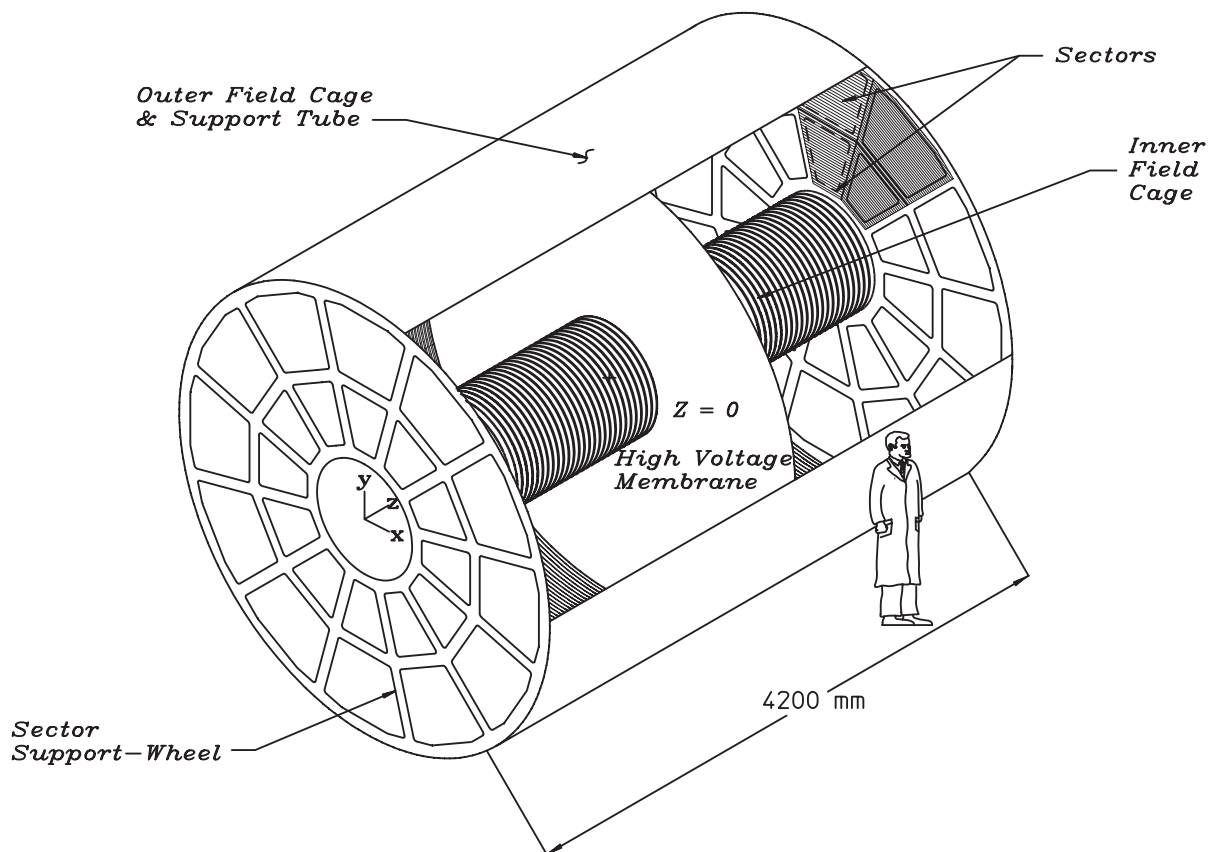


Figure 2.4: The STAR Time Projection Chamber.

radius of 2m (see Figure 2.4). The outer radius subtends a $|\eta| < 1$. The tracking volume is split in two at the center ($z = 0$) of TPC along the beam pipe by the High Voltage Membrane held at a voltage of -28 kV (TPC cathode). The bases of the cylinder are instrumented with grounded multi-wire proportional chambers (MWPC) which create together with the cathode a uniform electric field of ~ 135 V/cm. The volume of the cylinder is filled with P10 gas consisting of 10% methane and 90%. The P10 pressure is regulated at 2 mbar above the atmospheric pressure.

Charged particles traversing the volume of the TPC ionize the P10 gas atoms. The ionization electrons drift towards the bases at a constant velocity of ~ 5.45 cm/ μ s, resulting in a maximum drift time in the TPC of $\sim 40\mu$ s. The drift velocity is monitored each several hours by a laser calibration system [63]. The ionization cost the traversing particles some portion of their energy, concretely the path of a track crossing 150 cm is equivalent to 1.17% of a radiation length.

The MWPCs are split into 12 sectors, each with 45 pad rows. Each sector consists of an inner and outer sector with 13 and 32 pad rows, respectively. The inner and outer sectors differ from each other in their geometry as depicted in Figure 2.5. The inner sector pads were optimized to provide closer space points for an improved two-track resolution because of the higher track densities at smaller radius. The outer sectors have continuous pad coverage to optimize the resolution of the energy deposited by the ionization electrons. The (x, y) position obtained from the sectors together with the z position calculated from the drift time enable the charged particles's tracking in the TPC. The ionization energy loss per unit length, dE/dx , is obtained from the energy of the ionization electrons, and is used for particle identification.

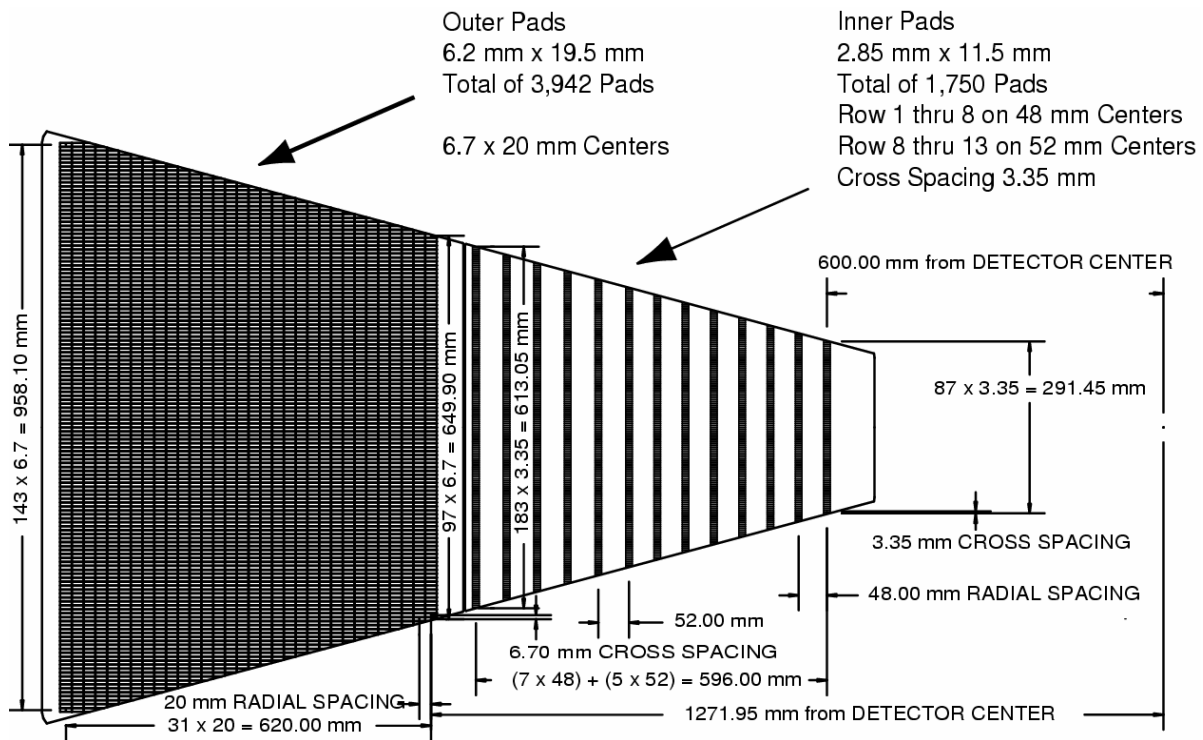


Figure 2.5: The 1/12th of the base of the TPC instrumented by MWPC split in an inner and outer sector. Figure taken from Ref. [61].

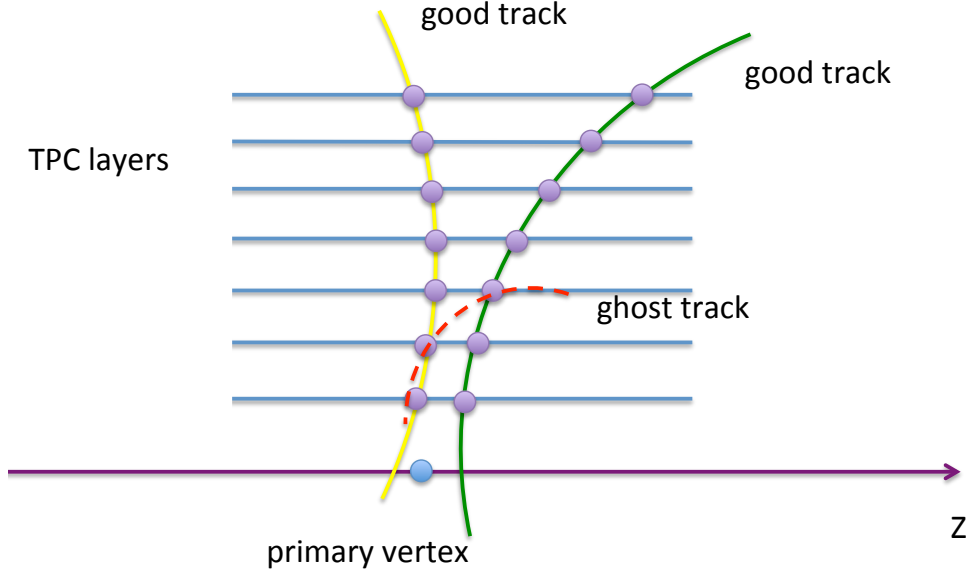


Figure 2.6: An illustration on how an artificial track can be formed from neighboring hits. Figure taken from Ref. [65].

2.4.1 Tracking

Particle tracks are formed from the reconstructed spatial hit points (hits) by using the canonical Kalman filter starting from the outer layers of the TPC, where track densities are smaller and there is less ambiguity in track formation [64]. It forms at the beginning a track seed, which is a collection of a few hits. The Kalman filter using helix then extrapolates inwards along the approximate direction and curvature to match hits in the next layer and stops once the inner-most layer is reached. A nearby hit is associated if the χ^2 of the track is below some maximum. In a case of multiple matches, the hit resulting in the smallest χ^2 is chosen. Whenever an additional hit is added to the forming track, the track segment is refit to refine the track parameters. Track segments are merged together if they appear to be the result of track splitting across sector boundaries. Any track candidate formed from less than 10 hits is automatically rejected which eliminates most cases of broken track segments to be considered as single tracks as well as so called *ghost tracks* whose formation is schemed in Figure 2.6.

The final helix fit to the track hits along the track segments is called a *global track*. The complete collection of global tracks in one event are used to determine the vertex position of the event. This is done by extrapolating the global tracks to the point with the distance of closest approach (DCA) to the beam pipe. The Pile-up Proof Vertexer (PPV) [66] is used in p+p collisions, and performs a one-dimensional truncated log-likelihood method to determine the z -position of the vertex. In Heavy Ion collisions, the Minuit Vertex Finder (Minuit VF) is used [66]. It determines the vertex position by minimizing the DCA for all tracks. Tracks with the global DCA (gDCA), the DCA of the track to the primary vertex, smaller than 3 cm are associated to the primary vertex, refitted and called *primary tracks*. The additional constraint of the vertex position improves the transverse momentum resolution of the primary tracks in comparison with the global tracks. The vertex position resolution decreases as the square root of the number of tracks that form the vertex. A resolution of $350\ \mu\text{m}$ is achieved when there are more than 1000 tracks. The transverse momentum p_T resolution, discussed closely in section 4.4, is for most tracks slightly below 1% and the minimum p_T is $0.1\ \text{GeV}/c$.

2.4.2 Particle Identification

The Particle Identification (PID) in TPC is based on the energy loss per unit length dE/dx of the particle interacting with the gas in the TPC. The dE/dx values of hits associated with the track are well described by distributions similar to Landau distribution for which its mean value doesn't exist ($\int \text{Landau dist.}(x)dx = \infty$). The hits with the top 30% of high dE/dx values are discarded and an average from the rest is derived for that track [67]. This so called *truncated mean* is used as the dE/dx value of a given track. The value decreases with increasing momentum to reach a minimum ionization, then increases due to the relativistic rise. For a minimum ionizing particle (MIP) the dE/dx resolution in the STAR TPC is 6-8% for a track with the maximum of 45 sampled dE/dx points. The pions are well separated from the rest of the particles (e, K, p) at p_T of 0.3 to 0.6

GeV/ c . To parametrize dE/dx , one must take the way of the a track formation, energy loss to ADC output conversion and factors related to atomic structure into account. It is done by using special Bichsel functions [68] developed for the STAR TPC. However, the dE/dx value and resolution may vary year by year, hence a method to improve PID in each particular year, i.e. TPC calibration, was developed [69]. The general idea is to obtain a pure sample of daughter particles by cut on the invariant mass of the

- Λ to get the pure sample of protons,

- K_S^0 to get the pure sample of pions,

- ϕ to get the rich sample of kaons (pure sample is not achievable).

Vertex resolution of the TPC is good enough to reconstruct decay vertices of the $\Lambda(1116)$ and the $K_S^0(498)$ so that a pure sample of pions and protons are achievable while ϕ meson is a strong resonant decay whose secondary vertex is impossible to reconstruct by any state-of-art detector. The Bichsel parametrization is then compared with values of the pure or rich samples. Such a comparison is shown in Figure 2.7. BEMC is used to enhance the yield of electrons relative to other particles. Additional hadron rejection is achieved from the shower shape and position from BSMD.

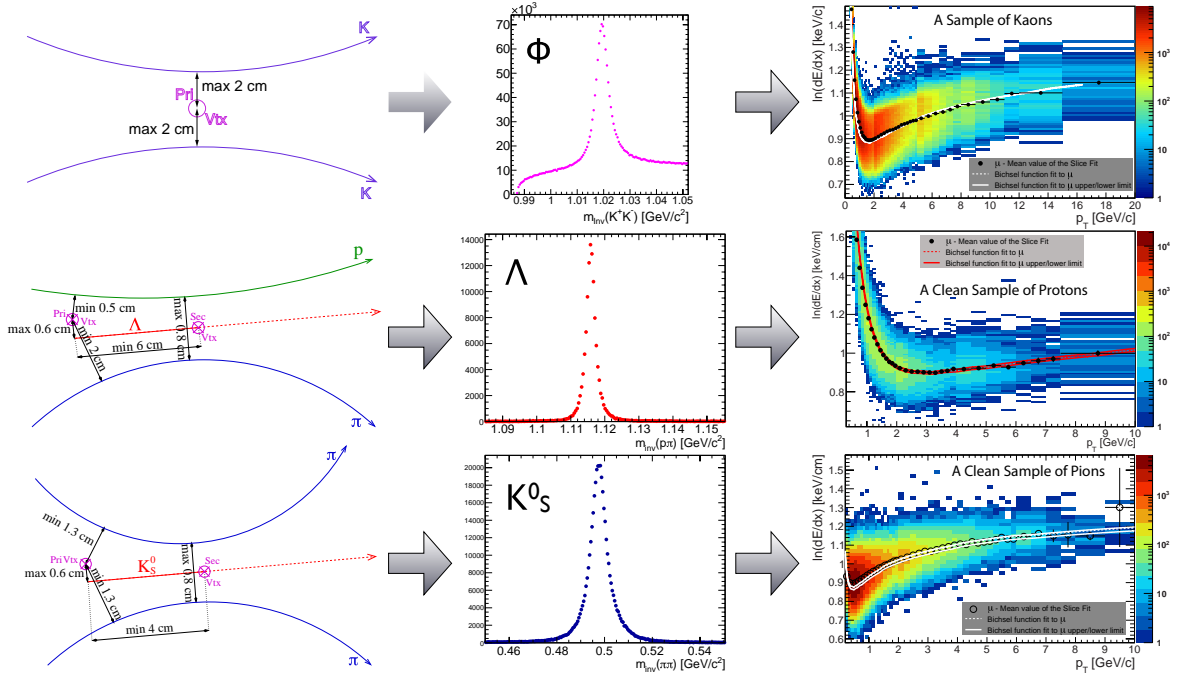


Figure 2.7: An illustration of the procedure of getting an enriched sample of kaons (top row) and a pure sample sample of protons (middle row) and pions (bottom row). The left column illustrates topological cuts on daughter particle tracks, the middle column shows reconstructed invariant mass and the right column shows dE/dx values of rich (pure) sample of the daughter particles after the cuts on invariant masses together with dE/dx mean values and their predictions from Bichsel functions.

2.5 Time of Flight Detector

The Time of Flight (TOF) system was developed to improve the PID capability of the STAR experiment for the particles with momenta between 0.6 and 3 GeV/ c [70]. It was partially installed (70% of its full acceptance) in the year 2009 and has been fully installed since 2010.

The STAR TOF system consists of the VPD which measures the start time (beside of being the triggering detector and providing the minimum bias trigger for whole STAR) and Barrel TOF (BTOF) which replaced the Central Trigger Barrel [61] and measures the stop time. Digitization is done versus a clock, and those digitized signals are subtracted, as

$$(\text{stop time} - \text{clock}) - (\text{start time} - \text{clock}) = \text{stop time} - \text{start time} \equiv \tau \quad (2.2)$$

so long as the clocks used on both the start and stop sides are the same to 10-20 ps in every event. The Leading edge time is sampled by 25 ps binning.

2.5.1 Barrel Time of Flight

The BTOF consists of 120 trays that cover $|\eta| < 1$ and $0 < \phi < 2\pi$. The detector uses Multi-gap Resistive Plate Chamber (MRPC) technology [71] based on collecting of currents induced by alternation of electrical field, penetrating through anodes made from graphite, caused by moving electrons in avalanches created in the detector gas. This principle is well discussed in [72].

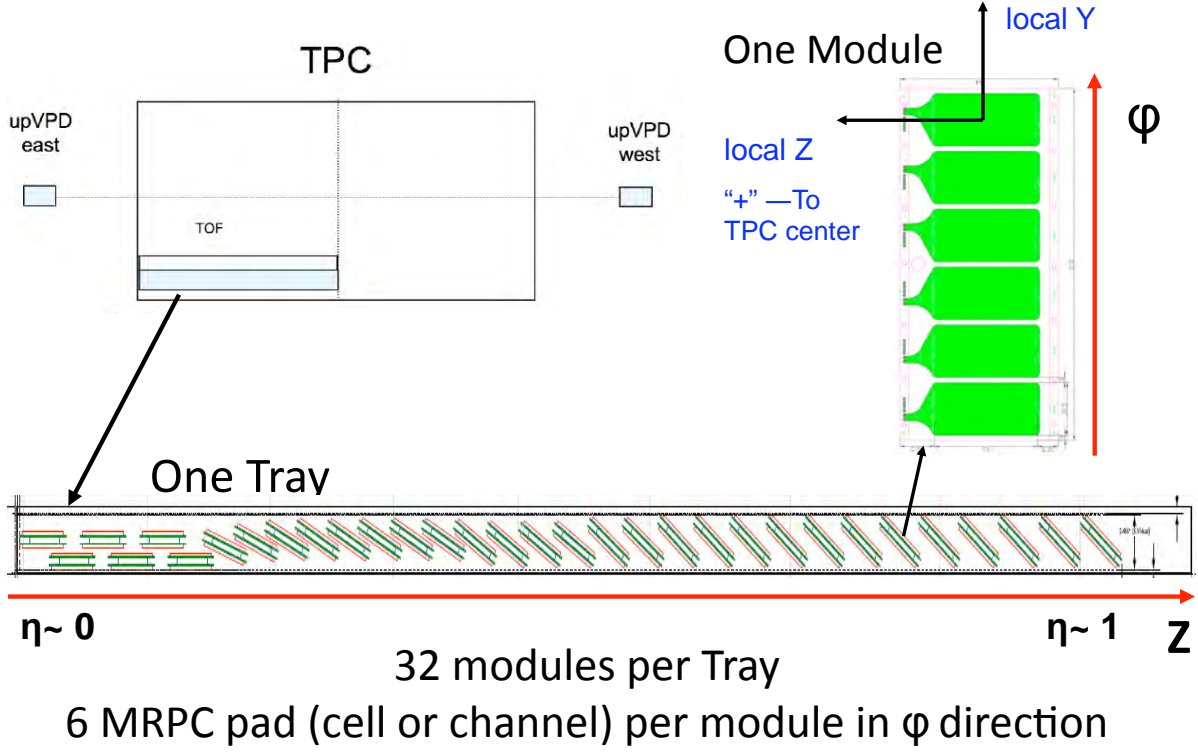


Figure 2.8: Barrel Time Of Flight geometry.

The BTOF geometry is displayed in Figure 2.8. Each tray has 32 MRPC modules, with each module containing 6 pads. The trays have dimensions $95 \times 8.5 \times 3.5$ inches, covering 6 degrees in ϕ and one unit in pseudorapidity, and surround the TPC at a radius of ~ 225 cm.

2.5.2 The Vertex Position Detector

The VPD [73] is designed as a coincidental detector and hence consists of two identical assemblies (Figure 2.8) mounted on the west and east side of the beam pipe at $z \pm 5.7$ m covering $4.24 < |\eta| < 5.1$. Each assembly is composed of 19 cylindrically shaped channels consisting of a lead layer enhancing signals by showering, a scintillator and a photo multiplier tube (PMT).

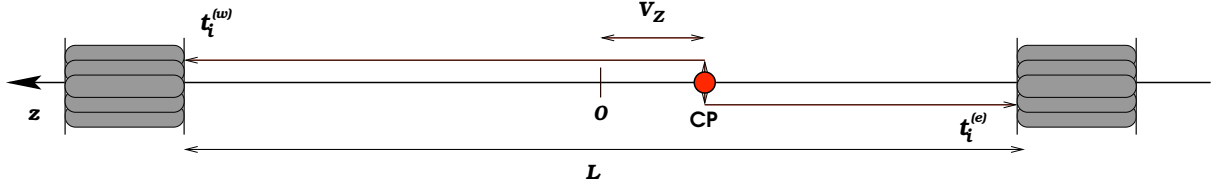


Figure 2.9: Start Time.

Let's assume that exact position of the collision point (CP) is known, as in Figure 2.9 shown. The collision occurs at time t_0 so that west side of VPD can observe signal at time

$$t_i^{(w)} = t_0 + (L/2 - V_Z)/c$$

and east side at

$$t_i^{(e)} = t_0 + (L/2 + V_Z)/c.$$

This leads to

$$t_0 = 1/2(t_i^{(w)} + t_i^{(e)}) - L/c.$$

Index i denotes i -th hit in East of West VPD. L and c are constants so their absolute values are not important and one has to take the improving time resolution with increasing number of hits into account. Hence the start time formula can be rewritten as

$$t_{\text{start}} = \frac{\sum_{i=1}^{N^{(w)}} t_i^{(w)} + \sum_{i=1}^{N^{(e)}} t_i^{(e)}}{N^{(w)} + N^{(e)}} - \frac{N^{(w)} - N^{(e)}}{N^{(w)} + N^{(e)}} \frac{V_Z}{c} \quad (2.3)$$

where $N^{(w)}, N^{(e)}$ denote number of hits in west, east side of VPD respectively. V_Z is provided by TPC with better precision than by VPD by

$$\frac{1}{2c} \left(\langle t_i^{(e)} \rangle - \langle t_i^{(w)} \rangle \right) \quad (2.4)$$

which is around 2.5 cm in p+p collisions.

2.5.3 Particle Identification by TOF

Global tracks are projected to BTOF cylinder radius and geometrically corresponding BTOF channel is linked to it. Let's note that the tracks must pass minimum track

quality cuts:

- $0 < flag < 1000$, where *flag* indicates the fit quality of the track
- number of TPC fit points is at least 15
- The ratio (number of TPC fit points) / (number of possible TPC fit points, i.e. all neighboring segments between TPC margins alongside the track) is at least 0.52

which are also standard track quality cuts in most analyses done from STAR data. If the linked itself or linked ± 1 (in the same module) channel has just one hit, the TOF information is stored in `StMuBTofPidTraits` object with *MatchFlag* = 1 value. If one track is associated with multiple TOF hits, the TOF hit with the largest time over threshold (ToT) is selected and stored with *MatchFlag* = 2. If the two ToTs are the same value, the TOF hit in the nearest cell from the track projection point is stored and *MatchFlag* = 3.

For the matched TPC track, the path length L is calculated as helix length from the primary vertex to the matched BTOF channel. Particle speed β is calculated then as

$$\beta = \frac{L}{c\tau},$$

where τ is the time of flight calculated by (2.2). From the relativistic particle momentum

$$p = m\beta\gamma \Rightarrow p^2 = \frac{m^2\beta^2}{1 - \beta^2} \Rightarrow p^2 = \beta^2(m^2 + p^2)$$

one can derive the relation between β and p where the only one unknown parameter is the particle mass m

$$\frac{1}{\beta} = \sqrt{\frac{m^2}{p^2} + 1} \quad (2.5)$$

Figure 2.10 shows $1/\beta$ versus track momentum scatter plot with predictions from (2.5) for pions, kaons and protons (solid black curves).

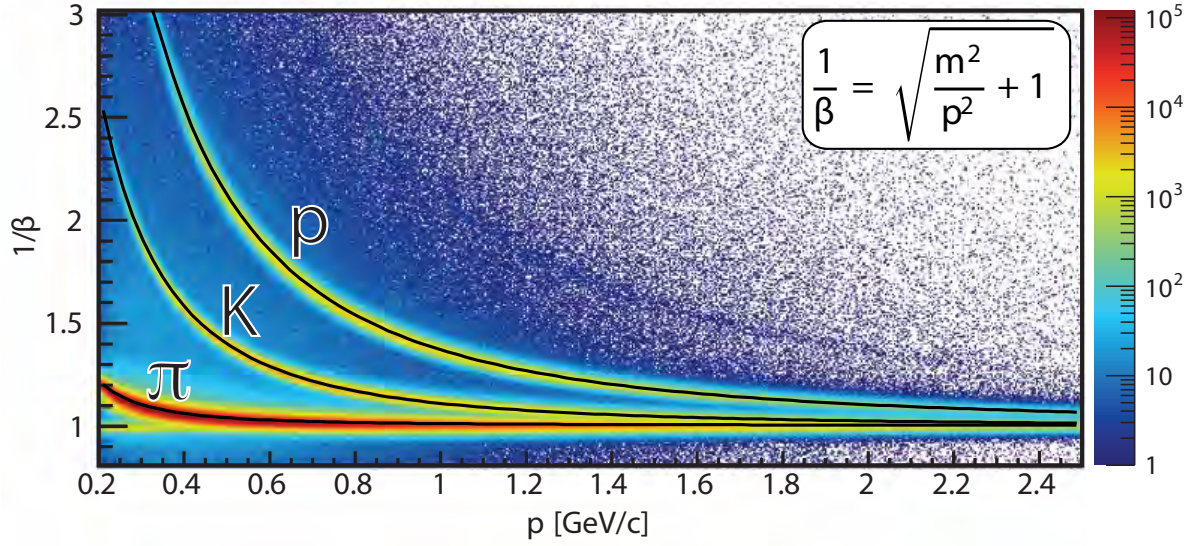


Figure 2.10: Particle Identification by STAR TOF.

2.6 Barrel Electromagnetic Calorimeter

STAR includes two main calorimetric subsystems - Endcap Electromagnetic Calorimeter EEMC [74] together with Endcap Shower Max Detector (ESMD), and Barrel Electromagnetic Calorimeter BEMC [75] together with Barrel Shower Max Detector (BSMD).

The BEMC surrounds the TPC and TOF with full azimuthal coverage and pseudorapidity coverage $|\eta| < 1$ within the STAR magnet as shown in Figure 2.11. Its inner radius is 223.5 cm and outer radius 263 cm including the rail mounting. It consists of 120 modules segmented into 40 towers covering $\Delta\eta \times \Delta\phi = 0.05 \times 0.05$. The BEMC is a sampling calorimeter, consisting of 20 layers of 5 mm thick lead absorber plates alternating with 21 scintillator plates. The BEMC amounts to a total radiation length of $\sim 20X_0$, where the radiation length X_0 is defined as the mean distance over which a high energy electron loses all but $1/e$ (37%) of its energy by Bremsstrahlung.

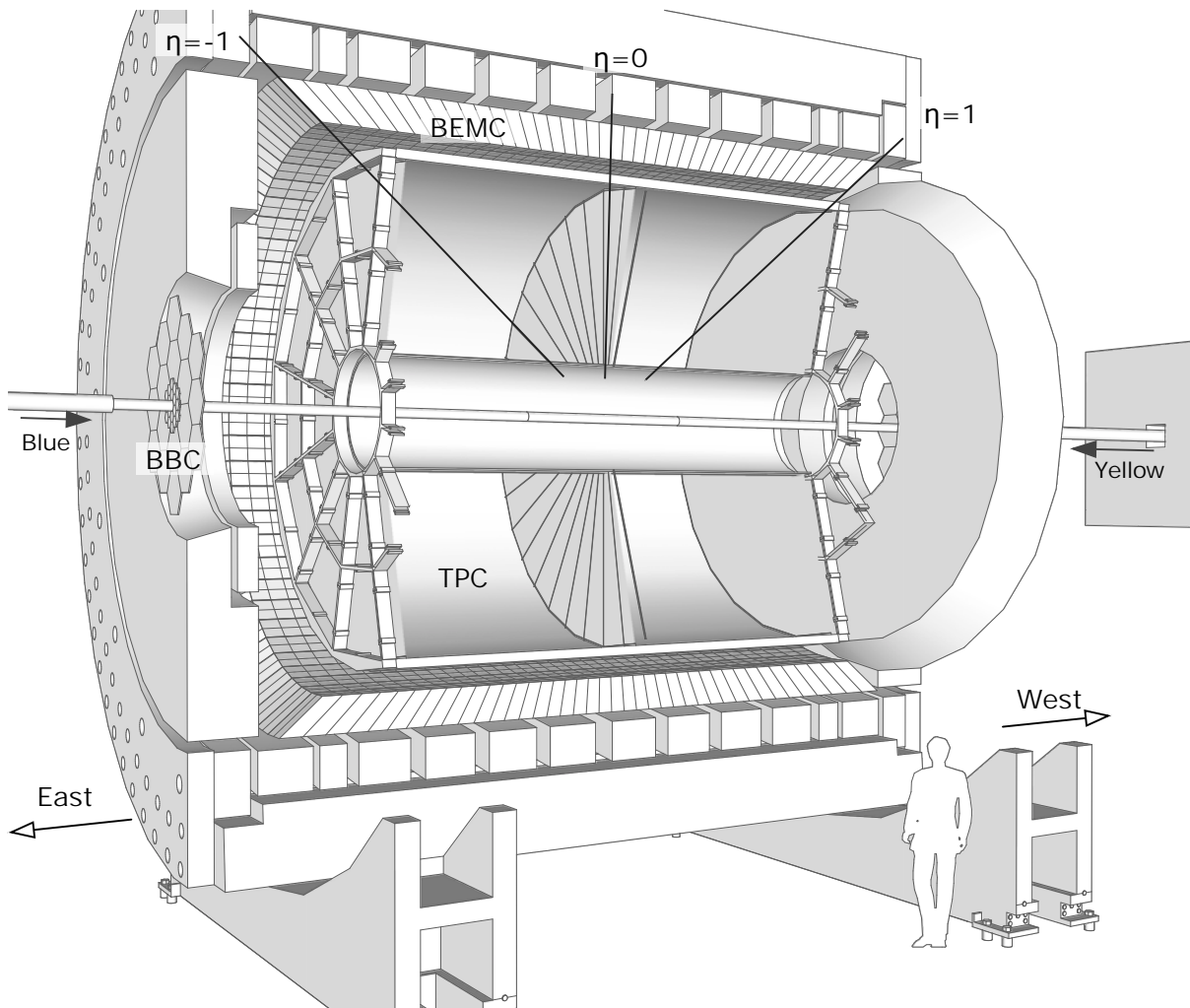


Figure 2.11: Placement of BEMC in STAR. Figure taken from Ref. [76].

Analysis Of the Experimental Data

This chapter describes the D^0 meson and $D^{*\pm}$ meson invariant masses reconstruction via their hadronic decay channels. The difference between the hadronic and semi-leptonic decay channels is discussed in section 1.5. The D^0 decay channel $D^0 \rightarrow K^- \pi^+$ with Branching ratio $\Gamma = 3.89\%$ [4] is also depicted in Figure 1.7. The D^0 raw yield is calculated as the area of the gaussian function fitted into the D^0 invariant mass spectrum after all background is subtracted in the invariant mass region around expected D^0 mass which is $1864.84 \text{ MeV}/c^2$ [4]. To calculate the raw yield D^* , one may exploit the softness of $D^{\pm*} \rightarrow D^0 \pi_S^\pm$ decay ($p_{\pi_S}^* = 39.4 \text{ MeV}$); combine pions with D^0 candidates ($K\pi$ pairs with $M(K\pi) \sim 1.865 \text{ GeV}/c^2$, and plot the difference $M(K\pi\pi_S) - M(K\pi)$ whose resolution is determined by mostly the π_S momentum resolution. The $M(K\pi\pi_S) - M(K\pi)$ has also a significant peak, hence the further procedure is analogous with the procedure regarding the D^0 .

As a matter of fact, this thesis describes two analyses which slightly differ from each other. The procedures of the reconstruction and calculation are the same, but some quality cuts

were different and there are also some differences in the detector's acceptances. Let's use the tag "Run9 pp200" for the analysis of the data in p+p collisions at $\sqrt{s} = 200$ GeV collected in year 2009 and the tag "Run11 pp500" for the analysis of the data in p+p collisions at $\sqrt{s} = 500$ GeV collected in year 2011. All figures in the further text carry either Run9 pp200 or Run11 pp500 tag as well as everywhere in the text both analyses are referred by either one or another tag.

3.1 Event Selection

The events selected for both Run9 pp200 and Run11 pp500 analyses were triggered by the minimum bias trigger. The minimum bias trigger for p+p collisions required a coincidence between the East and West VPD (see subsection 2.5.2). The RHIC proton beam luminosity was in Run9 pp200 at $5 \times 10^{31} \text{ cm}^{-2}\text{s}^{-1}$ resulting in event rate around 1.5 MHz (the non-singly-diffractive inelastic cross section was measured to be $30 \pm 3.5 \text{ mb}$ [77]). The luminosity at RHIC has been increasing over the time, thus its value for Run11 pp500 was already at $10^{32} \text{ cm}^{-2}\text{s}^{-1}$ resulting in event rate about 3 MHz. The TPC readout is about $80 \mu\text{s}$ which means that about 120 or 240 collisions occurred during one TPC readout when the luminosity was at maximum in Run9 pp200 or Run11 pp500 respectively. As a result, most of tracks and primary vertices reconstructed in TPC don't belong to the triggered event, such tracks and vertices are called pile-up tracks and pile-up vertices (let's call them shortly pile-ups).

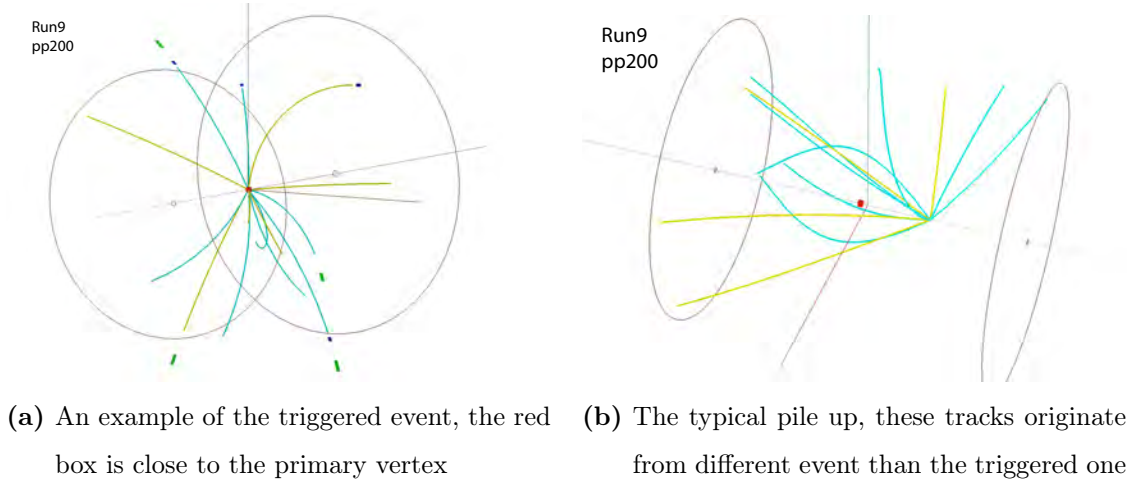


Figure 3.1: Event from a p+p collision reconstructed in TPC. Yellow and Green lines represent tracks and Red box represent z -position of vertex calculated by (2.4). Blue short thick lines represent matched hits in TOF and green short thick lines represent matched hits in BEMC.

STAR has developed two methods how to deal with pile-ups:

1. Usage of PPV algorithm [66] for vertex reconstruction. This algorithm sorts all vertices reconstructed from the global tracks according to the probability that they have come from the triggered event. Each vertex obtain a negative value called *ranking* proportional to the χ^2 value provided by PPV fitter. The first vertex has the highest ranking. All helices of the tracks assigned to the vertex are then extrapolated to BEMC and EEMC (EMC) towers and if at least two hereby matched towers have signals above a threshold (hits) the ranking is set to positive value. Matching in TOF wasn't implemented in PPV until year 2012, but TOF was partially installed in year 2009 and fully installed in year 2010. In Run11 pp500 analysis, all track's matchings in EMC or TOF were checked, and if at least two matched hits in those fast detectors have been found the event passed the cut called "2x matching in Fast". This cut was used instead of the cut on the vertex ranking.
2. Cut on the $|V_{z\text{VPD}} - V_{z[0]_{\text{TPC}}}|$, where $V_{z\text{VPD}}$ is the z-position of vertex given by (2.4) (VPD vertex) and $V_{z[0]_{\text{TPC}}}$ is the z-position of the first vertex (sorted by its ranking) from the PPV vertex finder (TPC vertex). The value of this cut is derived from the VPD time resolution of ~ 80 ps, i.e. for particle traveling at the speed of light 2σ of the resolution implies z-position resolution of 4.8 cm. The used value of the cut is thus relatively loose, 6 cm, in order to minimize a loss in statistics.

Figure 3.1a illustrates a triggered event where the red box representing $V_{z\text{VPD}}$ is close to the primary vertex and the event has matchings in the Fast detectors (TOF and EMC). Figure 3.1b illustrates a typical pile-up where the red box is far from the primary vertex and no track has matching in the Fast detectors.

Figure 3.2 depicts correlation between $V_{z\text{VPD}}$ and $V_{z[0]_{\text{TPC}}}$ as well as $|V_{z\text{VPD}} - V_{z[0]_{\text{TPC}}}|$ both before and after the 2x matching in Fast is applied. One can observe significant reduction of events whose vertex's z-positions provided by TPC and VPD are not in

correlation whereas the impact on the peak around zero in $|V_{z\text{VPD}} - V_{z[0]_{\text{TPC}}}|$ is much smaller. The impact of the cut on the vertex ranking used in Run9 pp200 is very similar [28].

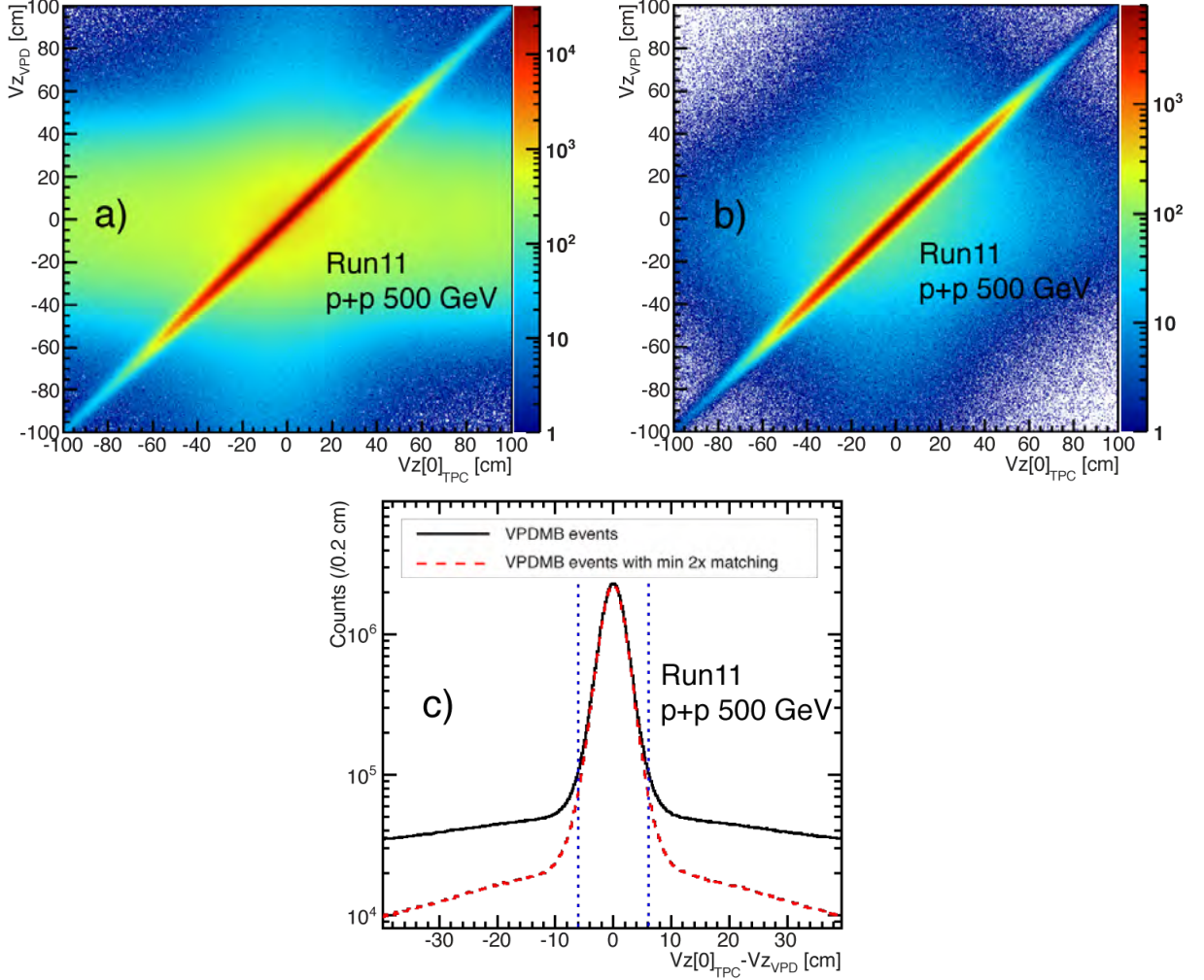


Figure 3.2: Correlation between z-position of the first TPC vertex and z-position of the VPD vertex from VPDMB trigger before (Panel a) and after (Panel b) 2x matching in Fast cut is applied. Panel c): Vertex z-position difference between the TPC vertex and the VPD vertex. The blue vertical lines indicate the cut window used to select the triggered events.

Let's summarize the required selection criteria on events:

1. events pass the minimum bias trigger,
2. $|V_{ZVPD} - V_{Z[0]_{TPC}}| < 6 \text{ cm}$,
3. 2x matching in the Fast (Run11 pp500) or Ranking > 0 (Run9 pp200),
4. $|V_{Z[0]_{TPC}}| < 50 \text{ cm}$

Histograms of number of events after subsequent application of cuts is shown in Figure 3.3. As one can see, the cut on the vertex ranking is tighter and causes significant decrease of the number of accepted events. The number of events that entered analysis N_{evt} was 107.8M in the Run9 pp200 and 51.8M in the Run11 pp500.

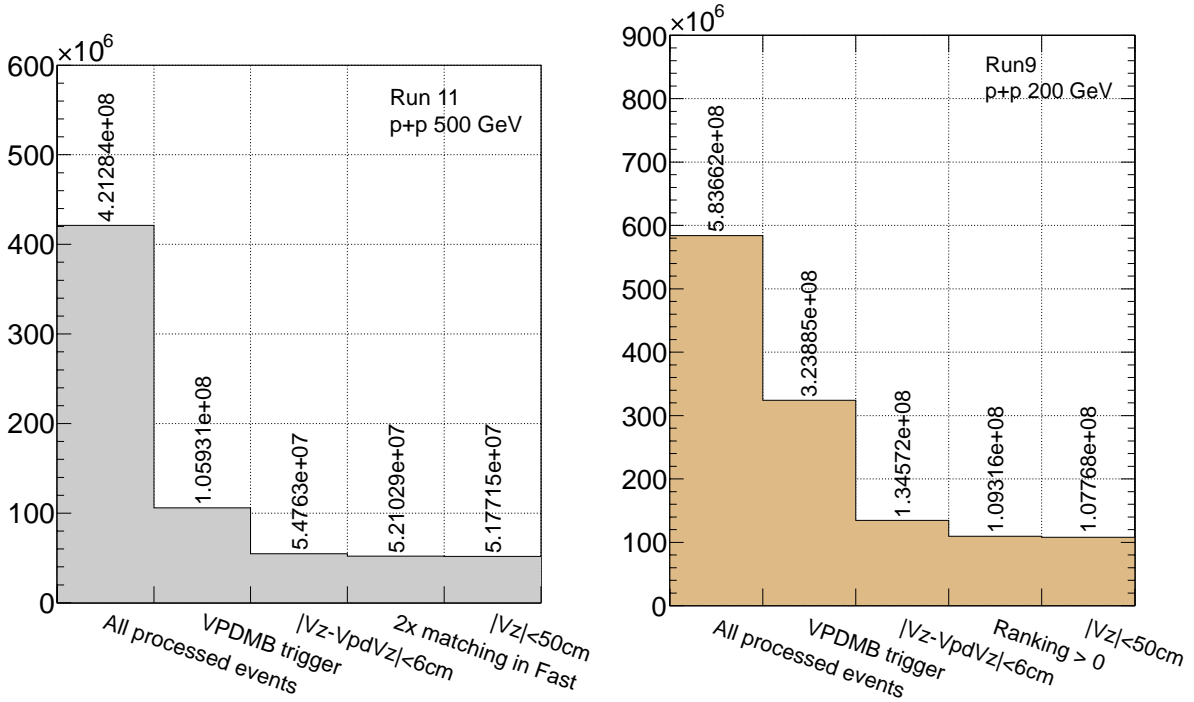


Figure 3.3: Number of events that passed cuts in the event chain. The left panel shows Run11 pp500 statistics while the right panel Run9 pp200 statistics.

3.2 Particle Selection

This section describes the selection criteria used to ensure a high track reconstruction quality. However, the stricter the criteria are the lower is the reconstruction efficiency which is discussed in chapter 4. Let's note that the selection criteria on tracks in the analysis of purely experimental data described in this chapter must be exactly the same as the selection criteria on tracks in the analysis of the data enriched by simulated data described in chapter 4. Further in this section, there is description of the particle identification used to select pion and kaon candidates whose momenta was then used to calculate invariant masses of open charm mesons.

3.2.1 Track Quality Cuts

For further analysis all primary tracks (see subsection 2.4.1) were considered. The track quality cuts in both Run9 pp200 and Run11 pp500 analyses were identical and are listed below:

1. $0 < \text{flag} < 1000$,
2. number of TPC fit points > 20
3. $\frac{\text{number of TPC fit points}}{\text{number of max possible TPC fit points}} > 0.52$
4. global DCA $< 2\text{cm}$
5. $p_T > 0.16 \text{ GeV}/c$
6. $|\eta| < 1$

where the $0 < \text{flag} < 1000$ is used to remove pile-up tracks which cross the central membrane of the TPC after the collision, known as Post-Crossing tracks and are identified

during the data production. "number of TPC fit points" denotes the number of spatial hit points in TPC from which a track is reconstructed (more details about the track reconstruction in subsection 2.4.1. $\frac{\text{number of TPC fit points}}{\text{number of max possible TPC fit points}} > 0.52$ is used to prevent split tracks, one track reconstructed into two tracks. "global DCA" means the distance of the closest approach of the helix representing a track to the primary vertex. The default value for primary tracks is 3 cm, but one can slightly improve the track momentum resolution if this value is set lower. The minimum values of track transverse momentum p_T and pseudorapidity η are set for tracks being able to reach TOF and BEMC.

The curvature radius R of a track helix that is able to reach TOF must be at least 1.05m. That corresponds to the track minimum $p_T = BRc = 0.158 \text{ GeV}/c$, where B is the magnetic field and c the speed of light. All tracks with $p_T < 0.16 \text{ GeV}/c$ are can't be used with TOF as well as all tracks with $p_T < 0.18 \text{ GeV}/c$ for BEMC.

The typical BBC trigger scaler rate was 1.6 MHz which suggests at least 130 events in one TPC readout. So that some tracks might be assigned to a vertex originating from a different event. These tracks (let's call them pile-up tracks) would have a different timing and no matching in the Fast detectors as displayed in Figure 3.1b. To check the fraction of those tracks, one can plot the track multiplicity as a function of the BBC coincidence (close and proportional to the event rate). As one can see in Figure 3.4 (Run11 pp500 analysis), the track multiplicity is proportional to the event rate if the matching is not required. Yet the multiplicity of the tracks with matchings seems to be independent on the event rate. Regarding the matching efficiency, discussed in section 4.2 (86% for pions and 83% for kaons in Run11 pp500, lower in Run9 pp200 due to incomplete TOF), one can estimate that almost each second pion and 60% of kaons are pile-ups causing potentially 5x higher combinatorial background in D^0 and 10x higher combinatorial background in D^* analysis. However, the matching requirement made the D^* reconstruction efficiency dwindling at $D^* p_T < 3 \text{ GeV}/c$ so it's very important to set the track low p_T cut as low as

possible together with the matching requirement (see appendix B for details). This issue wasn't so devastating in Run 09 (still significant though) so the matching requirement was not applied in Run 09 D^* analysis [28].

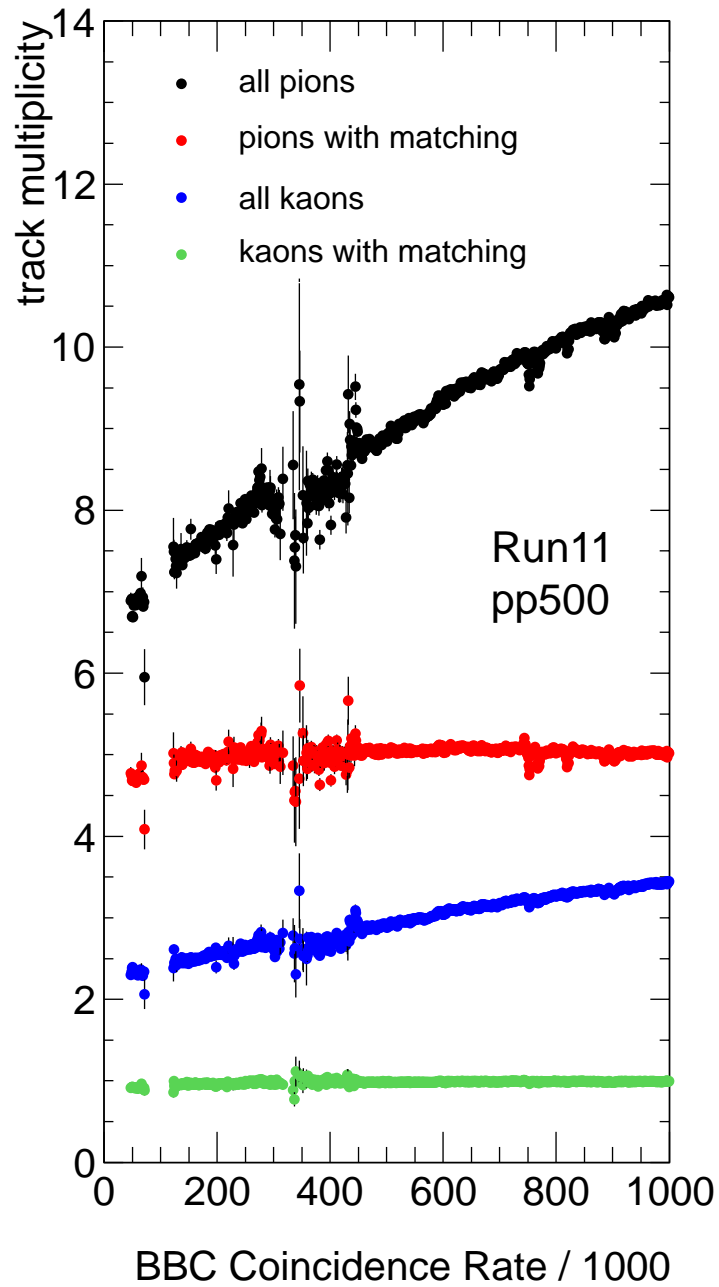


Figure 3.4: Pion multiplicity as a function of the BBC Coincidence Rate for tracks with matching in fast detectors and for all TPC primary tracks.

3.2.2 Particle identification

Particle identification (PID) for charged tracks was carried out with a combination of TPC dE/dx and the particle velocity β measurement from the barrel TOF detector.

Thus the normalized dE/dx ($n\sigma_X^{dE/dx}$) and $1/\beta$ ($n\sigma_X^{1/\beta}$) were used to select daughter particle candidates. They are defined as follows:

$$n\sigma_X^{dE/dx} = \frac{\ln \frac{dE/dx}{\langle dE/dx \rangle_X}}{R^{dE/dx}}, \quad (3.1)$$

$$n\sigma_X^{1/\beta} = \frac{\frac{1}{\beta} - \sqrt{\frac{m_X^2}{p_X^2} + 1}}{R^{1/\beta}}, \quad (3.2)$$

where the X denotes expected values which are calculated with respect to one kind of particle. The $\langle dE/dx \rangle_X$ is mean value of ionization loss in TPC given by the Bichsel function [68], $R^{dE/dx}$ and $R^{1/\beta}$ are corresponding resolutions. In the further text, X will be either pion π or kaon K . Different PID cuts were chosen for D^0 and D^* analysis as well as for pions and kaons.

3.2.2.1 TOF PID Quality Assurance

In a part of the Run9 pp200 data, there was a small fraction of tracks with their time of flight value shifted by 25ns, shown in Figure 3.5 which has the "Day number" on its x-axis and the time of flight value on its y-axis. The "Day number" represents the date when the data was collected. RHIC starts its operation each year on "Day number" = 1. According to the plot in Figure 3.5 the p+p collisions started on Day number = 113 and ended on Day number = 185. Figure 3.5 reveals that the time of flight value distributions have unnatural peaks around 34 ns in some days, shifted exactly by 25 ns from main peaks around 9 ns. The impact of this shift can be seen in $1/\beta$ vs momentum scatter plot

in Figure 3.6a where one can see the bands shifted in $1/\beta$ direction by 3.5 (the pion band from ~ 1 to ~ 4.5 for example).

To correct this shift, the time of flight, which is used to calculate particle velocity, is corrected so that all tracks with TOF higher than 30ns is shifted by 25ns backward. β is then recalculated by formula

$$\beta_{\text{new}} = \beta_{\text{old}} \frac{t}{t - 25}, \quad (3.3)$$

where t is time of flight in nanoseconds. Results of that shift is shown in Figure 3.6b where that shifted "copy" of the particle bands is not present anymore.

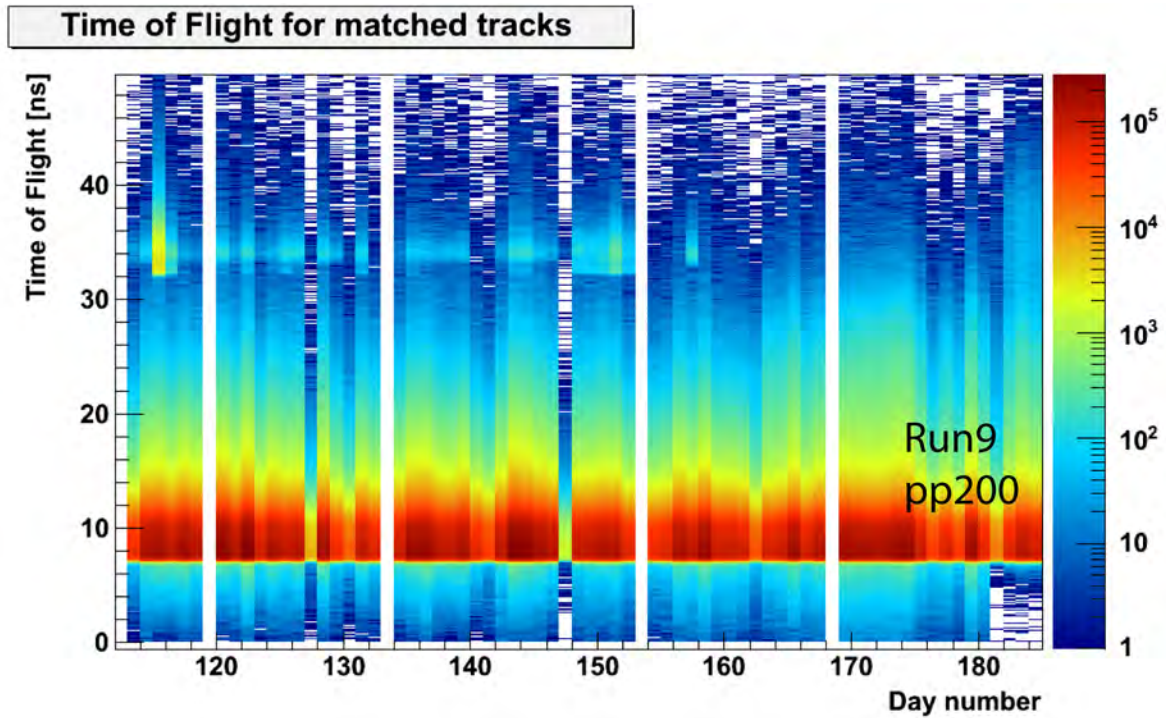


Figure 3.5: Time of Flight over the Run9 pp200 data taking period.

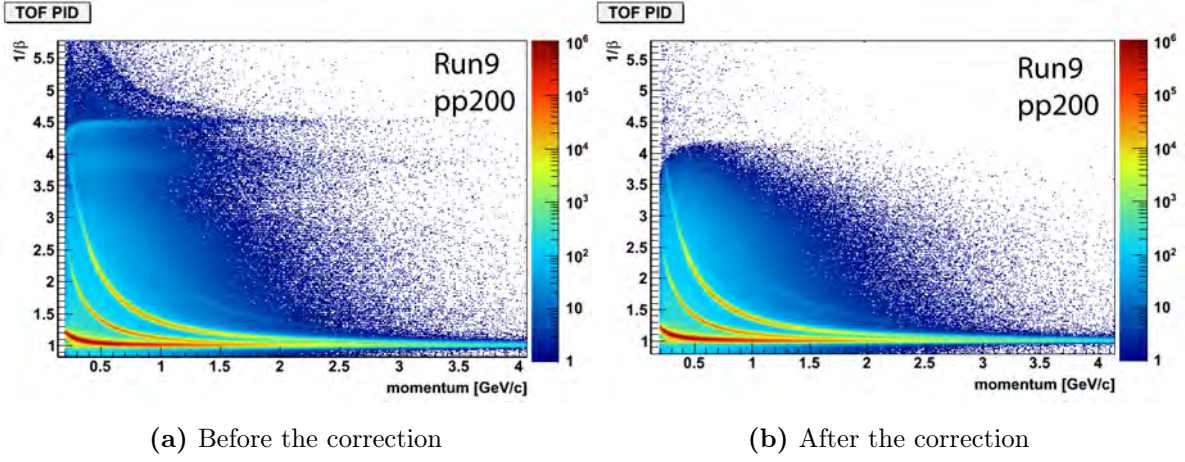


Figure 3.6: Results of Time of Flight 25ns shift correction.

In Run11 pp500, no such time of flight shift was observed.

3.2.2.2 The Identification of Pion and Kaon Candidates Used in D^0 Invariant Mass Reconstruction

This subsection describes the identification of pion and kaon candidates used in D^0 invariant mass reconstruction in Run11 pp500 analysis. The procedure in Run9 pp200 analysis was exactly the same, however the detectors (TPC and TOF) performance was slightly different (it changes every year) so the parameters of functions f_{Res} and f_{Pos} in equation (3.4) were different as well. Still, cuts used to select pion and kaon candidates were the same.

If a TPC track had matching to TOF the $n\sigma_K^{1/\beta}$ and $n\sigma_\pi^{1/\beta}$ were calculated. At low track momentum (up to 0.4 GeV/c), the $R_K^{1/\beta}$ becomes appreciably larger due to Coulomb re-scatterings of the particle in TPC volume. The re-scatterings make kaon fly along a longer path than the one parametrized by an ideal helix (which is used to calculate the path length) and reach the TOF later than expected, so $1/\beta$ is larger than expected. This

phenomenon is clearly visible in the scatter plot of the Figure 3.7, where one can see not only a larger $1/\beta$ but also its worse resolution. Hence a momentum dependent PID cut based on $n\sigma_K^{1/\beta}$ resolution depicted by the red open circles in Figure 3.7 was used. Both $n\sigma_K^{1/\beta}$ resolution and position as a function of the kaon momentum is parametrized by power-law type functions marked as f_{Res} and f_{Pos} respectively. Kaons are then defined as tracks that fulfill the condition:

$$-2f_{\text{Res}} + f_{\text{Pos}} < n\sigma_K^{1/\beta} < \begin{cases} 2f_{\text{Res}} + f_{\text{Pos}}, & \text{in } D^0 \text{ analysis} \\ 3f_{\text{Res}} + f_{\text{Pos}}, & \text{in } D^* \text{ analysis} \end{cases} \quad (3.4)$$

where $f_{\text{Res}} = 0.884 + \frac{0.0174}{(p + 0.0839)^{4.23}}$ and $f_{\text{Pos}} = 0.0316 + \frac{0.00137}{(p + 0.101)^{6.89}}$.

The $1/\beta$ of pions is much smaller at low momentum and hence relatively less affected by coulomb re-scatterings than this of kaons (the mean of the $n\sigma_\pi^{1/\beta}$ distribution is 0.1 with the $R_\pi^{1/\beta} = 0.011$, hence pions are defined as tracks that fulfill the condition:

$$-1.9 < n\sigma_\pi^{1/\beta} < 2.1 \quad (3.5)$$

To enhance statistics, if a track with $p_T > 1.6 \text{ GeV}/c$ hadn't matching to TOF, but had matching to BEMC, it was still accepted. Those tracks were identified as

- kaons if $-2 < n\sigma_K^{\text{dE/dx}} < 2$
- pions if $-2 < n\sigma_\pi^{\text{dE/dx}} < 2$

3.2.2.3 The Identification of Pion and Kaon Candidates Used in D^* Invariant Mass Reconstruction

D^* production in Run9 pp200 analysis was not done by the author of this thesis. Kaon and pion candidates were selected by requiring $|n\sigma_K^{\text{dE/dx}}| < 2$ and $|n\sigma_\pi^{\text{dE/dx}}| < 2$ respectively.

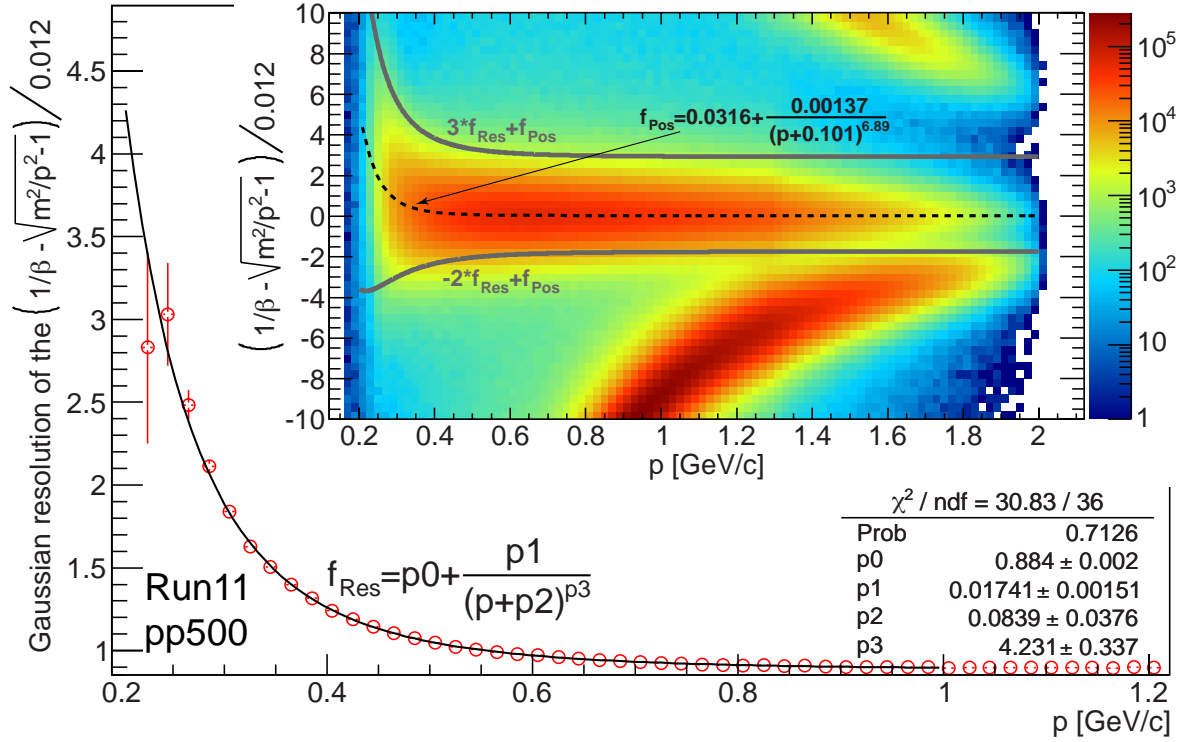


Figure 3.7: The scatter plot depicts $n\sigma_K^{1/\beta}$ as a function of the track momentum whose slices were projected along Y-axis and fitted by gaussian distributions. The red open circles represent second moments (σ) of those distributions that are fitted by power-law function f_{Res} and the dashed curve in the scatter plot is the power-law function f_{Pos} fit the first moments (μ) of the gaussian distributions. The grey curves in the scatter plot represent PID cuts used to select kaons.

TOF was not used at all because the signal suffered significant loss due to incomplete TOF acceptance in year 2009. Details of this reconstruction are presented in [28]. This subsection describes the identification of pion and kaon candidates used in D^* invariant mass reconstruction in Run11 pp500 analysis only.

As shown in appendix B, STAR can detect D^* with $p_T \gtrsim 2$ which decays into daughters whose momenta might be already beyond the region where TOF provides the best and

unequivocal PID and such daughter particles need to be identified by TPC dE/dx .

Therefore the tracks were separated into three groups according to their momentum (each detector provides the best separation of kaons from pions at different track momentum):

1. $p_T < 1.3 \text{ GeV}/c$ TOF provides clear separation of kaons from pions so it was main PID tool in this track region. Kaons were defined as tracks that fulfilled the condition (3.4) and pions as those fulfilling the condition

$$|n\sigma_\pi^{1/\beta}| < \begin{cases} 6 - 2p, & \text{if } p < 1.5 \text{ GeV}/c \\ 3, & \text{if } p > 1.5 \text{ GeV}/c \end{cases} \quad \text{see Figure 3.8 depicting the cut} \quad (3.6)$$

which is designed to make sure all pions went into the analysis. I didn't reject tracks that had matching in BEMC only. If those passed $-3 < n\sigma_\pi^{dE/dx} < 3$ I counted them as pions.

2. $1.3 < p_T < 2.07 \text{ GeV}/c$ If a track had matching in TOF then TOF was used so kaons were defined as tracks that fulfilled the condition (3.4) and pions as those fulfilling the $|n\sigma_\pi^{1/\beta}| < 3$. If a track had matching in BEMC and no matching in TOF then kaons were those passed $|n\sigma_K^{dE/dx}| < 2$ and pions $|n\sigma_\pi^{dE/dx}| < 3$.
3. $p_T > 2.07 \text{ GeV}/c$ TPC provides better, even if not fully clear, separation of kaons from pions. If a track had matching in any fast detector (BEMC or TOF) then kaons were those passed $|n\sigma_K^{dE/dx}| < 2$ and pions $|n\sigma_\pi^{dE/dx}| < 3$. There is a contribution from protons that might affect the raw yield of kaons (pion yield is less affected since pions dominate the particle production) so I didn't count the tracks that had matching in TOF and $n\sigma_K^{1/\beta} > 3$ as kaons.

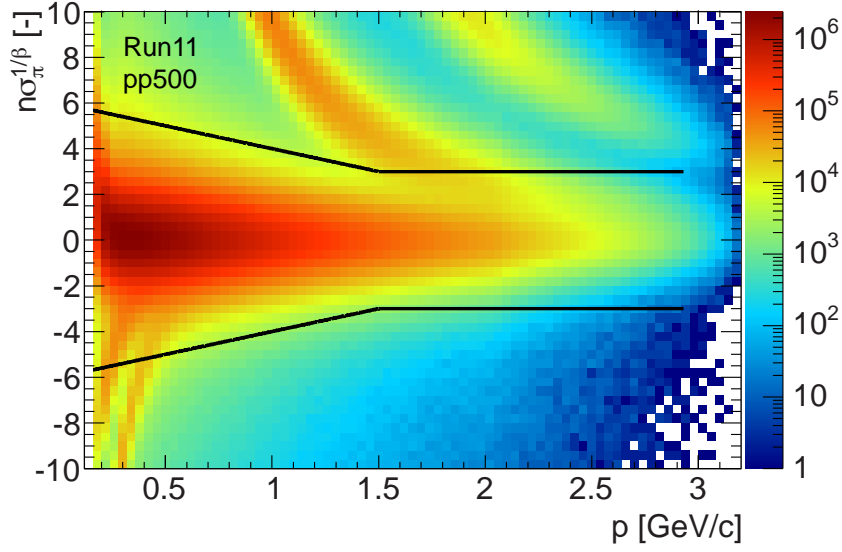


Figure 3.8: $n\sigma_{\pi}^{1/\beta}$ as a function of the track momentum. The black lines depict the TOF PID cut for pions. $1/\beta$ of pions is affected by Coulomb re-scatterings at lower momenta so I used a wider range according to (3.6).

3.3 D^0 reconstruction

D^0 and \overline{D}^0 was analyzed together ($(M_{K^-\pi^+} + M_{K^+\pi^-})$) in order to enhance observed signals. Each kaon candidate was combined with each pion candidate of opposite charge to form a D^0 candidate and the invariant mass of pair was calculated. Such invariant mass spectrum will be called "Unlike-sign" spectrum in further text. Let's note that the candidates whose rapidity exceeded the $(-1,1)$ interval were rejected.

K, π pairs consist of: pairs from D^0, \overline{D}^0 decays, pairs from other decays (like $K^{*0}(892)$ for example), and combinatorial background. The combinatorial background, that constitutes the dominant part of the D^0 candidates invariant mass spectrum, was reconstructed by two independent techniques:

- Like-Sign Method Pion candidates are paired with the kaon candidates of the same

charge. Then the geometric mean of the two subsets (the raw yield of positively $Y_{K^+\pi^+}$ and negatively $Y_{K^-\pi^-}$ charged pairs) is calculated by $2\sqrt{Y_{K^-\pi^-}Y_{K^+\pi^+}}$.

- Rotated Momentum Method Each pion candidate is paired with the kaon candidate with reversed 3-momentum. Track rotation technique is based on the assumption that by rotating one of the daughter track for 180 degree the decay kinematics is destroyed. Thus the distribution of a pair invariant mass with one track rotated is able to reproduce the random combinatorial background.

The spectrum of the $K\pi$ invariant mass is shown in Figures 3.9, 3.10, and 3.11 for pairs with p_T between 1.0 and 2.0 GeV/ c , 0.9 and 1.5 GeV/ c , and 1.5 and 2.0 GeV/ c respectively. The combinatorial background reconstructed by either Like-Sign or Rotated Momentum technique was scaled to match the original Unlike-Sign spectrum of $K\pi$ pairs within the invariant mass interval 1.7 - 1.8 GeV/ c^2 and it's shown also in Figures 3.9, 3.10, and 3.11, together with the Unlike-sign spectrum, revealing an excellent agreement of Unlike-sign spectrum with that scaled combinatorial background. Such agreement allowed to declare that both methods describe combinatorial background well and the background could be subtracted from Unlike-sign spectrum to extract the raw yield of D^0 meson. Results of the background subtractions, let's call them *signal*, are shown also in Figures 3.9, 3.10, and 3.11 in the same plot like the Unlike-sign and reconstructed backgrounds, it is zoomed by factor of 2 so that it regards the right scale while the Unlike-sign and combinatorial background regard the left scale. One can see a strong lorentzian peak corresponding to particle $K^{0*}(892)$ (together with its antiparticle), much smaller and wider peak of $K^{2*}(1430)$, and a tiny gaussian peak corresponding to $D^0 + \overline{D^0}$. There's still some residual background, especially between the $K^{0*}(892)$ peak and 0.6 GeV/ c^2 corresponding to the beginning of the $K\pi$ phase space, whose main origin lies in particle misidentification. This effect is particularly visible in Figure 3.11 where one can observe a significant peak around 0.7 GeV/ c^2 which corresponds $\phi(1019)$ meson decaying into K^+K^- whose one daughter was misidentified as pion. Since the invariant mass of the mother particle depends on invariant masses of daughter particles the wrong assignment

of mass happening at the particle misidentification causes a shift in the invariant mass of the mother particle. Hence the artificial exchange the kaon for pion causes shift in the invariant mass of the ϕ meson by $355 \text{ MeV}/c^2$.

Let's focus on lower panels in Figures 3.9, 3.10, and 3.11. They display zooms to the signal around the expected D^0 invariant mass, i.e. $\sim 1.865 \text{ GeV}/c^2$ (the position of the zoom is emphasized by the grey rectangle in the upper panel). The zoomed signals are shown separately for the signal obtained by the like-sign and for the signal obtained by the rotated-momentum background subtraction. The raw yield was calculated by fit the D^0 mass peak by gaussian function sitting on linear function that should describe the residual background with adequate precision. The fit method was based on minimizing of the χ^2 between the data and the function. The results of the fits are shown both in Figures 3.9, 3.10, and 3.11 and Table 3.1. They are:

- Raw Yield (tagged as $RwYld$ in the Figures): That's the area of the gaussian from the fit function.
- χ^2/ndf : That's a goodness of fit test, the acronym ndf means number of degrees of freedom.
- Mean (tagged as μ in the Figures): That's the position of the gaussian from the fit function.
- Resolution (tagged as σ in the Figures): That's the width of the gaussian from the fit function.
- Significance (only in the Table): It is calculated as the ratio of the Raw Yield and the Raw Yield error¹

¹The significance of a peak is defined as $\frac{S}{\sqrt{S+B}}$ (with S denoting a signal and B denoting a background) and one has to specify within what interval (usually $\pm 3\sigma$) the significance is calculated. If $S \ll B$ and both S, B have Poissonian errors the significance is $\frac{S}{\sqrt{B}}$ which is exactly the Yield over the Yield error.

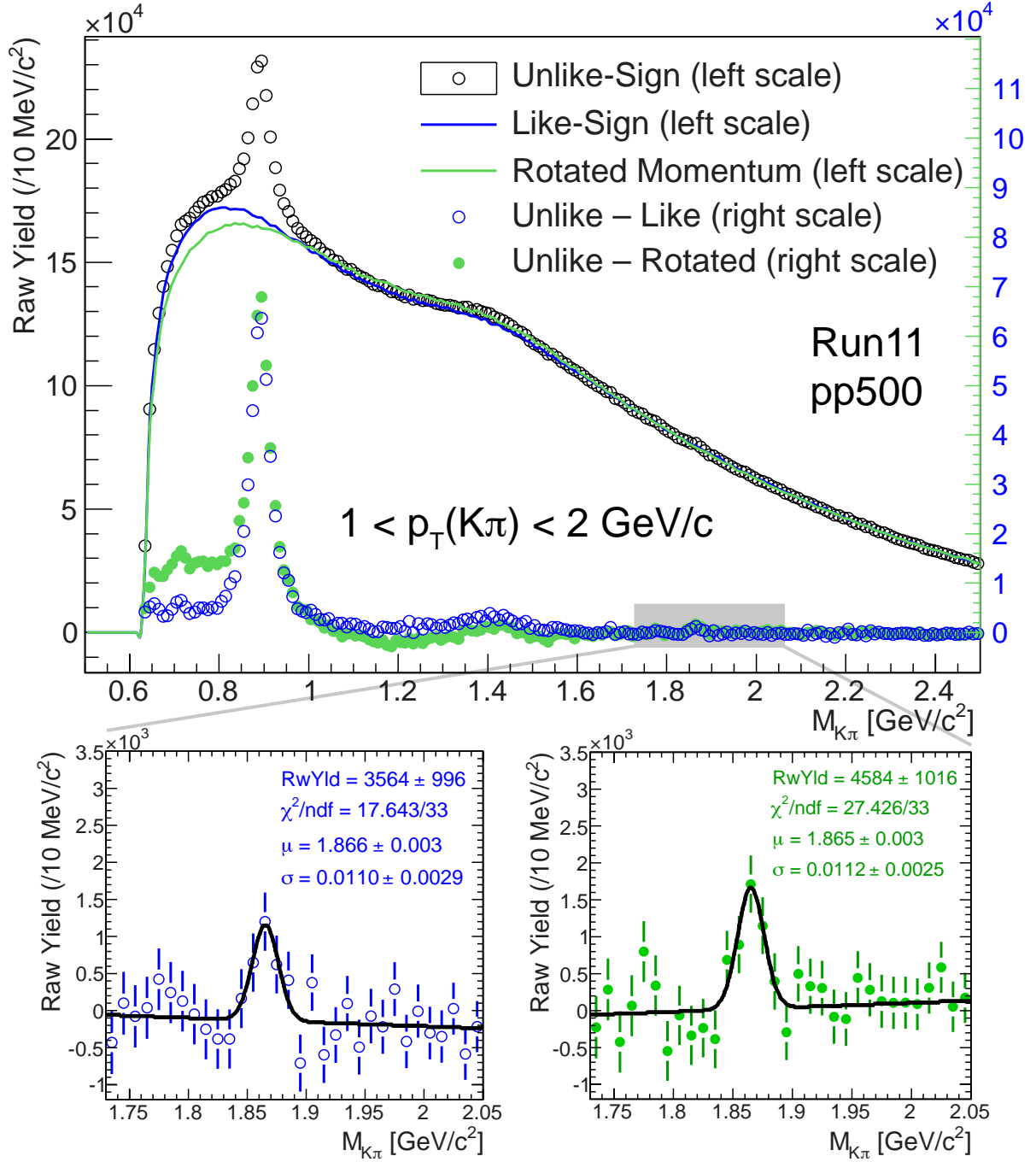


Figure 3.9: Upper Panel: Opposite-charged $K\pi$ invariant mass with the combinatorial background reconstructed by Like-Sign and Rotated Momentum techniques for all $K\pi$ pairs within $(1.0 < p_T < 2.0 \text{ GeV}/c)$ and $|y(K\pi)| < 1$. The gray rectangle illustrates the zoom to D^0 mass window. Lower left panel: Opposite-charged $K\pi$ pairs invariant mass after Like-Sign background subtracted. Lower right panel: Opposite-charged $K\pi$ pairs invariant mass after Rotated-Momentum background subtracted.

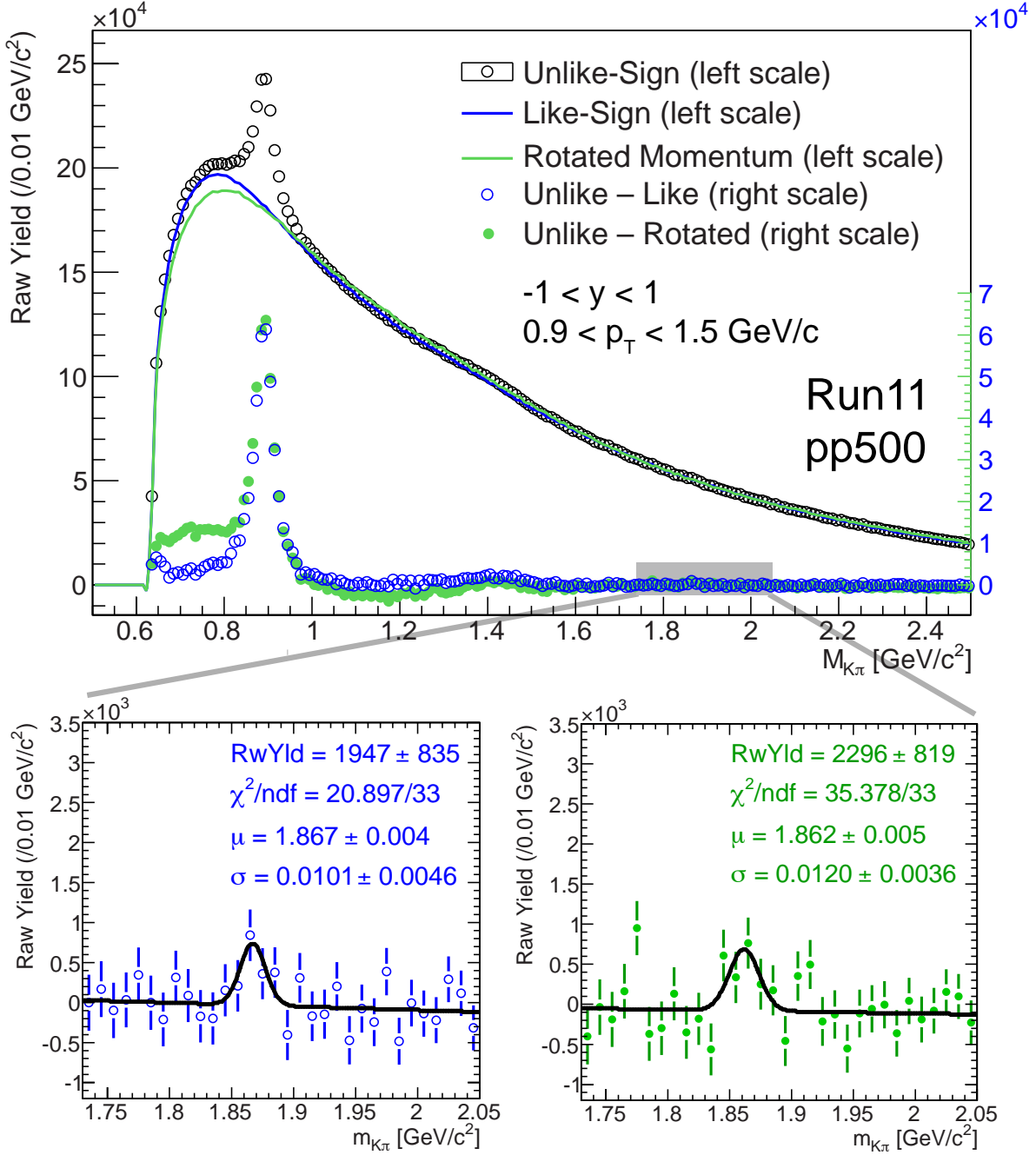


Figure 3.10: Upper Panel: Opposite-charged $K\pi$ invariant mass with the combinatorial background reconstructed by Like-Sign and Rotated Momentum techniques for all $K\pi$ pairs within $(0.9 < p_T < 1.5 \text{ GeV}/c)$ and $|y(K\pi)| < 1$. The gray rectangle illustrates the zoom to D^0 mass window. Lower left panel: Opposite-charged $K\pi$ pairs invariant mass after Like-Sign background subtracted. Lower right panel: Opposite-charged $K\pi$ pairs invariant mass after Rotated-Momentum background subtracted.

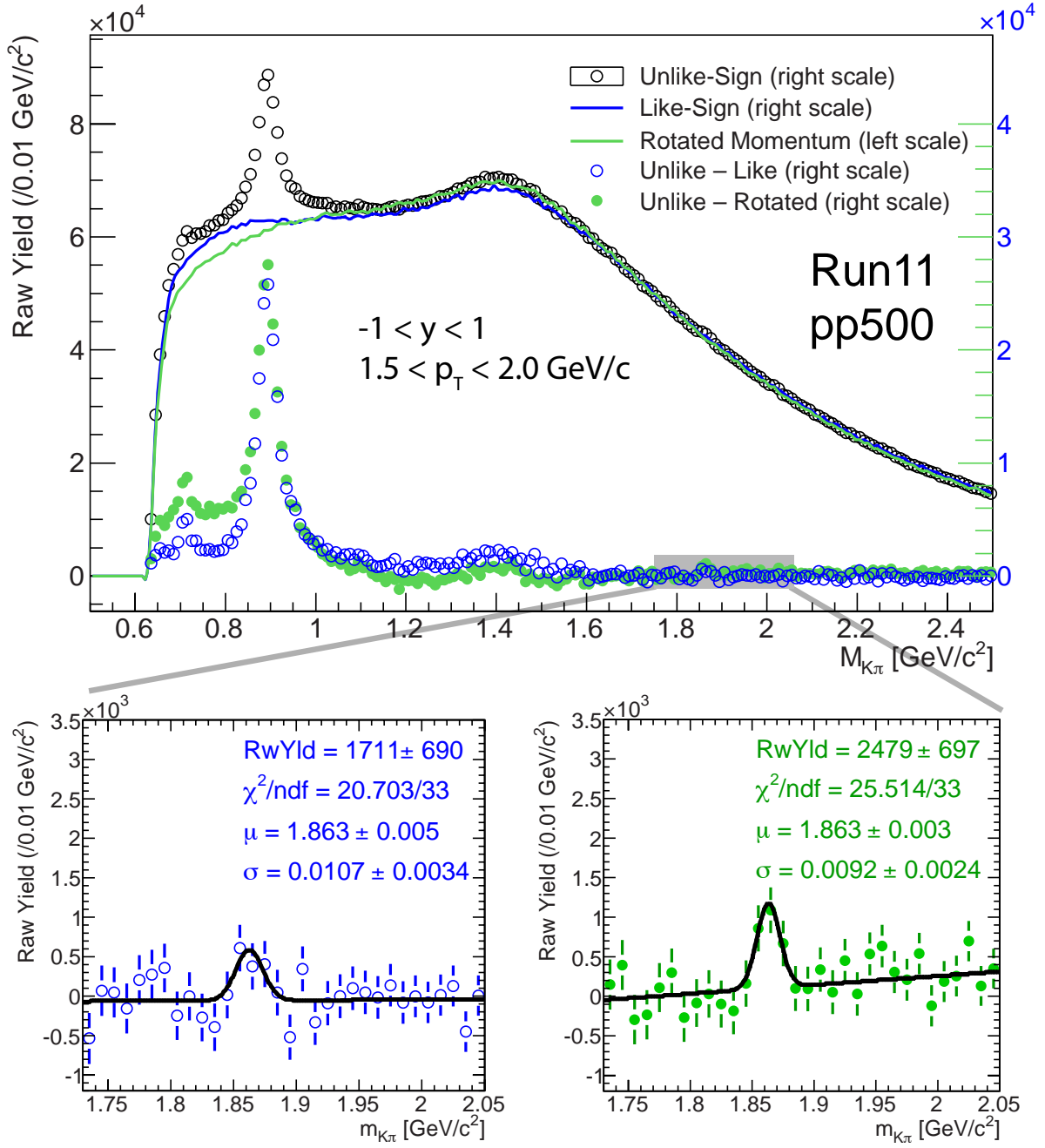


Figure 3.11: Upper Panel: Opposite-charged $K\pi$ invariant mass with the combinatorial background reconstructed by Like-Sign and Rotated Momentum techniques for all $K\pi$ pairs within $(1.5 < p_T < 2.0 \text{ GeV}/c)$ and $|y(K\pi)| < 1$. The gray rectangle illustrates the zoom to D^0 mass window. Lower left panel: Opposite-charged $K\pi$ pairs invariant mass after Like-Sign background subtracted. Lower right panel: Opposite-charged $K\pi$ pairs invariant mass after Rotated-Momentum background subtracted.

p_T bin [GeV/ c]		$1 < p_T < 2$	$.9 < p_T < 1.5$	$1.5 < p_T < 2$
Rotated Momentum	χ^2/ndf	27.4/33	27.4/33	25.5/33
	Raw Yield	4584 \pm 1016	2296 \pm 819	2479 \pm 697
	Mean [MeV/ c^2]	1865 \pm 3	1862 \pm 5	1863 \pm 3
	Resolution [MeV/ c^2]	11.2 \pm 2.5	12.0 \pm 3.6	9.2 \pm 2.4
	Significance	4.51	2.8	3.6
Like Sign	χ^2/ndf	17.6/33	20.9/33	20.7/33
	Raw Yield	3564 \pm 996	1947 \pm 835	1711 \pm 690
	Mean [MeV/ c^2]	1866 \pm 3	1867 \pm 4	1863 \pm 5
	Resolution [MeV/ c^2]	11.0 \pm 2.9	10.1 \pm 4.6	10.7 \pm 3.4
	Significance	3.58	2.33	2.5
Raw Yield - The Weihgted Average		4074 \pm 711	2122 \pm 585	2095 \pm 490

Table 3.1: Run11 pp500 results in p_T bins.

As seen in the summarizing Table 3.1, the Goodness of fit test shows that the signal can be well approximated by the fit function (Gaussian + linear) within statistical error bars. However, when the signal in p_T bins of 0.9-1.5 and 1.5-2 GeV/ c has its significance bellow 3 which is typically considered as questionable in the experimental community. Hence the statistical test of two hypotheses

- H_0 : there's no D^0 peak and the observed signal is entirely a product of statistical fluctuations,
- H_1 : there's a D^0 signal described by gaussian function + linear residual background,

was made to evaluate the likability of the signal occurrence. The Table 3.2 displays both the p -values of the linear function fits and gaussian+linear function fits to the data in the critical region of the invariant mass to be between 1.72 and 2.1 GeV/ c^2 . As one can see, the result of the signal obtained by Rotated-momentum background subtraction rejects

	no signal		gaussian signal	
p_T range [GeV/ c]	Like-Sign	Rotated-Momentum	Like-Sign	Rotated-Momentum
$1 < p_T < 2$	47.5%	10.6%	98.7%	74.7%
$.9 < p_T < 1.5$	74.7%	12.5%	95%	35.7%
$1.5 < p_T < 2$	80.9%	13.3%	95.3%	82.1%

Table 3.2: The results of the χ^2 test of two hypothesis, one assuming no signal in the sample and the other gaussian signal in the same sample. It shows p -values of the linear function and linear+gaussian function fits to data in critical region of the invariant mass between 1.72 and 2.1 GeV/ c^2 .

H_0 on the significance level $\alpha = 0.14$ for all p_T bins. In the case of the signal obtained by Like-sign background subtraction, the H_0 is entirely rejected on $\alpha = 0.81$ which is very weakly conclusive. H_1 has significantly higher p -value than H_0 for both methods and all p_T bins, however due to the ambiguity between H_0 and H_1 in cases of the Like-sign background and the narrower p_T bins (0.9-1.5, 1.5-2 GeV/ c) it was decided to use only the wider p_T bin 1-2 GeV/ c for the further analysis.

Finally, positions of all peaks (Mean values in Table 3.1 and μ values Figures 3.9, 3.10, and 3.11) are consistent within its errors with the "world average" value 1864.84 MeV/ c^2 [4]. The resolution is determined by p_T resolution of the daughter tracks (pion and kaon candidates) which are discussed in the next chapter in section 4.4 with references to section B.2. To determine the D^0 peak resolution while knowing p_T resolution of the daughter tracks, PYTHIA [32] was employed to simulate the D^0 hadronic decay and daughter particles's momenta were randomly smeared by gaussian functions with widths equal to known p_T resolution values of the daughter tracks. Invariant mass of pairs of such smeared kaon and pions was calculated and its spectrum is shown in Figure 3.12. Closed red circles represent the spectrum and the black curve is the gaussian fit to the peak around 1.865 GeV/ c^2 . The legend in the plot shows number of entries and results of the fit; "Mean" is the position of the gaussian and "Sigma" its width representing the D^0

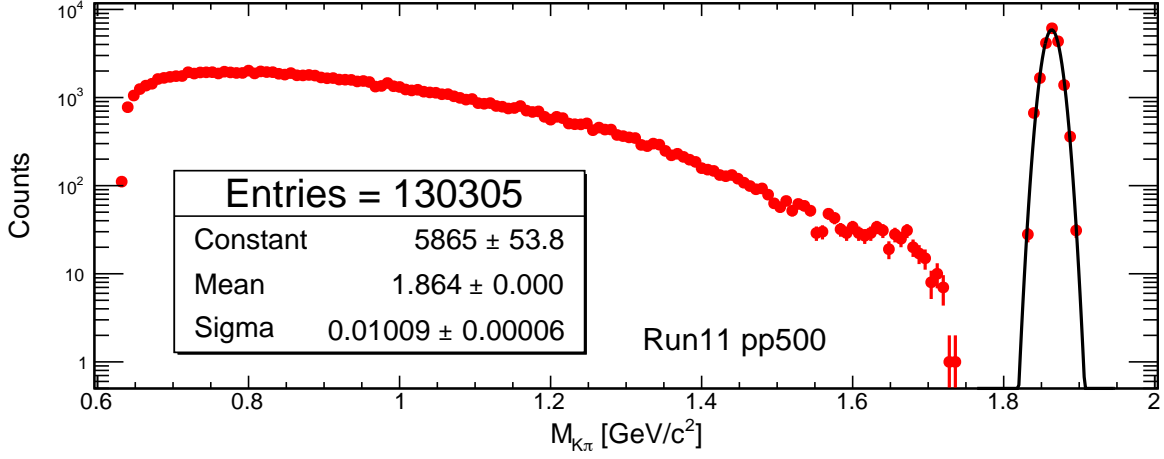


Figure 3.12: Invariant mass spectrum of oppositely charged kaon-pion pairs. Kaons pions came from D^0 hadronic decay generated by PYTHIA and their momenta were randomly smeared by gaussian functions with widths equal to known p_T resolution values.

invariant mass resolution. By comparing this value with the "Resolution" values in Table 3.1, one can see the consistency and conclude that D^0 signal resolution can be explained by the p_T resolution of the D^0 daughter particles.

The number of analyzed events from Run9 pp200 data was 2 times bigger than from Run11 pp500 data. That allowed getting good (significance at least 3) D^0 signal in two p_T bins even if the TOF acceptance was lower and the production cross section drops with energy. The procedure was exactly the same as the one described in previous paragraphs with results summarized in Table 3.3. This table is analogous with Table 3.1. One can observe larger fluctuations in Mean and Resolution values coherent with worse goodness of fit when compared to Run11 pp500. Simulation based on events reconstructed by GEANT from Monte-Carlo Pythia collisions determined the width of the D^0 invariant mass peak to be $10 \text{ MeV}/c^2$ and the position at $1865 \text{ MeV}/c^2$ [28]. Details are discussed in the next chapter.

method	p_T bin [GeV/ c]	$0.6 < p_T < 1.0$	$1.0 < p_T < 2.3$
Rotated Momentum	χ^2/ndf	158.74/177	161.30/177
	Raw Yield	1683 ± 525	1781 ± 598
	Mean [MeV/ c^2]	1844 ± 5	1871 ± 3
	Resolution [MeV/ c^2]	13.2 ± 3.8	7.7 ± 2.8
	Significance	3.21	2.98
Like Sign	χ^2/ndf	128.13/177	186.34/177
	Raw Yield	1716 ± 571	2054 ± 593
	Mean [MeV/ c^2]	1855 ± 11	1867 ± 2
	Resolution [MeV/ c^2]	14.9 ± 5.6	6.8 ± 2.2
	Significance	3.01	3.46

Table 3.3: Results in p_T bins from Run9 pp200 analysis. If the $\chi^2/\text{n.d.f.}$ is greater than 1 the contribution to averaged raw yield is scaled by.

3.4 D^* reconstruction

The D^* meson undergoes a cascade decay

$$D^{*\pm} \xrightarrow[p^*=39 \text{ MeV}/c]{B.R.=67.7\%} D^0 \pi^\pm \xrightarrow{B.R.=3.89\%} K^\mp \pi^\pm \pi^\pm$$

$M_{D^*} - M_{D^0} = 145.4 \text{ MeV}/c^2$, which is only slightly higher than the mass of the pion ($139.6 \text{ MeV}/c^2$). This gives opportunity to calculate the raw yield of the D^* meson as an area of the peak around $145.4 \text{ MeV}/c^2$ in $M_{K^\mp \pi^\pm \pi^\pm} - M_{K^\mp \pi^\pm}$ where $1.84 < M_{K^\mp \pi^\pm} < 1.89 \text{ GeV}/c^2$. The kinematics of such decay described in appendix B indicates that D^* mesons with $p_T \lesssim 1.6 \text{ GeV}/c$ are not detectable if the TOF is used to identify the daughter particles. It is hence reasonable to start D^* yield calculation at $p_T = 2 \text{ GeV}/c$.

The first step was exactly the same as the one in D^0 reconstruction described in previous paragraph. If the invariant mass M_2 of the $K^\mp \pi^\pm$ pair lay between 1.84 and 1.89 GeV/c^2 and $\cos(\theta^*)$ of the kaon in the CMS frame of the $K\pi$ pair was smaller than 0.77, such a

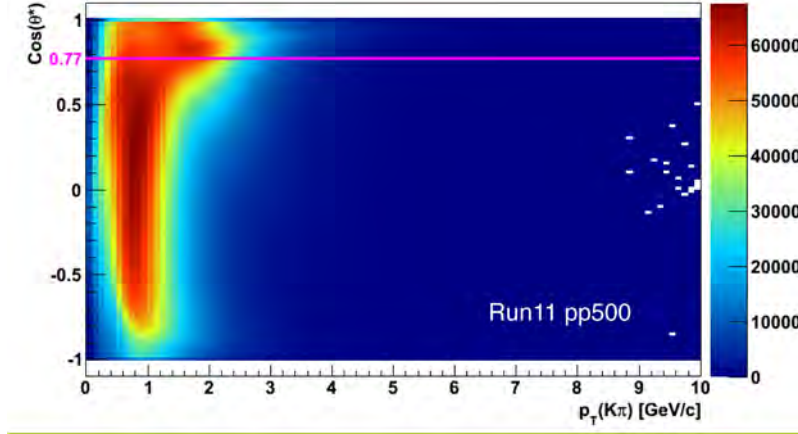


Figure 3.13: $\cos(\theta^*)$ of the kaon in the CMS of the $K\pi$ pair.

pair's four-vector was combined with pions to form a $K^\mp \pi^\pm \pi_S^\pm$ triplet¹ whose invariant mass M_3 was calculated and a histogram was filled with value $\Delta M \equiv M_3 - M_2$. The purpose of the $\cos(\theta^*)$ cut was to reduce the background coming from jets. As one can see in Figure 3.13, the background from jets becomes to be significant at higher p_T .

The combinatorial background was reconstructed by two independent techniques:

- **Wrong-sign Method** In the triplet of daughter particles, π_S had opposite sign to π .
- **Side-band Method** In the triplet of daughter particles, M_2 had been lying between 1.7 and 1.8 or 1.92 and 2.02 GeV/c^2 , i. e. outside the D^0 mass window.

The Wrong-sign background yield is “contaminated” by some real D^* signal whose kaon and pion daughters from D^0 decays are both mis-identified. The fraction of this over counting in the Wrong-sign background is estimated from a fast toy MC model described in subsection 5.1.1. The Side-band background yield doesn't suffer from this contamination so it was reasonable to use Side-band as the default method for combinatorial background reconstruction and the Wrong-sign (corrected on the over counting) as a

¹The symbol π_S denotes all pions which had different Track ID than the one in $K^\mp \pi^\pm$ pair.

source of systematic errors estimation.

Figure 3.14 depicts ΔM with both Wrong-sign and Side-band backgrounds which describe the combinatorial background so well that one doesn't even need to deal with any residual background. Figure 3.15 depicts same plots in $K^\mp \pi^\pm \pi^\pm$ p_T bins. The D^* raw yield was calculated as an area of the Gaussian peak obtained by fit into ΔM spectra after the Side-band background subtraction. Results of those fits are summarized in Table 3.4.

p_T bin [GeV/ c]	$2 < p_T < 3$	$3 < p_T < 4.2$	$4.2 < p_T < 5.5$	$5.5 < p_T < 8.0$
χ^2/ndf	3.02/4	1.88/4	3.98/4	1.63/4
Raw Yield	83.87 ± 18.1	82.49 ± 16.98	35.41 ± 7.71	16.77 ± 4.61
Mean [MeV/ c^2]	145.2 ± 0.1	145.6 ± 0.1	145.2 ± 0.1	145.4 ± 0.1
Resolution [MeV/ c^2]	0.3 ± 0.1	0.5 ± 0.3	0.4 ± 0.1	0.4 ± 0.1

Table 3.4: D^* raw yield results in p_T bins.

As shown both in Table 3.4 and Figure 3.15, the signal was split into 4 p_T bins with increasing widths as statistics drops with increasing p_T . Mean values fluctuate around 145.4 MeV/ c^2 up to 2 times Mean error and Resolution values are consistent within their errors around simulated value which was determined to be 0.3 MeV/ c^2 , slightly increasing with p_T . Goodness of fit test proved an excellent approximation of the signal by gaussian function. The background was very low so the significance calculation was not necessary.

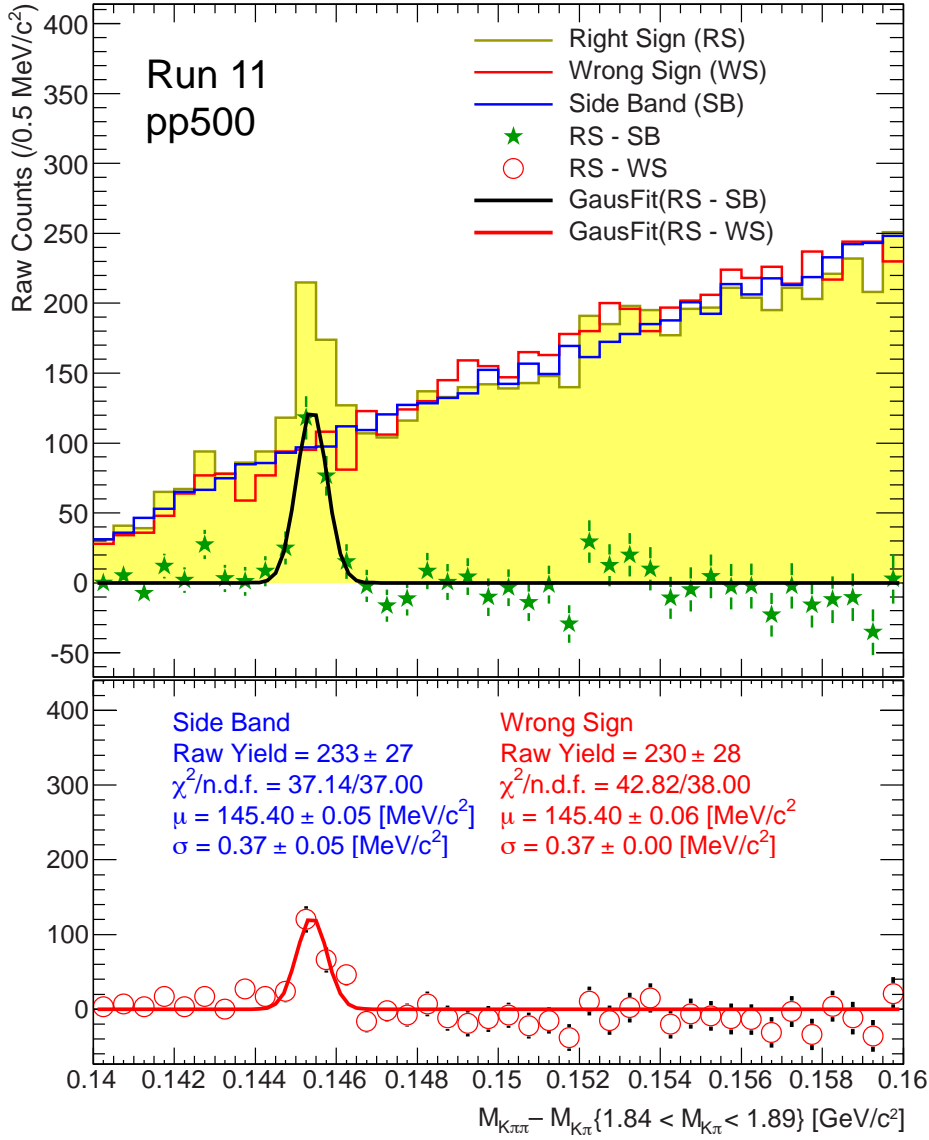


Figure 3.14: Upper panel: ΔM spectrum with combinatorial backgrounds reconstructed by Side-band and Wrong-sign technique. Green stars and the black line represent the ΔM with Side-band background subtracted and the gaussian fit to it respectively in the range from 0.14 to 0.16 GeV/c^2 . Lower panel: ΔM with Wrong-sign background subtracted and the gaussian fit to it in the range from 0.14 to 0.16 GeV/c^2 . The width of the gaussian function is fixed to be the same as in the case of the Side-band background subtracted.

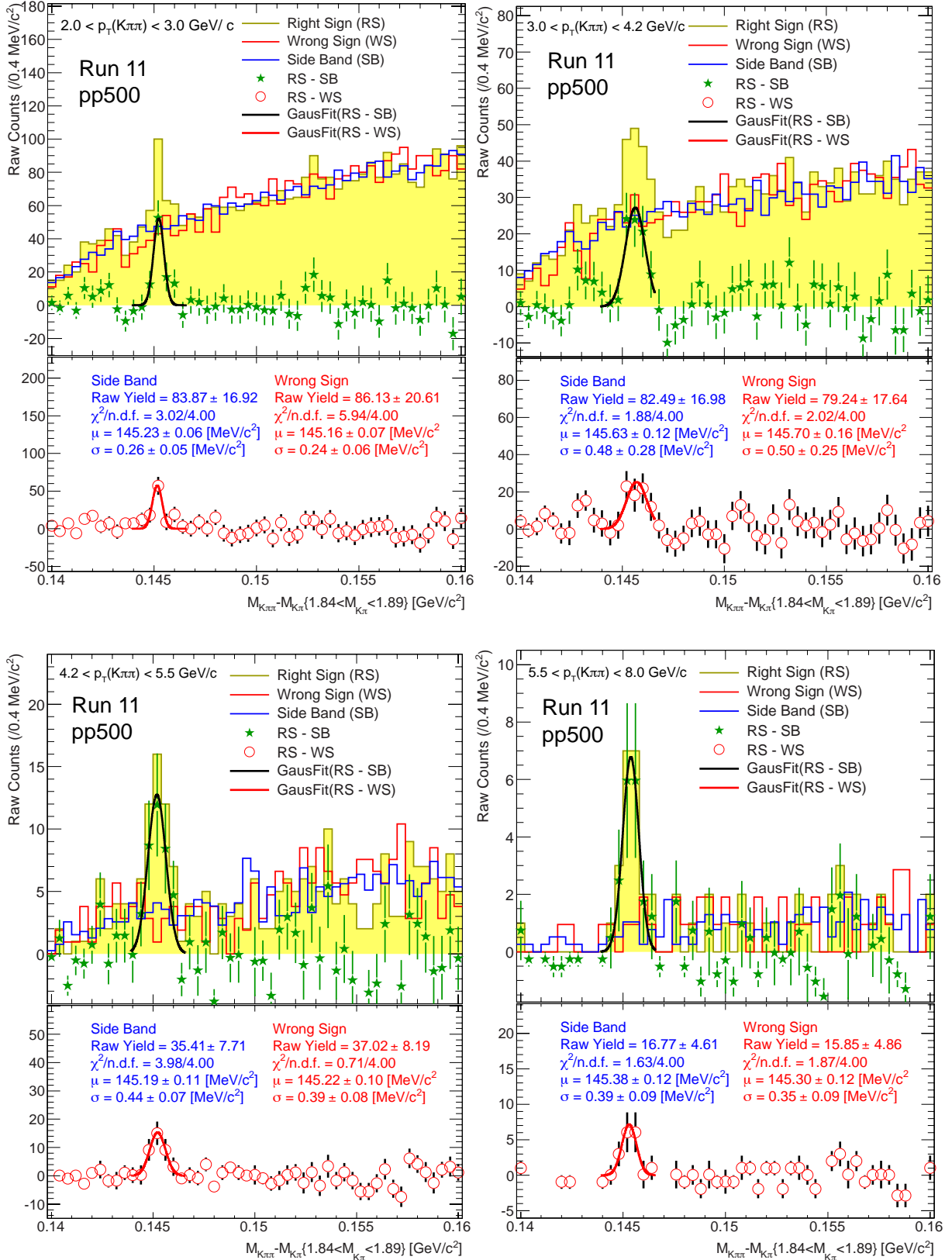


Figure 3.15: ΔM spectra with combinatorial backgrounds reconstructed by Side-band and Wrong-sign techniques in $K^\mp \pi^\pm \pi^\pm p_T$ bins.

Efficiency and Acceptance Correction

This chapter discusses the analysis of purely simulated data by PYTHIA [32], Toy Model (see sectionB.2), emperimental data embedded by simulated data, and experimental data to determine detector efficiency and acceptance corrections as well as for determinations of how much of signal is lost when various quality cuts are applied during the analysis of the Experimental data (discussed in previous chapter). In this analysis, it included the following:

1. Track Reconstruction Efficiency
2. Matching Efficiency
3. Particle Identification Efficiency
4. Kinematical Cuts Efficiency

4.1 Track Reconstruction Efficiency ε_R

The embedding of simulated data into experimental data is done by special group at STAR Collaboration who simulate the particle production by PYTHIA, those particles are processed by GEANT detector simulation [79] which implemented STAR geometry (it varies year by year). The data processed by GEANT has the same structure as raw data from collisions so it can be mixed together. Such embedded data are then processed through the full STAR offline reconstruction chain.

The track reconstruction efficiency was done through the embedding of PYTHIA simulated and GEANT processed D^0 tracks into Run9 pp200 data and PYTHIA simulated and GEANT processed K^+, K^-, π^+, π^- tracks into Run11 pp500 data in Run9 pp200 and Run11 pp500 analysis respectively. This section discusses the track reconstruction efficiency determined for Run11 pp500 analysis. The track reconstruction efficiency determined for Run9 pp200 analysis is described in [28].

K^-, K^+, π^-, π^+ Monte-Carlo (MC) particles were separately embedded into real events, each type with following setup:

- 50000 p+p 500GeV VPDMB trigger events
- Particles per event: 5
- $-50 < V_z < 50$ cm
- $0 < \phi < 6.39$ in radian, flat distribution
- $-1 < \eta < 1$, flat distribution
- $0 < p_T < 8\text{GeV}/c$, flat distribution

The embedding is realized through GEANT simulation of the STAR detector response on those MC particles, so that simulated TPC hits are included in the real hits and such

enriched events are then reconstructed through the same reconstruction chain as the real data events. This allows an analyst to track those MC particles down and count how many of them were properly reconstructed and how many were lost in order to calculate reconstruction efficiency. Figure 4.1 displays ε_R for π^+ , π^- , K^+ , K^- as a function of the p_T of PYTHIA generated track. The plot reveals that charge of the particle doesn't affect the reconstruction efficiency at all.

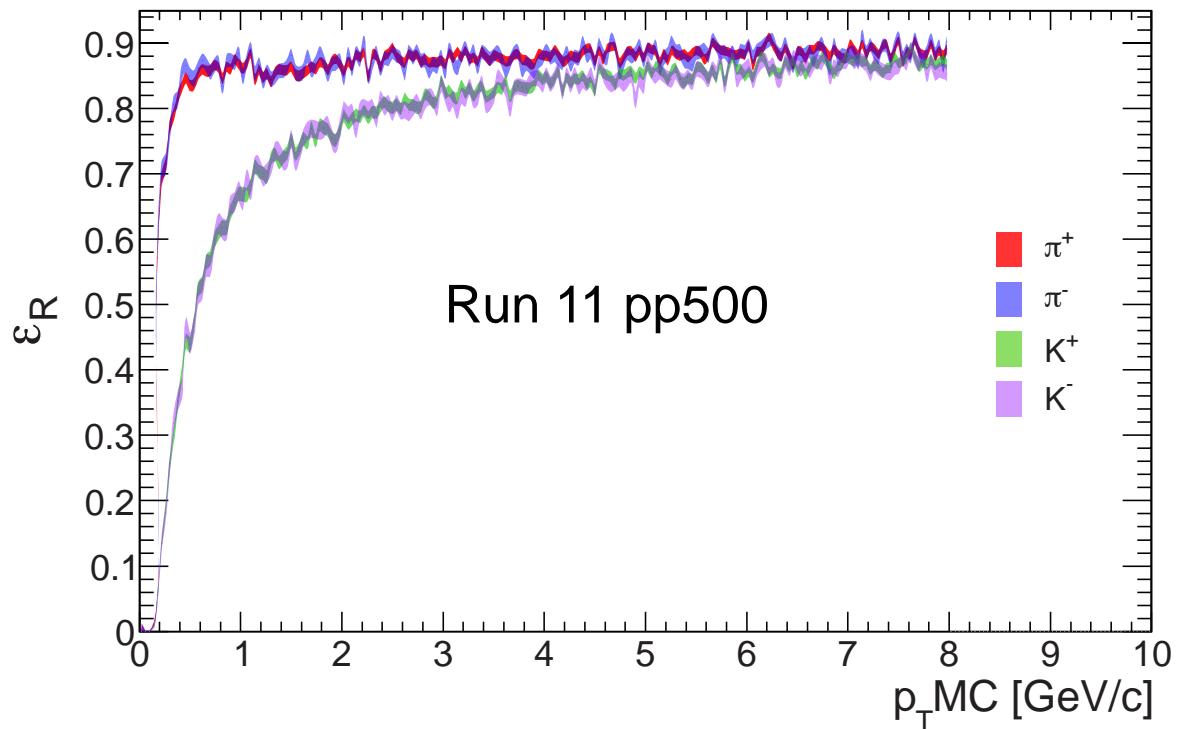


Figure 4.1: π^+ , π^- , K^+ , K^- track reconstruction efficiency. Errors are depicted by contours.

4.2 Matching Efficiency, ε_M

Let's consider $P(T)$ and $P(B)$ as a probability of matching in TOF (phenomenon T) and BEMC (phenomenon B) respectively. Then

$$P(T \cup B) = P(T) + P(B) - P(T \cap B). \quad (4.1)$$

If $P(B) > 0$ and T, B are independent phenomena, then

$$P(T) = \frac{P(T \cap B)}{P(B)}. \quad (4.2)$$

The TOF and BEMC matching efficiency as a function of the track p_T , ε_T and ε_B respectively, was then calculated as

$$\varepsilon_T(p_T) = \frac{h\left(p_T; |n\sigma_{K(\pi)}^{dE/dx}| < 2 \wedge B \wedge T\right)}{h\left(p_T; |n\sigma_{K(\pi)}^{dE/dx}| < 2 \wedge B\right)} \quad \varepsilon_B = \frac{h\left(p_T; |n\sigma_{K(\pi)}^{1/\beta}| < 2 \wedge T \wedge B\right)}{h\left(p_T; |n\sigma_{K(\pi)}^{1/\beta}| < 2 \wedge T\right)}, \quad (4.3)$$

where $h(p_T; x)$ denotes p_T histogram of the tracks fulfilling the condition x . ε_T is shown in Figure 4.2 as open and closed circles for pions and kaons respectively.

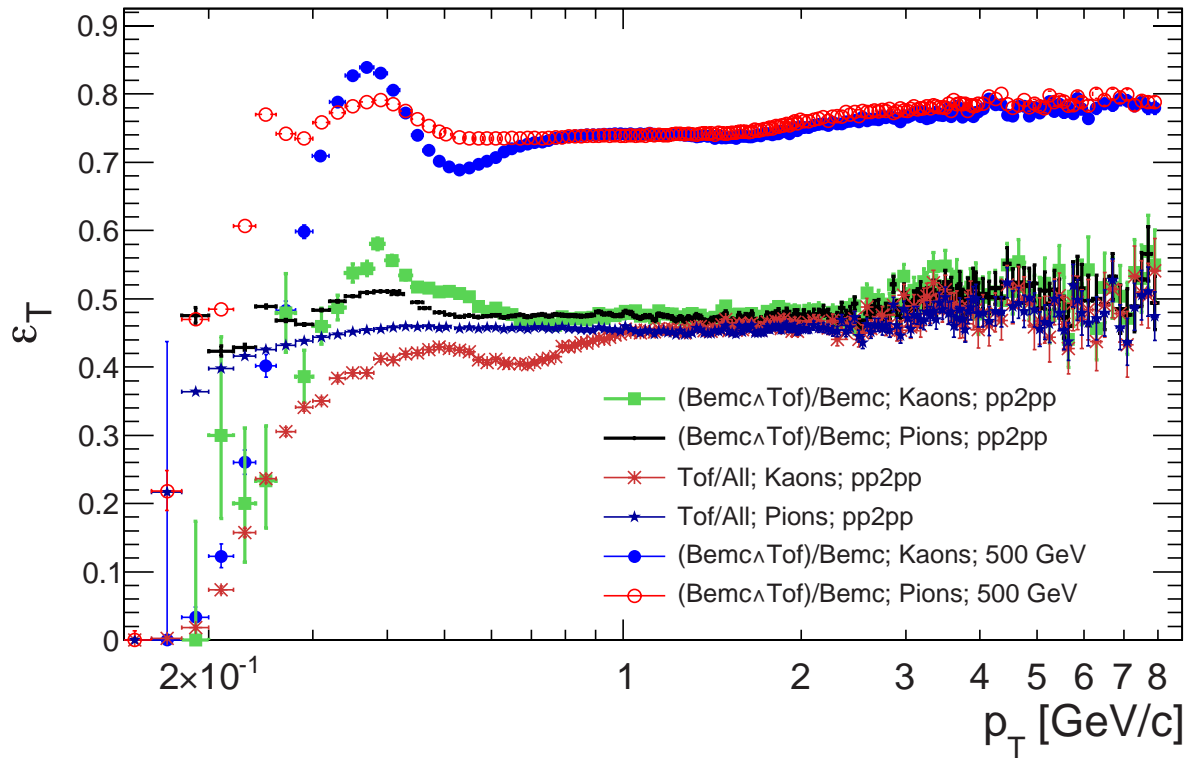


Figure 4.2: TOF Matching efficiency as a function of the track p_T . Open red (closed blue) circles depict the efficiency calculated according to (4.3) from the production P11id for pions (kaons). The pp2pp data were analyzed 1) by the same way with results depicted as green closed squares (kaons) and black thick dots (pions) 2) according to (4.4) with results depicted as dark red crosses (kaons) and dark blue (pions) asterisks.

As a matter of fact, phenomena T and B are not entirely independent and one must check the degree of their mutual correlation. To do so, there are low-luminosity data collected in year 2009 called **pp2pp st_physics**, trigger set **pp2pp_Production2009**; let's call them **pp2pp data** in the following text. Events in this trigger set don't contain pile-up

events/tracks, so that $\varepsilon_T, \varepsilon_B$ can be calculated as

$$\varepsilon_T^{\text{pp2pp}}(p_T) = \frac{h\left(p_T; |n\sigma_{K(\pi)}^{\text{dE/dx}}| < 2 \wedge T\right)}{h\left(p_T; |n\sigma_{K(\pi)}^{\text{dE/dx}}| < 2\right)} \quad \varepsilon_B^{\text{pp2pp}}(p_T) = \frac{h\left(p_T; |n\sigma_{K(\pi)}^{1/\beta}| < 2 \wedge B\right)}{h\left(p_T; |n\sigma_{K(\pi)}^{1/\beta}| < 2\right)}, \quad (4.4)$$

respectively. By comparing the matching efficiency calculated according to (4.4) and the one calculated according to (4.3), it is possible to estimate the degree of correlation between phenomena T and B :

$$\varrho_T = \frac{\varepsilon_T^{\text{pp2pp}}}{\varepsilon_T} \quad \varrho_B = \frac{\varepsilon_B^{\text{pp2pp}}}{\varepsilon_B} \quad (4.5)$$

Figure 4.2 displays the TOF matching efficiency obtained from pp2pp data, tagged with the "pp2pp" term in the legend. Compared to the efficiency obtained from P11id production (tagged with the "500 GeV" term in the legend), the lower ε_T value is caused by lower TOF acceptance; the TOF detector was not fully installed during Run 9. Further the in the legend of Figure 4.2, there are terms "(Bemc^Tof)/Bemc" and "Tof/All" denoting the efficiency calculated according to formulas (4.3) and (4.4) respectively. One can see that the efficiency calculated by (4.3) is higher than the other one and has a "bump" structure at p_T around 0.4 GeV/ c (compare the green squares with dark red stars for kaons and black thick dots with dark blue stars for pions) indicating the correlation of phenomena T and B . The Figure 4.3 displays the same as Figure 4.2 for BEMC Matching Efficiency ε_B . Figures 4.4 and 4.5 display ϱ_T and ϱ_B respectively. As one can see from the plots, unsurprisingly $\varrho_T \simeq \varrho_B$, which confirms the mutual correlation of the phenomena T and B . Figure 4.6 shows corrected TOF and BEMC matching efficiency separately both for pions and kaons while Figure 4.7 shows it combined. Kaons with no TOF information and $p_T < 1.3$ GeV/ c were rejected (see subsection 3.2.2), so that $\varepsilon_M = \varrho_T \varepsilon_T$ for kaons up to $p_T < 1.3$ GeV/ c whereas

$$\varepsilon_M \equiv \varepsilon_{\text{TUB}} = \varrho_T \varepsilon_T + \varrho_B \varepsilon_B - \varrho_T \varrho_B \varepsilon_T \varepsilon_B \quad (4.6)$$

for all other cases. Corrected efficiency $\varrho_T \varepsilon_T$ or $\varrho_B \varepsilon_B$ represents the phenomenon T or B already independent on the phenomenon B or T respectively. Let's note that this is

the case of D^* analysis. PID cuts in D^0 analysis were different (see subsection 3.2.2), so that this "jump" in ε_M shown in Figure 4.7 doesn't occur. In Run9 pp200 analysis, the situation was much simpler. Due to the same detector calibrations and geometry the pp2pp data could be used to determine the matching efficiency. It calculated by (4.4) and it's shown already in Figure 4.2 as dark red crosses (kaons) and dark blue (pions) asterisks.

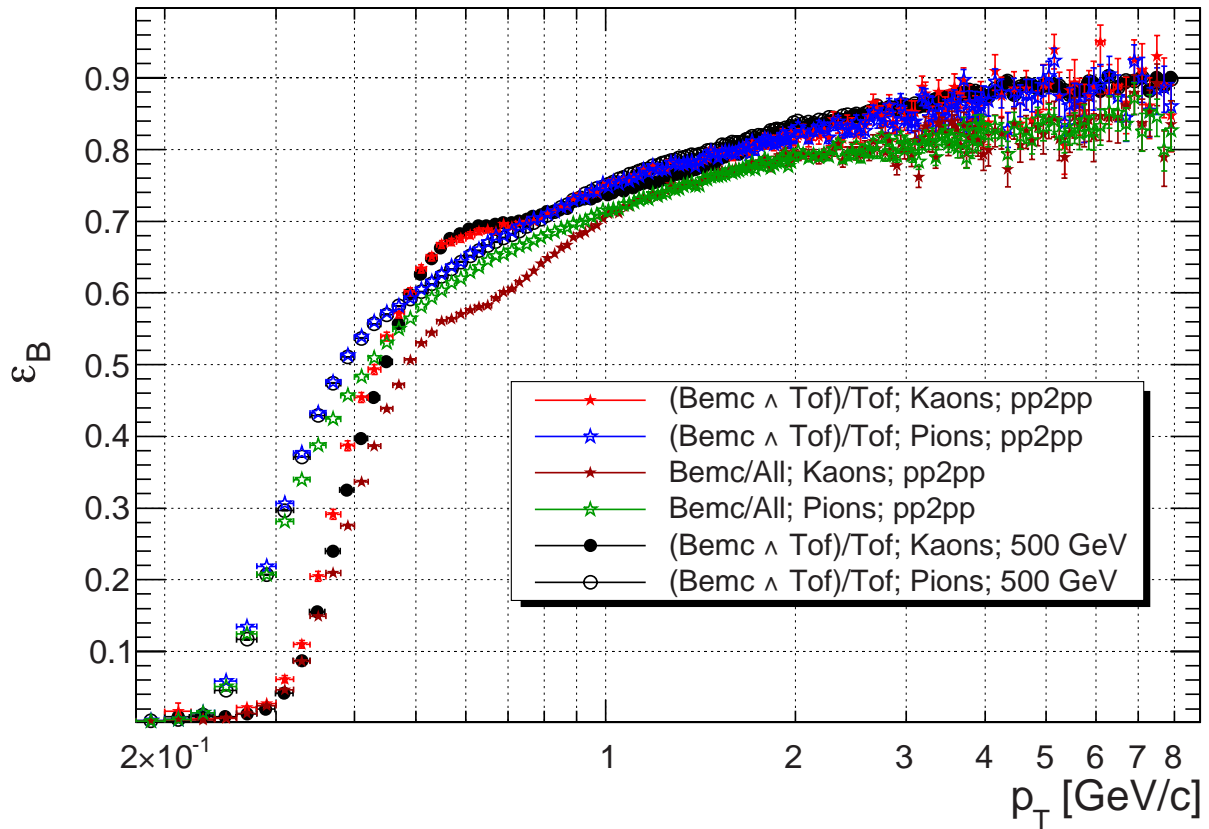


Figure 4.3: BEMC Matching efficiency as a function of the track p_T . Open (closed) black circles depict the efficiency calculated according to (4.3) from the production P11id for pions (kaons). The pp2pp_Production2009 trigger set was analyzed 1) by the same way with results depicted as red closed asterisks (kaons) and blue open asterisks (pions) 2) according to (4.4) with results depicted as brown closed asterisks (kaons) and green open stars (pions) asterisks.

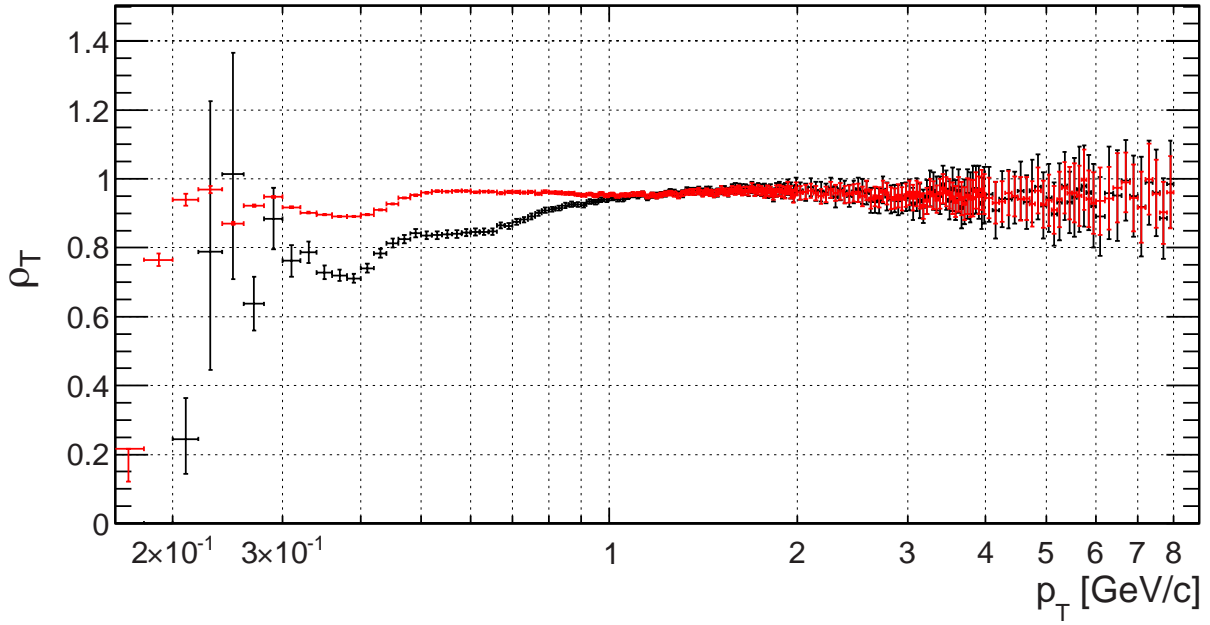


Figure 4.4: The degree of correlation between phenomena T and B calculated according to (4.5). Red color is dedicated to pions while the black represents kaons.

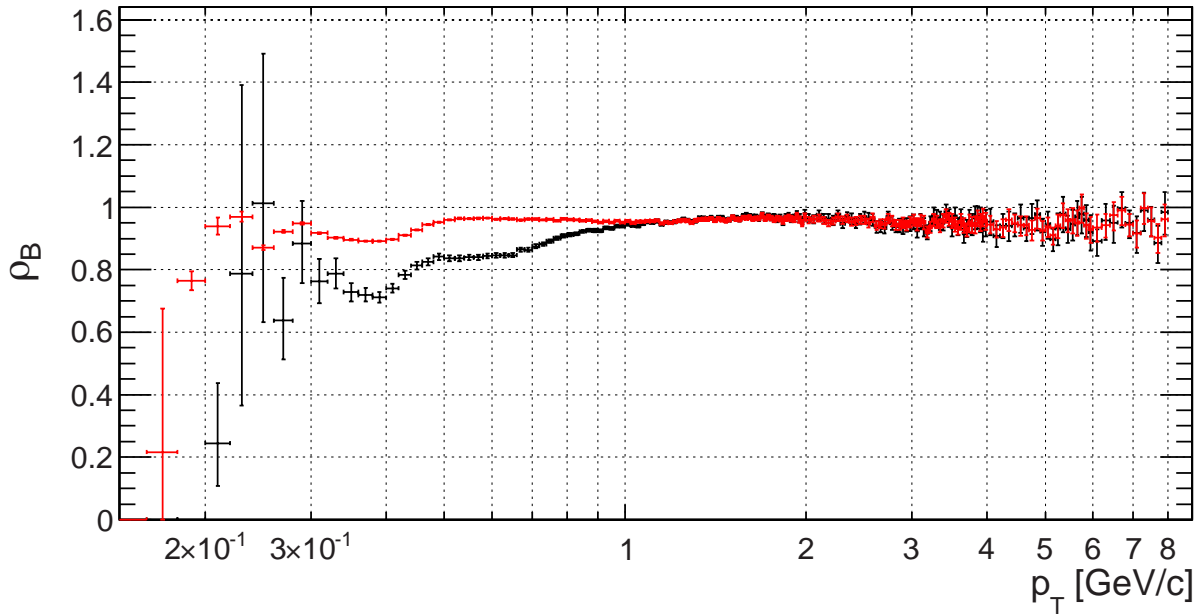


Figure 4.5: The degree of correlation between phenomena B and T calculated according to (4.5). Red color is dedicated to pions while the black represents kaons.

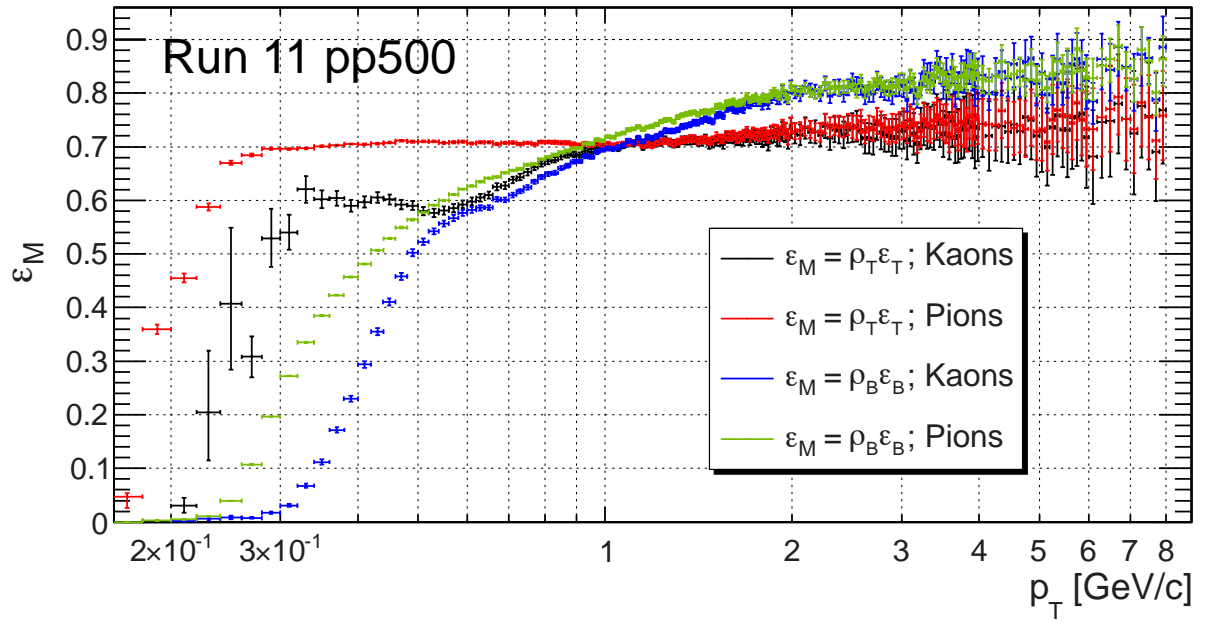


Figure 4.6: The TOF and BEMC matching efficiency separately.

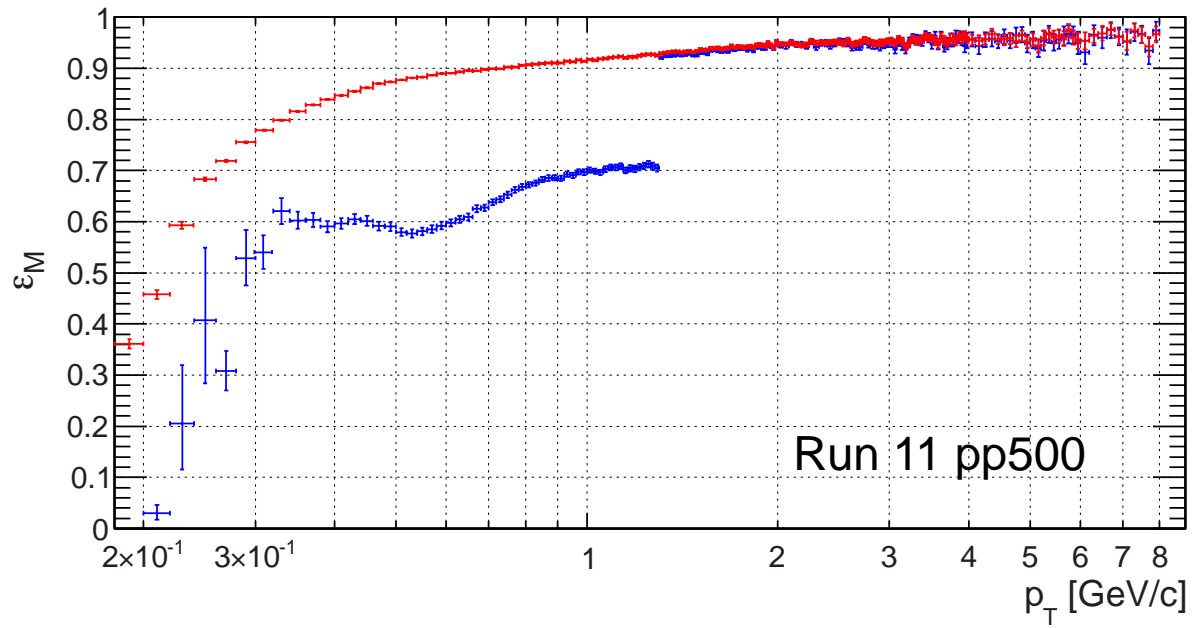


Figure 4.7: TOF and BEMC matching efficiency combined. Kaons with no TOF information and $p_T < 1.3$ GeV/ c were rejected (see subsection 3.2.2 , so that $\varepsilon_M = \rho_T \varepsilon_T$ for kaons up to $p_T < 1.3$ GeV/ c .

The expected value of the efficiency ξ in given D^0/D^* transverse momentum bin (a, b) was calculated as the inner product of the single track efficiency $\varepsilon(p_T)$ and the track p_T distribution $G^{(a,b)}(p_T)$ for D^0/D^* $p_T \in (a, b)$:

$$\xi \equiv E^{(a,b)}(\varepsilon(p_T)) = \int_0^8 \varepsilon(p_T) G^{(a,b)}(p_T) dp_T, \quad (4.7)$$

$$G^{(a,b)}(p_T) \equiv \int_a^b g(t, p_T) dt, \quad (4.8)$$

where t denotes p_T of a mother particle. $g(t, p_T)$ for all mother and daughter particles are shown in Figures B.2 and B.3.

The results of the track reconstruction and matching efficiency separately for D^0/D^* transverse momentum bins (a, b) used in the analysis of experimental data (see Tables 3.1 and 3.4) in Run11 pp500 analysis are presented in Table 4.1. The first column in Table 4.1 shows D^0/D^* transverse momentum bins (a, b) , the second column shows corresponding p_T profiles $G^{(a,b)}(p_T)$ of the daughter particles in (a, b) , and further columns show corresponding values. They are shown separately for track reconstruction and matching efficiency as well as for particular daughters.

The results of the track reconstruction and matching efficiency of D^0 Run9 pp200 analysis done by author of this thesis is shown in Figure 4.8. It includes also particle identification (PID) efficiency ε_{PID} which is discussed in the next section for Run11 pp500 D^* analysis. The PID cuts for D^0 analysis were the same in Run9 pp200 as in Run11 pp500. The PID efficiency ε_{PID} for both was 95.45%.

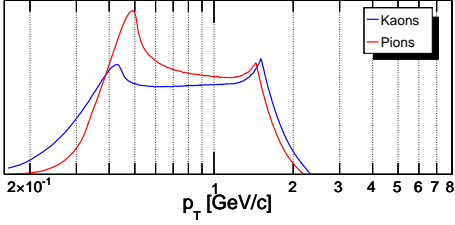
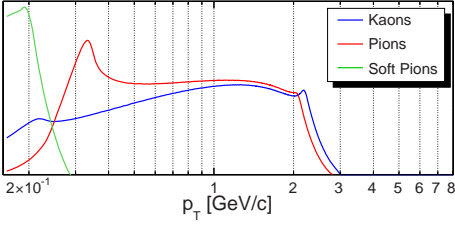
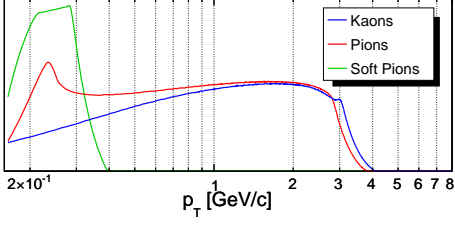
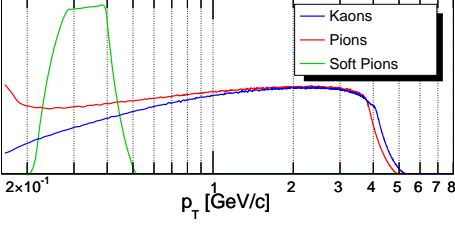
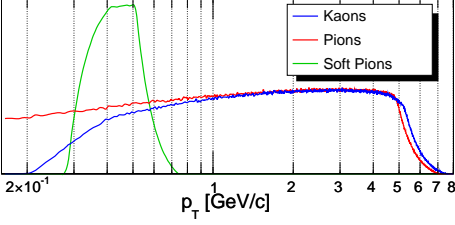
(a, b) [GeV/c]	$G^{(a,b)}(p_T)$	ξ_R [%]			ξ_M [%]		
		K	π	π_S	K	π	π_S
(1.0,2.0)		62.78 +1.48 -1.50	85.26 +1.14 -1.20		70.48 +0.88 -0.86	73.30 +0.39 -0.39	
(2.0,3.0)		66.00 +1.15 -1.16	85.20 +0.95 -0.98	37.70 +0.98 -1.00	78.43 +0.75 -0.73	90.79 +0.22 -0.22	22.01 +0.45 -0.70
(3.0,4.2)		70.81 +1.04 -1.05	85.33 +0.88 -0.92	68.82 +1.45 -1.48	83.59 +0.73 -0.72	90.99 +0.32 -0.33	58.46 +0.44 -0.54
(4.2,5.5)		74.62 +0.90 -0.91	85.35 +0.77 -0.79	78.47 +1.32 -1.37	87.28 +0.86 -0.86	91.48 +0.46 -0.47	78.51 +0.16 -0.16
(5.5,8.0)		78.04 +0.75 -0.76	85.85 +0.64 -0.66	82.85 +1.22 -1.27	90.17 +1.02 -1.05	92.40 +0.63 -0.65	85.39 +0.09 -0.09

Table 4.1: Track reconstruction ε_R and matching efficiency ε_M for daughter particles from D^0 (first row) or D^* (second to last row) decay. D^0/D^* transverse momentum bins (a, b) correspond to the bins in the analysis of experimental data. Column $G^{(a,b)}(p_T)$ shows p_T profiles of the daughter particles in (a, b) . Let's note that $\xi^{D^0} = \xi^K \times \xi^\pi$ and $\xi^{D^*} = \xi^K \times \xi^\pi \times \xi^{\pi_S}$.

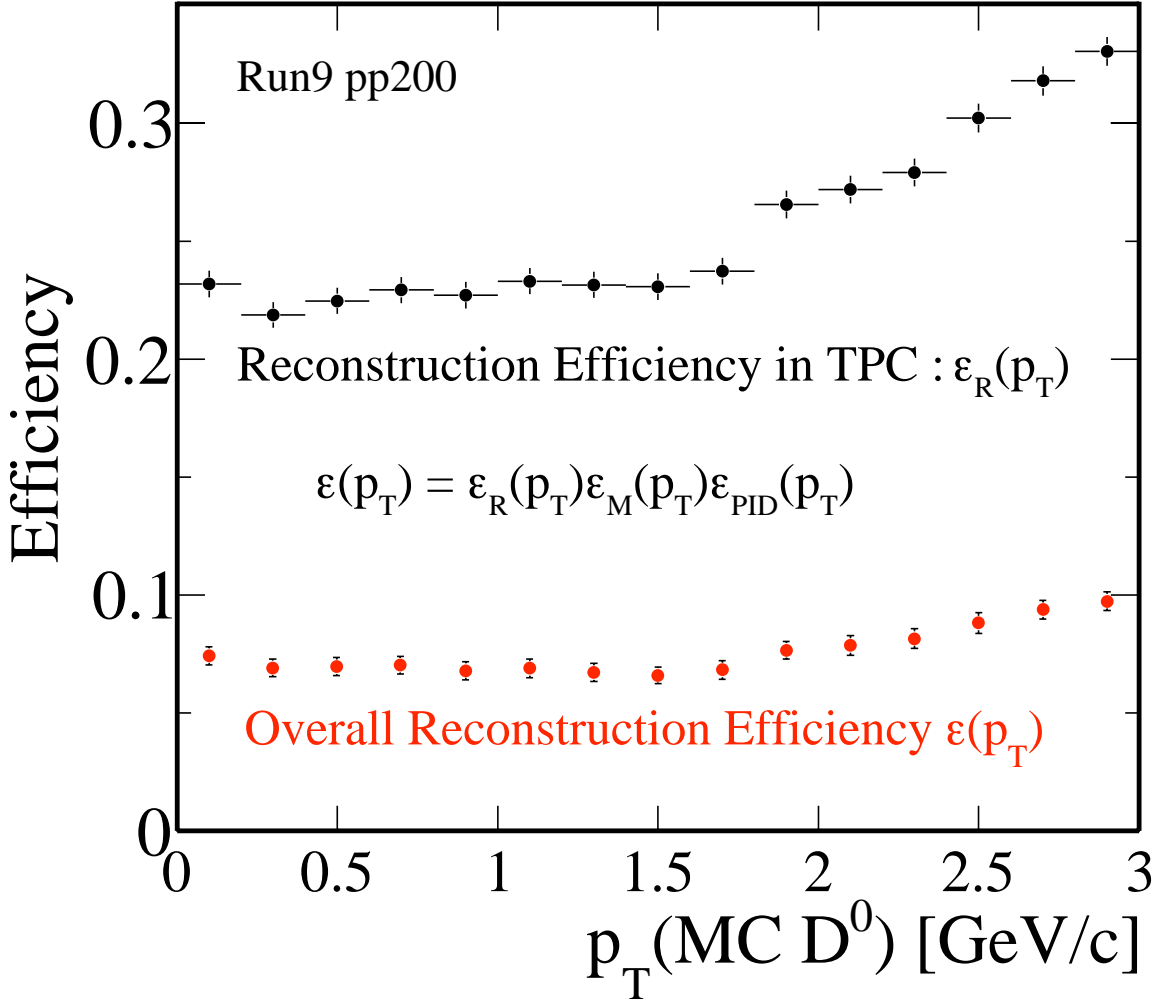


Figure 4.8: D^0 meson reconstruction efficiency as a function of PYTHIA generated D^0 meson p_T .

4.3 Particle Identification Efficiency, ϵ_{PID}

PID cuts were momentum dependent (see subsection 3.2.2). They were different in D^0 and D^* reconstruction. The first paragraph describes D^* and the second D^0 .

The cut for pions corresponds to gaussian area between $-3\sigma, +3\sigma$, i.e. 99.6%. The cut

for kaons is split into 3 p_T regions:

- $0.2 < p_T < 1.3 \text{ GeV}/c$ corresponds to gaussian area between $-2\sigma, +3\sigma$, i.e. 97.6%.
- $1.3 < p_T < 2.07 \text{ GeV}/c$ 74 % of kaons candidates identified by TOF, while 26 % by TPC with PID efficiency corresponding to gaussian area between $-2\sigma, +2\sigma$, i.e. 95.45%. The overall PID efficiency in this region was then $0.74 \times 97.6 + 0.26 \times 95.45 = 97\%$
- $p_T > 2.07 \text{ GeV}/c$ corresponds to gaussian area between $-2\sigma, +2\sigma$, i.e. 95.45%.

The PID cuts for D^0 analysis were the same in Run9 pp200 as in Run11 pp500 and corresponds to gaussian between its $(-2\sigma, +2\sigma)$ which is 95.45%.

4.4 Kinematical cuts efficiency

Kinematical cuts were applied only in D^* reconstruction so this section is entirely dedicated to Run11 pp500 analysis.

The reconstructed D^0 invariant mass peak width depends almost exclusively on the daughter particle p_T resolution. When carrying the D^* analysis out the invariant mass of $K\pi\pi$ triplet was calculated only if the $K\pi$ pair invariant mass had been between 1.84 and 1.89 GeV/c^2 and $\cos(\theta^*)$ of the kaon in the CMS frame of the $K\pi$ pair was smaller than 0.77. These cuts introduce a loss in the D^* yield. This section describes the simulation to evaluate the loss.

One can calculate the daughter particle p_T resolution from embedding as a gaussian sigma of the relative difference between reconstructed p_T^{RC} and Monte-carlo p_T^{MC} transverse momentum: $\sigma \left(\frac{p_T^{\text{RC}} - p_T^{\text{MC}}}{p_T^{\text{MC}}} \right)$. Figure 4.9 shows hereby calculated p_T resolution for kaons

and pions. The resolution was parametrized by function

$$\rho(m, p_T) \equiv \sqrt{c^2 p_T^2 + \frac{d^2 m^2}{p_T^2} + d^2}, \quad (4.9)$$

where c, d are free parameters obtained by a fit into $\sigma \left(\frac{p_T^{\text{RC}} - p_T^{\text{MC}}}{p_T^{\text{MC}}} \right)$ and m is the mass of the particle. The values of c, d are also displayed in Figure 4.9.

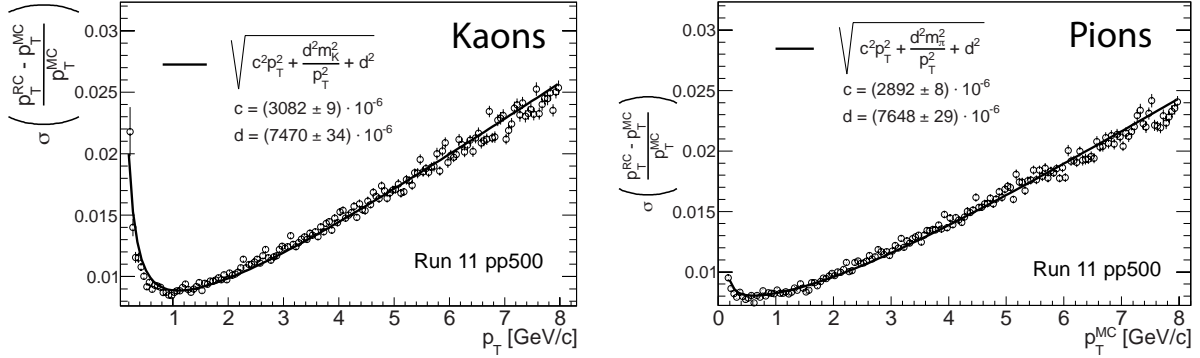


Figure 4.9: p_T resolution kaons and pion by TPC.

The Monte-carlo Toy model described in section B.2 was used to produce the daughter particles transverse momenta which were smeared according to a gaussian function with the sigma parameter given by $\rho(m, p_T)$. Hereby smeared particles underwent the same cuts on p_T and η as those in the data analysis. $g(t, p_T)$ defined in section B.2 describes the physical D^* kinematics, but man must take $\varepsilon_R(p_T)$ and $\varepsilon_M(p_T)$ into account if man wants estimate the impact of the $K\pi$ pair invariant mass cut on the raw yield. This was carried out by the placing the condition

$$\text{if}(\text{Rndm} > \varepsilon_R(p_T^{\text{SM}}) \varepsilon_M(p_T^{\text{SM}})) \text{ continue} \quad (4.10)$$

after every daughter particle transverse momentum smearing. Rndm denotes a random number between 0 and 1 and p_T^{SM} the already smeared transverse momentum. The D^0 invariant mass M^{RC} and $\cos(\theta^*)$ were then calculated from p_T^{SM} of kaons and pions only after both passed the condition (4.10). Figure 4.10 shows scatter plot, represented by the function $g^{\text{RC}}(t, M^{\text{RC}})$, of D^* transverse momentum t and reconstructed D^0 invariant mass

M^{RC} . Figure 4.11 displays projections $\int_a^b g^{\text{RC}}(t, \cos(\theta^*)) dt$. The kinematical cut efficiency on D^0 candidates's mass $\varepsilon_{\text{Mass}}$ was calculated for given $D^* p_T$ bin (a, b) as

$$\varepsilon_{\text{Mass}} \equiv \frac{\int_{1.84}^{1.89} \int_a^b g^{\text{RC}}(t, M^{\text{RC}}) dt dM^{\text{RC}}}{\int_0^\infty \int_a^b g^{\text{RC}}(t, M^{\text{RC}}) dt dM^{\text{RC}}} \quad (4.11)$$

and the kinematical cut efficiency of $\cos(\theta^*)$, ε_θ , was calculated for given $D^* p_T$ bin (a, b) as

$$\varepsilon_\theta \equiv \frac{\int_{-1}^{0.77} \int_a^b g^{\text{RC}}(t, \cos(\theta_{\text{RC}}^*)) dt d\cos(\theta^*)}{\int_{-1}^1 \int_a^b g^{\text{RC}}(t, \cos(\theta^*)) dt d\cos(\theta^*)} \quad (4.12)$$

The numerical results of $\varepsilon_{\text{Mass}}$ and ε_θ in D^* transverse momentum bins (a, b) , corresponding to the bins in the analysis of experimental data, are summarized in Table 4.2.

(a, b) [GeV/c]	(2.0,3.0)	(3.0,4.2)	(4.2,5.5)	(5.5,8.0)
$\varepsilon_{\text{Mass}}$ [%]	98.46	97.68	96.04	91.97
ε_θ [%]	85.15	88.98	90.87	91.35

Table 4.2: The kinematical cut efficiency on D^0 candidates's mass $\varepsilon_{\text{Mass}}$ and on $\cos(\theta^*)\varepsilon_\theta$ in D^* transverse momentum bins (a, b) correspond to the bins in the analysis of experimental data.

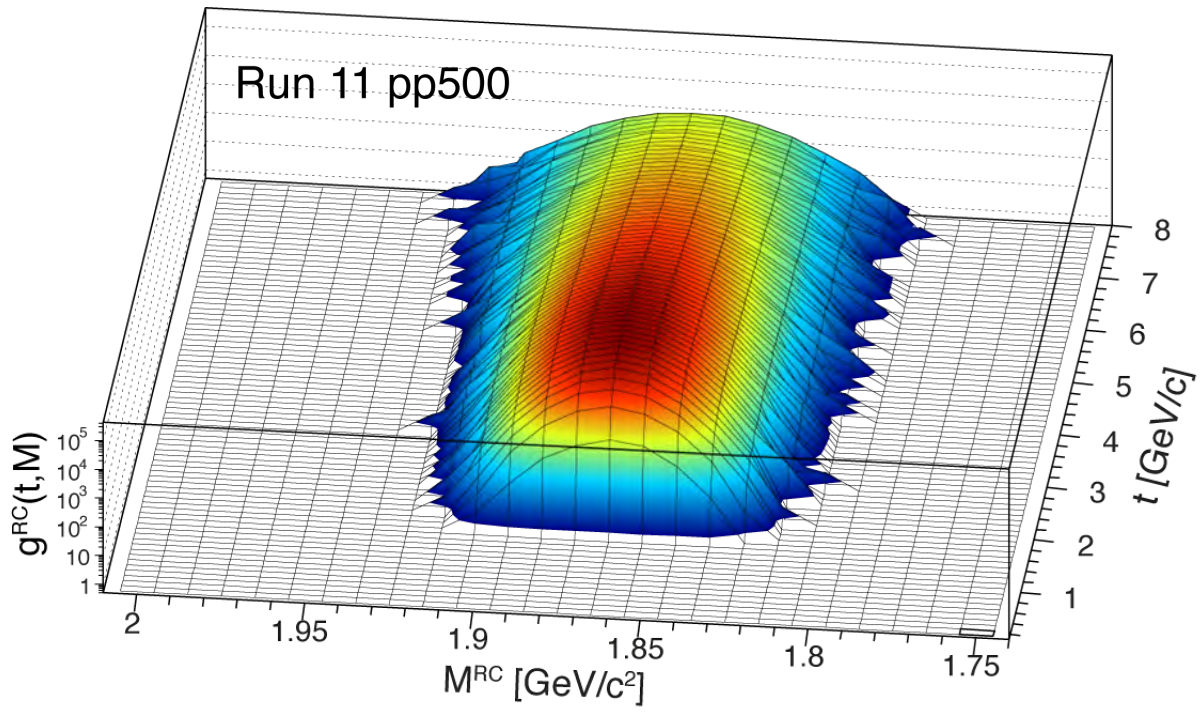


Figure 4.10: Surface plot of D^* transverse momentum t and reconstructed D^0 invariant mass M^{RC} .

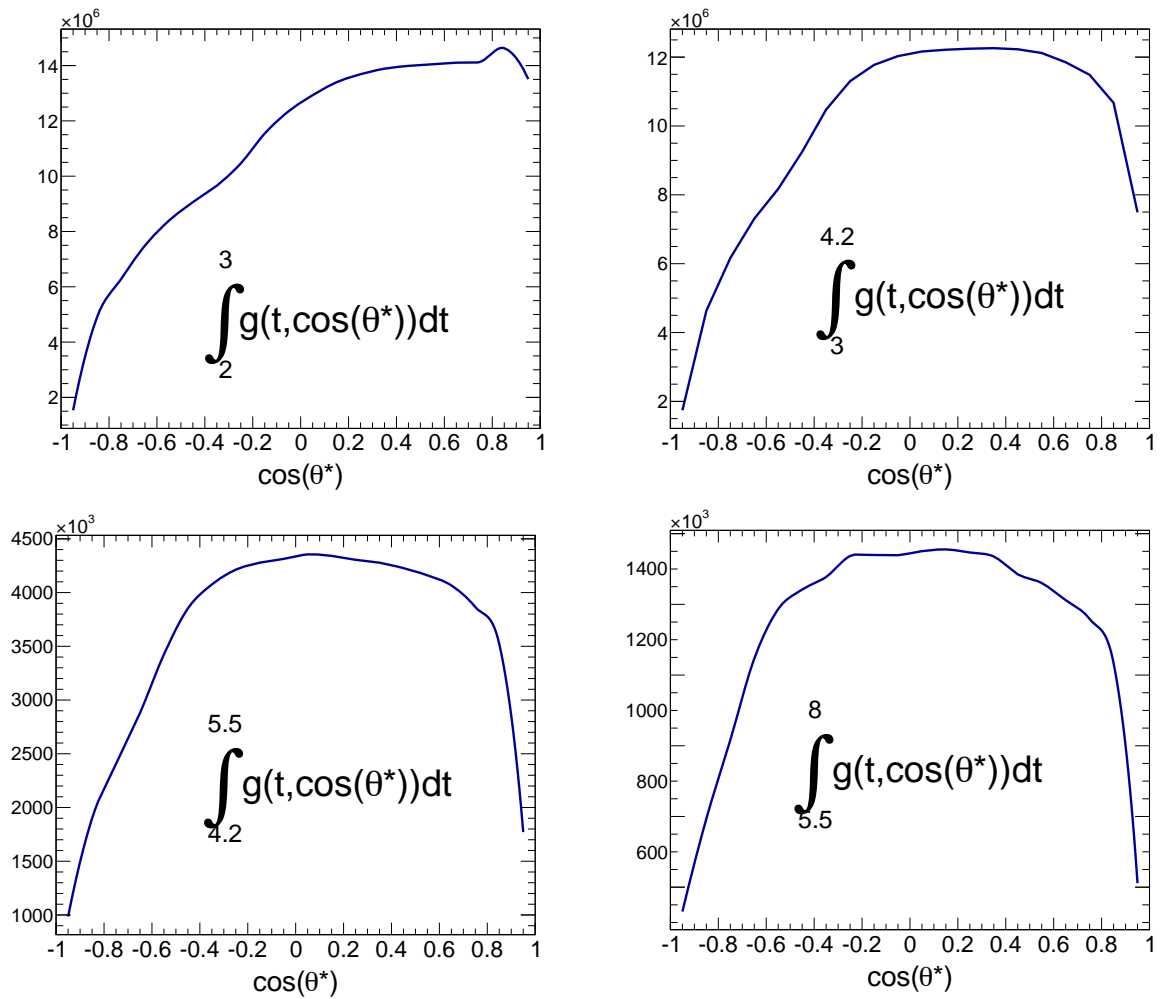


Figure 4.11: Projections $\int_a^b g^{\text{RC}}(t, \cos(\theta^*)) dt$. The drop at $\cos(\theta^*)$ close to -1 is the result of the kaon momentum at D^0 rest going against the D^0 momentum direction resulting in a much smaller momentum in the lab frame, thus lower reconstruction efficiency.

4.5 Trigger bias correction

Heavy quarks are produced during initial hard scatterings creating high p_T particles penetrating easier into calorimeters which makes a higher probability of reconstruction of a

collision vertex and such events are more likely to pass the event selection criteria discussed in section 3.1. This introduces bias skewed towards events containing charmed particles. Such bias was calculated as a ratio

$$\beta(t) \equiv \frac{\epsilon_{\text{VPD}}\epsilon_{\text{Vtx}}}{\xi_{\text{VPD}}(t)\xi_{\text{Vtx}}(t)}, \quad (4.13)$$

where ϵ_{VPD} is the VPD trigger efficiency, ϵ_{Vtx} is the efficiency vertex reconstruction, $\xi_{\text{VPD}}(t)$ is the VPD trigger efficiency for events containing D^* mesons, $\xi_{\text{Vtx}}(t)$ is the vertex reconstruction efficiency for events containing D^* mesons, and t a transverse momentum of D^* meson.

The PYTHIA [32] version 6.205 with minimum processes selected and with the CDF TuneA settings [80] was used as the event generator in GEANT to simulate events which were then reconstructed the same way as real events had been. Those reconstructed events were analyzed in order to get BBC and VPD trigger response and vertex. Figure 4.12 shows histogram of number of generate events denoted as "MB" and events containing D^* mesons denoted as "Charmed". One can see that the main discrepancy between "MB" and "Charmed" events lies in vertex reconstruction efficiency. Let's note that events containing charmed particles comprise actually high- p_T particles more likely to leave some signal in EMC, which is necessary to give an event positive ranking. Furthermore, D^0 itself decays into particles e^\pm, η which very likely directly or through their decay products leave signal in EMC. Figure 4.13 then depicts $\xi_{\text{VPD}}(t)\xi_{\text{Vtx}}(t)$ together with the Trigger bias $\beta(t)$ calculated according to (4.13), where $\epsilon_{\text{VPD}}\epsilon_{\text{Vtx}}$ was found to be 38.82%, and Table 4.3 summarizes results for D^0/D^* transverse momentum bins (a, b) .

$t \in (a, b)$ [GeV/c]	(1.0,2.0)	(2.0,3.0)	(3.0,4.2)	(4.2,5.5)	(5.5,8.0)
$\beta(t)$	0.696	0.652	0.630	0.629	0.636

Table 4.3: Trigger Bias $\beta(t)$ in D^0/D^* transverse momentum bins (a, b) .

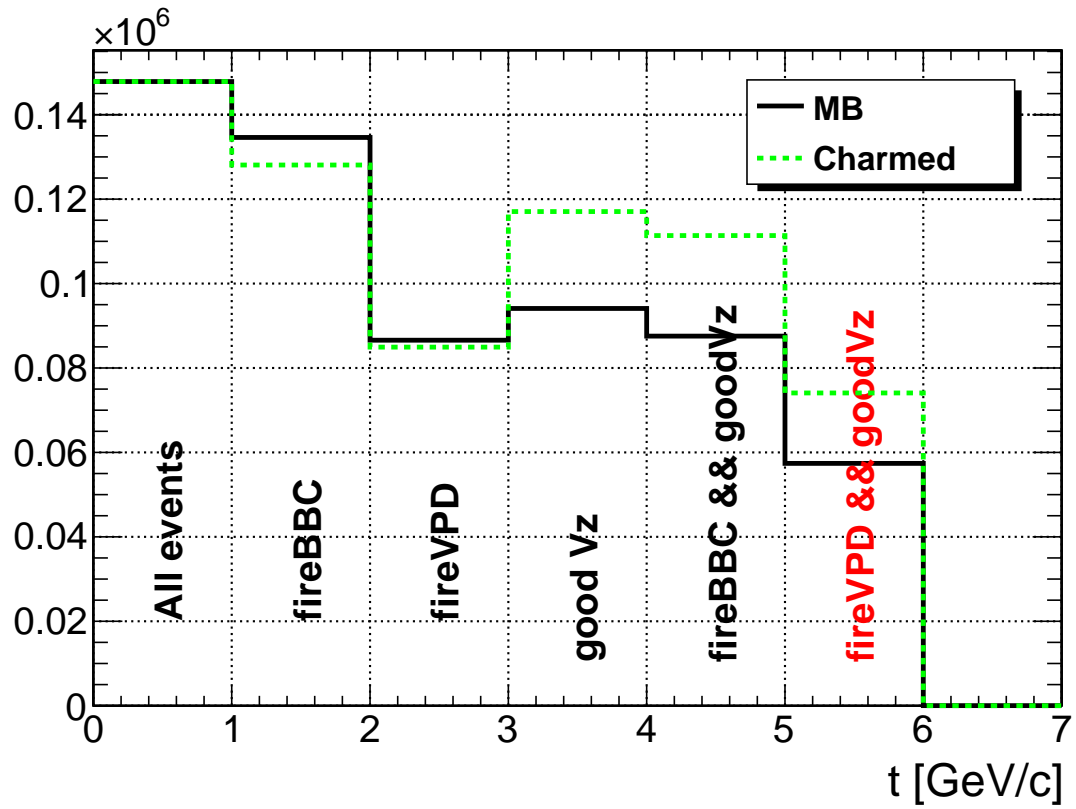


Figure 4.12: Event counter for general events denoted as "MB" and events containing D^* mesons denoted as "Charmed". "fireBBC" and "FireVPD" columns represent events that initialized BBC and VPD trigger respectively. "good Vz" denotes events from which vertices with positive ranking were successfully reconstructed.

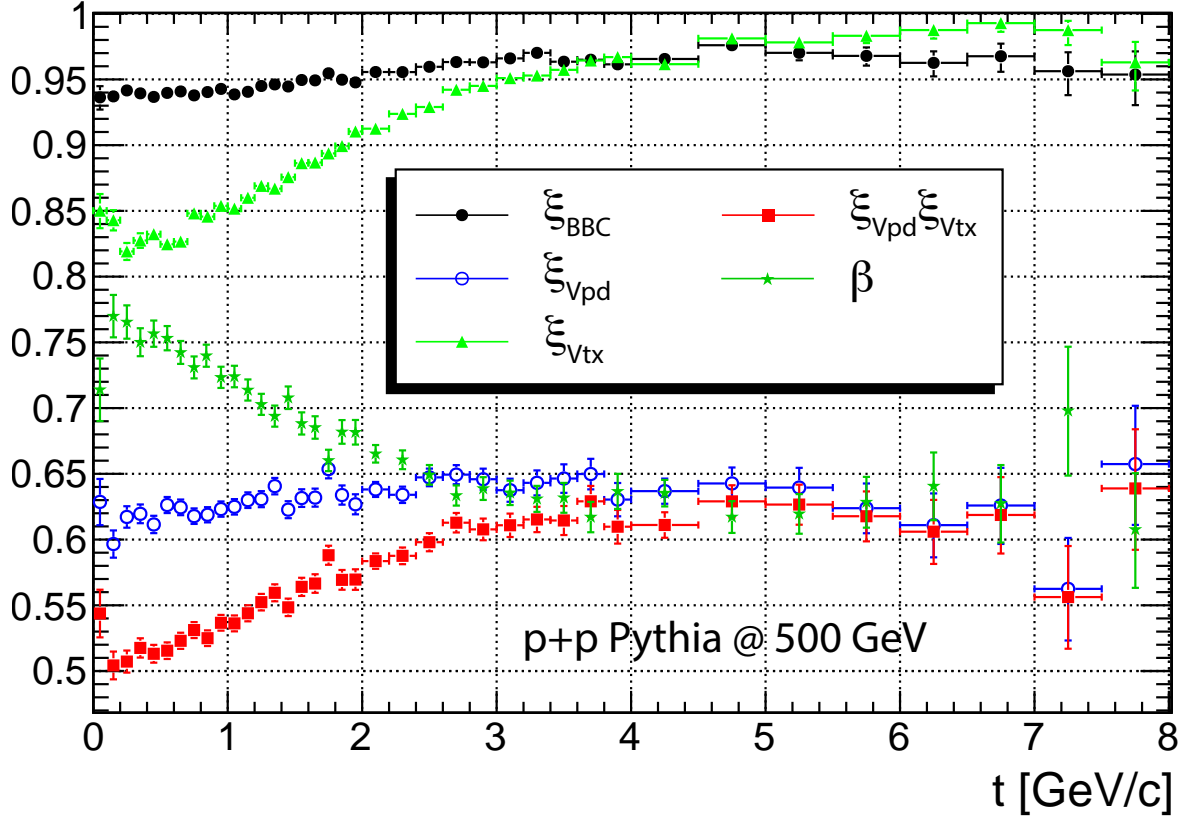


Figure 4.13: Trigger, Vertex reconstruction efficiency and Trigger Bias.

4.5.1 Trigger Bias Correction in Run9 pp200 Analysis

The Trigger bias correction was done according to the same technique on D^0 and D^* separately [28]. However, as one can see in Figure 4.14, the $\beta(t)$ for events containing the D^0 mesons are the same as the $\beta(t)$ for events containing the D^* mesons. Hence, the $\beta(t)$ for events containing D^* mesons only was calculated in Run11 pp500 analysis. It was found that the trigger bias increases with D^*p_T in Run11 pp500 while remains constant in Run9 pp200.

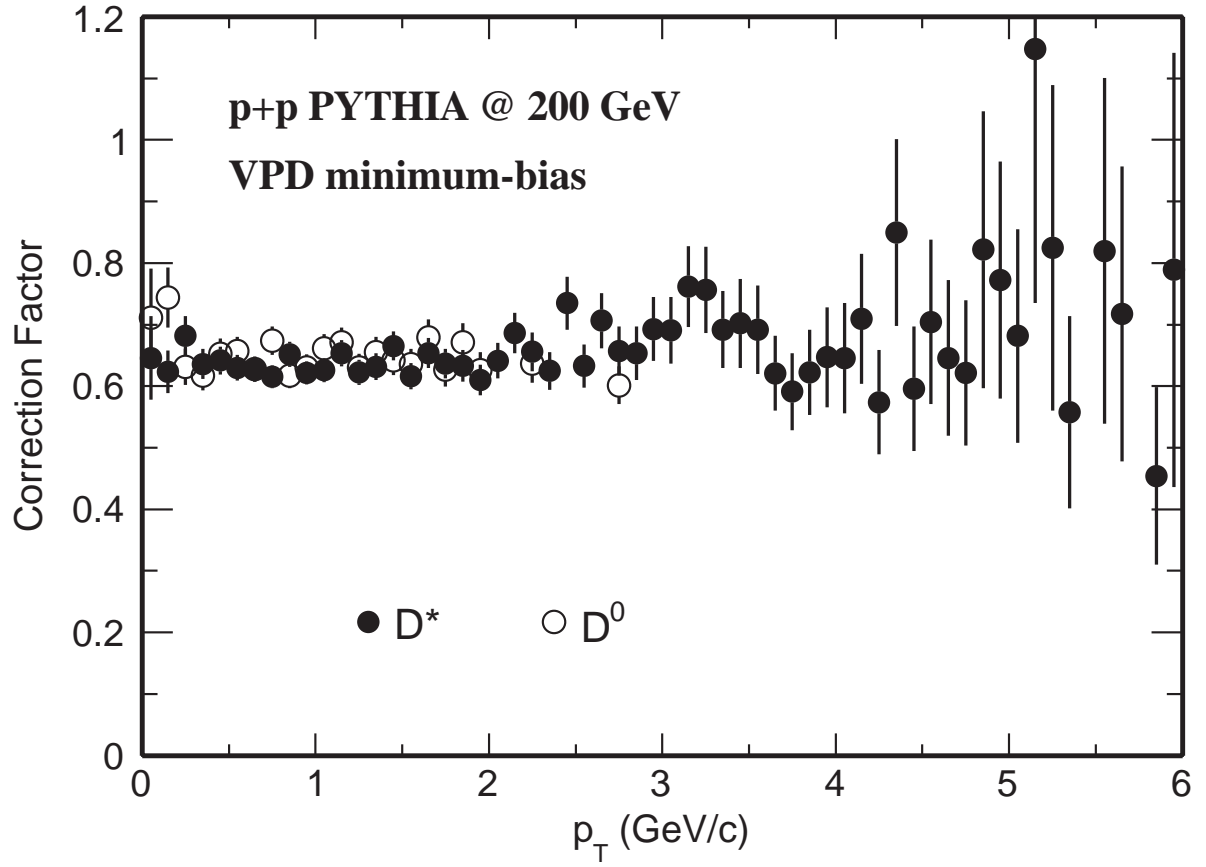


Figure 4.14: The $\beta(t)$ for events containing the D^0 and events containing the D^* mesons.
Figure taken from Ref. [28].

Systematic Errors Evaluation

Systematic errors are uncertainties in the bias of the data. Each experiment must generally be considered individually. One example of a bias was already presented in section 4.5 when the events with open charm mesons were more likely to pass the event selection criteria. STAR Heavy Flavor group developed criteria for systematic errors determination. This chapter is focused on bin-to-bin systematic errors which are categorized into two parts: uncertainty on the raw yield determination and uncertainty on the efficiency determination.

5.1 Uncertainty on the Raw Yield Determination

The determination of the uncertainty on the raw yield determination in Run9 pp200 analysis is described in paper [28] whose whole section V. is dedicated to systematic uncertainties. In Run11 pp500 analysis, ideas of Roger Barlow [81] was implemented. Those ideas are summarized in appendix section C.2. This section contains also subsection

5.1.1 which regards D^* analysis and is common for both Run11 pp500 and Run9 pp200 analyses.

The systematic uncertainty in determining the D^* raw yields was calculated as a discrepancy δ between bin counting and gaussian fit and a discrepancy Δ between the Side-band background and Wrong-sign background. Let's note that those raw yields shown Figure 3.15 calculated after Wrong-sign background subtraction has been already corrected on the Wrong-sign over counting described in paragraph bellow. Results are summarized in Table 5.1. The systematic uncertainty in determining the D^0 raw yield was calculated as a discrepancy Δ between raw yields calculated after Like-sign and Rotated-momentum background.

$$\Delta = Y_1 - Y_2 = U - B_1 - U + B_2 = B_2 - B_1 \quad (5.1)$$

where U is number of Unlike-signs, B_1 is background reconstructed by one method and B_2 by second method. B_1 and B_2 are not correlated, thus

$$\sigma_\Delta^2 = \sigma_1^2 + \sigma_2^2. \quad (5.2)$$

where σ_1, σ_2 are statistical errors of B_1, B_2 respectively.

(a, b) [GeV/ c]	(1.0,2.0)	(2.0,3.0)	(3.0,4.2)	(4.2,5.5)	(5.5,8.0)
Δ	1020	2.2	-3.3	1.6	-0.9
δ		0.7	1.5	2.4	0.8
$\sigma_\Delta, \sigma_\delta$	1004	14.6	12.6	4.5	1.3

Table 5.1: Discrepancy Δ between signals obtained by subtraction of backgrounds reconstructed by different methods in D^0/D^* transverse momentum bins (a, b) and discrepancy δ between bin counting and gaussian fit to the signal in D^* transverse momentum bins (a, b) .

$\sigma_\Delta \gtrsim \Delta$, $\sigma_\delta \gtrsim \delta$ for all p_T bins, as one can see in Table 5.1. So that the systematic error of raw yield can be entirely a product of statistical fluctuations of background, and

was hence not included into total systematic uncertainty. This approach to systematic uncertainties prevents from overestimations.

5.1.1 Double counting

The D^0 is reconstructed via hadronic decay channel: $D^0 \rightarrow K^- + \pi^+$. If K^- is misidentified as a π^- and π^+ is mis-identified as a K^+ , the $(K^+\pi^-)$ combination will contribute in the \overline{D}^0 reconstruction, and if it falls into the \overline{D}^0 mass selection window, this D^0 signal will be then also counted as a \overline{D}^0 signal. This is called double counting.

For D^* reconstruction via $D^\pm \rightarrow D^0 \pi_S^\pm \rightarrow K^\mp \pi^\pm \pi_S^\pm$, the situation is different. If K^\mp is misidentified as π^\mp and π^\pm as K^\pm , then the combination becomes $K^\pm \pi^\mp \pi_S^\pm$ which doesn't contribute to the ΔM peak, but into the Wrong-sign background. Hence the raw yield obtained by the Wrong-sign background subtraction is undercounted.

Once again, the Monte-carlo Toy model (section B.2) was employed to produce $g^{\text{RC}}(t, M^{\text{RC}})$ (see section 4.4, particularly Figure 4.10). Furthermore, if both kaon and pion happened to be in the overlapping PID region, an additional histogram $g^{\text{RC}}(t, M^{\text{Mis}})$ was filled. M^{Mis} is the invariant mass of mis-identified kaon (actually a pion) and pion (actually a kaon). This so called mis-identified kaon/pion was simply created by replacement of the rest mass in the first particles's four-momentum with the second particles's rest mass and vice versa. The fraction of the over counting in the Wrong-sign background was calculated then as:

$$f_{\text{OC}}(t) \equiv \frac{\int_{1.84}^{1.89} g^{\text{RC}}(t, M^{\text{Mis}}) dM^{\text{Mis}}}{\int_{1.84}^{1.89} g^{\text{RC}}(t, M^{\text{RC}}) dM^{\text{RC}}} \quad (5.3)$$

The probabilities of a kaon and a pion in the overlapping PID region are shown in Figure 5.1, $g^{\text{RC}}(t, M^{\text{RC}})$ and $g^{\text{RC}}(t, M^{\text{Mis}})$ in Figure 5.2, and $f_{\text{OC}}(t)$ in Figure 5.3.

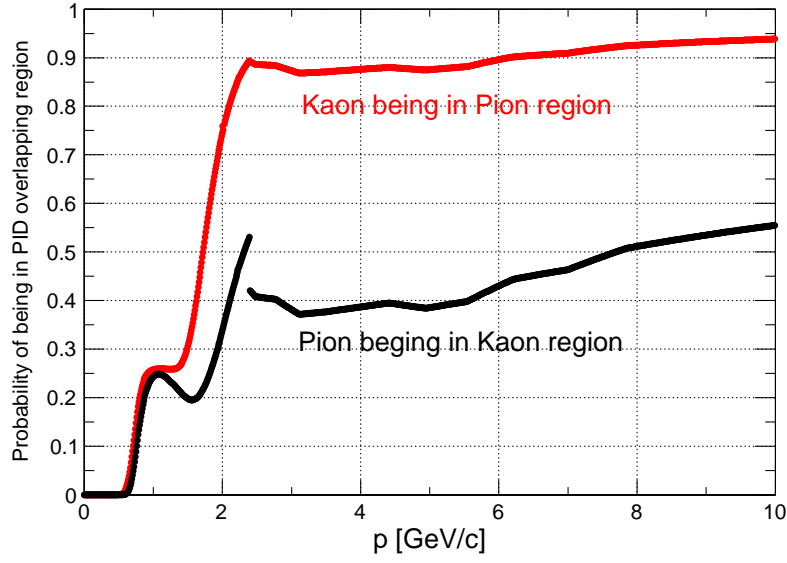


Figure 5.1: Probability of a particle being in overlapping PID region.

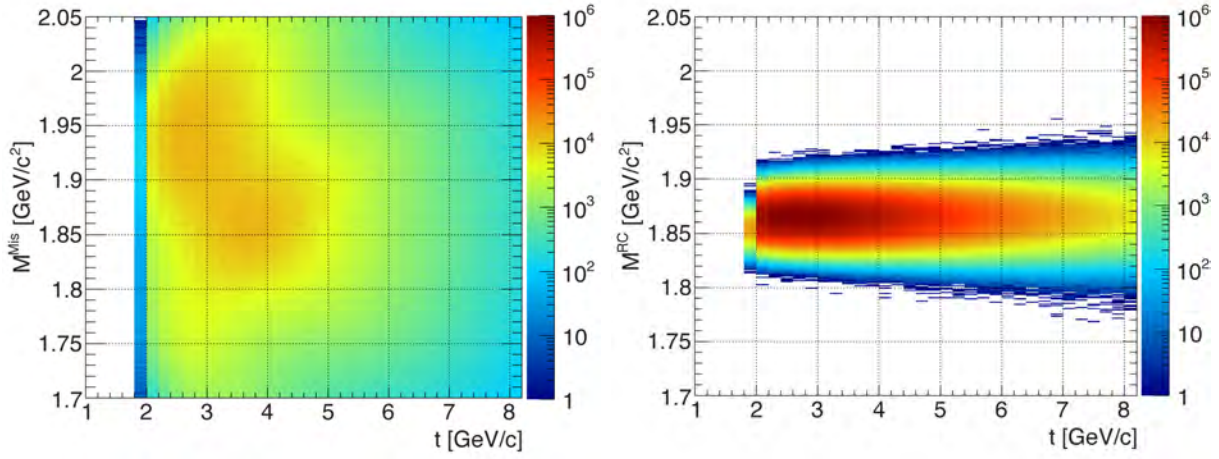


Figure 5.2: Left panel: Reconstructed invariant mass of D^0 meson where both daughter particles were misidentified so that the kaon was assigned the pion mass and vice versa, i. e. $g^{\text{RC}}(t, M^{\text{Mis}})$. Right panel: Reconstructed invariant mass of D^0 meson with correct daughter particle identification, i. e. $g^{\text{RC}}(t, M^{\text{RC}})$.

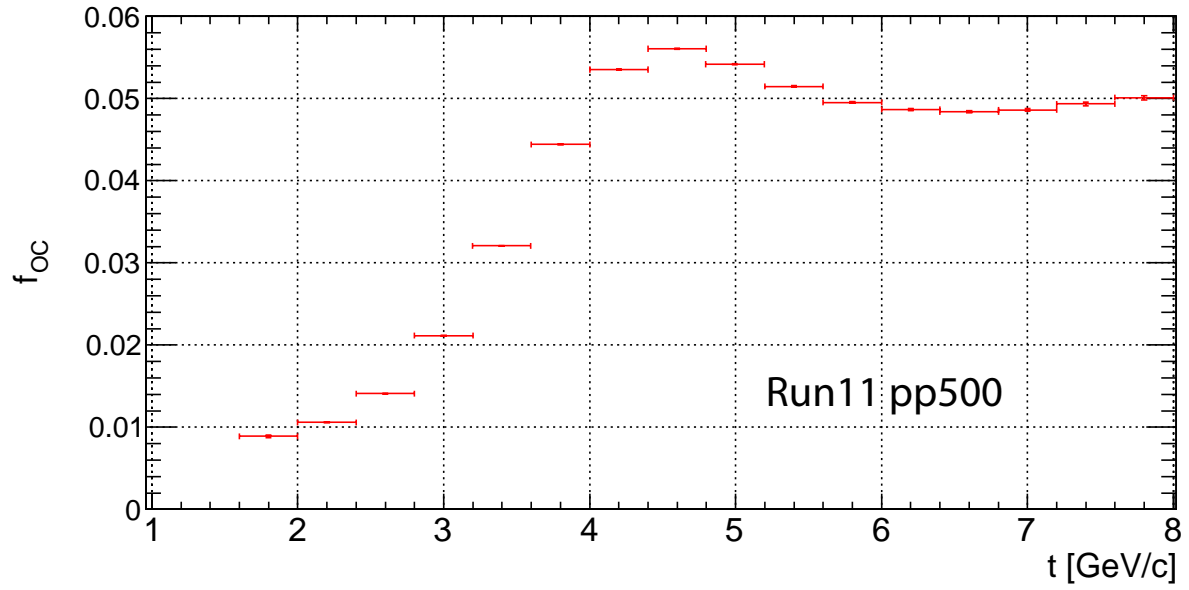


Figure 5.3: The fraction of the over counting in the Wrong-sign background.

5.2 Uncertainty on the Efficiency Determination

This section describes in detail the uncertainty on the efficiency determination whose procedure is common for Run9 pp200 and Run11 pp500 analyses.

The absolute (“true”) reconstruction efficiency in data is unknown, so it is calculated from embedding, which is an approximation. The degree of how the basic track quality distributions (DCA, NHITS) from embedding matches those from the data represents how good is the approximation. And the difference between them is considered as systematic uncertainty due to this approximation.

It’s difficult to calculate the absolute efficiency of the Number of TPC Hit Points (Nhits) or DCA from the data, because of the contamination of Pile-up and "ghost" tracks, so

the relative efficiencies $\varepsilon_{\text{DCA}}^{(rel)}, \varepsilon_{\text{Nhits}}^{(rel)}$ was used instead:

$$\varepsilon_{\text{DCA}}^{(rel)}(p_T) \equiv \frac{\int_0^1 h(p_T, r) dr}{\int_0^3 h(p_T, r) dr}, \quad \varepsilon_{\text{Nhits}}^{(rel)}(p_T) \equiv \frac{\int_{25}^{45} h(p_T, n) dn}{\int_{15}^{45} h(p_T, n) dn}, \quad (5.4)$$

where $h(p_T, r), h(p_T, n)$ are DCA, Nhits distributions respectively at given p_T . Systematic discrepancy at given p_T was then:

$$\delta_{\text{DCA}}(p_T) \equiv \frac{\varepsilon_{\text{DCA}}^{(rel)}(p_T) \text{ from data}}{\varepsilon_{\text{DCA}}^{(rel)}(p_T) \text{ from embedding}}, \quad \delta_{\text{Nhits}}(p_T) \equiv \frac{\varepsilon_{\text{Nhits}}^{(rel)}(p_T) \text{ from data}}{\varepsilon_{\text{Nhits}}^{(rel)}(p_T) \text{ from embedding}}, \quad (5.5)$$

Figure 5.4 depicts $\delta_{\text{DCA}}(p_T)$ and $\delta_{\text{Nhits}}(p_T)$.

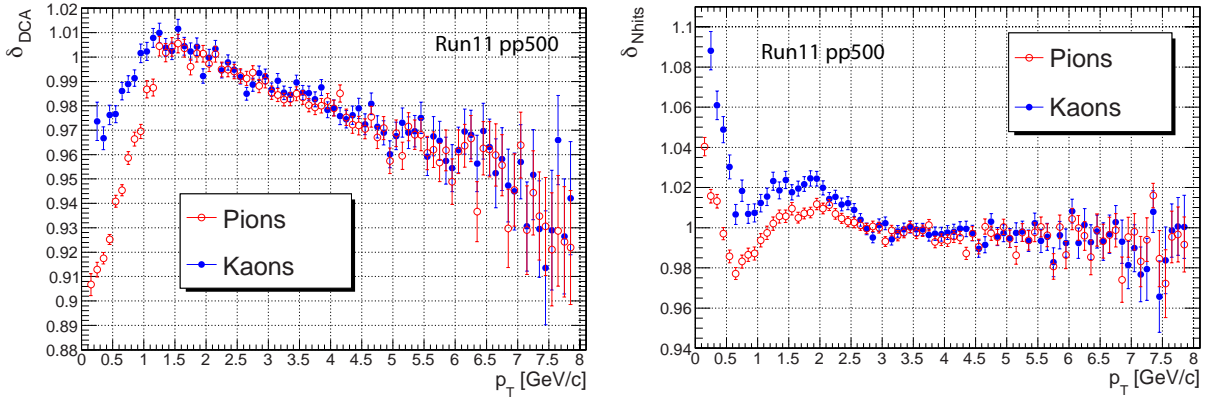


Figure 5.4: Systematic discrepancy between the data and the embedding.

The expected value of the systematic uncertainty from embedding ς in given D^0/D^* transverse momentum bin (a, b) was calculated analogously with the reconstruction/matching efficiency calculated according to (4.7):

$$\varsigma \equiv E^{(a,b)}(|1 - \delta(p_T)|) = \int_0^8 |1 - \delta(p_T)| G^{(a,b)}(p_T) dp_T, \quad (5.6)$$

where $G^{(a,b)}(p_T)$ is defined by (4.8). Results are summarized in Table 5.2. With the assumption of an ideal correlation among daughter particles's systematic uncertainties, the systematic error on the efficiency determination (and in this analysis also total systematic

uncertainty) could have been directly calculated as

$$\varsigma_{\text{tot}} = \sqrt{\left(\sum_{i=1}^{\text{\#daughters}} \varsigma_{\text{Nhits}}^i \right)^2 + \left(\sum_{i=1}^{\text{\#daughters}} \varsigma_{\text{DCA}}^i \right)^2} \quad (5.7)$$

and is listed in the last column in Table 5.2.

(a, b) [GeV/ c]	ς_{Nhits} [%]				ς_{DCA} [%]				ς_{tot} [%]
	K	π	π_S	Sum	K	π	π_S	Sum	
(1.0,2.0)	2.36	0.95		3.32	1.06	3.07		4.13	5.30
(2.0,3.0)	2.14	0.94	3.34	6.42	0.88	2.51	9.16	12.55	14.10
(3.0,4.2)	1.65	0.80	2.00	4.44	0.90	2.08	8.75	11.73	12.54
(4.2,5.5)	1.27	0.70	1.21	3.17	1.13	2.01	8.25	11.39	11.83
(5.5,8.0)	1.01	0.65	1.01	2.67	1.62	2.27	7.22	11.10	11.42

Table 5.2: Systematic errors from discrepancy between embedded and experimental data. First column presents D^0/D^* transverse momentum bins (a, b) and the last column corresponding systematic uncertainty obtained from values shown in middle columns by (5.7).

The contribution from matching efficiency uncertainty was found to be negligible (below 3% of ς_{tot}). Let's compare the total uncertainty on the efficiency determination, values in the last column of Table 5.2, with statistical errors of yields in corresponding D^0/D^* transverse momentum bins (a, b) , 17.5% for D^0 (1,2) GeV/ c and 21.6%, 20.6%, 21.8%, and 27.5% for D^* (2, 3), (3, 4.2), (4.2, 5.5), and (5.5, 8) GeV/ c respectively. In all p_T bins the statistical uncertainty is higher than the total systematic uncertainty (let's remember that the discrepancies in the raw yields were found to originate in statistical fluctuations) from which one can conclude that the whole analysis procedure was good enough for given amount of data. To improve the overall precision of this analysis one can just triple the amount of experimental data to reduce statistical errors to match systematic uncertainties without any change of the analysis procedure.

Results

The reconstruction of D^0 in p+p collisions at $\sqrt{s} = 200$ GeV (Run9 pp200 analysis) and reconstruction of D^0 and $D^{*\pm}$ in p+p collisions at $\sqrt{s} = 500$ GeV (Run11 pp500 analysis) at STAR via the hadronic decay channels

$$D^{*\pm} \xrightarrow[p^*=39 \text{ MeV}/c]{B.R.=67.7\%} D^0 \pi^\pm \xrightarrow{B.R.=3.89\%} K^\mp \pi^\pm \pi^\pm$$

$$D^0 \xrightarrow{B.R.=3.89\%} K^\mp \pi^\pm,$$

where $B.R.$ are branching ratios of these open charm mesons to pions and kaons [4], were done. 51.8 million and 107.8 minimum bias events have been analyzed in Run11 pp500 and Run9 pp200 analysis respectively. Both are described in chapter 3. Detector efficiency and acceptance and other efficiencies and corrections were discussed in chapter 4. Systematic uncertainties were discussed in chapter 5.

This chapter presents final results of the both p_T -differential and p_T -integrated invariant cross section of charm-anticharm quark pair production at mid-rapidity measurements and total charm-anticharm quark pair cross section estimation using PYTHIA [32] simulation.

These results are compared to theoretical model calculations and physics implications are discussed.

The differential invariant cross section $E \frac{d^3\sigma}{dp^3}$ of an charm quark pair $c\bar{c}$ production at mid-rapidity was calculated according to equation

$$E \frac{d^3\sigma}{dp^3} \Big|_{y=0} = \frac{d^2\sigma}{2\pi p_T dp_T dy} \Big|_{y=0} = \frac{1}{2} \frac{1}{2\pi} \frac{\sigma^{\text{NSD}} \beta}{N f_c \Gamma} \frac{Y}{p_T \Delta p_T \Delta y} \frac{1}{\varepsilon}, \quad (6.1)$$

where σ^{NSD} is inelastic non-singly diffractive p+p cross section, β is the trigger bias (section 4.5), N is the total number of events entered the analysis, f_c represents the ratio of a charm quark hadronizing to an open charm meson, Γ denotes the branching ratio of a decay, and Y is the raw yield in a p_T bin of the width Δp_T within the rapidity window Δy . ε is the combined efficiency of the experiment including the track reconstruction efficiency ε_R (see section 4.1), the track matching efficiency ε_M (see section 4.2), the particle identification efficiency ε_{PID} (see section 4.3), and the kinematical cuts efficiencies $\varepsilon_{\text{Mass}}$ and ε_θ (see section 4.4). Results from Run9 pp500 analysis are summarized in Table 6.1 and results from Run11 pp500 analysis are summarized in Table 6.2. Both tables show values of all variables used in equation (6.1). Some variables don't depend on reconstructed D^0/D^* p_T so they are displayed in cells stretched over more columns. Rows between thick horizontal rules show variables and values which are then corrected on bin widths (the bin width correction is discussed further in the text) and plotted in Figures 6.4, 6.1, 6.2, and 6.3.

Values of f_c and Γ were taken from Ref. [4]. σ^{NSD} was measured for p+p collisions at $\sqrt{s} = 200$ GeV at STAR [77]. There is no such measurement at $\sqrt{s} = 500$ GeV, hence the measured value from p+p collisions at $\sqrt{s} = 200$ GeV was scaled by Pythia with assumption that the systematic error at $\sqrt{s} = 500$ GeV differs negligibly from the one at $\sqrt{s} = 200$ GeV.

σ^{NSD} [mb]	30 ± 3.5	
N	107.8M	
f_c [%]	56.5 ± 3.2	
Γ [%]	3.89	
β	0.67	
p_T [GeV/ c]	0.8	1.15
Δp_T [GeV/ c]	0.4	1.3
Δy	2	
Y	1708 ± 497	1860 ± 635
ε [%]	0.0695	0.0746
$E \frac{d^3\sigma}{dp^3} \Big _{y=0}$ [nb]	25660 ± 7646	3886 ± 1328
ς_{tot} [%]	6.3	9.8

Table 6.1: Final results from Run9 pp200 analysis. Table show values of all variables in equation (6.1). Some variables don't depend on reconstructed D^0 p_T so they are displayed in cells stretched over more columns. Let's note those results are not corrected on bin widths.

Let's note that the p_T values shown in both Tables 6.2 and 6.1 were chosen arbitrarily as bin centers because the real values hadn't been known. To know correct p_T values, one must know the exact shape of the $E \frac{d^3\sigma}{dp^3} \Big|_{y=0}$ and that had also been unknown. This problem can be solved iteratively. Let's define the new transverse momentum

$$p_T^{(i+1)} = \mathcal{F}^{(i)-1} \left(\int_a^b \mathcal{F}^{(i)}(p_T) dp_T \right), \quad (6.2)$$

where $\mathcal{F}^{(i)} \equiv p_T f(p_T)$ with parameters obtained from the $f(p_T)$ fit into $\frac{d^2\sigma^{(i)}}{2\pi p_T^{(i)} dp_T dy} \Big|_{y=0}$

σ^{NSD} [mb]	34 ± 4				
N	51 771 500				
f_c [%]	56.5 ± 3.2	22.4 ± 2.8			
Γ [%]	3.89	2.63			
β	0.696	0.652	0.630	0.629	0.636
p_T [GeV/ c]	1.5	2.5	3.6	4.85	6.75
Δp_T [GeV/ c]	1.0	1.0	1.2	1.3	2.5
Δy	2				
Y	4064 ± 1006	83.9 ± 18.1	82.5 ± 17.0	35.4 ± 7.7	16.8 ± 4.6
ε_{tot} [%]	26.2	5.08	17.3	27.5	32.7
$E \frac{d^3\sigma}{dp^3} \Big _{y=0}$ [nb]	8508 ± 2106	1927 ± 389	312.1 ± 64.25	57.5 ± 12.52	8.674 ± 2.377
ς [%]	5.3	14.1	12.54	11.83	11.42

Table 6.2: Final results from Run11 pp500 analysis. Table show values of all variables in equation (6.1). Some variables don't depend on reconstructed D^0/D^* p_T so they are displayed in cells stretched over more columns. Let's note those results are not corrected on bin widths.

calculated according to (6.1). $f(p_T)$ is the power law function either of Hagedorn's (A.2) or Lévy's (A.4) shape. $\frac{d^2\sigma^{(0)}}{2\pi p_T^{(0)} dp_T dy} \Big|_{y=0}$ and $p_T^{(0)}$ were set to have values from Table 6.2. After the third iteration the results became very stable. Table 6.3 exposes results from Run11 pp500 analysis after 6th iteration. The values of the differential invariant cross section after the iterations are model dependent. That's why Table 6.2 have three main columns dedicated to usage of Hagedorn's and Lévy's shapes. Those main columns have each two sub-columns with the p_T value after the 6th iteration and with the differential invariant cross section after the 6th iteration. Those data are plotted in Figures 6.1, 6.2,

6.3 together with corresponding $f(p_T)$.

Hagedorn's shape		Lévy's shape ($m_0 = 1.5$)		Lévy's shape ($m_0 = 1.27$)	
$p_T^{(6)}$	$E \frac{d^3\sigma^{(6)}}{dp^3} \Big _{y=0} \text{ [mb]}$	$p_T^{(6)}$	$E \frac{d^3\sigma^{(6)}}{dp^3} \Big _{y=0} \text{ [mb]}$	$p_T^{(6)}$	$E \frac{d^3\sigma^{(6)}}{dp^3} \Big _{y=0} \text{ [mb]}$
1.46	$(8.75 \pm 1.53) \cdot 10^{-3}$	1.49	$(8.57 \pm 1.50) \cdot 10^{-3}$	1.49	$(8.60 \pm 1.50) \cdot 10^{-3}$
2.45	$(19.7 \pm 3.97) \cdot 10^{-4}$	2.45	$(19.7 \pm 3.97) \cdot 10^{-4}$	2.45	$(19.7 \pm 3.97) \cdot 10^{-4}$
3.53	$(31.8 \pm 6.55) \cdot 10^{-5}$	3.52	$(31.9 \pm 6.56) \cdot 10^{-5}$	3.53	$(31.9 \pm 6.56) \cdot 10^{-5}$
4.77	$(5.84 \pm 1.27) \cdot 10^{-5}$	4.77	$(5.85 \pm 1.27) \cdot 10^{-5}$	4.77	$(5.85 \pm 1.27) \cdot 10^{-5}$
6.50	$(8.98 \pm 2.47) \cdot 10^{-6}$	6.51	$(8.97 \pm 2.47) \cdot 10^{-6}$	6.51	$(8.97 \pm 2.47) \cdot 10^{-6}$

Table 6.3: The results after bin width correction having used three differential cross section parametrization: 1) Hagedorn parametrization where $f(p_T) = (\text{A.2})$; 2) Lévy parametrization where $f(p_T) = (\text{A.4})$ with $m_0 = 1.5 \text{ GeV}/c^2$; 3) Lévy parametrization where $f(p_T) = (\text{A.4})$ with $m_0 = 1.27 \text{ GeV}/c^2$. $p_T^{(6)}$ is in units GeV/c .

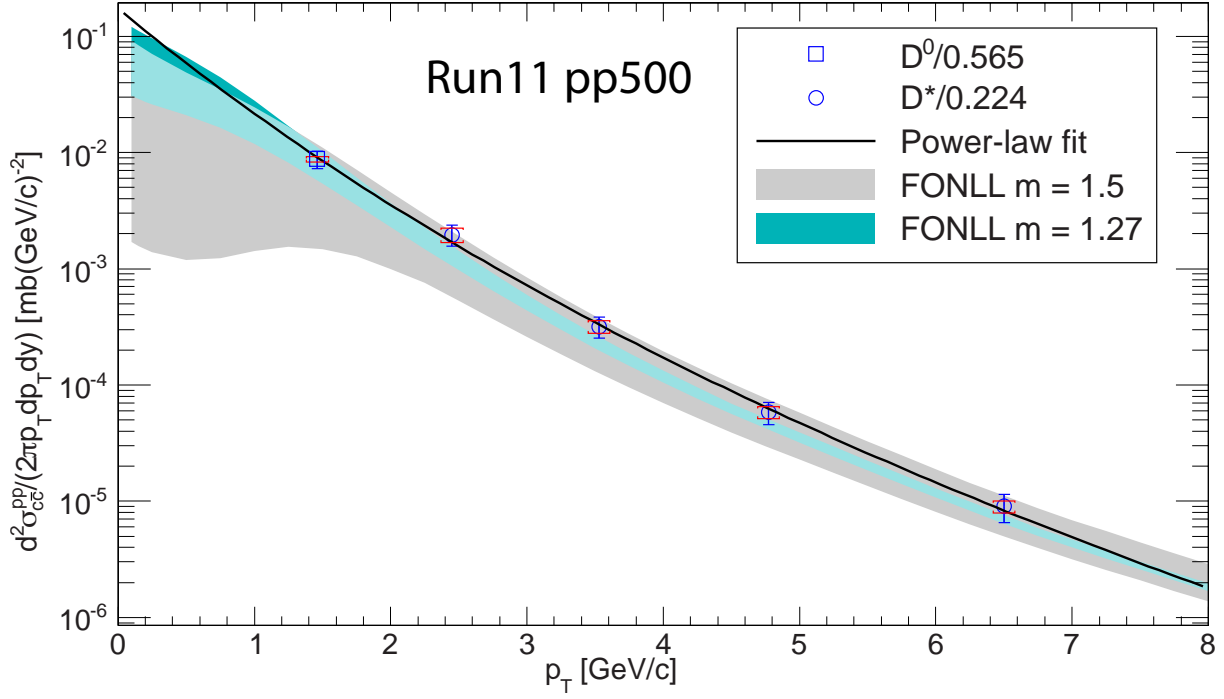


Figure 6.1: Charm quark production cross section as inferred from D^0 and D^* production in p+p collisions at $\sqrt{s} = 500$ GeV compared with FONLL predictions. The D^0 and D^* data points were divided by the charm quark fragmentation ratios $f_c = 0.565$ and $f_c = 0.224$ respectively. FONLL calculations [83] used $\mu_R = \mu_F = m_c$ where μ_R is the renormalization scale, μ_F is the factorization scale and m_c is the charm quark mass. "m = 1.5" in the legend denotes $m_c = 1.5$ GeV/ c^2 and "m = 1.27" denotes $m_c = 1.27$ GeV/ c^2 . Data points are already corrected on bin widths and fitted by Hagedorn Power-law function (A.2).

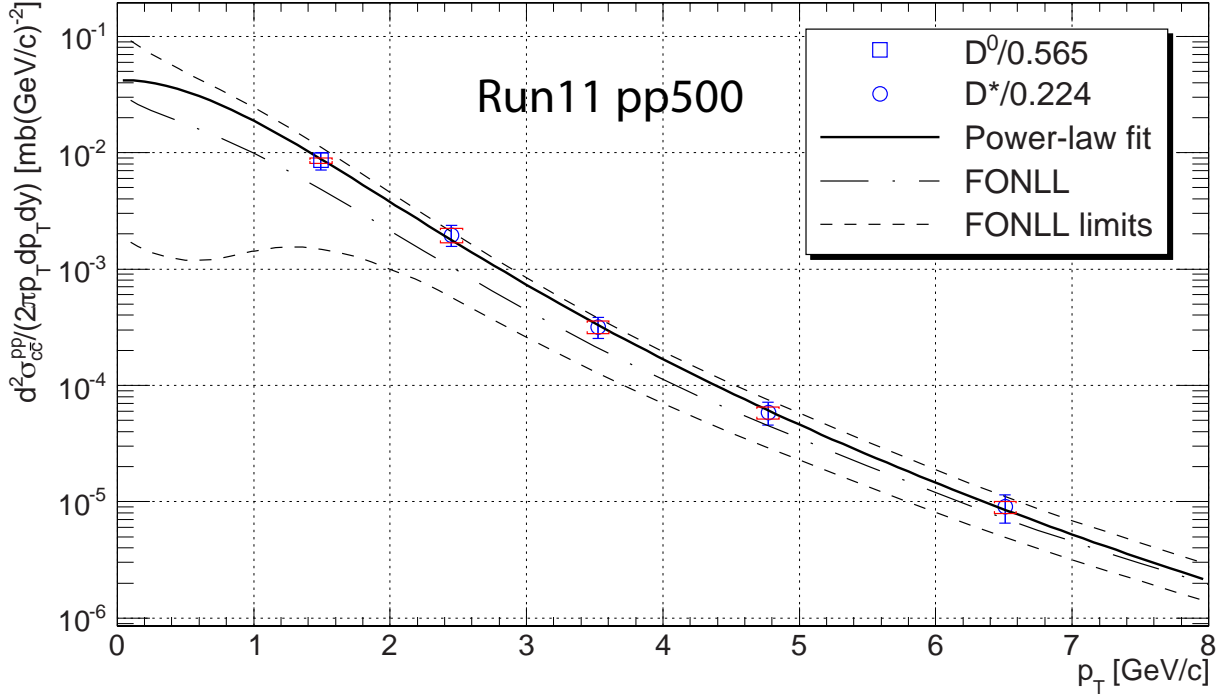


Figure 6.2: Charm quark production cross section as inferred from D^0 and D^* production in p+p collisions at $\sqrt{s}=500$ GeV compared with FONLL prediction. The D^0 and D^* data points were divided by the charm quark fragmentation ratios $f_c = 0.565$ and $f_c = 0.224$ respectively. FONLL prediction [83] used $\mu_R = \mu_F = m_c = 1.5$ GeV/ c^2 where μ_R is the renormalization scale, μ_F is the factorization scale and m_c is the charm quark mass. Data points are already corrected on bin widths and fitted by Lévy Power-law function (A.4) with m_0 chosen to be 1.5 GeV/ c^2 .

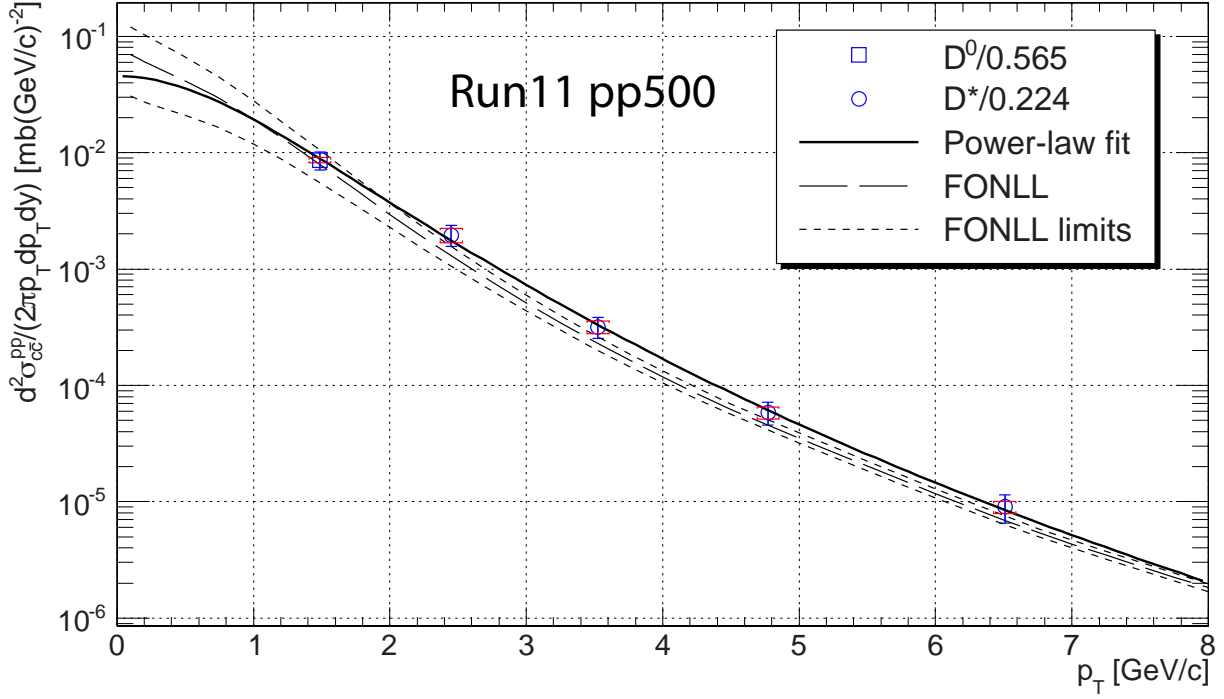


Figure 6.3: Charm quark production cross section as inferred from D^0 and D^* production in p+p collisions at $\sqrt{s} = 500$ GeV compared with FONLL prediction. The D^0 and D^* data points were divided by the charm quark fragmentation ratios $f_c = 0.565$ and $f_c = 0.224$ respectively. FONLL prediction [83] used $\mu_R = \mu_F = m_c = 1.27$ GeV/ c^2 where μ_R is the renormalization scale, μ_F is the factorization scale and m_c is the charm quark mass. Data points are already corrected on bin widths and fitted by Lévy Power-law function (A.4) with m_0 chosen to be 1.27 GeV/ c^2 .

Hagedorn parametrization

$$\left. \frac{d\sigma}{dy} \right|_{y=0} = 272 \pm 77(\text{stat}) \pm 31(\text{sys}) \mu\text{b} \quad \langle p_T \rangle = 1.14 \pm 0.16 \text{ GeV}/c \quad n = 13.7 \pm 7.3$$

Lévy parametrization with $m_0 = 1.5 \text{ GeV}/c^2$

$$\left. \frac{d\sigma}{dy} \right|_{y=0} = 211 \pm 43(\text{stat}) \pm 15(\text{sys}) \mu\text{b} \quad T = 0.19 \pm 0.14 \quad n = 8.7 \pm 3.0$$

Lévy parametrization with $m_0 = 1.27 \text{ GeV}/c^2$

$$\left. \frac{d\sigma}{dy} \right|_{y=0} = 216 \pm 45(\text{stat}) \pm 16(\text{sys}) \mu\text{b} \quad T = 0.25 \pm 0.14 \quad n = 9.5 \pm 3.6$$

Table 6.4: The results of fits.

Results of the $f(p_T)$ fits into already p_T bin width corrected data are shown in Table 6.4. They show strong dependence of the $\left. \frac{d\sigma}{dy} \right|_{y=0}$ on the power-law function parametrization. Only 7% of its value and 5% of its statistical error was measured. The rest was got by extrapolation of Hagedorn parametrization of Power-law into zero transverse momentum. Similarly, the extrapolation by Lévy parametrization of Power-law accounted for 90% of the $\left. \frac{d\sigma}{dy} \right|_{y=0}$ value and 92% of the statistical error. The final result to be published is a combination of the result obtained with the help of Hagedorn parametrization (bin with correction and extrapolation to zero p_T) and Lévy parametrization with $m_0 = 1.5 \text{ GeV}/c^2$. Lévy parametrization with $m_0 = 1.27 \text{ GeV}/c^2$ gives very similar result to the one with $m_0 = 1.5 \text{ GeV}/c^2$, so the Lévy does not have to be counted twice. Both Lévy and Hagedorn parametrization were fitted into the same data points, which implicates that 8% of $43 \mu\text{b}$ (statistical error from Lévy extrapolation) and 5% of $77 \mu\text{b}$ (statistical error from Hagedorn extrapolation) are correlated with correlation coefficient to be 1. The rest

of statistical errors are totally independent with correlation coefficient to be 0. Appendix section C.3 explains how to deal with such correlated errors. It's based on article by Paul Avery [92]. Let $x_1 = 272 \pm 77 \pm 4$ and $x_2 = 211 \pm 43 \pm 3$, where the first error is the uncorrelated statistical error purely from the extrapolation and the second is the 100% correlated with the second of the x_2 . The covariance matrix is then (see section C.3)

$$\mathbb{V} = \begin{pmatrix} 77^2 & 4 \times 3 \\ 3 \times 4 & 43^2 \end{pmatrix},$$

Hence inverse matrix is

$$\mathbb{V}^{-1} = \frac{1}{10962577} \begin{pmatrix} 1849 & -12 \\ -12 & 5929 \end{pmatrix}.$$

According to (C.20), the weights for the cross section estimator $\bar{x} = w_1 x_1 + w_2 x_2$ and statistical error estimator $\sqrt{w_1^2 \mathbb{V}_{11} + 2w_1 w_2 \mathbb{V}_{12} + w_2^2 \mathbb{V}_{22}}$ are $w_1 = 0.237, w_2 = 0.763$. One can see that $\mathbb{V}_{12} = \mathbb{V}_{21} \ll \mathbb{V}_{11}$ or \mathbb{V}_{22} . This is implication of the correlated part of the statistical error being too small to have any significant impact. The final result can be thus calculated as weighted average of $\left. \frac{d\sigma}{dy} \right|_{y=0}$ determined using the Hagedorn parametrization and $\left. \frac{d\sigma}{dy} \right|_{y=0}$ determined using the Lévy parametrization with $m_0=1.5 \text{ GeV}/c^2$ since both are independent. Lévy parametrization with $m_0=1.27 \text{ GeV}/c^2$ is correlated with the $m_0=1.5 \text{ GeV}/c^2$ one. Thus the $m_0=1.5 \text{ GeV}/c^2$ one was picked arbitrarily, because it matches the measured points better. The extrapolated bin-by-bin systematic errors were treated the same way as values. All of this above gives the final result:

$$\left. \frac{d\sigma}{dy} \right|_{y=0} = 225 \pm 38(\text{stat}) \pm 19(\text{sys}) \pm 26(\text{norm}) \mu\text{b} \quad (6.3)$$

where the term "norm" denotes error non-singly-diffractive cross section. The errors of f_c have not been propagated into the final result yet. The Run11 pp500 analysis results are still presented as preliminary.

The charm cross section at mid rapidity was extrapolated to full rapidity using two PYTHIA simulations with the following sets of parameters:

- PHENIX tune: MSEL=0 with MSUB(11, 12, 13, 28, 53, 68) on, PARP(91)($\langle k_T \rangle$) = 1.5 GeV/ c , MSTP(32) (Q^2 scale) = 4, CKIN(3) (minimum parton \hat{p}_T) = 2 GeV/ c .
- STAR tune: MSEL=1, PARP(91) ($\langle k_T \rangle$) = 1.0 GeV/ c , PARP(67) (parton shower level) = 1.0.

The extrapolation factor was found to be 5.6 ± 0.1 giving the total charm production cross section value:

$$\sigma_{cc}^{pp} = 1260 \pm 211(\text{stat}) \pm 109(\text{sys}) \pm 146(\text{norm}) \mu\text{b} \quad (6.4)$$

This result is displayed with results from other experiments in Figure 6.5, revealing very good agreement with NLO prediction [89].

In the Run9 pp200 analysis, only Hagedorn's shape power law function was used to fit to the data points. The $E \frac{d^3\sigma}{dp^3} \Big|_{y=0}$ from Run9 pp200 analysis is shown in Figure 6.4. As mentioned in chapter "Author's Contribution" there have been two independent analyses on D^0 production. One done by Prof. Yifei Zhang and one done by author of this thesis which was used as a crosscheck, because it was first reconstruction of D^0 meson in hadronic decay channel. The results published in [28] were picked from the analysis of Prof. Zhang. The consistency between those results are shown in Figure 6.4 where black triangles together with black circles represent results published in [28] and green triangles results done by author of this thesis. The published $c\bar{c}$ production cross section at mid-rapidity is

$$\frac{d\sigma}{dy} \Big|_{y=0} = 170 \pm 45(\text{stat})_{-59}^{+38}(\text{sys}) \mu\text{b} \quad (6.5)$$

The charm cross section at mid-rapidity (6.5) was extrapolated to full phase space using the same extrapolation factor, 4.7 ± 0.7 , as in [82], and the extracted charm total cross section at $\sqrt{s} = 200$ GeV is

$$\sigma_{cc}^{pp} = 797 \pm 210(\text{stat})_{-295}^{+208}(\text{sys}) \mu\text{b} \quad (6.6)$$

The value (6.6) is also displayed in Figure 6.5.

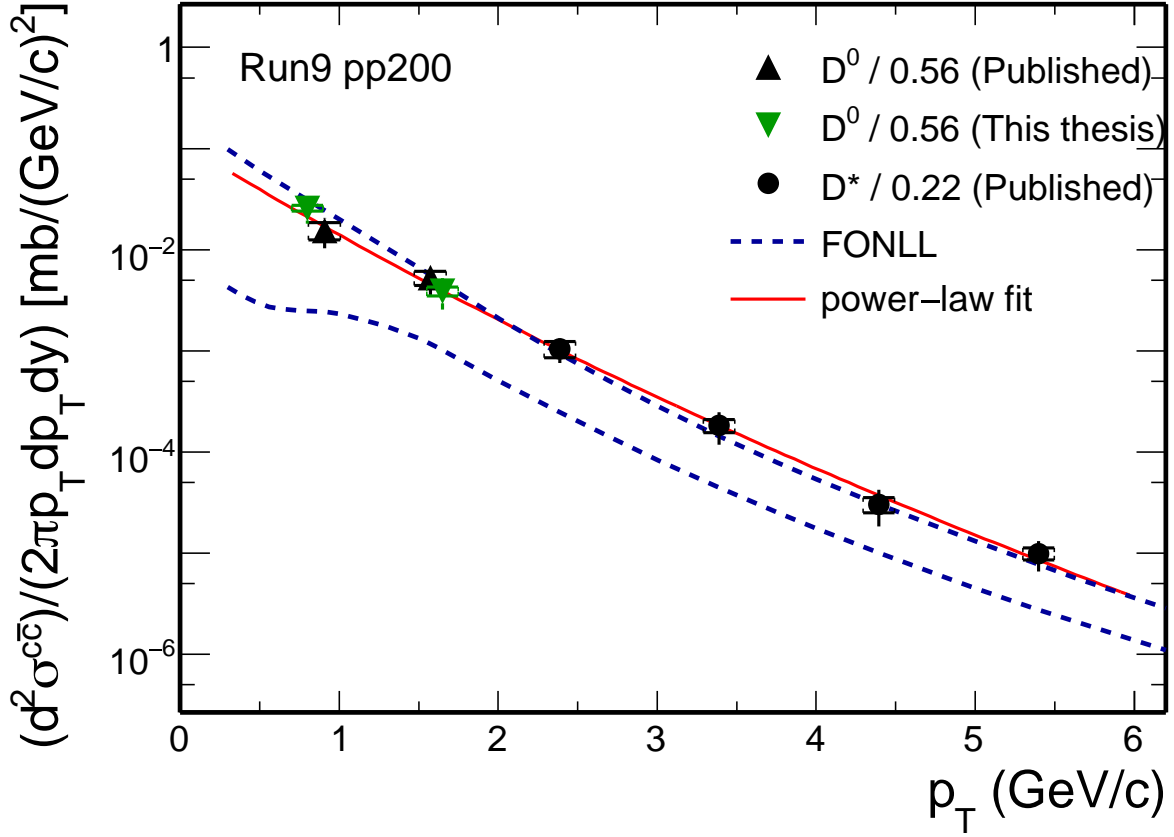


Figure 6.4: Charm quark production cross section as inferred from D^0 and D^* production in p+p collisions at $\sqrt{s} = 200$ GeV compared with FONLL calculation [26]. The D^0 and D^* data points were divided by the charm quark fragmentation ratios $f_c = 0.565$ and $f_c = 0.224$ respectively. D^0 data points from this analysis are shown as green triangles, compared with results from [28] having the tag "(Published)" in the legend. Data points are already corrected on bin widths and fitted by Hagedorn Power-law function (A.2).

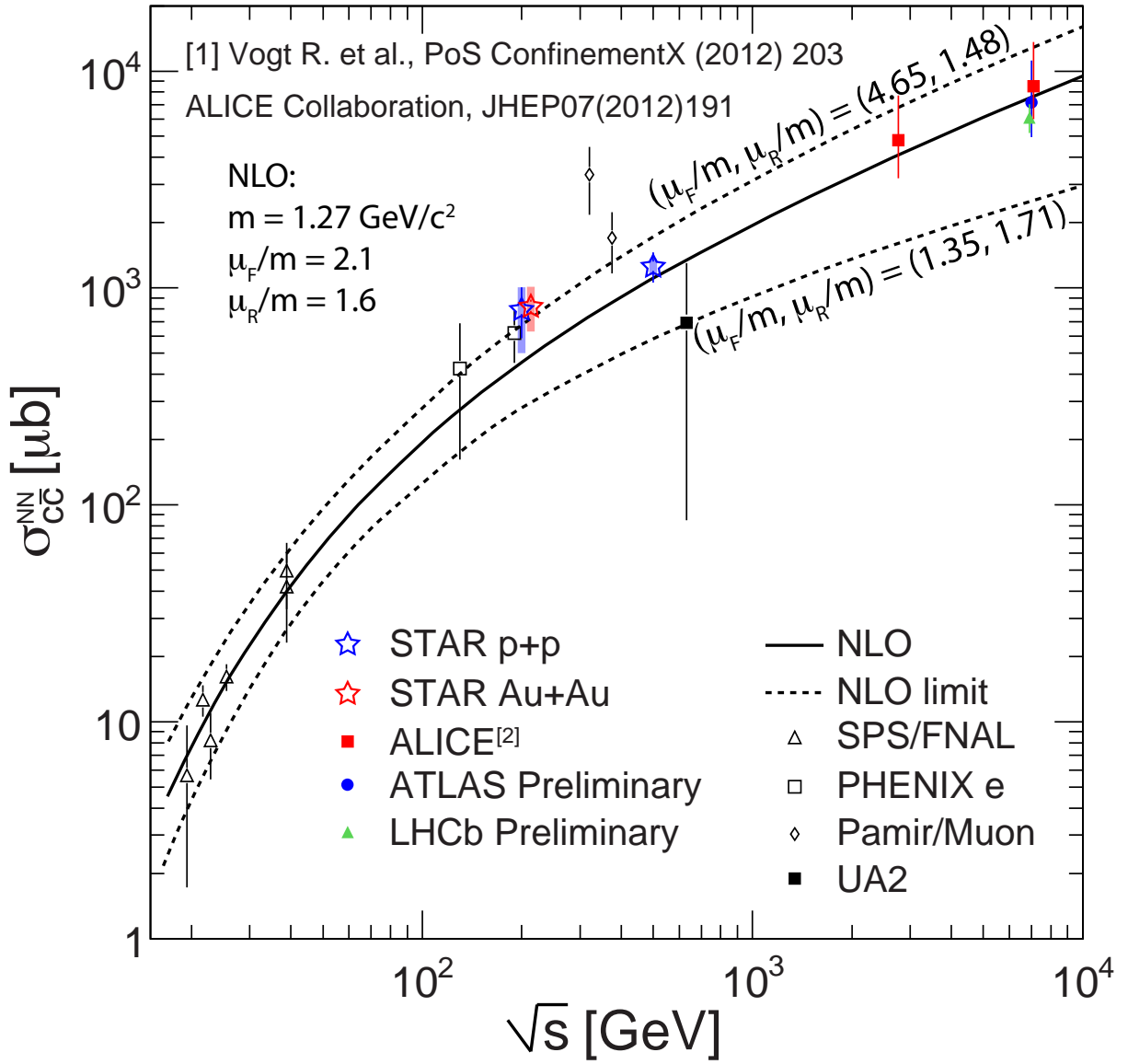
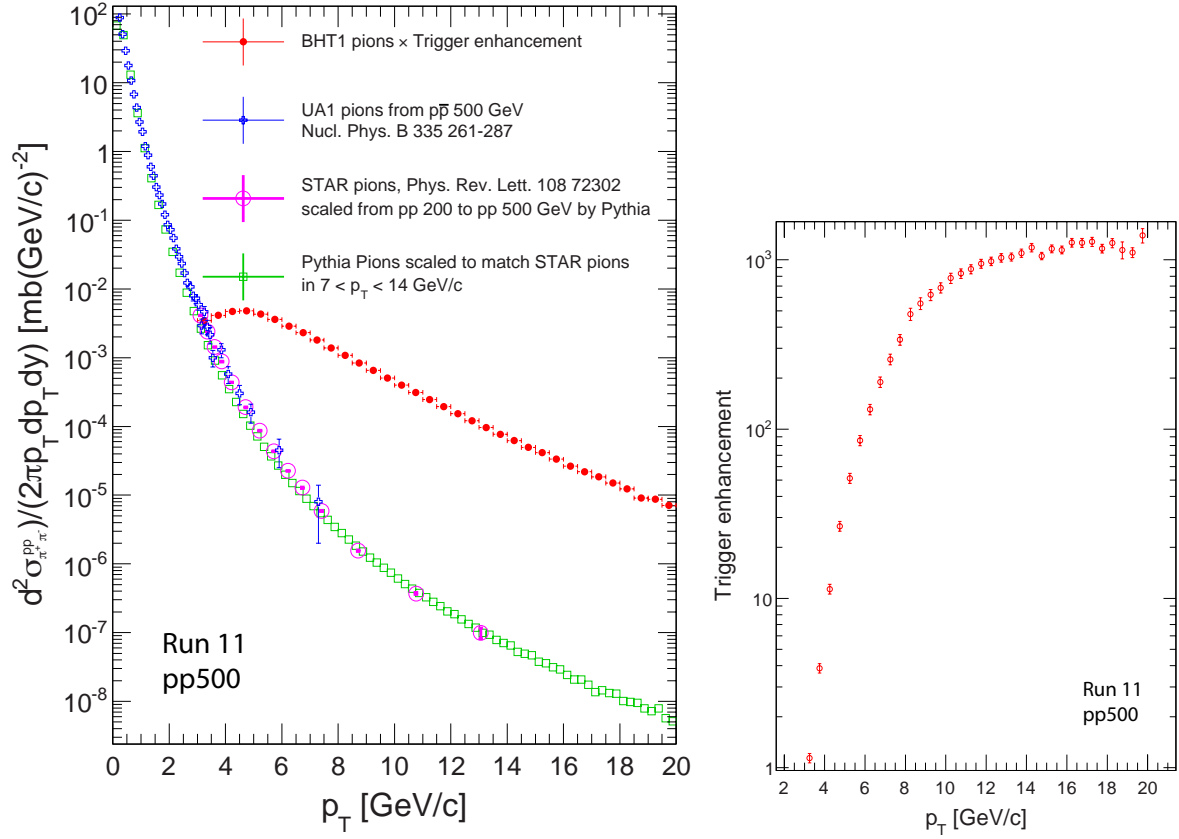


Figure 6.5: Total Charm quark production cross section as a function of Centre-of-mass collision energy \sqrt{s} .

Finally, let's briefly introduce another improvement which has been currently developed and which extends the transverse momentum p_T range of open charm meson reconstruction. This thesis discussed closely the analysis of data triggered by the minimum bias trigger (see section 3.1). Run11 pp500 data also contain events triggered on energy deposition in a Barrel Electromagnetic Calorimeter (BEMC) tower (see section 2.6) above

certain thresholds, i.e., High E_T triggers (BHT). There are 160 millions events triggered by BHT1 whose triggering condition is $E_T > 4.2$ GeV in at least one tower. The raw yield of $D^{*\pm}$ meson in this sample is 1547 ± 61 which can be split into 9 p_T bins with last p_T bin being (16, 20) GeV/ c . The pion from $D^* \rightarrow D^0 \pi_S \rightarrow K \pi \pi_S$ decay (not the soft pion π_S) is required to be the triggering particle, i.e. the pion candidate track projected to BEMC matched the tower with $E_T > 4.2$ GeV. As was shown already in [90], this requirement almost entirely eliminates the trigger bias. The analysis follows the same procedure as described in chapters 3, 4, and 5. The only thing which is extra is the BHT1 trigger enhancement. The trigger enhancement is calculated as ratio $\frac{\text{BHT1_pions}}{\text{MinBias_pions}}$, where BHT1_pions is $\pi^+ \pi^-$ differential invariant production cross section in events triggered by BHT1 and MinBias_pions is $\pi^+ \pi^-$ differential invariant production cross section in events triggered by minimum bias trigger. BHT1_pions are plotted in Figure 6.6a as closed red circles. MinBias_pions are in Figure 6.6a for p_T 3 and 14 GeV/ c open magenta circles and for p_T above 14 GeV/ c open green squares. The magenta circles are results from previous STAR analysis [90] scaled by PYTHIA [32] from $\sqrt{s} = 200$ GeV to $\sqrt{s} = 500$ GeV. The green squares are PYTHIA simulation at 500 GeV scaled to match the magenta circles for $7 < p_T < 14$ GeV/ c . UA1 data [91] (blue open crosses) are shown in Figure 6.6a just for cross check. The Figure 6.6b shows the ratio $\frac{\text{BHT1_pions}}{\text{MinBias_pions}}$.



(a) $\pi^+\pi^-$ differential invariant production cross section in events triggered by BHT1 (closed red circles) and in events triggered by minimum bias trigger (open magenta circles). The magenta circles are results from previous STAR analysis [90] scaled by PYTHIA [32] from $\sqrt{s} = 200$ GeV to $\sqrt{s} = 500$ GeV. The green squares are PYTHIA simulation at 500 GeV. UA1 data [91] are displayed by blue open crosses.

(b) BHT1 trigger enhancement as a function of pion p_T .

The differential invariant cross section $E \frac{d^3\sigma}{dp^3}$ of an charm quark pair $c\bar{c}$ production at mid-rapidity, after correcting on the BHT1 trigger enhancement, is consistent with the results in minimum bias data in the overlapping p_T region, as demonstrated in Figure 6.6. The new analysis extends the p_T range up to 18 GeV/c . These new results are in agreement with FONLL prediction [83].

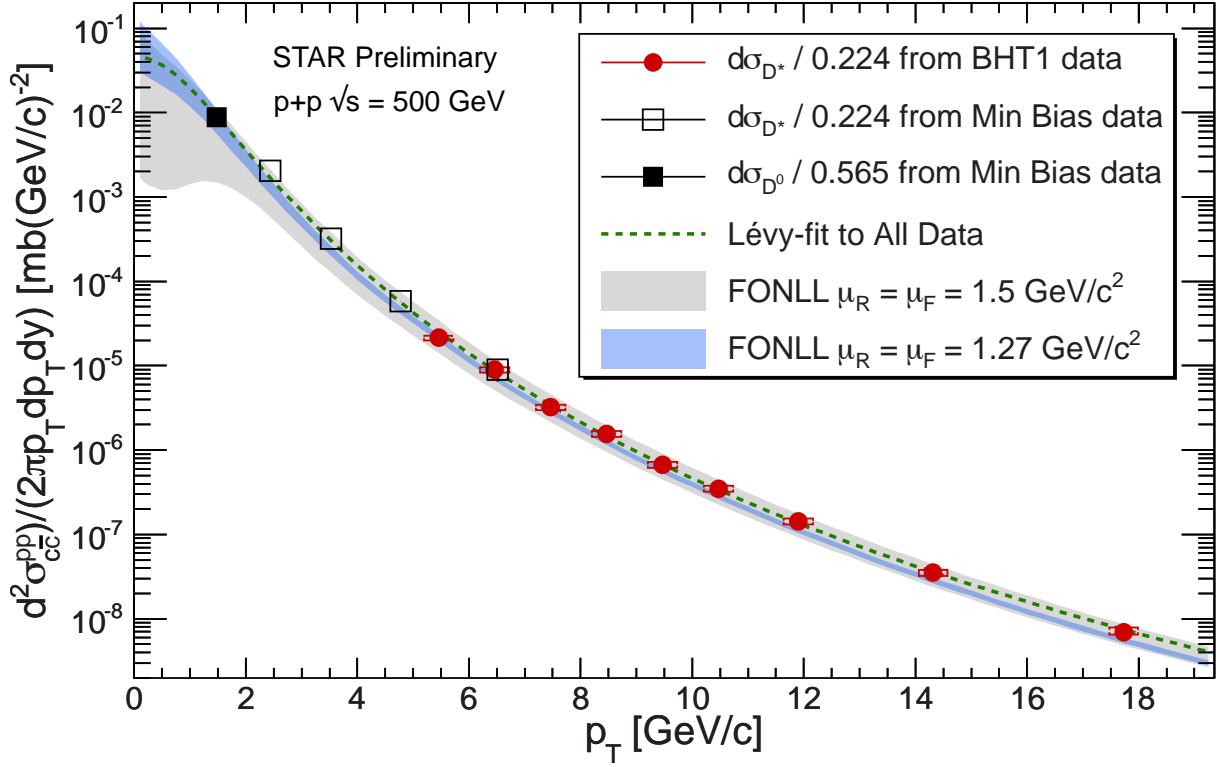


Figure 6.6: Charm quark production cross section as inferred from D^0 and D^* production in p+p collisions at $\sqrt{s}=500$ GeV compared with FONLL prediction [83]. The D^0 and D^* data points were divided by the charm quark fragmentation ratios $f_c = 0.565$ and $f_c = 0.224$ respectively. Data points are already corrected on bin widths and fitted by Lévy Power-law function (A.4) with m_0 chosen to be $1.5 \text{ GeV}/c^2$. D^* data points came from datasets triggered by minimum bias trigger (open black squares) and BHT1 trigger (closed red circles).

Discussion and Outlook

In summary, the first measurement of the charm pair production cross section in p+p collisions at RHIC at $\sqrt{s} = 500$ GeV and 200 GeV has been reported. The cross section was calculated from the production of open charmed-meson D^0 and D^* reconstructed via their hadronic decays, covering the p_T range from 1 to 8 GeV/ c . The measured transverse momentum differential cross section is consistent with the prediction of a Fixed-Order Next-to-Leading Logarithm perturbative QCD calculation. The charm pair production cross section at mid-rapidity is measured to be

$$\left. \frac{d\sigma}{dy} \right|_{y=0} = 225 \pm 38(\text{stat}) \pm 19(\text{sys}) \pm 26(\text{norm}) \mu\text{b}$$

in p+p collisions at $\sqrt{s} = 500$ GeV and

$$\left. \frac{d\sigma}{dy} \right|_{y=0} = 170 \pm 45(\text{stat})_{-59}^{+38}(\text{sys}) \mu\text{b}$$

in p+p collisions at $\sqrt{s} = 200$ GeV. The total charm pair cross section is estimated as

$$\sigma_{cc}^{pp} = 1260 \pm 211(\text{stat}) \pm 109(\text{sys}) \pm 146(\text{norm}) \mu\text{b}$$

in p+p collisions at $\sqrt{s} = 500$ GeV and

$$\sigma_{cc}^{pp} = 797 \pm 210(\text{stat})_{-295}^{+208}(\text{sys}) \mu\text{b}$$

in p+p collisions at $\sqrt{s} = 200$ GeV. Results measured at both energies are in agreement with Next-To-Leading order perturbative QCD calculation.

In Run11 pp500 analysis, the new approach towards systematic uncertainties on the raw yield determination has been used and it was found that the statistical uncertainty is higher than the total systematic uncertainty in all reconstructed D^0/D^*p_T bins (discussed at the end of chapter 5). Owing to the usage of both Hagedorn and Lévy parametrization, the result from Run11 pp500 analysis has significantly lower both statistical and systematic error.

All these experiences will be used in analyses of data using two significant upgrades of STAR subsystems. The STAR upgrade with Heavy Flavor Tracker (HFT) and Muon Telescope Detector (MTD) is keystone for the future of Heavy Flavor Physics. Measurements of identified hadrons containing heavy quarks will play key roles in exploring the properties of the strongly coupled system, thermalization, and the mechanism for partonic energy loss.

HFT will significantly reduce the large combinatorial background this analysis had to deal with. This will allow not only reduce statistical uncertainties of measurements described in this thesis but also reconstruction of D^+ , D_s , Λ_c hadrons. Furthermore, STAR will be able to separate the prompt J/ψ from the J/ψ coming from B meson decays. This will allow to study suppression of bottom quarks. The details about HFT can be found in HFT technical design report [93].

MTD will enable experimenters to collect a large sample of J/ψ events with its trigger capabilities, to separate different $\Upsilon \rightarrow \mu^+\mu^-$ decay channels, to provide a unique measurement of μ - e correlations from heavy-flavor decays, and enable the study of the rare

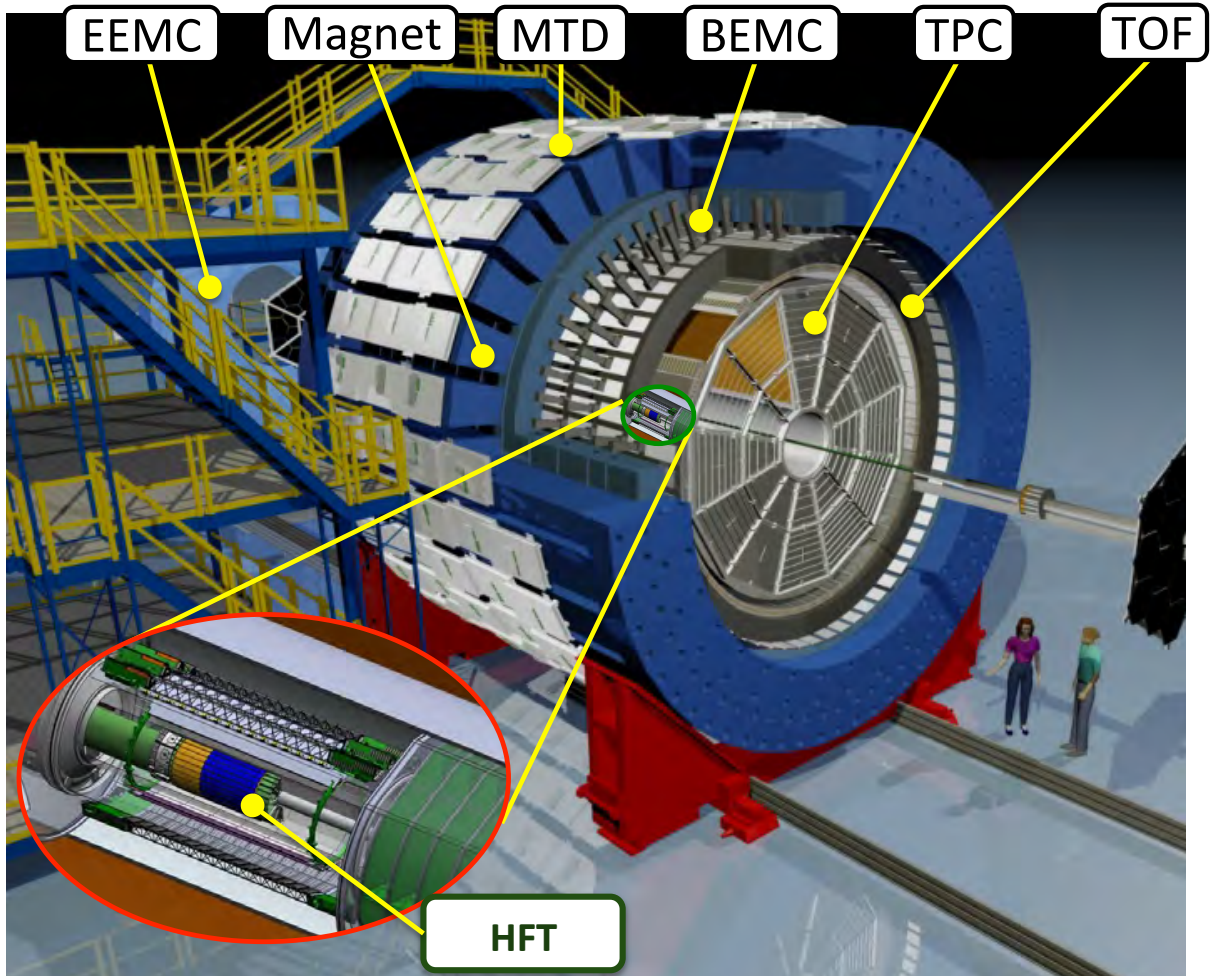


Figure 7.1: The Artistic view of the STAR detector with two new upgrades, the Heavy Flavor Tracker (HFT) and Muon Telescope Detector (MTD).

decays (e.g. $\Sigma^+ \rightarrow p\mu^+\mu^-$) and exotic states, such as the muonic atoms of $\mu\pi$, μK and μp^- . The details about MTD can be found in [94].

Both MTD and HFT are currently successfully installed and fully operational. Their placement is shown in Figure 7.1 with HFT being close the beam pipe and MTD being beyond the magnet yokes which act like hadron absorbers.

APPENDIX A

Differential Invariant Cross Section

A.1 As a Hagedorn Shape Function

Hard scattering amplitudes follow a power-law function giving us assumption of open charm invariant cross section power-law behavior. Long time ago Hagedorn proposed the QCD inspired empirical formula describing the data of the invariant cross section of hadrons as a function of p_T over a wide range [85]:

$$\frac{d^2\sigma}{p_T dp_T dy} = A \left(1 + \frac{p_T}{p_0}\right)^{-n} \longrightarrow \begin{cases} \exp\left(-\frac{np_T}{p_0}\right) & \text{for } p_T \rightarrow 0 \\ \left(\frac{p_0}{p_T}\right)^n & \text{for } p_T \rightarrow \infty \end{cases} \quad (\text{A.1})$$

where A, p_0, n are arbitrary constants. This function has indeed become a purely exponential function for small p_T and a purely power law function for large p_T ¹. The mean p_T becomes:

¹It is widely known from experimental data that, as expected from pQCD calculations [84], a pure power law shape successfully describes the high p_T region of particle spectra. At low p_T , suggests a

$$\langle p_T \rangle = \frac{A \int_{-\infty}^{\infty} \frac{d\sigma}{dy} dy \int_0^{\infty} p_T^2 \left(1 + \frac{p_T}{p_0}\right)^{-n}}{A \int_{-\infty}^{\infty} \frac{d\sigma}{dy} dy \int_0^{\infty} p_T \left(1 + \frac{p_T}{p_0}\right)^{-n}} = \frac{2p_0}{n-3}$$

The normalization constant A can be obtained from the relation:

$$d\sigma/dy = A \int_0^{\infty} p_T \left(1 + \frac{2p_T}{p_0}\right)^{-n} = \frac{Ap_0^2}{(n-1)(n-2)}$$

so we get

$$A = 4 \frac{d\sigma}{dy} \frac{(n-1)(n-2)}{\langle p_T \rangle^2 (n-3)^2}, \quad p_0 = \frac{\langle p_T \rangle}{2} (n-3)$$

and $c\bar{c}$ invariant cross section can be represented by

$$\frac{d^2\sigma^{c\bar{c}}}{2\pi p_T dp_T dy} = \frac{2}{\pi} \frac{d\sigma^{c\bar{c}}}{dy} \frac{(n-1)(n-2)}{\langle p_T \rangle^2 (n-3)^2} \left(1 + \frac{2p_T}{\langle p_T \rangle (n-3)}\right)^{-n} \quad (\text{A.2})$$

with three free parameters $d\sigma^{c\bar{c}}/dy$, $\langle p_T \rangle$, n need to be obtained from the least square fit of the real corrected data points.

A.2 As a Lévy Function

As an alternative to Hagedorn (A.1) formula, one can use a different approach based on the Tsallis statistics [86] to fit particle spectra. The Tsallis distribution was derived from a generalized form of the Boltzmann-Gibbs entropy. However, there are other origins thermal interpretation in which the bulk of the produced particles are emitted by a system in thermal equilibrium with a Boltzmann-Gibbs statistical description of their spectra:

$$E \frac{d^3\sigma}{d\mathbf{p}^3} = A e^{-E/T}$$

where A is a normalization factor and E is the particle energy. At mid-rapidity one can replace E by $m_T = \sqrt{p_T^2 + m_0^2}$, where m_0 is the particle rest mass.

discussed in recent days [87] suggesting for example hard collisions approach [88]. The distribution could be written in the form:

$$\frac{d^2\sigma}{2\pi p_T dp_T dy} = C_n \left(1 + \frac{\sqrt{p_T^2 + m_0^2}}{nT} \right)^{-n} \quad (\text{A.3})$$

where C_n is the normalization constant, n the power and T an inverse slope parameter.

To calculate C_n , one must integrate (A.3) over p_T

$$C_n = \frac{1}{\int_0^\infty p_T \left(1 + \frac{\sqrt{p_T^2 + m_0^2}}{nT} \right)^{-n} dp_T} = \frac{1}{\frac{(nT + m_0)^{1-n}}{(nT)^{-n}} \frac{m(n-1) + nT}{(n-1)(n-2)}}$$

to get the (A.3) into the form appropriate to fitting:

$$\frac{d^2\sigma^{c\bar{c}}}{2\pi p_T dp_T dy} = \frac{1}{2\pi} \frac{d\sigma^{c\bar{c}}}{dy} \frac{(n-1)(n-2)}{(nT + m_0)[m_0(n-1) + nT]} \left(\frac{nT + \sqrt{p_T^2 + m_0^2}}{nT + m_0} \right)^{-n} \quad (\text{A.4})$$

with three free fitting parameters $d\sigma^{c\bar{c}}/dy, n, T$.

APPENDIX B

D^* Decay Kinematics

B.1 General Relations

Consider the decay of a D^* of mass M in its CMS frame. Then its 4-momentum is $P^* = (M, 0, 0, 0)$. Denote the 4-momenta of the daughter particles in CMS by p_1^* (for D^0) and p_2^* (for π_S): $p_1^* = (E_1^*, \mathbf{p}_1^*)$, $p_2^* = (E_2^*, \mathbf{p}_2^*)$. The 4-momentum conservation requires $P^* = p_1^* + p_2^*$ and hence $\mathbf{p}_2^* = -\mathbf{p}_1^*$. We can therefore omit the subscript on the daughter particle momenta and hence energy conservation takes on the form $E_1 + E_2 = \sqrt{m_1^2 + p^{*2}} + \sqrt{m_2^2 + p^{*2}} = M$. Solving this equation for p^* we get

$$p^* = \frac{1}{2M} \sqrt{[M^2 + (m_1 - m_2)^2][M^2 - (m_1 - m_2)^2]} = 39.397 \text{ MeV}, \quad (\text{B.1})$$

where $M = 2010.28 \text{ MeV}$, $m_1 = 1864.84 \text{ MeV}$, and $m_2 = 139.57 \text{ MeV}$.

If the D^* moves in one direction with velocity β the basic Lorentz transformation equations in Cartesian form give the daughter particle 4-momentum components the following

relations:

$$p_T = p_\perp^*, \text{ transverse component}^1 \quad (\text{B.2a})$$

$$p_\parallel = \gamma p_\parallel^* + \gamma\beta E_\parallel^*, \text{ longitudinal component}^1 \quad (\text{B.2b})$$

$$E = \gamma\beta p_\parallel^* + \gamma E_\parallel^*, \text{ energy component} \quad (\text{B.2c})$$

Let's note that all variables are considered to be in natural units.

More specifically, if the D^* transverse momentum is P then the soft pion's transverse momentum² p will be between

$$\begin{aligned} \gamma\beta E_\pi^* - \gamma p^* \leq p \leq \gamma\beta E_\pi^* + \gamma p^*, \quad \beta = \frac{P}{E}, \quad \gamma = \frac{E}{M}, \quad \gamma\beta = \frac{P}{M} \\ \frac{P}{M} \sqrt{p^{*2} + m_\pi^2} - \frac{\sqrt{P^2 + M^2}}{M} p^* \leq p \leq \frac{P}{M} \sqrt{p^{*2} + m_\pi^2} + \frac{\sqrt{P^2 + M^2}}{M} p^* \end{aligned} \quad (\text{B.3})$$

To illustrate this inequality, we plotted the two maximum and minimum curves shown in Figure B.1. If $P < \frac{M}{m_\pi^2} p^*$ then the π_S 3-momenta has negative sign, but the Figure B.1 shows absolute values. The Magenta horizontal dashed line illustrates the track p_T cut corresponding to the minimum track p_T value for the track to be able to reach the TOF detector.

¹transverse or longitudinal relative to the momentum vector in the LAB frame

² $p \equiv p_T$ in LAB

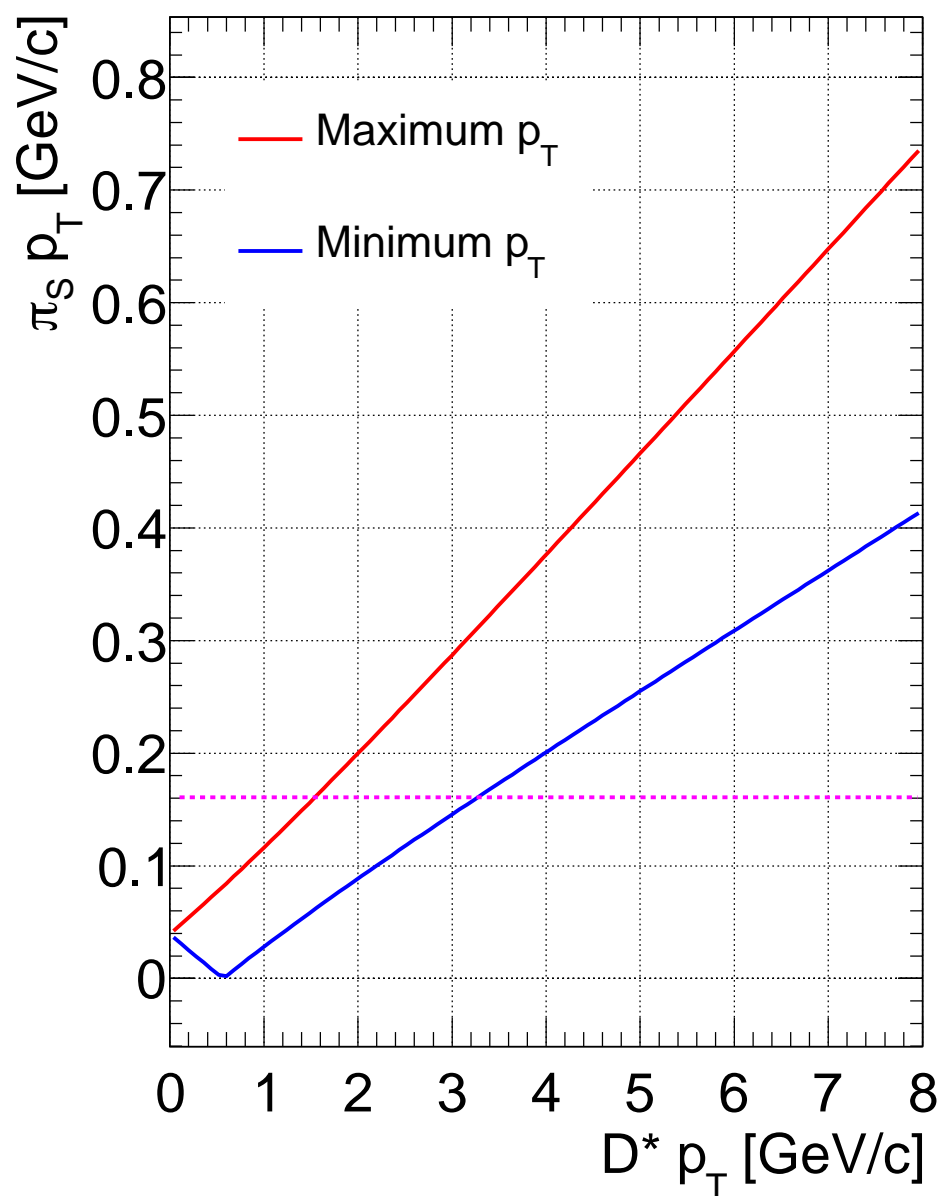


Figure B.1: Kinematically possible values of the soft pion transverse momentum from the $D^* \rightarrow D^0 \pi_S$ decay.

B.2 Monte-Carlo Toy Model

In order to get the exact daughter particle p_T distribution for any given mother particle p_T , the Monte-Carlo (MC) mother particle (D^0 or D^*) was generated by the ROOT `TRandom3` MC generator with p_T distributed according to $p_T \times (A.4)$, $\frac{d\sigma^{c\bar{c}}}{dy} = 0.19$, $T = 0.12$, $n = 8.37$, and azimuthal angle ϕ and rapidity y were distributed uniformly from $(0, 2\pi)$ and $(-1, 1)$ respectively. Such MC particle was let to decay isotropically and daughter particles were boosted then in the direction of the mother particle. Figures B.2 and B.3 show results of this simulation in the form of $\mathbb{R} \times \mathbb{R} \rightarrow \mathbb{R}$ function $g(t, p_T)$, where t denotes a transverse momentum of D^* and p_T a transverse momentum of the respective daughter particle.

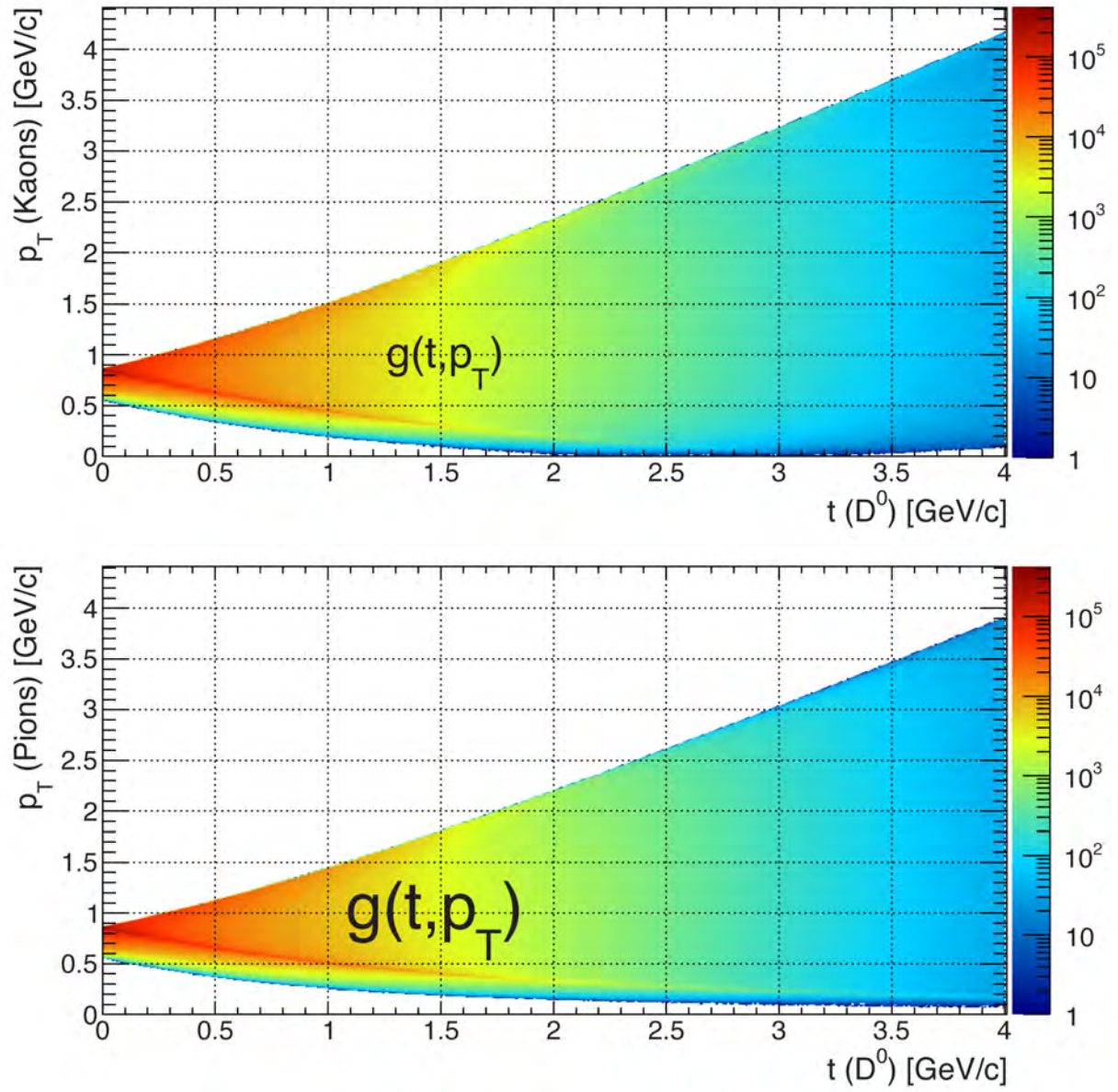


Figure B.2: D^0 decay kinematics $g(t, p_T)$.

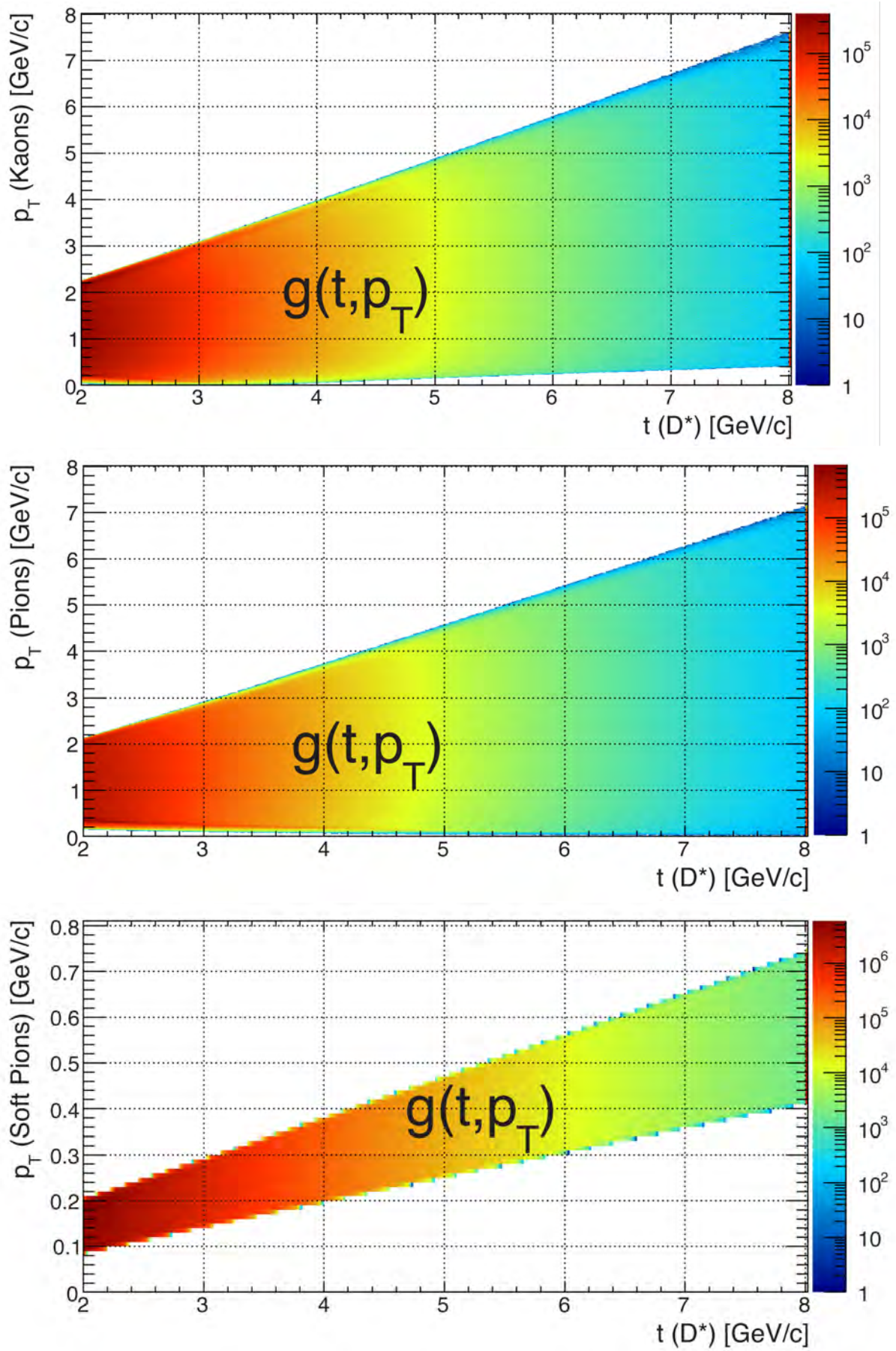


Figure B.3: D^* decay kinematics $g(t, p_T)$.

APPENDIX C

Treatment of Errors

C.1 Treatment of Errors in Efficiency Calculations

An Application of a cut can be considered a Binomial process. $P(k; \varepsilon, n)$ defined as

$$P(k; \varepsilon, n) = \binom{n}{k} \varepsilon^k (1 - \varepsilon)^{n-k} \quad (\text{C.1})$$

denotes the probability that k events will pass the cut, given the conditions that the true efficiency is ε and that there are n events in the sample. The probability density function $P(\varepsilon; k, n)$, which gives the probability function of ε for a given n and k , can be determined by Bayesian theorem:

$$P(\varepsilon; k, n) = \frac{P(k; \varepsilon, n)P(\varepsilon; n)}{C}, \quad (\text{C.2})$$

where C is a constant to be determined by normalization, and $P(\varepsilon; n)$ is the probability assigned for the true efficiency before the data are considered. There is no reason to favor

one value of the efficiency over another, so it's reasonable to take

$$P(\varepsilon; n) = \begin{cases} 1 & \text{if } 0 \leq \varepsilon \leq 1 \\ 0 & \text{otherwise} \end{cases}$$

independent of n .

$$\begin{aligned} \int_{-\infty}^{+\infty} P(\varepsilon; k, n) d\varepsilon &= \frac{1}{C} \binom{n}{k} \int_0^1 \varepsilon^k (1 - \varepsilon)^{n-k} d\varepsilon = 1 \\ \int_0^1 \varepsilon^k (1 - \varepsilon)^{n-k} d\varepsilon &= \frac{\Gamma(k+1)\Gamma(n-k+1)}{\Gamma(n+2)} = \frac{k!(n-k)!}{(n+1)!} \\ \frac{1}{C} \frac{n!}{(n-k)!k!} \frac{k!(n-k)!}{(n+1)!} &\Rightarrow C = \frac{1}{n+1} \end{aligned}$$

The final efficiency probability density function thus reads:

$$P(\varepsilon; k, n) = (n+1) \binom{n}{k} \varepsilon^k (1 - \varepsilon)^{n-k} \quad (\text{C.3})$$

The mean value of C.3:

$$\bar{\varepsilon} = \int_0^1 \varepsilon P(\varepsilon; k, n) d\varepsilon = \frac{(n+1)!}{k!(n-k)!} \int_0^1 \varepsilon^{k+1} (1 - \varepsilon)^{n-k} d\varepsilon = \frac{k+1}{n+2}, \quad (\text{C.4})$$

the mode of C.3:

$$\frac{dP}{d\varepsilon} = 0 \Rightarrow \varepsilon = \frac{k}{n}, \quad (\text{C.5})$$

and variance of C.3:

$$\begin{aligned} V(\varepsilon) &= \int_0^1 (\varepsilon - \bar{\varepsilon})^2 P(\varepsilon; k, n) d\varepsilon = \int_0^1 \varepsilon^2 P(\varepsilon; k, n) d\varepsilon - \bar{\varepsilon}^2 \\ &= \frac{(k+1)(k+2)}{(n+2)(n+3)} - \frac{(k+1)^2}{(n+2)^2}. \end{aligned} \quad (\text{C.6})$$

$$V(\varepsilon)|_{k=0, n} = \frac{n+1}{(n+2)^2(n+3)} > 0$$

$$\lim_{n \rightarrow \infty} V(\varepsilon) = 1/n^2$$

To find the shortest interval $[\alpha, \beta]$ which contains probability content $\lambda = 0.683$ (corresponds to $\pm 1\sigma$ interval of a Normal distribution), the interval $\beta - \alpha$ must be minimized, subject to the constraint

$$\int_{\alpha}^{\beta} P(\varepsilon; k, n) d\varepsilon = \lambda$$

A formal solution can be found using the method of Lagrange multipliers. The solution for α and β is found by the simultaneous solutions of the nonlinear equations:

$$\mathcal{G} + \rho \alpha^k (1 - \alpha)^{n-k} = 0$$

$$\mathcal{G} + \rho \beta^k (1 - \beta)^{n-k} = 0$$

$$\mathcal{B}_{\beta}(k+1, n-k+1) - \mathcal{B}_{\alpha}(k+1, n-k+1) = \lambda \mathcal{G}$$

where $\mathcal{G} = \frac{\Gamma(k+1)\Gamma(n-k+1)}{\Gamma(n+2)}$, ρ is a Lagrange multiplier introduced for the constraint, and $\mathcal{B}_x(k+1, n-k+1)$ is the incomplete Beta function, defined by

$$\mathcal{B}_x(k+1, n-k+1) = \int_0^x t^k (1-t)^{n-k} dt.$$

The calculation of λ is implemented in the ROOT routine `TGraphAsymmErrors::BayesDivide`.

C.2 Treatment of Systematic Errors

This appendix is based on the article [81].

Suppose a yield is estimated from a data sample by two different methods, giving estimates Y_1 and Y_2 , with statistical errors σ_1 and σ_2 . It is required to find error on the difference

$$\Delta = Y_1 - Y_2 \tag{C.7}$$

and thus to establish whether the estimates agree within one standard deviation. The error on the difference is given by

$$\sigma_{\Delta}^2 = \sigma_1^2 + \sigma_2^2 - 2\rho\sigma_1\sigma_2 \quad (\text{C.8})$$

where ρ is the correlation between the two estimates. If two estimates are, at any rate to some extent, independent, they can be weighted and combined to give an improved estimate that is more efficient than either one separately. Let the joint estimator be

$$Y = wY_1 + (1 - w)Y_2 \quad (\text{C.9})$$

where w is some chosen weight. Then the error on Y is given by

$$\sigma^2 = w^2\sigma_1^2 + (1 - w)^2\sigma_2^2 + 2w(1 - w)\rho\sigma_1\sigma_2. \quad (\text{C.10})$$

Setting the derivative with respect to w to zero to find the minimum of σ gives

$$w = \frac{\sigma_2^2 - \rho\sigma_1\sigma_2}{\sigma_1^2 + \sigma_2^2 - 2\rho\sigma_1\sigma_2} \quad 1 - w = \frac{\sigma_1^2 - \rho\sigma_1\sigma_2}{\sigma_1^2 + \sigma_2^2 - 2\rho\sigma_1\sigma_2} \quad (\text{C.11})$$

and the resulting minimum error on Y is given by

$$\sigma = \frac{\sigma_1^2\sigma_2^2(1 - \rho^2)}{\sigma_1^2 + \sigma_2^2 - 2\rho\sigma_1\sigma_2} \quad (\text{C.12})$$

(If the results are uncorrelated this gives the familiar form for the best combination of estimates with different errors).

However no estimator can be more efficient than the Minimum Variance Bound (MVB)

$$\sigma_0 = \frac{1}{N \int \left(\frac{d \ln P(x; Y)}{dY} \right)^2 P(x; Y) dx} \quad (\text{C.13})$$

where $P(x; Y)$ is the probability density function for the distribution being measured.

Thus

$$\frac{\sigma_1^2\sigma_2^2(1 - \rho^2)}{\sigma_1^2 + \sigma_2^2 - 2\rho\sigma_1\sigma_2} \geq \sigma_0 \quad (\text{C.14})$$

which gives an expression for ρ which is satisfied only between the two roots of the quadratic

$$\rho = \frac{\sigma_0^2 \pm \sqrt{(\sigma_1^2 - \sigma_0^2)(\sigma_2^2 - \sigma_0^2)}}{\sigma_1 \sigma_2} \quad (\text{C.15})$$

The maximum value for σ_Δ comes from the minimum value for ρ , and vice versa

$$\begin{aligned} \sigma_\Delta^{max} &= \sqrt{(\sigma_1^2 - \sigma_0^2)} + \sqrt{(\sigma_2^2 - \sigma_0^2)} \\ \sigma_\Delta^{min} &= \left| \sqrt{(\sigma_1^2 - \sigma_0^2)} - \sqrt{(\sigma_2^2 - \sigma_0^2)} \right| \end{aligned} \quad (\text{C.16})$$

C.3 Treatment of Correlated Errors

This appendix is based on the article [92].

Suppose n measurements x_i . Let's define the covariance matrix \mathbb{V} , whose terms are given by

$$\mathbb{V}_{ij} = \text{E}[(x_i - \mu_i)(x_j - \mu_j)] = \text{E}[x_i x_j] - \mu_i \mu_j$$

where E denotes expected value and μ mean value ($\mu \equiv \text{E}(x)$). The diagonal members of \mathbb{V} are the variances, e.g., $\mathbb{V}_{ii} = \sigma_i^2$. The correlation coefficient r_{ij} is given by

$$r_{ij} = \frac{\mathbb{V}_{ij}}{\sigma_i \sigma_j}.$$

The best linear estimator accounting for all measurements can be defined generally as

$$\bar{x} \equiv \sum_i w_i x_i \quad (\text{C.17})$$

where the weights w_i must be found. Assuming that the x_i each provide an unbiased estimate and requiring that the estimator \bar{x} be unbiased gives the condition $\sum_i w_i = 1$. Writing $\bar{x} - \text{E}(\bar{x}) = \sum_i w_i (x_i - \text{E}(x_i))$ and using the definition of the standard deviation, one can obtain the relation for the standard deviation of \bar{x} :

$$\sigma_{\bar{x}}^2 = \sum_{ij} w_i w_j \mathbb{V}_{ij} \quad (\text{C.18})$$

To minimize $\sigma_{\bar{x}}^2$ subject to condition $\sum_i w_i = 1$, the Lagrange multiplier technique can be used. Writing

$$\sigma_{\bar{x}}^2 = \sum_{ij} w_i w_j \mathbb{V}_{ij} + \lambda \left(\sum_i w_i - 1 \right) \quad (\text{C.19})$$

and setting the derivative of $\sigma_{\bar{x}}^2$ with respect to the w_i and λ to zero, one gets the solution¹

$$w_i = \frac{\sum_k \mathbb{V}_{ik}^{-1}}{\sum_{jk} \mathbb{V}_{jk}^{-1}} \quad (\text{C.20})$$

¹Actually, \mathbb{V}^{-1} does not have to exist for the weights to be determined. Such singular covariance matrices arise when only a fully correlated error is present. The simplest way to deal with this situation numerically is to add a small term ϵ to the diagonal elements of \mathbb{V} , calculate \mathbb{V}^{-1} , and neglect ϵ afterwards.

Bibliography

- [1] E. D. Bloom *et al.*, Phys. Rev. Lett. **23**, 930 (1969).
- [2] M. Breidenbach *et al.*, Phys. Rev. Lett. **23**, 935 (1969).
- [3] F. Abe *et al.*, Phys. Rev. Lett. **74**, 2626 (1995).
- [4] J. Beringer *et al.*, Phys. Rev. D **86**, 010001 (2012).
- [5] A. Alves, J. Augusto *et al.*, JINST **3**, S08005 (2008).
- [6] R. Aaij *et al.*, arXiv:1404.1903 (2014).
- [7] M. Gell-Mann, Phys. Lett. **8**, 214 (1964).
- [8] W. N. Cottingham, D. A. Greenwood: An Introduction to the Standard Model of Particle Physics, Cambridge University Press (1998), ISBN 0-521-58191-5.
- [9] S. Bethke, Eur. Phys. J **C64**, 689 (2009).
- [10] G. Sterman *et al.*, Rev. Mod. Phys. **67**, 157 (1995).
- [11] P. Petreczky, Nucl. Phys. B **140**, 78 (2004).
- [12] Z. Fodor, S. D. Katz, JHEP **04** 050 (2004).

-
- [13] A. Chodos, R. L. Jaffe, K. Johnson, C. B. Thorn, and V. F. Weisskopf, Phys. Rev. D **9**, 3471 (1974).
 - [14] J Donoghue, E Golowich and B Holstein, "Dynamics of the Standard Model", Cambridge University Press, (1994).
 - [15] Y. Nambu and G. Jona-Lasinio, "Dynamical Model of Elementary Particles Based on an Analogy with Superconductivity", Phys. Rev. **122** (1961).
 - [16] J. Berges, K. Rajagopal, Nucl. Phys. B **538**, 1 215 (1999).
 - [17] X. Zhu *et al.*, Phys. Let. B **647**, 366 (2007).
 - [18] J. Adams *et al.* Nucl. Phys. A **757**, 102 (2005).
 - [19] H. Caines., J. Phys. G **31**, S101 (2005).
 - [20] J. D. Bjorken, Phys. Rev. D **27**, 140 (1983).
 - [21] F. Karsch, Nucl. Phys. A **698**, 199c (2002).
 - [22] S. Adler *et al.*, Phys. Rev. C **71**, 034908 (2005).
 - [23] T. Hirano, N. van der Kolk, A. Bilandzic, Hydrodynamics and Flow, Springer Berlin Heidelberg (2010).
 - [24] M. L. Miller, K. Reygers, S. J. Sanders, P. Steinberg, arXiv:nucl-ex/0701025 (2007).
 - [25] P. Nason and S. Dawson, Nucl. Phys. B. **303**, 607 (1988).
 - [26] M. Cacciari, M. Greco, and P. Nason, Jour. High Energy Phys. **05**, 007 (1998).
 - [27] M. Cacciari, P. Nason and R. Vogt, Phys. Rev. Lett. **95**, 122001 (2005).
 - [28] L. Adamczyk *et al.*, Phys. Rev. D **86**, 072013 (2012).
 - [29] R. Vogt, Eur. Phys. J. Special Topics **155**, 213 (2008).

- [30] R. Vogt *et al.*, Phys. Rev. C **87**, 014908 (2013).
- [31] STAR Collaboration, [http://www.bnl.gov/npp/docs/STAR_Decadal_Plan_Final\[1\].pdf](http://www.bnl.gov/npp/docs/STAR_Decadal_Plan_Final[1].pdf) (2010).
- [32] T. Sjöstrand, <http://home.thep.lu.se/~torbjorn/Pythia.html> (2014).
- [33] M. M. Aggarwal *et al.*, Phys. Rev. Lett. **105**, 202301 (2010).
- [34] X. Lin, arXiv:hep-ph/0602067 (2006).
- [35] D. Acosta *et al.*, Phys. Rev. Lett. **91**, 241804 (2003).
- [36] B. Abelev *et al.*, J. High Energy Phys. **128**, 1201 (2012).
- [37] A. Adare *et al.*, Phys. Rev. Lett. **104**, 132301 (2010).
- [38] B. I. Abelev *et al.*, Phys. Rev. Lett. **97**, 152301 (2006).
- [39] L. Adamczyk *et al.*, arxiv:1404.6185 (2014).
- [40] Yu. L. Dokshitzer and D.E. Kharzeev, Phys. Lett. B **519**, 199 (2001); N. Armesto, A. Dainese, C.A. Salgado and U.A. Wiedemann, Phys. Rev. D **71**, 054027 (2005).
- [41] B. I. Abelev *et al.*, Phys. Rev. Lett. **98**, 192301 (2007).
- [42] S. S. Adler *et al.*, Phys. Rev. Lett. **96**, 032301 (2006).
- [43] B. I. Abelev *et al.*, J. High Energy Phys. **09**, 112 (2012); B. I. Abelev *et al.*, Phys. Rev. Lett. **109**, 112301 (2012).
- [44] M. Djordjevic, M. Gyulassy and S. Wicks, Phys. Rev. Lett. **94**, 112301 (2005).
- [45] A. Adil and I. Vitev, Phys. Lett. B **649**, 139 (2007).
- [46] M. He, R.J. Fries, R. Rapp, Phys. Rev. C **86**, 014903 (2012); M. He, R.J. Fries, R. Rapp, Phys. Rev. Lett. **110**, 112301 (2013).

-
- [47] P. B. Gossiaux *et al.*, J. Phys. G **37**, 094019 (2010); P. B. Gossiaux *et al.*, Nucl. Phys. A **904-905**, 992c (2013).
- [48] B. I. Abelev *et al.*, Phys. Rev. C **75**, 064901 (2007).
- [49] W. M. Alberico *et al.*, Eur. Phys. J. C **71**, 1666 (2011); W. M. Alberico *et al.*, Eur. Phys. J. C **73**, 2481 (2013).
- [50] S.S. Cao, G.Y. Qin, and S.A. Bass, Phys. Rev. C **88**, 044907 (2013).
- [51] K. Aamodt *et al.*, JINST **3**, S08002 (2008).
- [52] S. Chatrchyan *et al.*, JINST **3**, S08004 (2008).
- [53] The CMS Collaboration, CMS-PAS-HIN-12-014 (2014).
- [54] M. Djordjevic and M. Djordjevic, arxiv:1307.4098 (2013).
- [55] Y. Mori *et al.*, Rev. Sci. Instrum. **73**, 888 (2002).
- [56] I. Alekseev *et al.*, Nucl. Inst. Meth. A **499**, 392 (2003).
- [57] H. Hahn *et al.*, Nucl. Inst. Meth. A **499**, 245 (2003).
- [58] M. Harrison, T. Ludlam, and S. Ozaki., Nucl. Instr. Meth. A **499**, 235 (2003).
- [59] P. Thieberger, M. McKeown, H.E. Wegner, IEEE Transactions on Nuclear Science, Vol. NS-30 No. 4 (1983).
- [60] R. L. Brown, A. Etkin, K. J. Foley *et al.*, “The STAR Detector Magnet Subsystem,” in Particle Accelerator Conference, 1997. Proceedings of the 1997, vol. **3** 3230–3232 (1997).
- [61] K. H. Ackermann *et al.*, Nucl. Instrum. Meth. A **499**, 624 (2003).
- [62] Nucl. Instrum. Meth. in Physics Research A **499**, 766 (2003).
- [63] J. Abele *et al.*, Nucl. Instrum. Meth. A **499**, 692 (2003).

-
- [64] A. Rose, arXiv:nucl-ex/0307015 (2003).
- [65] Yifei Zhang, private communication (2013).
- [66] R. Reed *et al.*, J. Phys.: Conf. Ser. **219**, 032020 (2010).
- [67] M. Anderson *et al.*, Nucl. Instrum. Meth. A **499**, 679 (2003).
- [68] H. Bichsel, Nucl. Instrum. Meth. A **562**, 154 (2006).
- [69] Y. Xu *et al.*, Nucl. Instrum. Meth. A **614** Issue 1 Pages 28-33 (2009).
- [70] Letter of Intent, RICE-TOF Group, Proposal for a single tray of MRPC-TOF for STAR, 2001-6 (2004).
- [71] E. C. Zeballosa *et al.*, Nucl. Instr. Meth. A **374** 132 (1996).
- [72] S. RAMO: Currents induced in electron motion, PROC. IRE27 584 (1939).
- [73] W. J. Llope *et al.*, The STAR Vertex Position Detector, arXiv:1403.6855 (2014).
- [74] C.E. Allgower *et al.*, Nucl. Instrum. Meth. A **499** 740 (2003).
- [75] M. Beddo *et al.*, Nucl. Instrum. Meth. A **499** 725 (2003).
- [76] Tai Sakuma, private communication (2012).
- [77] <http://www.star.bnl.gov/protected/highpt/dunlop/pp/normalization> (2014).
- [78] B. I. Abelev *et al.*, Phys. Rev. D **79**, 112006 (2009).
- [79] GEANT 3.21, <http://wwwasdoc.web.cern.ch/wwwasdoc/22geanthtml3/geantall.html> (2014).
- [80] R. D. Field *et al.*, arXiv:hep-ph/0510198 (2005).
- [81] R. Barlow, arXiv:hep-ex/0207026 (2002).
- [82] J. Adams *et al.*, Phys. Rev. Lett. **94**, 062301 (2005).

-
- [83] R. Vogt, private communication (2012).
- [84] D. de Florian and R. Sassot, Phys. Rev. D **69**, 074028 (2004).
- [85] Riv. Nuovo Cim. **6N10**, 1-50 CERN-TH-3684 (1984).
- [86] C. Tsallis, J. Stat. Phys. **52** 479 (1988).
- [87] G. Wilk and Z. Wlodarczyk, Eur. Phys. J. A **40** 299 (2009).
- [88] G. Wilk and Ch. Wong, Phys. Rev. D **87**, 114007 (2013).
- [89] Vogt R. *et al.*, PoS ConfinementX 203 (2012).
- [90] G. Agakishiev *et al.*, Phys. Rev. Lett. **108**, 072302 (2012).
- [91] C. Albajar *et al.*, Nucl. Phys. B **335**, 261-287 (1990).
- [92] P. Avery, "Combining Measurements with Correlated Errors", CBX 95-55 (1996).
- [93] D. Beavis, *et al.*, The STAR Heavy Flavor Tracker Technical Design Report, <https://drupal.star.bnl.gov/STAR/starnotes/public/sn0600> (2011).
- [94] L. Ruan *et al.*, J. Phys. G Nucl. Part. Phys. **36**, 095001 (2009).

Published Papers

Following pages contain full texts of published papers.

Measurements of D^0 and D^* production in $p + p$ collisions at $\sqrt{s} = 200$ GeV

L. Adamczyk,¹ G. Agakishiev,¹⁹ M. M. Aggarwal,³⁰ Z. Ahammed,⁴⁹ A. V. Alakhverdyants,¹⁹ I. Alekseev,¹⁷ J. Alford,²⁰ B. D. Anderson,²⁰ C. D. Anson,²⁸ D. Arkhipkin,³ E. Aschenauer,³ G. S. Averichev,¹⁹ J. Balewski,²⁴ A. Banerjee,⁴⁹ Z. Barnovska,¹² D. R. Beavis,³ R. Bellwied,⁴⁵ M. J. Betancourt,²⁴ R. R. Betts,⁹ A. Bhasin,¹⁸ A. K. Bhati,³⁰ H. Bichsel,⁵¹ J. Bielcik,¹¹ J. Bielcikova,¹² L. C. Bland,³ I. G. Bordyuzhin,¹⁷ W. Borowski,⁴² J. Bouchet,²⁰ A. V. Brandin,²⁷ S. G. Brovko,⁵ E. Bruna,⁵³ S. Bueltmann,²⁹ I. Bunzarov,¹⁹ T. P. Burton,³ J. Butterworth,³⁷ X. Z. Cai,⁴¹ H. Caines,⁵³ M. Calderón de la Barca Sánchez,⁵ D. Cebra,⁵ R. Cendejas,⁶ M. C. Cervantes,⁴³ P. Chaloupka,¹² S. Chattopadhyay,⁴⁹ H. F. Chen,³⁹ J. H. Chen,⁴¹ J. Y. Chen,⁸ L. Chen,⁸ J. Cheng,⁴⁶ M. Cherney,¹⁰ A. Chikanian,⁵³ W. Christie,³ P. Chung,¹² J. Chwastowski,⁴³ M. J. M. Coddington,⁴³ R. Corliss,²⁴ J. G. Cramer,⁵¹ H. J. Crawford,⁴ X. Cui,³⁹ A. Davila Leyva,⁴⁴ L. C. De Silva,⁴⁵ R. R. Debbé,³ T. G. Dedovich,¹⁹ J. Deng,⁴⁰ R. Derradi de Souza,⁷ S. Dhamija,¹⁶ L. Didenko,³ F. Ding,⁵ A. Dion,³ P. Djawotho,⁴³ X. Dong,²³ J. L. Drachenberg,⁴³ J. E. Draper,⁵ C. M. Du,²² L. E. Dunkelberger,⁶ J. C. Dunlop,³ L. G. Efimov,¹⁹ M. Elnimr,⁵² J. Engelage,⁴ G. Eppley,³⁷ L. Eun,²³ O. Evdokimov,⁹ R. Fatemi,²¹ S. Fazio,³ J. Fedorisin,¹⁹ R. G. Fersch,²¹ P. Filip,¹⁹ E. Finch,⁵³ Y. Fisyak,³ C. A. Gagliardi,⁴³ D. R. Gangadharan,²⁸ F. Geurts,³⁷ S. Gliske,² Y. N. Gorbunov,¹⁰ O. G. Grebenyuk,²³ D. Grosnick,⁴⁸ S. Gupta,¹⁸ W. Guryn,³ B. Haag,⁵ O. Hajkova,¹¹ A. Hamed,⁴³ L.-X. Han,⁴¹ J. W. Harris,⁵³ J. P. Hays-Wehle,²⁴ S. Heppelmann,³² A. Hirsch,³⁴ G. W. Hoffmann,⁴⁴ D. J. Hofman,⁹ S. Horvat,⁵³ B. Huang,³ H. Z. Huang,⁶ P. Huck,⁸ T. J. Humanic,²⁸ L. Huo,⁴³ G. Igo,⁶ W. W. Jacobs,¹⁶ C. Jena,¹⁴ J. Joseph,²⁰ E. G. Judd,⁴ S. Kabana,⁴² K. Kang,⁴⁶ J. Kapitan,¹² K. Kauder,⁹ H. W. Ke,⁸ D. Keane,²⁰ A. Kechechyan,¹⁹ A. Kesich,⁵ D. Kettler,⁵¹ D. P. Kikola,³⁴ J. Kiryluk,²³ A. Kisiel,⁵⁰ V. Kizka,¹⁹ S. R. Klein,²³ D. D. Koetke,⁴⁸ T. Kollegger,¹³ J. Konzer,³⁴ I. Koralt,²⁹ L. Koroleva,¹⁷ W. Korsch,²¹ L. Kotchenda,²⁷ P. Kravtsov,²⁷ K. Krueger,² L. Kumar,²⁰ M. A. C. Lamont,³ J. M. Landgraf,³ S. LaPointe,⁵² J. Lauret,³ A. Lebedev,³ R. Lednický,¹⁹ J. H. Lee,³ W. Leight,²⁴ M. J. LeVine,³ C. Li,³⁹ L. Li,⁴⁴ W. Li,⁴¹ X. Li,³⁴ X. Li,⁴⁰ Y. Li,⁴⁶ Z. M. Li,⁸ L. M. Lima,³⁸ M. A. Lisa,²⁸ F. Liu,⁸ T. Ljubicic,³ W. J. Llope,³⁷ R. S. Longacre,³ Y. Lu,³⁹ X. Luo,⁸ A. Luszczak,⁴¹ G. L. Ma,⁴¹ Y. G. Ma,⁴¹ D. M. M. D. Madagadgettige Don,¹⁰ D. P. Mahapatra,¹⁴ R. Majka,⁵³ O. I. Mall,⁵ S. Margetis,²⁰ C. Markert,⁴⁴ H. Masui,²³ H. S. Matis,²³ D. McDonald,³⁷ T. S. McShane,¹⁰ S. Mioduszewski,⁴³ M. K. Mitrovski,³ Y. Mohammed,⁴³ B. Mohanty,⁴⁹ B. Morozov,¹⁷ M. G. Munhoz,³⁸ M. K. Mustafa,³⁴ M. Naglis,²³ B. K. Nandi,¹⁵ Md. Nasim,⁴⁹ T. K. Nayak,⁴⁹ L. V. Nogach,³³ J. Novak,²⁶ G. Odyniec,²³ A. Ogawa,³ K. Oh,³⁵ A. Ohlson,⁵³ V. Okorokov,²⁷ E. W. Oldag,⁴⁴ R. A. N. Oliveira,³⁸ D. Olson,²³ P. Ostrowski,⁵⁰ M. Pachr,¹¹ B. S. Page,¹⁶ S. K. Pal,⁴⁹ Y. X. Pan,⁶ Y. Pandit,²⁰ Y. Panebratsev,¹⁹ T. Pawlak,⁵⁰ B. Pawlik,³¹ H. Pei,⁹ C. Perkins,⁴ W. Peryt,⁵⁰ P. Pile,³ M. Planinic,⁵⁴ J. Pluta,⁵⁰ D. Plyku,²⁹ N. Poljak,⁵⁴ J. Porter,²³ A. M. Poskanzer,²³ C. B. Powell,²³ D. Prindle,⁵¹ C. Pruneau,⁵² N. K. Pruthi,³⁰ M. Przybycien,¹ P. R. Pujahari,¹⁵ J. Putschke,⁵² H. Qiu,²³ R. Raniwala,³⁶ S. Raniwala,³⁶ R. L. Ray,⁴⁴ R. Redwine,²⁴ R. Reed,⁵ C. K. Riley,⁵³ H. G. Ritter,²³ J. B. Roberts,³⁷ O. V. Rogachevskiy,¹⁹ J. L. Romero,⁵ J. F. Ross,¹⁰ L. Ruan,³ J. Rusnak,¹² N. R. Sahoo,⁴⁹ I. Sakrejda,²³ S. Salur,²³ A. Sandacz,⁵⁰ J. Sandweiss,⁵³ E. Sangaline,⁵ A. Sarkar,¹⁵ J. Schambach,⁴⁴ R. P. Scharenberg,³⁴ A. M. Schmah,²³ B. Schmidke,³ N. Schmitz,²⁵ T. R. Schuster,¹³ J. Seele,²⁴ J. Seger,¹⁰ P. Seyboth,²⁵ N. Shah,⁶ E. Shahaliev,¹⁹ M. Shao,³⁹ B. Sharma,³⁰ M. Sharma,⁵² S. S. Shi,⁸ Q. Y. Shou,⁴¹ E. P. Sichtermann,²³ R. N. Singaraju,⁴⁹ M. J. Skoby,³⁴ D. Smirnov,³ N. Smirnov,⁵³ D. Solanki,³⁶ P. Sorensen,³ U. G. deSouza,³⁸ H. M. Spinka,² B. Srivastava,³⁴ T. D. S. Stanislaus,⁴⁸ S. G. Steadman,²⁴ J. R. Stevens,¹⁶ R. Stock,¹³ M. Strikhanov,²⁷ B. Stringfellow,³⁴ A. A. P. Suaide,³⁸ M. C. Suarez,⁹ M. Sumner,¹² X. M. Sun,²³ Y. Sun,³⁹ Z. Sun,²² B. Surrow,²⁴ D. N. Svirida,¹⁷ T. J. M. Symons,²³ A. Szanto de Toledo,³⁸ J. Takahashi,⁷ A. H. Tang,³ Z. Tang,³⁹ L. H. Tarini,⁵² T. Tarnowsky,²⁶ D. Thein,⁴⁴ J. H. Thomas,²³ J. Tian,⁴¹ A. R. Timmins,⁴⁵ D. Tlusty,¹² M. Tokarev,¹⁹ T. A. Trainor,⁵¹ S. Trentalange,⁶ R. E. Tribble,⁴³ P. Tribedy,⁴⁹ B. A. Trzeciak,⁵⁰ O. D. Tsai,⁶ J. Turnau,³¹ T. Ullrich,³ D. G. Underwood,² G. Van Buren,³ G. van Nieuwenhuizen,²⁴ J. A. Vanfossen, Jr.,²⁰ R. Varma,¹⁵ G. M. S. Vasconcelos,⁷ F. Videbæk,³ Y. P. Viyogi,⁴⁹ S. Vokal,¹⁹ S. A. Voloshin,⁵² A. Vossen,¹⁶ M. Wada,⁴⁴ F. Wang,³⁴ G. Wang,⁶ H. Wang,²⁶ J. S. Wang,²² Q. Wang,³⁴ X. L. Wang,³⁹ Y. Wang,⁴⁶ G. Webb,²¹ J. C. Webb,³ G. D. Westfall,²⁶ C. Whitten, Jr.,^{6,*} H. Wieman,²³ S. W. Wissink,¹⁶ R. Witt,⁴⁷ W. Witzke,²¹ Y. F. Wu,⁸ Z. Xiao,⁴⁶ W. Xie,³⁴ K. Xin,³⁷ H. Xu,²² N. Xu,²³ Q. H. Xu,⁴⁰ W. Xu,⁶ Y. Xu,³⁹ Z. Xu,³ L. Xue,⁴¹ Y. Yang,²² Y. Yang,⁸ P. Yepes,³⁷ Y. Yi,³⁴ K. Yip,³ I.-K. Yoo,³⁵ M. Zawisza,⁵⁰ H. Zbroszczyk,⁵⁰ J. B. Zhang,⁸ S. Zhang,⁴¹ W. M. Zhang,²⁰ X. P. Zhang,⁴⁶ Y. Zhang,³⁹ Z. P. Zhang,³⁹ F. Zhao,⁶ J. Zhao,⁴¹ C. Zhong,⁴¹ X. Zhu,⁴⁶ Y. H. Zhu,⁴¹ and Y. Zoukarnieva¹⁹

(STAR Collaboration)

¹AGH University of Science and Technology, Cracow, Poland²Argonne National Laboratory, Argonne, Illinois 60439, USA

- ³Brookhaven National Laboratory, Upton, New York 11973, USA
- ⁴University of California, Berkeley, California 94720, USA
- ⁵University of California, Davis, California 95616, USA
- ⁶University of California, Los Angeles, California 90095, USA
- ⁷Universidade Estadual de Campinas, Sao Paulo, Brazil
- ⁸Central China Normal University (HZNU), Wuhan 430079, China
- ⁹University of Illinois at Chicago, Chicago, Illinois 60607, USA
- ¹⁰Creighton University, Omaha, Nebraska 68178, USA
- ¹¹Czech Technical University in Prague, FNSPE, Prague, 115 19, Czech Republic
- ¹²Nuclear Physics Institute AS CR, 250 68 Řež/Prague, Czech Republic
- ¹³University of Frankfurt, Frankfurt, Germany
- ¹⁴Institute of Physics, Bhubaneswar 751005, India
- ¹⁵Indian Institute of Technology, Mumbai, India
- ¹⁶Indiana University, Bloomington, Indiana 47408, USA
- ¹⁷Alikhanov Institute for Theoretical and Experimental Physics, Moscow, Russia
- ¹⁸University of Jammu, Jammu 180001, India
- ¹⁹Joint Institute for Nuclear Research, Dubna, 141 980, Russia
- ²⁰Kent State University, Kent, Ohio 44242, USA
- ²¹University of Kentucky, Lexington, Kentucky, 40506-0055, USA
- ²²Institute of Modern Physics, Lanzhou, China
- ²³Lawrence Berkeley National Laboratory, Berkeley, California 94720, USA
- ²⁴Massachusetts Institute of Technology, Cambridge, Massachusetts 02139-4307, USA
- ²⁵Max-Planck-Institut für Physik, Munich, Germany
- ²⁶Michigan State University, East Lansing, Michigan 48824, USA
- ²⁷Moscow Engineering Physics Institute, Moscow, Russia
- ²⁸Ohio State University, Columbus, Ohio 43210, USA
- ²⁹Old Dominion University, Norfolk, Virginia, 23529, USA
- ³⁰Panjab University, Chandigarh 160014, India
- ³¹Institute of Nuclear Physics PAS, Cracow, Poland
- ³²Pennsylvania State University, University Park, Pennsylvania 16802, USA
- ³³Institute of High Energy Physics, Protvino, Russia
- ³⁴Purdue University, West Lafayette, Indiana 47907, USA
- ³⁵Pusan National University, Pusan, Republic of Korea
- ³⁶University of Rajasthan, Jaipur 302004, India
- ³⁷Rice University, Houston, Texas 77251, USA
- ³⁸Universidade de Sao Paulo, Sao Paulo, Brazil
- ³⁹University of Science and Technology of China, Hefei 230026, China
- ⁴⁰Shandong University, Jinan, Shandong 250100, China
- ⁴¹Shanghai Institute of Applied Physics, Shanghai 201800, China
- ⁴²SUBATECH, Nantes, France
- ⁴³Texas A&M University, College Station, Texas 77843, USA
- ⁴⁴University of Texas, Austin, Texas 78712, USA
- ⁴⁵University of Houston, Houston, Texas, 77204, USA
- ⁴⁶Tsinghua University, Beijing 100084, China
- ⁴⁷United States Naval Academy, Annapolis, Maryland 21402, USA
- ⁴⁸Valparaiso University, Valparaiso, Indiana 46383, USA
- ⁴⁹Variable Energy Cyclotron Centre, Kolkata 700064, India
- ⁵⁰Warsaw University of Technology, Warsaw, Poland
- ⁵¹University of Washington, Seattle, Washington 98195, USA
- ⁵²Wayne State University, Detroit, Michigan 48201, USA
- ⁵³Yale University, New Haven, Connecticut 06520, USA
- ⁵⁴University of Zagreb, Zagreb, HR-10002, Croatia

(Received 19 April 2012; revised manuscript received 15 October 2012; published 31 October 2012)

We report measurements of charmed-hadron (D^0 , D^{*+}) production cross sections at midrapidity in $p + p$ collisions at a center-of-mass energy of 200 GeV by the STAR experiment. Charmed hadrons were reconstructed via the hadronic decays $D^0 \rightarrow K^- \pi^+$, $D^{*+} \rightarrow D^0 \pi^+ \rightarrow K^- \pi^+ \pi^+$ and their charge conjugates, covering the p_T range of 0.6–2.0 and 2.0–6.0 GeV/ c for D^0 and D^{*+} , respectively. From this analysis,

*Deceased.

the charm-pair production cross section at midrapidity is $d\sigma/dy|_{y=0}^{c\bar{c}} = 170 \pm 45(\text{stat})_{-59}^{+38}(\text{sys}) \mu\text{b}$. The extracted charm-pair cross section is compared to perturbative QCD calculations. The transverse momentum differential cross section is found to be consistent with the upper bound of a fixed-order next-to-leading logarithm calculation.

DOI: [10.1103/PhysRevD.86.072013](https://doi.org/10.1103/PhysRevD.86.072013)

PACS numbers: 25.75.-q, 25.75.Cj

I. INTRODUCTION

The primary goal of ultrarelativistic heavy-ion experiments at the Relativistic Heavy Ion Collider (RHIC) is to search for and characterize the new state of matter with partonic degrees of freedom, namely, the quark-gluon plasma, predicted by quantum chromodynamics (QCD) [1]. In high-energy collisions at RHIC, heavy quarks (c , b) are expected to be created from initial hard scatterings [2] and the relative changes in their masses are small by the strong interactions with the QCD medium [3]. Thus they carry clean information from the system at the early stage. The interaction between heavy quarks and the medium is sensitive to the medium dynamics; therefore, heavy quarks are suggested as an “ideal” probe to quantify the properties of the strongly interacting QCD matter [4–6]. Consequently, measurements of heavy-quark production over a wide transverse momentum (p_T) region in proton-proton ($p + p$) collisions are critical to provide a baseline for understanding the results from heavy-ion collisions. In particular, precise knowledge of the total charm production cross sections from $p + p$ to central heavy-ion collisions is critical to understand both open charm and charmonium production mechanisms in the quark-gluon plasma medium formed in central heavy-ion collisions at RHIC [7,8].

In elementary particle collisions, processes involving heavy quarks with masses much larger than the QCD scale (Λ_{QCD}) are, in principle, amenable to perturbative QCD (pQCD) calculations. For heavy-quark production cross sections at large momentum transfer Q^2 , fixed-order next-to-leading logarithm (FONLL) pQCD calculations, where $p_T \gg m_c$, are expected to work reasonably well [9]. However, calculations of the charm cross section at low p_T become complicated because charm quarks cannot be treated as a massless flavor. Furthermore, in the low momentum transfer region there is a large uncertainty in the gluon density function, and the strong coupling constant increases dramatically. Thus, perturbative QCD calculations have little predictive power for the total charm cross section in high-energy hadron-hadron collisions [10]. In view of these theoretical issues, experimental measurements become necessary and in turn provide constraints that improve theoretical calculations.

Measurements of inclusive charm production have been carried out through two main approaches: (i) single leptons from heavy-flavor semileptonic decays and (ii) charmed hadrons from hadronic decays. The advantages of the first method include an experimentally triggerable observable

and relatively large decay branching ratios, thus resulting in relatively large statistics. However, interpretations of the experimental results contain ambiguities because (a) leptons are produced by various charmed and bottomed hadron decays, and (b) heavy-flavor hadrons contributing to leptons at a certain p_T can come from a wide kinematic region due to the decay smearing. The second method suffers from a large combinatorial background when all particles from the collision vertex are included, without any reconstruction of the secondary weak-decay vertices. This background is particularly large (S/B is on the order of $1:10^3$) in heavy-ion collisions.

There are many measurements of the charm production cross section in low energy $p + p$ or $p + A$ collisions via both semileptonic and hadronic decays at CERN and Fermilab [11,12]. Results for the total charm cross sections (from measurements with reasonable extrapolations) are consistent with next-to-leading-order pQCD calculations. At high energies, the Collider Detector at Fermilab (CDF) Collaboration at the Tevatron measured the charmed-hadron cross sections at $p_T > 5 \text{ GeV}/c$ in $p + \bar{p}$ collisions at $\sqrt{s} = 1.96 \text{ TeV}$, and results for D^0 , D^+ and D^{*+} mesons are consistent with the upper bounds of FONLL pQCD calculations [13]. At RHIC energies, charm production has been studied mainly via semileptonic decay electrons from $p + p$ to Au + Au collisions [14–18]. The result from $p + p$ collisions is also consistent with the upper bound of FONLL pQCD calculations at $p_T(e) > 2 \text{ GeV}/c$. Measurements of the D^0 cross section by the reconstruction of hadronic decays were carried out in $d + \text{Au}$ collisions [14], but no measurement of the charmed-hadron production cross section in $p + p$ collisions has been made at RHIC until now.

In this paper, we report measurements from the STAR experiment of the charmed-hadron (D^0 , D^*) production cross section at midrapidity in $p + p$ collisions at $\sqrt{s} = 200 \text{ GeV}$. Charmed hadrons, D^0 and D^* , were reconstructed via hadronic decays in the transverse momentum ranges of 0.6–2.0 and 2–6 GeV/c , respectively. The p_T differential production cross sections are compared to pQCD theoretical calculations, and a total charm cross section is extracted.

The paper is organized as follows: Section II describes the experimental setup, the data set, and the particle-identification method used in this analysis. Section III explains the hadronic reconstruction for D^0 and D^* mesons in detail. Section IV discusses the reconstruction efficiency, acceptance, and trigger and vertex corrections.

Details of the systematic uncertainties are discussed in Sec. V. The transverse momentum differential production cross section is presented in Sec. VI and it is compared with pQCD FONLL and PYTHIA [19] calculations. The results are summarized in Sec. VII.

II. EXPERIMENTAL SETUP

A. Detector apparatus

The data used in this analysis were recorded by the Solenoidal Tracker at RHIC (STAR) detector [20]. The STAR detector is a multipurpose spectrometer with large rapidity coverage. The major subsystems at midrapidity sit inside a solenoidal magnet which provides a uniform magnetic field of 0.5 T along the beam axis. Subsystems used in this analysis are the time projection chamber (TPC) [21], the time-of-flight (TOF) detector [22], the barrel and end cap electromagnetic calorimeters [23,24], and two trigger detector subsystems: the vertex position detector (VPD) [25] and the beam beam counters (BBCs) [26].

The TPC is the main tracking detector, covering the full azimuthal angle at pseudorapidity $|\eta| < 1$ for tracks crossing all 45 padrows [21]. It measures the charged-particle momenta and provides particle-identification (PID) capability via the ionization energy loss (dE/dx) in the TPC gas, allowing a clean separation between charged kaons and pions up to momentum $p \sim 0.6$ GeV/ c . The barrel TOF detector is a newly installed subsystem, utilizing the multigap resistive plate chamber technology [22]. The full system consists of 120 trays covering the full azimuth at $|\eta| < 0.9$ surrounding the TPC cylinder. In the year 2009 run, 84 trays out of 120 for the full barrel were installed and used for this analysis. The TOF detector uses the timing recorded in the forward VPD as the start time to calculate the particle time of flight, which is combined with the momentum from the TPC to identify particles. The timing resolution of the TOF system, including the start timing resolution in $\sqrt{s} = 200$ GeV $p + p$ collisions, is about 110 ps, allowing separation of K and π up to $p \sim 1.5$ GeV/ c . The barrel and end cap electromagnetic calorimeters are designed to identify electrons and photons, covering the full azimuthal angle at $|\eta| < 1$ and $1 < \eta < 2$, respectively [23,24]. They are fast-response detectors (< 100 ns) and were used to suppress the TPC pileup-track contribution in the event-vertex finder by matching with charged tracks from the TPC.

In addition to providing the start time for the barrel TOF detector, the VPD is also one of the trigger detectors in STAR. It has two parts surrounding the beam pipe, located on the east and west sides, 5.7 m away from the center of the STAR detector and covering $4.24 < |\eta| < 5.1$ [25]. The minimum-bias trigger was defined as a coincidence signal in the east and west VPDs and a selection was made on the vertex position along the beam axis (V_z) to be within 40 cm of the center of the STAR detector. The BBC [26] consists of two identical counters located on each side of

the TPC covering full azimuth and $2.1 < |\eta| < 5.0$ in pseudorapidity. Each part consists of a set of hexagonal scintillator tiles grouped into a ring and mounted around the beam pipe at a distance of 3.7 m from the center of STAR. The BBC detector had been used to define the main minimum-bias trigger in $p + p$ collisions before the minimum-bias trigger was used in 2009. A small sample of BBC minimum-bias-triggered events were collected in 2009 to check for a trigger bias. Details of the minimum-bias trigger bias and correction will be discussed in Sec. IV.

B. Data sets and event selection

The data sample used in this analysis consisted of minimum-bias-triggered $p + p$ collisions at $\sqrt{s} = 200$ GeV, recorded in 2009 by the STAR experiment at RHIC.

The intrinsic drift time for electrons from the center to one end of the TPC is on the order of 40 μ s. Thus, in high-luminosity $p + p$ collisions, one TPC event usually contains tracks from collisions originating from nontriggered bunch crossings. These “pileup events” will lead to additional tracks recorded in the TPC, in addition to those from the triggered event. This effect was not significant in previous RHIC runs, but the increase in the collision rate during 2009 to several hundred kilohertz made this a significant effect. The V_z position from offline VPD data has a resolution of 2.5 cm for minimum-bias events, which can provide a useful constraint to select the real event that fired the trigger. Figure 1, upper panel, shows the correlation between the V_z positions from the TPC and the VPD. Events with TPC vertices along the diagonal correlated band are real ones that fired the VPD minimum-bias trigger. In Fig. 1, bottom panel, the solid black histogram shows the 1D V_z difference between the first TPC-determined vertex position and VPD-determined vertex position. By applying a V_z difference cut $|\Delta V_z| < 6$ cm, most of the TPC pileup events can be removed. There still remain random associated correlations that enter into this cut window ($\sim 7\%$ level, calculated using a two-Gaussian fit). To further suppress this contamination, we required the TPC event vertices to have at least two tracks that match with hits in the barrel and end cap electromagnetic calorimeters (this vertex is treated as a “good” vertex). The red dashed histogram in Fig. 1, bottom panel, shows the ΔV_z distribution after this selection. The random associated pileup events in the V_z difference cut window are now suppressed to $\sim 2\%$ of the total, while the corresponding loss of real events is $\sim 15\%$. In total, 105×10^6 minimum-bias events were used in the charmed-hadron analysis.

C. Track reconstruction and particle identification

Charged-particle tracks are required to point within $|\eta| < 1$ in order minimize TPC acceptance effects during reconstruction. Tracks must have 15 out of a maximum of 45 points used in track fitting (nFitPts) and at least 52% of

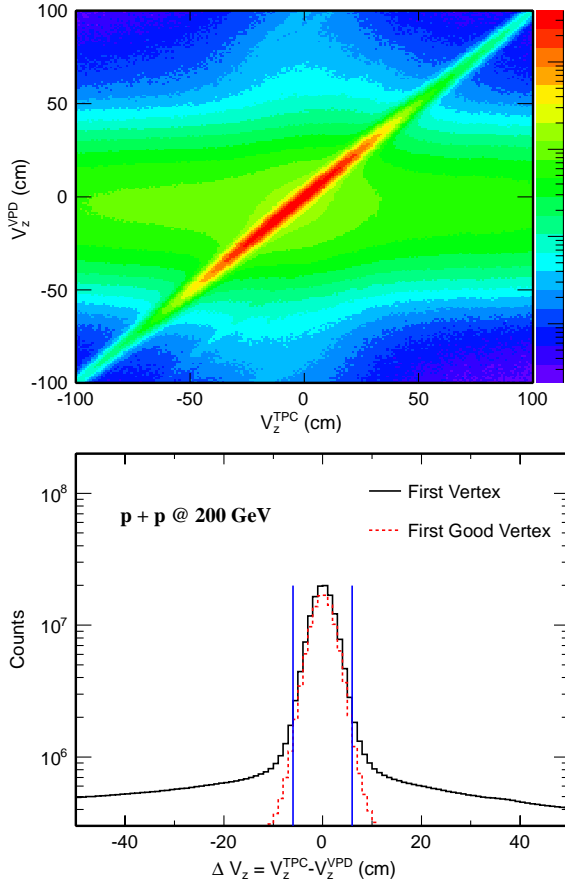


FIG. 1 (color online). Upper panel: Correlation of V_z^{TPC} versus V_z^{VPD} . Bottom panel: ΔV_z distributions. A good vertex requirement rejects most of the pileup events. Blue vertical lines indicate the cuts for the V_z selection.

the total possible fit points in order to avoid double-counting split tracks. Tracks are required to have a distance-of-closest-approach (DCA) to the collision vertex of less than 2 cm to suppress background tracks produced by secondary scattering in the detector and also long-lived particle decays. The STAR track pointing resolution with the TPC alone does not have the precision to separate charm secondary decay vertices from the collision vertices.

Particle identification for final-state charged hadrons was carried out with a combination of dE/dx in the TPC and the particle velocity (β) measurement from the barrel TOF detector. Thus the normalized dE/dx ($n\sigma_X^{dE/dx}$) and $1/\beta$ ($n\sigma_X^{\text{TOF}}$) distributions were used to select daughter particle candidates. They are defined as follows:

$$n\sigma_X^{dE/dx} = \frac{\ln \left(\frac{\langle dE/dx \rangle^{\text{mea}}}{dE/dx_X^{\text{th}}} \right)}{R_{dE/dx}}, \quad (1)$$

$$n\sigma_X^{\text{TOF}} = \frac{\frac{1}{\beta^{\text{mea}}} - \frac{1}{\beta_X^{\text{th}}}}{R_{1/\beta}}, \quad (2)$$

where the superscripts “mea” and “th” are measured and theoretical values, respectively. The X denotes expected

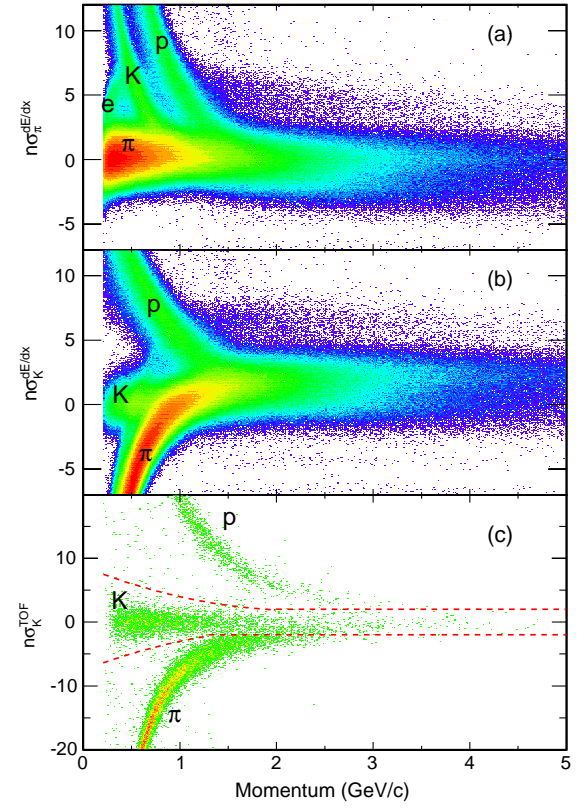


FIG. 2 (color online). Distributions of $n\sigma_\pi^{dE/dx}$, $n\sigma_K^{dE/dx}$, and $n\sigma_K^{\text{TOF}}$ versus momentum are shown in panels (a), (b), and (c), respectively. The latter is shown after dE/dx cuts were applied.

values which are calculated with respect to one kind of particle species (π or K). $R_{dE/dx}$ and $R_{1/\beta}$ are the experimental dE/dx and $1/\beta$ resolutions, respectively. With the above definitions, the two resulting distributions can be approximated by Gaussian distributions with mean ~ 0 and $\sigma \sim 1$. Figure 2 shows the $n\sigma_K^{dE/dx}$, $n\sigma_\pi^{dE/dx}$, and $n\sigma_K^{\text{TOF}}$ distributions versus particle momentum.

Daughter kaon (pion) candidates are selected by requiring $|n\sigma_K^{dE/dx}| < 2$ ($|n\sigma_\pi^{dE/dx}| < 2$). In addition, to improve the significance of the reconstructed D^0 signal, the kaon daughter tracks were required to have a valid hit in the TOF detector and then selected with a TOF PID cut, which is denoted as the red dashed lines in Fig. 2(c). In order to have good efficiency and considering pion identification is good enough with dE/dx only, we did not require pion to match with TOF.

III. CHARMED-HADRON RECONSTRUCTION AND RAW YIELD EXTRACTION

A. D^0 Reconstruction

D^0 and \bar{D}^0 mesons were reconstructed via the hadronic decay $D^0(\bar{D}^0) \rightarrow K^\pm \pi^\mp$ with a branching ratio of 3.89%. The analysis technique is the same as that used for a D^0 analysis in $d + \text{Au}$ collisions [14]. In $p + p$ collisions, the

mixed-events technique is not suitable for describing the background due to the large contribution of correlated jets. Therefore, two different techniques were used to reproduce the background: the like-sign and track-rotation methods. Since the π^- and π^+ production is symmetric in the STAR uniform acceptance and their yield ratio is measured to be 0.988 ± 0.043 [27], the like-sign (LS) method is used and a pair combination with the same charged sign is expected to reproduce the background without the signal correlation. The opposite-sign backgrounds, which go into the residual background, are only several percent of the total background and will be discussed later. The track-rotation (Rot) technique has been used in many measurements [28]. This method is based on the assumption that by rotating the daughter kaon track by 180° in azimuth, the decay kinematics are destroyed. Thus the invariant mass distribution after rotation is able to reproduce the random combinatorial background. Figure 3 shows the invariant mass distributions of $K\pi$ candidates. Figure 3(a) shows the invariant mass distributions for $K\pi$ pairs [$0.6 < p_T(K\pi) < 2.0$ GeV/c] with unlike sign (US) before background subtraction, with like sign, and with rotated kaon momentum. The distributions from the like-sign and track-rotation techniques describe the background well. Figure 3(b) is the unlike-sign $K\pi$ invariant mass distribution after combinatorial background subtraction. A significant $K^*(892)$ peak is observed. The secondary small peak at about 1.4 GeV/c² is the $K_2^*(1430)$. A direct zoom-in view of the vicinity around the D^0 mass region is shown in Fig. 4 [panel (a) for subtraction of like-sign background, and panel (b) for the rotational case]. Solid symbols depict the same distributions as shown in Figs. 3 and 5 in two different D^0 p_T bins. One can see there is still some “residual” background after like-sign or rotational background subtraction. The possible sources to the residual background have been investigated using PYTHIA simulations. We performed the same reconstruction as we did on the data, for the foreground and background distributions.

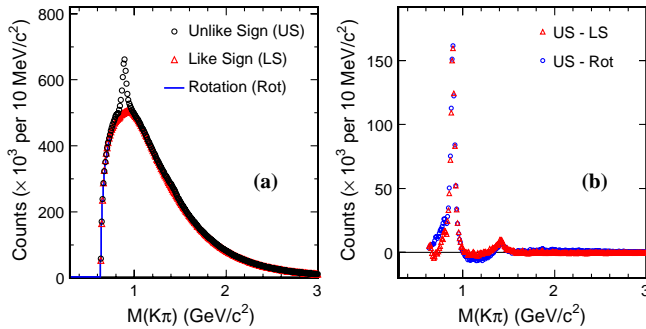


FIG. 3 (color online). (a) Invariant mass distributions of raw $K\pi$ combinations for unlike-sign pairs (circles), like-sign pairs (triangles), and kaon momentum rotated pairs (line). (b) Residual distributions after subtracting the like-sign distribution (triangles) and rotation pair distribution (dots) from the unlike-sign distribution.

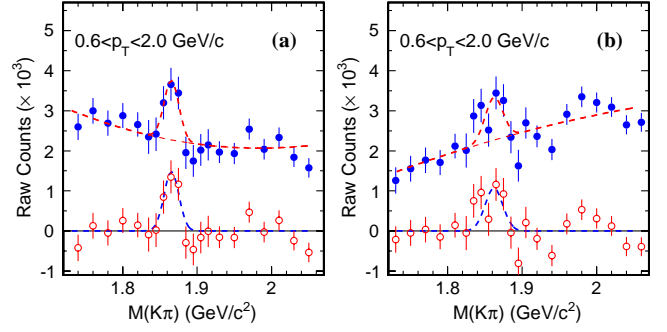


FIG. 4 (color online). Invariant $K\pi$ mass distributions in the D^0 mass region after like-sign (a) and track-rotation (b) background subtraction. Solid circles show the signal and a residual background. A Gaussian function and a second-order polynomial function were used to describe the signal and residual background, respectively. Open circles show the signal after residual background subtraction.

From these simulations, we have learned that the possible sources that can contribute to this residual correlated background include: correlated hadron pairs from decays (mostly resonances) where the real daughters were misidentified as $K\pi$ pairs; $K\pi$ pair from other decay channels of D^0 (e.g. $K^- \pi^+ \pi^0$) where the other daughters are missed in the reconstruction; same-charge $K^- \pi^-$ pairs from multibody decays of $D^0 \rightarrow K^- \pi^+ \pi^+ \pi^-$; $K\pi$ pairs from jet fragmentations; etc. The different shape of the residual background from LS and Rot background subtraction in the data can be qualitatively reproduced by PYTHIA simulation. The magnitude of the residual background depends

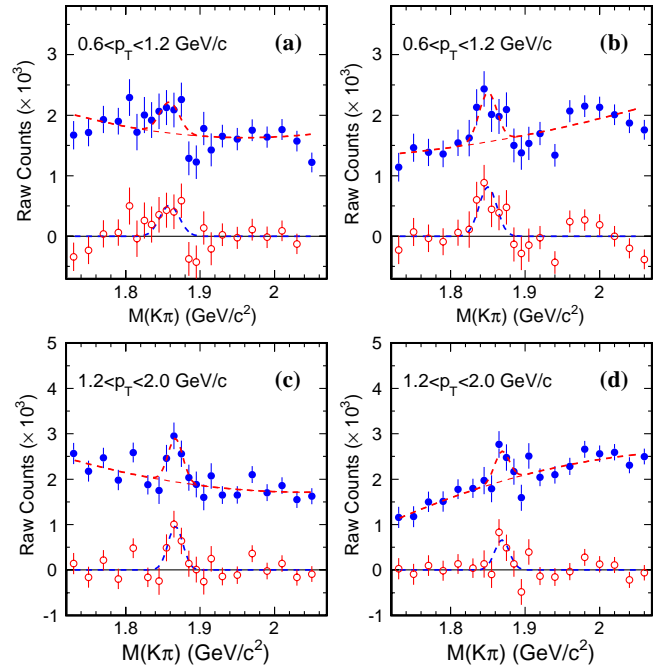


FIG. 5 (color online). Raw D^0 signals in different p_T bins after like-sign (a),(c) and track-rotation (b),(d) subtraction.

TABLE I. D^0 raw yields.

p_T range (GeV/c)	0.6–1.2	1.2–2
p_T (GeV/c)	0.908	1.57
Raw yields $\times 10^3$ (Rot)	2.45 ± 0.66	1.65 ± 0.63
Raw yields $\times 10^3$ (LS)	1.67 ± 0.74	2.40 ± 0.64

on how to choose the normalization for the like-sign or rotational background, as qualitatively understood from the PYTHIA simulations. However, the change of the residual background magnitude due to different normalizations has a very small impact on the final extracted signal counts, and it has been included in the systematic uncertainties. We used an empirical polynomial function to describe it and the choice of this empirical function was also included as one of the systematic source to the raw yields. A Gaussian function is used to fit the signal. The raw yield of the D^0 is obtained by fitting the data (blue solid circles) with a fit function representing the sum of signal and background (red dashed curve) in the mass region of $1.72 < M_{K\pi} < 2.05 \text{ GeV}/c^2$. The signal after the residual background subtraction is shown as the red open circles. The Gaussian function used to describe the signal is shown as the blue dashed curve. The total D^0 signal consists of 4085 ± 938 counts.

The signals after background subtraction for two p_T bins are shown in Fig. 5. Panels (a), (c) and (b), (d) show the signals from LS and Rot background subtraction, respectively. The D^0 raw yields and statistical errors extracted from the two background methods are listed in Table I. The average values of the D^0 counts from the LS and Rot background methods are used to calculate the final D^0 raw yield in each p_T bin. The mean and width from the Gaussian fits are compared with Monte Carlo (MC) simulation in Fig. 6 (left panels). The single D^0 and D^* are embedded into the real data and simulated in the full STAR GEANT reconstruction chain, taking into account detector response and material effect. The D^0 signal mean value from an open-parameter fit shifts to lower mass due to kaon energy loss at low p_T , which is not fully accounted in the simulation due to possibly missing material budget. The systematic uncertainty in determining the D^0 raw yields as well as the potential double-counting issue due to particle misidentification will be discussed in Sec. VA.

B. D^* Reconstruction

$D^{*\pm}$ mesons were reconstructed via the decay sequence $D^{*+} \rightarrow D^0 \pi^+$ (BR = 67.7%), $D^0 \rightarrow K^- \pi^+$ and its charge conjugate. We followed the same analysis technique as described in Ref. [29]. The daughter particles were still identified by dE/dx in the TPC because (a) most of the D^* decay daughter particles that fall inside the STAR acceptance with higher momenta are located in the region where the TOF PID improvement is very limited and (b) the

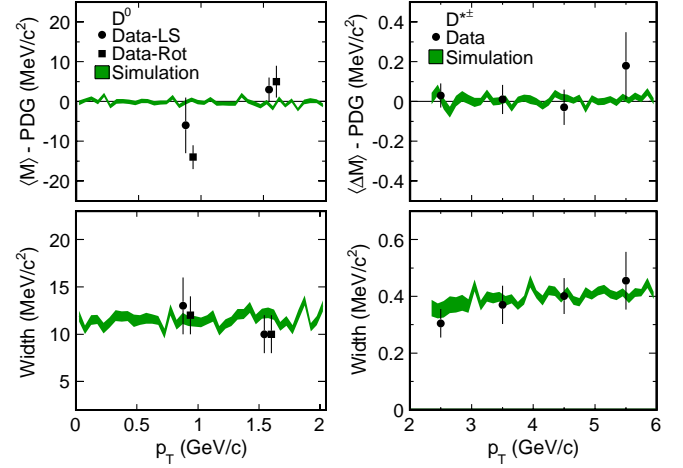


FIG. 6 (color online). The mean and width from Gaussian fit to data (symbols) compared with MC simulations (bands) for D^0 and D^* are shown in left and right panels, respectively.

signal suffers significant losses due to incomplete TOF acceptance in 2009. Compared to the cuts used in Ref. [29], the p_T threshold cut for the π^+ (from D^* decays), denoted as π_s^+ , was lowered to $0.15 \text{ GeV}/c$. The ratio r of transverse momenta from the D^0 and π_s^+ was required to be $7 < r < 20$. These two changes were implemented to improve the statistics near the lower bound in p_T . The remainder of the analysis cuts were the same as those used in Ref. [29].

The invariant mass difference $\Delta M = M(K\pi\pi) - M(K\pi)$ was calculated in reconstructing the D^* signal to take advantage of the partial cancellation in the detector resolution in measured mass distributions. The ΔM distributions are shown in the upper panel of Fig. 7. The “right-sign” combinations $K^\mp \pi^\pm \pi_s^\pm$ were used to select the $D^{*\pm}$ candidates. Two independent methods—“wrong-sign” combinations $K^\pm \pi^\mp \pi_s^\pm$ and D^0 “sideband” combinations—were used for combinatorial background reconstruction. The plot illustrates that both methods reproduce the combinatorial background very well. The events displayed in this figure are all minimum-bias events without event-vertex selections, which demonstrates the significance of D^* signal. The lower panel in Fig. 7 shows the $K\pi$ invariant mass distribution after requiring the D^* candidate cut ($0.144 < \Delta M < 0.147 \text{ GeV}/c^2$). The cross-hatched area indicates D^0 candidate mass selection in the $K\pi\pi$ right-sign and wrong-sign combination reconstruction. The line-hatched area indicates the D^0 sideband region [$1.72 < M(K\pi)/(\text{GeV}/c^2) < 1.80$ or $1.92 < M(K\pi)/(\text{GeV}/c^2) < 2.00$] used in sideband combinatorial background reconstruction for D^* . The sideband combinatorial background was used to obtain the raw D^* yields for better statistics and also because sideband distributions do not suffer from the double-counting issue due to particle misidentification. The difference between the yields obtained from the sideband method and the

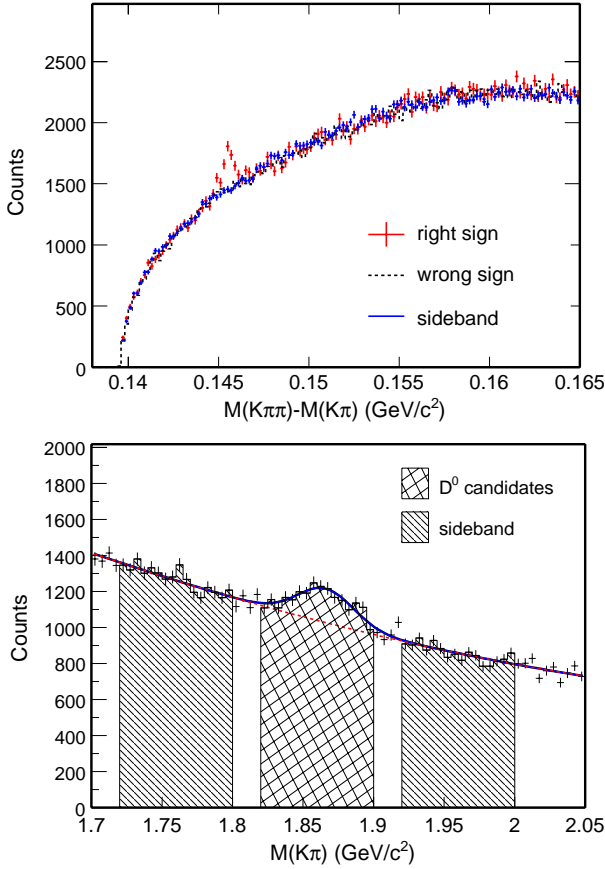


FIG. 7 (color online). Upper: Raw D^* candidate signal from the right-sign combinations in all $p + p$ minimum-bias events. Histograms are combinatorial background distributions from wrong-sign and sideband methods. Lower: Raw D^0 candidates after requiring the D^* candidate cut ($0.144 < \Delta M < 0.147 \text{ GeV}/c^2$).

wrong-sign method was included in the systematic uncertainties. Details in determining the uncertainties on the raw D^* yields including the double-counting effect will be discussed in Sec. VA. The D^* raw yields are summarized in Table II.

To obtain the cross section, the event-selection criteria described in the previous section were applied. The raw distributions were further divided into p_T slices to obtain the raw D^* yields in each p_T bin. Figure 8 shows the D^* candidates and background distributions in different p_T bins. The bottom panel on each plot was generated by subtracting the sideband background from the right-sign candidates. The mean and width from Gaussian fits are compared with MC simulation in the right panel of Fig. 6,

TABLE II. D^* raw yields.

p_T range (GeV/c)	2–3	3–4	4–5	5–6
p_T (GeV/c)	2.45	3.44	4.45	5.45
Raw yields	209 ± 58	98 ± 35	27 ± 11	12.3 ± 4.1

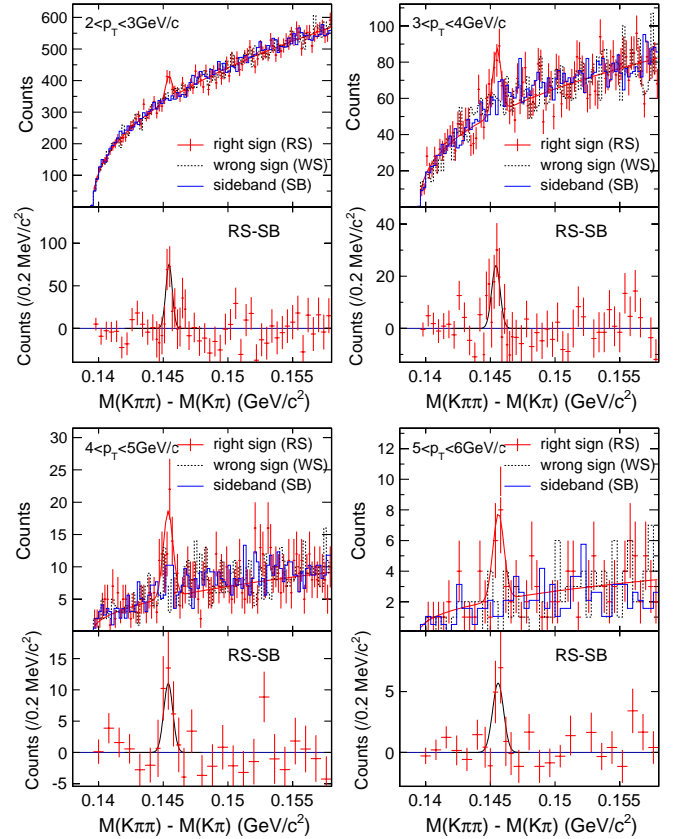


FIG. 8 (color online). Raw D^* signals in different p_T bins. In each plot, the bottom panel distribution is generated by subtracting the sideband background from the right-sign distribution. Variable binning is used in the bottom panel for better illustration.

and it shows the obtained D^* peak positions and widths agree with the MC simulation well. From this analysis, the total signal consisted of 364 ± 68 counts, and the raw yield ratio of D^{*-}/D^{*+} is 0.93 ± 0.37 .

IV. EFFICIENCY AND TRIGGER OR VERTEX BIAS CORRECTION

The final charmed-hadron cross section in $p + p$ collisions is calculated as follows:

$$E \frac{d^3\sigma}{dp^3} = \frac{1}{2\pi} \cdot \frac{1}{\epsilon_{\text{rec}}} \cdot \frac{1}{\text{BR}} \cdot \frac{\Delta N_D}{p_T \Delta p_T \Delta y} \cdot \frac{\sigma_{\text{NSD}}}{N_{\text{MB}}} \cdot f_{\text{trg, vtx}}, \quad (3)$$

where σ_{NSD} is the total nonsingly diffractive (NSD) cross section, which is measured at STAR to be $30.0 \pm 2.4 \text{ mb}$ [30]. N_{MB} is the total number of minimum-bias events used for the analysis. ΔN_D is the raw charmed-hadron signal in each p_T bin within a rapidity window Δy . BR is the hadronic decay branching ratio for the channel of interest. There are two correction factors: ϵ_{rec} , which is the reconstruction efficiency including geometric acceptance, track selection efficiency, PID efficiency, and analysis cut efficiency; and $f_{\text{trg, vtx}}(p_T)$, which is the correction factor to

account for the bias between the minimum-bias sample used in this analysis and the total NSD sample. This bias is mainly caused by the VPD trigger and event-vertex reconstruction, and it may have a dependence on the charmed-hadron p_T . In the following sections of the paper, the condition that requires the event to fire the VPD trigger and to have a good vertex will be referred to as the “analysis condition.”

A. Reconstruction efficiency

The reconstruction efficiency for charmed hadrons was obtained by embedding MC simulated charmed-hadron tracks into the real minimum-bias events. The MC charmed-hadron tracks were processed through a full GEANT detector simulation [31] with a representation of the 2009 STAR geometry. The raw detector-response signals were mixed together with those from the real data and processed through the full STAR offline reconstruction chain to obtain the detector-response efficiency in a realistic environment. The input MC track multiplicity was constrained to have negligible effect on the final tracking efficiency due to increased occupancy in the TPC.

Figures 9 and 10 show the D^0 and D^* reconstruction efficiency versus p_T within $|y| < 1$. In Fig. 9, the solid squares denote the reconstruction efficiency for both daughters selected and identified by the TPC, while the solid circles denote the reconstruction efficiency with additional PID selection from the TOF detector for the kaon daughter. The combined TOF efficiency, including the acceptance, matching between TPC tracks and TOF hits, and PID selection efficiency, is around 45% studied from the data in 2009.

B. Trigger and vertex bias corrections

The trigger and vertex bias corrections were studied by simulating PYTHIA events [19] processed through the full GEANT detector-response and offline reconstruction. The PYTHIA generator versions 6.205 and 6.416 were both used

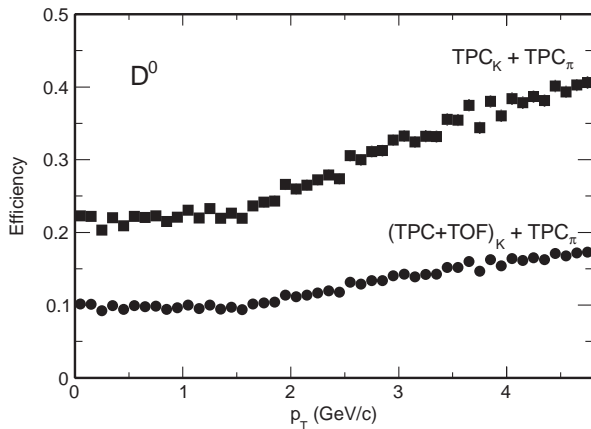


FIG. 9. Total D^0 reconstruction efficiency versus $D^0 p_T$.

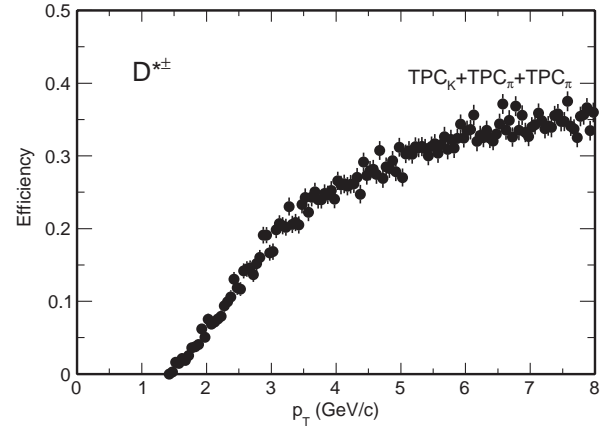


FIG. 10. Total D^* reconstruction efficiency versus $D^* p_T$.

in this study. We chose the PYTHIA version 6.205 with minimum-bias processes selected and with the CDF TUNEA settings [32] to give the centroid value of the correction factor because it gives better description for the particle production in the forward rapidities than the 6.416 version [33]. The differences between the two versions as well as different parameter settings have been included to estimate the systematic uncertainty of the trigger and vertex bias correction factor.

To validate the PYTHIA generator in simulating particle production in the forward region for the VPD trigger study, we first compared the VPD trigger efficiencies (from the BBC triggered minimum-bias sample) from MC simulation and real data. The BBC trigger has been well studied and was used to calculate the $p + p$ NSD cross section [16]. Figure 11 shows the comparison of the VPD trigger efficiency, with the requirement that there is a BBC trigger and a good vertex. The efficiency is studied as a function of the charged hadron p_T . The real data used are BBC triggered minimum-bias events taken in 2009 during a very low luminosity run, which minimizes TPC pileup tracks.

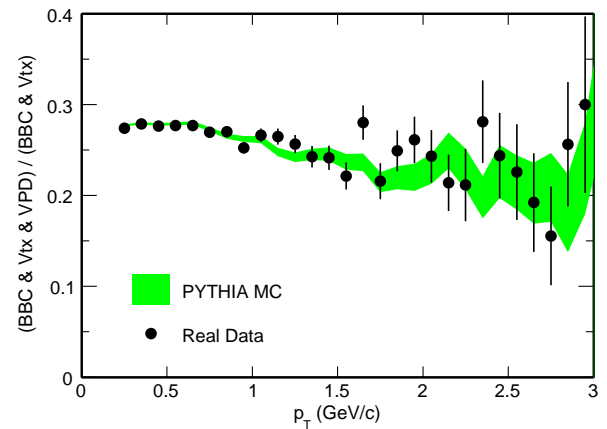


FIG. 11 (color online). VPD trigger efficiency comparison between data and Monte Carlo versus charged-particle p_T in BBC minimum-bias conditions.

Figure 11 shows that the efficiency goes down with increasing p_T of midrapidity particles indicating an anti-correlation between midrapidity particle production and forward VPD triggering. Most importantly, within the momentum range under study, the PYTHIA MC simulation agrees well with the data. This agreement provides confidence in using PYTHIA simulations to evaluate this correction.

The correction factor $f_{\text{trg,vtx}}$ can be related to the ratio (N_D/N_{mb}) for the pure minimum-bias condition and the analysis condition, i.e.

$$f_{\text{trg,vtx}}(p_T) \equiv \frac{N_D(p_T)/N_{\text{mb}}}{N_D^{\text{trg,vtx}}(p_T)/N_{\text{mb}}^{\text{trg,vtx}}} \quad (4)$$

Two simulation samples were generated to obtain the correction factor. One sample consisted of PYTHIA-simulated $p + p$ events and was used to obtain the fraction of minimum-bias events that satisfy the analysis condition $N_{\text{mb}}^{\text{trg,vtx}}/N_{\text{mb}}$. This fraction was found to be 12.7% from this PYTHIA simulation. The other simulation sample was generated using the same PYTHIA settings, but only events with at least one charmed hadron were saved to enhance the statistics. This sample was used to obtain the fraction of charmed-hadron signals that satisfy the analysis condition $N_D^{\text{trg,vtx}}/N_D$. We also studied this fraction as a function of charmed-hadron p_T . Figure 12 shows the calculated efficiencies for D^* from different event-selection criteria. The BBC coincidence study provides a baseline for this simulation, which demonstrates consistency with previous STAR results [30]. As expected, the vertex finding efficiency increases with increasing p_T . The VPD trigger efficiency shows an anticorrelation with increasing $D^* p_T$, similar to that observed with increasing charged-hadron p_T . The final efficiency (with requirements for both vertexing and VPD triggering) is almost flat versus p_T , leveling off at $\sim 19\%$. The simulation for D^0 hadrons shows very

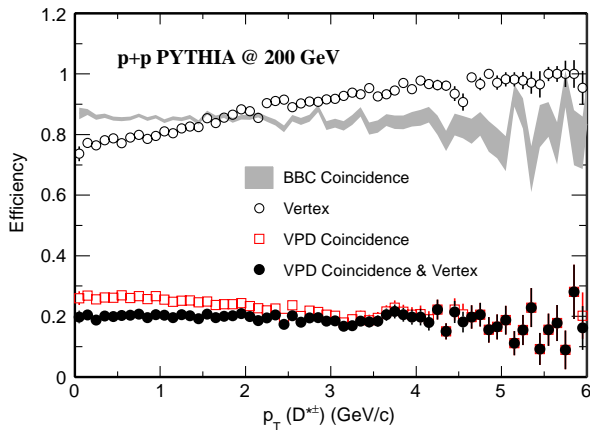


FIG. 12 (color online). D^* efficiency versus $D^* p_T$ with different event-selection criteria.

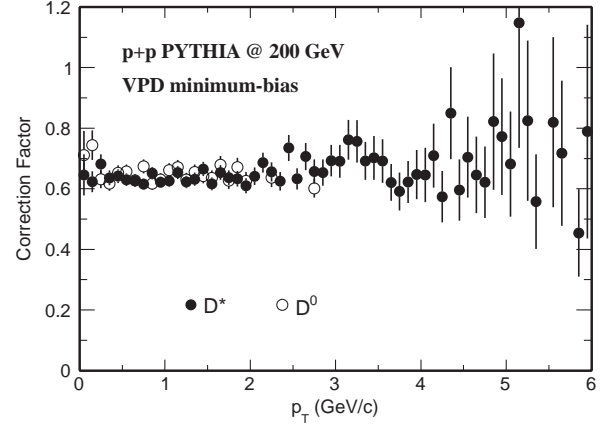


FIG. 13. The correction factor $f_{\text{trg,vtx}}$ versus charmed-hadron p_T for cross section calculations for D^0 and D^* .

similar results. Figure 13 shows the correction factor $f_{\text{trg,vtx}}$ for cross section calculations for D^0 and D^* .

V. SYSTEMATIC UNCERTAINTIES

Sources that contribute to the systematic uncertainties in the final D -meson cross sections include: (a) uncertainty in determining the raw D -meson yields; (b) uncertainty in determining the reconstruction efficiency; (c) uncertainty of the total NSD cross section; and (d) uncertainty in determining the trigger or vertex correction factor. Uncertainties due to particle identifications will enter in both (a) and (b) which will be discussed in the following subsections. We consider (a) as point-by-point uncorrelated systematic uncertainties. Although (b) is correlated in p_T , it is not simply a normalization uncertainty, and the exact correlation in p_T is not known. Therefore we include (b) in the point-by-point uncorrelated systematic uncertainties. Finally, (c) and (d) are overall normalization uncertainties.

A. Uncertainty in raw yields

Different choices on background reconstruction methods, function fits and mass binning were used to evaluate the systematic uncertainty in the raw D -meson yields. In the D^0 analysis, the difference between the yields extracted from Rot and LS methods is 15.6%–18.9%. Fitting the D^0 peak with fixed parameters from simulation estimates lower yields of 28.2% and 6.1% for the two $D^0 p_T$ bins. The systematic uncertainties from different mass binning and different fit regions are estimated to be $\sim 5\%$ – 7% . The systematic uncertainties in determining the raw D^* yields include contributions from the difference obtained between the sideband and the wrong-sign methods, and the difference between bin counting and Gaussian fitting methods, varying $\sim 6\%$ – 11% in the p_T range 2–6 GeV/c. The choice of mass binning and fitting range had a negligible effect on the extracted yields.

In D^0 meson reconstruction, if the kaon (pion) daughter is misidentified as a pion (kaon), then two daughters from a real D^0 decay will show up as additional \bar{D}^0 combinations with a wider mass distribution due to wrong mass assignments. Thus one D^0 signal will be counted twice, once as a D^0 and again as a \bar{D}^0 . A Monte Carlo simulation was used to evaluate the fraction of such double-counting occurrences in the D^0 reconstruction. Based on realistic dE/dx and TOF PID resolutions extracted from real data, the probability that kaons (pions) can be misidentified as pions (kaons) at a given p_T , using these PID selections, was obtained. Assuming a D^0 candidate, this procedure provides an estimate of the probability that both daughters are misidentified and then reconstructed as a \bar{D}^0 . In Fig. 14, the open and closed circles show the double-counting fraction, relative to the total real signal, for two different PID selections: (a) both daughters are identified by TPC dE/dx ; (b) the kaon daughters are identified by the TOF, while pions are identified by the TPC. The sharp increase at very low p_T (identifying both daughters using dE/dx) is due to the case where a D^0 decays almost at rest ($p_T \sim 0$), and the two daughters are produced in the momentum region where the kaon and pion dE/dx bands cross, therefore maximizing the misidentification probability. The plot shows that when the kaon daughter is identified by the TOF, the double-counting fraction is negligible in our D^0 p_T coverage region (0.6–2.0 GeV/c).

Double counting the D^0 may also impact reconstruction of D^* . However, the impact is different because of a charge sign requirement on the soft pions. If both daughters from a D^0 are misidentified (D^0 is reconstructed as \bar{D}^0), then the combination from the same signal will become $K^+ \pi^- \pi^+$. It will not contribute to the right-sign distributions but, instead, will enter into the wrong-sign (background) distributions if the mass also falls into the D^0 (\bar{D}^0) mass selection window. Thus the double counting in wrong-sign background will contribute to an undercounting in

the total signal if the wrong-sign background is subtracted from the right-sign distribution. Since the right-sign combination was also required, the misidentification does not affect the sideband background distributions. In the real analysis, the sideband background subtraction was used to extract the raw signal, but also the difference between sideband and wrong-sign methods was used for systematic uncertainty estimation. Since the wrong-sign distribution can be overestimated due to particle misidentification, the systematic error from the difference between the two methods would be overestimated. This was avoided with better understanding of the wrong-sign overcounting. The red triangles in Fig. 14 denote the overcounting fraction in the D^* wrong-sign background to real signals. It is very close to the D^0 double-counting fraction, since they are from the same source. The slight difference comes from the additional D^0 candidate selection cuts used in the D^* reconstruction. This fraction was used to compensate for the difference between the two background methods and as a way to improve the assessment of the systematic uncertainties in the extraction of the raw D^* yields.

B. Uncertainty in reconstruction efficiency

The systematic uncertainties of the reconstruction efficiencies were obtained following similar methods used in other particle cross section measurements by changing the daughter track selection criteria and comparing the difference between the data and the MC. In this analysis, it was studied by changing the minimum number of fit points (nFitPts) in the TPC from 15 to 25 and the DCA to the collision vertex from 2 to 1 cm. The uncertainty was then quantified by the difference in the remaining fractions after cut changes between the data and the MC. For each cut change, the uncertainties were calculated for each decay daughter and added together linearly to obtain the total for D^0 and D^* . The systematic uncertainties on the PID cut efficiencies (from both dE/dx and TOF) were estimated to be $<1\%$ and neglected in the total uncertainty. Then the uncertainties from the cut changes on nFitPts and DCA were added in quadrature to obtain the total systematic uncertainty on the reconstruction efficiency.

The point-by-point systematic errors including uncertainties in raw yields and reconstruction efficiency for the D^0 and D^* cross sections in each p_T bin are summarized in Table III.

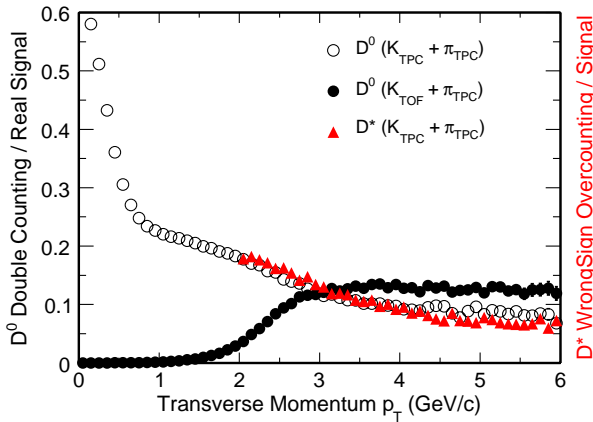


FIG. 14 (color online). D^0 double-counting fraction due to particle misidentification in two PID selections and D^* wrong-sign overcounting fraction versus D -meson p_T .

TABLE III. D^0 (0.6–2 GeV/c) and D^* (2–6 GeV/c) point-by-point systematic errors (%).

p_T (GeV/c)	0.6–1.2	1.2–2	2–3	3–4	4–5	5–6
Raw yields	+18.9 –33.9	+15.6 –16.8	9.4	6.5	11.0	6.6
nFitPts 15 → 25	3.8	3.2	7.2	4.7	5.9	4.7
DCA 2 → 1 (cm)	6.6	7.1	13.6	12.7	11.6	10.7
Quadratic sum	+20.8 –34.8	+17.8 –18.5	18.1	15.1	17.1	13.5

C. Overall normalization uncertainty

The overall normalization uncertainty for the total NSD cross section has been studied before and reported in a previous STAR publication [30]. It was estimated to be 8.1%, including the uncertainty from measuring the absolute BBC cross section and that of BBC triggering efficiency. The uncertainty from the trigger or vertex bias correction factor amounts to 5.2% by varying different PYTHIA versions (6.205 vs 6.416) and different parameter settings in the simulation. We also considered the impact from pileup TPC tracks as an additional systematic source on the correction factor, and the uncertainty was estimated to be 4.0% by comparing the result with a conservative luminosity level for this data set to that from pure PYTHIA simulation without pileup.

These uncertainties were added in quadrature, which gives 10.4% overall normalization uncertainty for the D -meson cross sections.

VI. RESULT AND DISCUSSION

After the reconstruction efficiency and trigger or vertex bias correction factor were applied, the differential production cross sections for D^0 and D^* in $p + p$ collisions at $\sqrt{s} = 200$ GeV were extracted, as shown in Fig. 15. The vertical bars on the data points indicate the statistical uncertainties, while the brackets indicate the bin-to-bin systematic uncertainties described in the previous section. The D^0 and D^* cross sections were divided by the charm quark fragmentation ratios 0.565 ± 0.032 ($c \rightarrow D^0$) and 0.224 ± 0.028 ($c \rightarrow D^{*+}$), respectively, to convert to the $c\bar{c}$ production cross section. The charm quark fragmentation ratios are measured from CLEO and BELLE experiments near the Υ resonance [34]. The uncertainties of the fragmentation ratios are taken into account as systematic

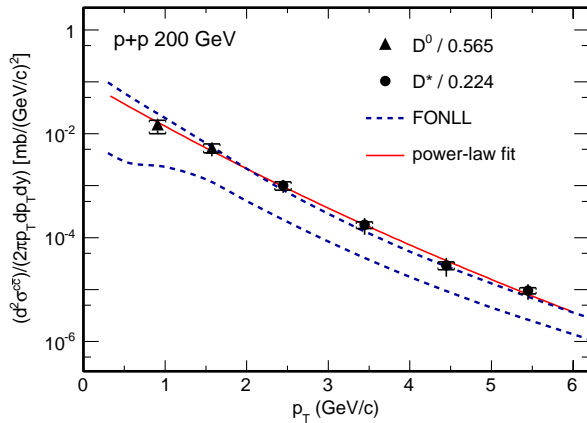


FIG. 15 (color online). $c\bar{c}$ production cross section as inferred from D^0 and D^* production in $p + p$ collisions at $\sqrt{s} = 200$ GeV compared with FONLL calculations. The D^0 and D^* data points were divided by the charm quark fragmentation ratios 0.565 ($c \rightarrow D^0$) and 0.224 ($c \rightarrow D^{*+}$) [34], respectively, to convert to the $c\bar{c}$ production cross section.

errors in calculating the $c\bar{c}$ production cross section. A power-law fit to the data points was performed with the following function [14]:

$$E \frac{d^3 \sigma}{dp^3} = \frac{d\sigma}{dy} \frac{2(n-1)(n-2)}{\pi(n-3)^2 \langle p_T \rangle^2} \left(1 + \frac{p_T}{\langle p_T \rangle (n-3)/2} \right)^{-n} \quad (5)$$

and shown as the solid red line in the figure. The fit quality with the power-law function, measured as χ^2/ndf , is 0.9/3 with statistical errors and 3.7/3 with point-by-point systematic errors, respectively. The latter was used to extract the systematic uncertainty on the p_T integrated cross section from point-by-point systematic sources. The obtained $c\bar{c}$ production cross section at midrapidity is

$$\left. \frac{d\sigma}{dy} \right|_{y=0}^{c\bar{c}} = 170 \pm 45(\text{stat})_{-39}^{+38}(\text{sys}) \mu\text{b}. \quad (6)$$

The term with sys includes the uncertainty arising from the bin-to-bin systematic uncertainties and from the extrapolation to the low- p_T region, which is not measured. The FONLL upper limit and PYTHIA + tune fits are used for the low- p_T extrapolation, which gives +6.2% and -16.4% uncertainties, respectively. At midrapidity, about 67% of the D meson yield falls in the measured p_T region. The mean transverse momentum of charmed mesons is found to be $1.06 \pm 0.14(\text{stat}) \pm 0.09(\text{sys})$ GeV/c. The charm-pair cross section at midrapidity from this measurement is consistent with STAR's previous measurement in $d + \text{Au}$ collisions [14] at 1.7σ (σ is the averaged total uncertainty between two results), providing negligible nuclear effects in $d + \text{Au}$ collisions.

Also shown in Fig. 15 are the upper and lower edges (blue dashed lines) of a FONLL pQCD calculation taken from Ref. [9]. Our results are consistent with the upper limit of the FONLL pQCD calculation in a wide p_T region. It is observed that the charmed-hadron cross sections measured by CDF [13] and ALICE [35] at energies up to 7 TeV are also close to the upper limits of FONLL pQCD calculations. This may help set constraints on the parameters used in the FONLL calculations, e.g. on the choice of renormalization or factorization scales, which are the main parameters varied to obtain the upper and lower limits on these calculations. However one should note the valid p_T region of FONLL calculations when applying such an analysis since FONLL calculations are supposed to work when $p_T \gg m_c$.

The charm cross section at midrapidity was extrapolated to full phase space using the same extrapolation factor, 4.7 ± 0.7 , as in a previous publication [14], and the extracted charm total cross section at $\sqrt{s} = 200$ GeV is

$$\sigma_{c\bar{c}} = 797 \pm 210(\text{stat})_{-295}^{+208}(\text{sys}) \mu\text{b}. \quad (7)$$

Shown in Fig. 16, the data were also compared with PYTHIA calculations. PYTHIA version 6.416 was used as it has been tuned to describe the midrapidity Tevatron data.

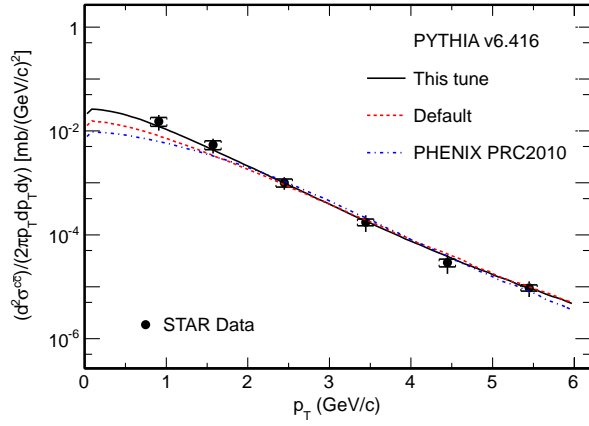


FIG. 16 (color online). $c\bar{c}$ production cross section as inferred from D^0 and D^* production in $p + p$ collisions at $\sqrt{s} = 200$ GeV compared with PYTHIA calculations. Data are fitted with PYTHIA spectra with an overall scale parameter for the purpose of shape comparison only.

We tried PYTHIA calculations with the following sets of parameters to compare with our measurements:

- (a) Default MSEL = 1.
- (b) PHENIX tune: MSEL = 0 with MSUB(11, 12, 13, 28, 53, 68) on, PARP(91) ($\langle k_{\perp} \rangle$) = 1.5 GeV/c, MSTP(32) (Q^2 scale) = 4, CKIN(3) (min. parton \hat{p}_{\perp}) = 2 GeV.
- (c) This tune: MSEL = 1, PARP(91) ($\langle k_{\perp} \rangle$) = 1.0 GeV/c, PARP(67) (parton shower level) = 1.0.

The choice of modifying the primordial $\langle k_{\perp} \rangle$ (the Gaussian width of primordial k_T in hadrons) and the parton shower level parameters from default values (2 GeV/c and 4, respectively) in this tune was suggested by the matching of scales in heavy-flavor production at lower energies [36], which has been noted in PYTHIA [19]. The CDF TUNEA parameters [32], which were tuned to reproduce midrapidity jet and “underlying event” results at Tevatron energies, are included as defaults in PYTHIA v6.416. “PHENIX tune” parameters are those used in the PHENIX charm continuum contribution estimation from dielectron measurements [37]. The default parton distribution function (CTEQ5L) was used in all three cases.

All ground-state charmed hadrons (D^0 , D^+ , D_s^+ , and Λ_c^+) were added together in the rapidity window $|y| < 1$ to

obtain charm cross sections. The data were then fitted with the PYTHIA calculations with an overall scale factor as the unique free parameter. The charm production p_T spectrum with this tune gives best χ^2 : 1.41 (this tune), 4.97 (default), 5.96 (PHENIX tune). This is the first direct D -meson measurement that goes down to such a low p_T , which constrains the model parameters better.

VII. SUMMARY

In summary, measurement on the charmed meson (D^0 and D^*) production cross sections via their hadronic decays in $p + p$ collisions at $\sqrt{s} = 200$ GeV has been reported. The charm-pair production cross section at midrapidity extracted from this analysis is $d\sigma/dy|_{y=0}^{c\bar{c}} = 170 \pm 45(\text{stat})^{+38}_{-59}(\text{sys}) \mu\text{b}$. The charm total cross section at $\sqrt{s} = 200$ GeV is estimated as $797 \pm 210(\text{stat})^{+208}_{-295}(\text{sys}) \mu\text{b}$. The reconstructed charmed mesons cover the p_T range 0.6–6 GeV/c. The charm-pair transverse momentum differential cross sections from this analysis are consistent with the upper bound of a fixed-order next-to-leading logarithm perturbative QCD calculation. When comparing to PYTHIA model calculations, we found that a calculation with smaller primordial $\langle k_{\perp} \rangle$ and parton shower level compared to CDF TUNEA settings describes the shape of the p_T distribution of data.

ACKNOWLEDGMENTS

We thank the RHIC Operations Group and RCF at BNL, the NERSC Center at LBNL and the Open Science Grid consortium for providing resources and support. This work was supported in part by the Offices of NP and HEP within the U.S. DOE Office of Science, the U.S. NSF, the Sloan Foundation, the DFG cluster of excellence “Origin and Structure of the Universe” of Germany, CNRS/IN2P3, FAPESP CNPq of Brazil, Ministry of Education and Science of the Russian Federation, NNSFC, CAS, MoST, and MoE of China, GA and MSMT of the Czech Republic, FOM and NWO of the Netherlands, DAE, DST, and CSIR of India, Polish Ministry of Science and Higher Education, Korea Research Foundation, Ministry of Science, Education and Sports of the Republic of Croatia, and RosAtom of Russia.

[1] J. Adams *et al.* (STAR Collaboration), *Nucl. Phys.* **A757**, 102 (2005).
[2] Z. Lin and M. Gyulassy, *Phys. Rev. C* **51**, 2177 (1995); **52**, 440(E) (1995).
[3] B. Mueller, *Nucl. Phys.* **A750**, 84 (2005).
[4] G.D. Moore and D. Teaney, *Phys. Rev. C* **71**, 064904 (2005).

[5] H. van Hees and R. Rapp, *Phys. Rev. C* **71**, 034907 (2005); R. Rapp and H. van Hees, arXiv:0803.0901.
[6] J. Uphoff, O. Fochler, Z. Xu, and C. Greiner, *Phys. Rev. C* **82**, 044906 (2010).
[7] R.L. Thews, M. Schroedter, and J. Rafelski, *Phys. Rev. C* **63**, 054905 (2001).

- [8] A. Andronic, P. Braun-Munzinger, K. Redlich, and J. Stachel, *Phys. Lett. B* **571**, 36 (2003).
- [9] M. Cacciari, P. Nason, and R. Vogt, *Phys. Rev. Lett.* **95**, 122001 (2005).
- [10] R. Vogt, *Eur. Phys. J. Special Topics* **155**, 213 (2008).
- [11] S. P. K. Tavernier, *Rep. Prog. Phys.* **50**, 1439 (1987).
- [12] X. Dong, Ph.D. thesis, University of Science and Technology of China, 2005, [arXiv:nucl-ex/0509011](http://arxiv.org/abs/nucl-ex/0509011), Appendix C and references therein.
- [13] D. Acosta *et al.* (CDF Collaboration), *Phys. Rev. Lett.* **91**, 241804 (2003).
- [14] J. Adams *et al.* (STAR Collaboration), *Phys. Rev. Lett.* **94**, 062301 (2005).
- [15] B. I. Abelev *et al.* (STAR Collaboration), *Phys. Rev. Lett.* **106**, 159902(E) (2011).
- [16] H. Agakishiev *et al.* (STAR Collaboration), *Phys. Rev. D* **83**, 052006 (2011).
- [17] A. Adare *et al.* (PHENIX Collaboration), *Phys. Rev. Lett.* **97**, 252002 (2006).
- [18] S. S. Adler *et al.* (PHENIX Collaboration), *Phys. Rev. Lett.* **96**, 032301 (2006); A. Adare *et al.* (PHENIX Collaboration), *Phys. Rev. Lett.* **98**, 172301 (2007).
- [19] T. Sjöstrand, S. Mrenna, and P. Skands, *J. High Energy Phys.* **05** (2006) 026.
- [20] Special Issue on RHIC and Its Detectors, edited by M. Harrison, T. Ludlam, and S. Ozaki [*Nucl. Instrum. Methods Phys. Res., Sect. A* **499**, No. 2–3 (2003)].
- [21] M. Anderson *et al.*, *Nucl. Instrum. Methods Phys. Res., Sect. A* **499**, 659 (2003).
- [22] STAR TOF proposal, <http://drupal.star.bnl.gov/STAR/files/future/proposals/tof-5-24-2004.pdf>.
- [23] M. Beddo *et al.*, *Nucl. Instrum. Methods Phys. Res., Sect. A* **499**, 725 (2003).
- [24] C. E. Allgower *et al.*, *Nucl. Instrum. Methods Phys. Res., Sect. A* **499**, 740 (2003).
- [25] W. J. Llope, in *Proceedings of 24th Winter Workshop on Nuclear Dynamics*, 2008 (unpublished).
- [26] J. Koryluk, *AIP Conf. Proc.* **675**, 424 (2003).
- [27] B. I. Abelev *et al.* (STAR Collaboration), *Phys. Rev. C* **79**, 034909 (2009).
- [28] C. Adler *et al.* (STAR Collaboration), *Phys. Rev. Lett.* **89**, 132301 (2002); J. Adams *et al.* (STAR Collaboration), *Phys. Rev. Lett.* **95**, 122301 (2005); *Phys. Rev. C* **70**, 44902 (2004); B. I. Abelev *et al.* (STAR Collaboration), *Science* **328**, 58 (2010); K. Aamodt *et al.* (ALICE Collaboration), *Phys. Lett. B* **704**, 442 (2011).
- [29] B. I. Abelev *et al.* (STAR Collaboration), *Phys. Rev. D* **79**, 112006 (2009).
- [30] J. Adams *et al.* (STAR Collaboration), *Phys. Rev. Lett.* **91**, 172302 (2003).
- [31] GEANT 3.21, CERN program library. <http://wwwasdoc.web.cern.ch/wwwasdoc/22geanthtml3/geantall.html>.
- [32] R. D. Field *et al.*, [arXiv:hep-ph/0510198](http://arxiv.org/abs/hep-ph/0510198).
- [33] N. Poljak (for the STAR Collaboration), *Nuovo Cimento Soc. Ital. Fis. C* **035N2**, 193 (2012).
- [34] C. Amsler *et al.*, *Phys. Lett. B* **667**, 1 (2008).
- [35] A. Dainese *et al.* (ALICE Collaboration), *J. Phys. G* **38**, 124032 (2011).
- [36] E. Norrbin and T. Sjöstrand, *Phys. Lett. B* **442**, 407 (1998); *Eur. Phys. J. C* **17**, 137 (2000).
- [37] A. Adare *et al.* (PHENIX Collaboration), *Phys. Rev. C* **81**, 034911 (2010), footnote in reference [51].

Open charm measurements in $p + p$ collisions at STAR

David Tlustý for the STAR collaboration

Nuclear Physics Institute, Academy of Sciences Czech Republic, Na Truhlářce 39/64, 180 86 Praha 8, Czech Republic
Czech Technical University in Prague, Faculty of Nuclear Sciences and Physical Engineering, Břehová 7, 11519, Prague 1, Czech Republic

E-mail: tlustdav@fjfi.cvut.cz

Abstract.

In this article, we will present the STAR results of open charm hadron and non-photonic productions at mid-rapidity in $p + p$ collisions at $\sqrt{s} = 200$ and 500 GeV. Open charm mesons are reconstructed directly via hadronic decay channels with daughter particles identified by STAR Time Projection Chamber (TPC) and Time Of Flight (TOF) detectors. Non-photonic electron yields are calculated by subtracting photonic electrons from inclusive electrons identified using TPC and Electromagnetic Calorimeter. These measurements are compared to theoretical model calculations and physics implications will be discussed.

1. Introduction

Heavy quark production at RHIC energies is dominated by initial gluon fusion and can be described by perturbative QCD (pQCD) due to their large mass [1]. The measurement of the charm quark production in $p + p$ collisions provides both pQCD test and baseline for any measurement in Heavy-Ion collisions. The study of heavy quark production in relativistic nuclear collisions follows two different approaches: (i) the direct reconstruction of heavy flavor mesons and (ii) the identification of electrons from semi-leptonic decays of such mesons, the so-called non-photonic electrons.

2. Data Analysis

2.1. The Direct Reconstruction of Open Charm Mesons

Invariant yield of charm quark Y is obtained from fitting the reconstructed invariant mass spectrum of open charm mesons through hadronic decays: $D^0(\bar{D}^0) \rightarrow K^\mp \pi^\pm$ (BR = 3.89%) and $D^{*\pm} \rightarrow D^0(\bar{D}^0) \pi^\pm$ (BR = 67.7%) $\rightarrow K^- \pi^+ \pi^\pm$ (total BR = 2.63%). The Y is calculated then as

$$Y \equiv \frac{d^2 N_{c\bar{c}}}{2\pi p_T dp_T dy} = \frac{1}{N_{\text{trig}}} \frac{N(p_T, y)}{2\pi p_T \Delta p_T \Delta y} \frac{f_{\text{trg}}}{\text{BR } f_{\text{frag}} \epsilon_{\text{rec}}} \quad (1)$$

where N_{trig} is the total number of triggered events used for the analysis. $N(p_T, y)$ is the raw charm hadron signal in each p_T bin within a rapidity window $\Delta y = 2$. BR is the hadronic decay branching ratio for the channel of interest. ϵ_{rec} is the reconstruction efficiency including geometric acceptance, track selection efficiency, PID efficiency, and analysis cut efficiency. f_{frag} represents the ratio of charm quarks hadronized to open charm mesons. And f_{trg} is the correction factor to account for the bias between the minimum-bias sample used in this analysis and the total Non-single Diffractive (NSD) sample [2]. f_{trg} is found to be 0.65 for D^0 and 0.67 for D^* at $\sqrt{s} = 200$ GeV and 0.6 and 0.59 at $\sqrt{s} = 500$ GeV respectively.



The identification of daughter particles is done in the STAR experiment [3] at mid-rapidity $|y| < 1$ at $\sqrt{s} = 200$ and 500 GeV. The analysis presented herein is done using two datasets; the first one collected in year 2009 ($N_{\text{trig}} \sim 105$ million 200 GeV $p + p$ collisions), and the second one in 2011 ($N_{\text{MB}} \sim 50$ million 500 GeV $p + p$ collisions).

2.2. Identification of electrons from semi-leptonic decays

The invariant cross section for non-photonic electron production is calculated according to

$$E \frac{d^3\sigma}{dp^3} = \frac{1}{\mathcal{L}} \frac{1}{2\pi p_T \Delta p_T \delta y} \frac{N_{\text{npe}}}{\varepsilon_{\text{rec}} \varepsilon_{\text{trig}} \varepsilon_{\text{eid}} \varepsilon_{\text{BBC}}}, \quad (2)$$

where N_{npe} is the nonphotonic electron raw yield, ε_{rec} is the product of the single electron reconstruction efficiency and the correction factor for momentum resolution and finite spectrum bin width, $\varepsilon_{\text{trig}}$ is the high-tower trigger efficiency, ε_{eid} is the electron identification efficiency, \mathcal{L} is the integrated luminosity with the z-position of vertex cuts, and $\varepsilon_{\text{BBC}} = 0.87 \pm 0.08$ is the BBC trigger efficiency.

The analysis of non-photonic electrons consists of three main steps: selection of a clean electron sample; subtraction of electron background arising from conversion and Dalitz decays; and residual corrections of the signal yield. The analysis details and a discussion of the sources of uncertainty can be found in [4]. The main background in this analysis is the substantial flux of photonic electrons from photon conversion in the detector material and Dalitz decay of π^0 and η mesons. These contributions need to be subtracted in order to extract the non-photonic electron yield according to formula

$$N_{\text{npe}} = N_{\text{inc}} \varepsilon_{\text{purity}} - \frac{N_{\text{pho}}}{\varepsilon_{\text{pho}}}, \quad (3)$$

where N_{npe} is the non-photonic electron yield, N_{inc} is the inclusive electron yield, N_{pho} is the photonic electron yield, ε_{pho} is the photonic electron reconstruction efficiency defined as the fraction of the photonic electrons identified through invariant mass reconstruction, and $\varepsilon_{\text{purity}}$ is the purity reflecting hadron contamination in the inclusive electron sample.

3. Results

3.1. The Direct Reconstruction of Heavy Flavor Mesons

Yields $N(p_T, y)$ are calculated in six p_T bins (first two for D^0 , the next four for D^*) in $p + p$ 200 GeV and five p_T bins (first for D^0 , the next four for D^*) in $p + p$ 500 GeV. The charm cross section at mid-rapidity $d\sigma^{c\bar{c}}/dy$ was obtained from the power-law function fit [2] to $d^2\sigma^{c\bar{c}}/(2\pi p_T dp_T dy) = Y \cdot \sigma_{\text{NSD}}$, where Y is calculated according to (1). σ^{NSD} is the total NSD cross section, which is measured at STAR to be 30.0 ± 2.4 mb at $\sqrt{s} = 200$ GeV [5]. In the case of $\sqrt{s} = 500$ GeV, σ^{NSD} is extrapolated from 200 GeV measurement with the help of PYTHIA simulation to be 34 mb.

The charm production cross section at mid rapidity $\left. \frac{d\sigma_{c\bar{c}}}{dy} \right|_{y=0}$ is $170 \pm 45(\text{stat.})_{-51}^{+37}(\text{sys.}) \mu\text{b}$ at $\sqrt{s} = 200$ GeV and is $217 \pm 86(\text{stat.}) \pm 73(\text{sys.}) \mu\text{b}$ at $\sqrt{s} = 500$ GeV. FONLL predictions for p_T spectra [6] shown in Fig. 1. In order to compare STAR results with other experiments, we extrapolated $\left. \frac{d\sigma_{c\bar{c}}}{dy} \right|_{y=0}$ to $\sigma_{c\bar{c}}^{\text{NN}}$ using PYTHIA simulations with various parameter tunings giving extrapolation factors 4.7 ± 0.7 for 200 GeV and 5.6 ± 0.1 for 500 GeV collisions. The results are depicted in Figure 1 revealing agreement with with NLO prediction [7]. Note that the STAR result at 200 GeV was used in [7] to fit the μ_R and μ_F parameters, so only the STAR result at 500 GeV can be used as a test of this prediction.

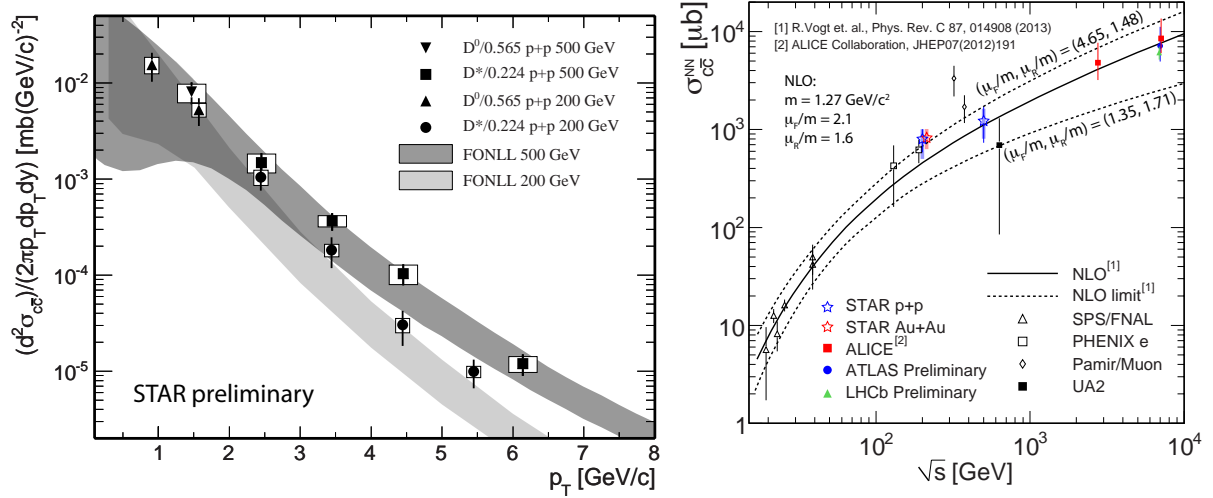


Figure 1. Left Panel: Charm quark production invariant cross section as a function of D meson p_T in 200 and 500 GeV $p + p$ collisions with two FONLL predictions [6] using normalization and factorization scale equal to charm quark mass m_c . Right Panel: Total charm cross section as a function of \sqrt{s}

3.2. Identification of electrons from semi-leptonic decays

Electrons from bottom and charm meson decays are the two dominant components of the non-photonics electrons. Mostly due to the decay kinematics, the azimuthal correlations between the daughter electron and daughter hadron are different for bottom meson decays and charm meson decays. A study of these azimuthal correlations has been carried out on STAR data and is compared with a PYTHIA simulation to obtain the ratio of the bottom electron yield to the heavy-flavor decay electron yield $\frac{e_b}{e_b + e_c}$ [8], where PYTHIA was tuned to reproduce STAR measurements of D mesons p_T spectra [9]. Using the measured $e_b/(e_b + e_c)$ together with the measured non-photonics electron cross section with the electrons from J/Ψ , Υ decay and Drell-Yan processes subtracted, we are able to disentangle these two components. Figure 2 shows the invariant cross section of electrons $\left(\frac{e^+ + e^-}{2}\right)$ from bottom (upper left) and charm (upper right) mesons as a function of p_T and the corresponding FONLL predictions, along with the ratio of each measurement to the FONLL calculations (lower panels).

From the measured spectrum, we determine the integrated cross section of electrons $\left(\frac{e^+ + e^-}{2}\right)$ at $3 \text{ GeV}/c < p_T < 10 \text{ GeV}/c$ from bottom and charm meson decays to be, respectively,

$$\begin{aligned} \left. \frac{d\sigma_{(B \rightarrow e) + (B \rightarrow D \rightarrow e)}}{dy} \right|_{y_e=0} &= 4.0 \pm 0.5(\text{stat}) \pm 1.1(\text{syst}) \text{ nb} \\ \left. \frac{d\sigma_{D \rightarrow e}}{dy} \right|_{y_e=0} &= 6.2 \pm 0.7(\text{stat}) \pm 1.5(\text{syst}) \text{ nb} \end{aligned}$$

4. Conclusions

Open charm hadron (D^0, D^{*+}) cross section in $p + p$ minimum bias collisions at $\sqrt{s} = 200$ and 500 GeV at STAR is measured with results:

$d\sigma_{cc}^{NN}/dy|_{y=0} = 170 \pm 45(\text{stat.})_{-51}^{+37}(\text{syst.}) \mu\text{b}$ at 200 GeV, $217 \pm 86(\text{stat.}) \pm 73(\text{syst.}) \mu\text{b}$ at 500 GeV. The total charm cross section at 500 GeV is within statistical and systematic uncertainties consistent with the latest NLO pQCD prediction.

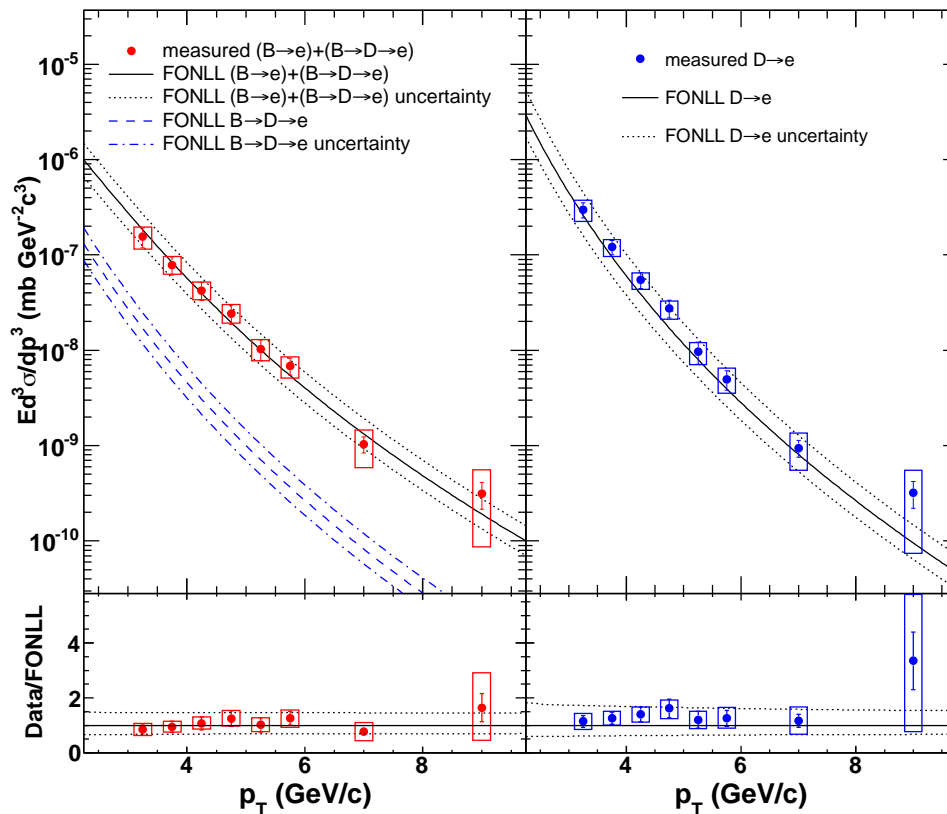


Figure 2. Invariant cross section of electrons from bottom (upper left) and charm meson (upper right) decay, together with the ratio of the corresponding measurements to the FONLL predictions for bottom (lower left) and charm electrons (lower right). The solid circles are experimental measurements. The error bars and the boxes are, respectively, the statistical and systematic uncertainties. The solid and dotted curves are the FONLL predictions and their uncertainties. The dashed and dot-dashed curves are the FONLL prediction for $B \rightarrow D \rightarrow e$.

Acknowledgments

This work has been supported by the grant 13-02841S of the Czech Science Foundation (GACR) and by the Grant Agency of the Czech Technical University in Prague, grant No. SGS13/215/OHK4/3T/14.

References

- [1] Cacciari M, Nason P and Vogt R 2005 *Phys. Rev. Lett.* **95** 122001
- [2] Adamczyk L et al. [STAR Collaboration] 2012, *Phys. Rev. D* **86** 072013
- [3] Shao M et al. 2003, *Nucl. Instrum. Methods A* **499** 624
- [4] Agakishiev B I et al. [STAR Collaboration] 2011, *Phys. Rev. D* **83** 052006
- [5] Adams J et al. [STAR Collaboration] 2003 *Phys. Rev. Lett.* **91** 172302
- [6] Vogt R 2012 *private communication*
- [7] Vogt R et al. 2013 *Phys. Rev. C* **87** 014908
- [8] Aggarwal M M et al. [STAR Collaboration] *Phys. Rev. Lett.* **105** 202301
- [9] Lin X, [arXiv:hep-ph/0602067](https://arxiv.org/abs/hep-ph/0602067)

Open charm hadron production in $p + p$ and Au+Au collisions at STAR

David Tlusty for the STAR Collaboration*

Nuclear Physics Institute, Academy of Sciences and Czech Technical University, Prague, Czech Republic

E-mail: tlustdat@fjfi.cvut.cz

In relativistic heavy ion collisions at RHIC, heavy quarks are expected to be created from initial hard scatterings. Their large masses are not easily affected by the strong interaction with QCD medium, thus they carry clean information from the system at early stage. The interaction between heavy quarks and the medium is sensitive to the medium dynamics, therefore heavy quarks are suggested as ideal probes to quantify the properties of the strongly interacting QCD matter. In this paper, we present the STAR results of open charm hadron production at mid-rapidity in $p + p$ and Au+Au collisions at $\sqrt{s_{NN}} = 200$ GeV. Open charm mesons were reconstructed directly via hadronic decay channels with daughter particles identified by TPC and TOF detectors. With abundant statistics of Au+Au collisions collected by STAR in the year 2010 and 2011, the D-meson is measured at p_T from 0.2 to 6 GeV/c in minimum bias Au+Au collisions. The centrality dependence of D-meson p_T spectra as well as the nuclear modification factor is presented. A first measurement of the D^0 elliptic flow in 200 GeV Au+Au collisions is reported. These measurements are compared to theoretical model calculations and physics implications is discussed. Finally, we discuss the open charm hadron measurement in $\sqrt{s} = 500$ GeV $p + p$ collisions to study the energy dependence of charm production.

*The European Physical Society Conference on High Energy Physics -EPS-HEP2013
18-24 July 2013
Stockholm, Sweden*

*A list of members of the STAR Collaboration and acknowledgements can be found at the end of this issue.

1. Introduction

The heavy quark production at RHIC is dominated by initial gluon fusion at initial hard partonic collisions and can be described by perturbative QCD (pQCD) due to their large mass [1]. The heavy constituent quark mass is almost exclusively generated through its coupling to the Higgs field in the electroweak sector, while masses of (u, d, s) quarks are dominated by spontaneous breaking of chiral symmetry (CS) in QCD [2]. This means that charm quarks remain heavy even if CS is restored, as it likely is in a QGP. One expects therefore that charm production total cross section $\sigma_{c\bar{c}}^{NN}$ should scale as a function of number-of-binary-collisions N_{bin} . In addition, if charm quarks participate in the collective expansion of the medium, there must have been enough interactions to easily thermalize light quarks. Hence, charm quark is an ideal probe to study early dynamics in high-energy nuclear collisions.

2. Analysis Method and Datasets

Invariant yield of charm quark production InvY is calculated as

$$\text{InvY} \equiv \frac{d^2 N_{c\bar{c}}}{2\pi p_T dp_T dy} = \frac{1}{N_{\text{trig}}} \frac{Y(p_T, y)}{2\pi p_T \Delta p_T \Delta y} \frac{f_{\text{trg}}}{\text{BR} f_{\text{frag}} \epsilon_{\text{rec}}} \quad (2.1)$$

where N_{trig} is the total number of triggered events used for the analysis. $Y(p_T, y)$ is the raw charm hadron signal in each p_T bin within a rapidity window $\Delta y = 2$. BR is the hadronic decay branching ratio for the channel of interest. ϵ_{rec} is the reconstruction efficiency including geometric acceptance, track selection efficiency, PID efficiency, and analysis cut efficiency. f_{frag} represents the ratio of charm quarks hadronized to open charm mesons. And f_{trg} is the correction factor to account for the bias between the minimum-bias sample used in this analysis and the total NSD sample [3]. f_{trg} is found to be unity in Au+Au, 0.65 in $p + p$ collisions at $\sqrt{s} = 200$ GeV and 0.58 in $p + p$ collisions at $\sqrt{s} = 500$ GeV.

$Y(p_T, y)$ is obtained from fitting the invariant mass spectrum (Fig. 1) of open charm mesons through hadronic decays: $D^0(\bar{D}^0) \rightarrow K^\mp \pi^\pm$ (BR = 3.89%) and $D^{*\pm} \rightarrow D^0(\bar{D}^0) \pi^\pm$ (BR = 67.7%) $\rightarrow K^- \pi^+ \pi^\pm$ (total BR = 2.63%)

The daughter particles were identified by Time Projection Chamber (TPC) and Time Of Flight (TOF) subsystems of the STAR experiment [5] at mid-rapidity $|y| < 1$ at $\sqrt{s_{NN}} = 200$ and 500 GeV. The analysis presented herein is done using three datasets; the first one collected in year 2009 ($N_{\text{trig}} \sim 105$ million 200 GeV $p + p$ collisions), the second one collected in 2010 and 2011 ($N_{\text{trig}} \sim 800$ million Au+Au 200 GeV collisions), and the third one in 2011 ($N_{\text{MB}} \sim 50$ million 500 GeV $p+p$ collisions).

At present, STAR does not have the capability to reconstruct the secondary vertex of D^0 decay; one must calculate the invariant mass of all $K\pi$ pairs coming from the vicinity of the primary vertex. This results in a large combinatorial background which was reconstructed via the mixed-event method (Au+Au dataset), same-charge-sign, and kaon momentum-rotation ($p + p$ dataset) and subtracted from invariant mass spectra of all particle pairs [6]. To reconstruct D^* , one may exploit the softness of $D^* \rightarrow D^0 \pi$ decay; combine low momentum pions with D^0 candidates, i.e. pairs with $1.82 < M(K\pi) < 1.9$ GeV/c², and plot difference $M(K\pi\pi) - M(K\pi)$ whose resolution

is determined by mostly the soft pion high momentum resolution. The combinatorial background is reconstructed by side-band (picking $K\pi$ pair outside the D^0 mass region) and wrong-sign (picking soft pion with opposite charge) methods. The dominant source of systematic uncertainties for both D^0 and D^* analyses is the difference between yields obtained from subtractions of combinatorial background from all particle combinations.

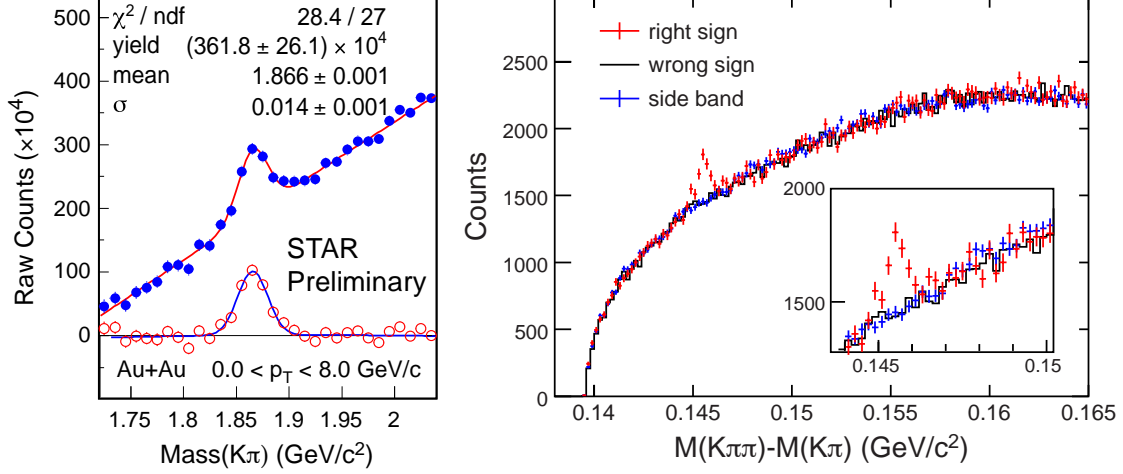


Figure 1: Left panel: D^0 signal in Au+Au 200 GeV collisions after mixed-event background subtraction. Right panel: D^* signal in $p + p$ 200 GeV collisions with comb. background reproduced by wrong-sign and side-band methods [3].

3. Results

3.1 D meson production in $p + p$ collisions

Yields $Y(p_T, y)$ are calculated in six p_T bins (first two for D^0 , the next four for D^*) in $p + p$ 200 GeV and five p_T bins (first for D^0 , the next four for D^*) in $p + p$ 500 GeV. The charm cross section at mid-rapidity $d\sigma^{c\bar{c}}/dy$ was obtained from the power-law function

$$\frac{d^2\sigma^{c\bar{c}}}{2\pi p_T dp_T dy} = 4 \frac{d\sigma^{c\bar{c}}}{dy} \frac{(n-1)(n-2)}{\langle p_T \rangle^2 (n-3)^2} \left(1 + \frac{2p_T}{\langle p_T \rangle (n-3)} \right)^{-n}$$

fit [3] to $d^2\sigma^{c\bar{c}}/(2\pi p_T dp_T dy) = \text{Inv}Y \cdot \sigma^{\text{NSD}}$, where $\text{Inv}Y$ is obtained from (2.1). σ^{NSD} is the total Non-single Diffractive (NSD) cross section, which is measured at STAR to be 30.0 ± 2.4 mb at $\sqrt{s} = 200$ GeV [7]. In the case of $\sqrt{s} = 500$ GeV, there's no STAR measurement yet; σ^{NSD} is extrapolated from 200 GeV measurement with the help of PYTHIA simulation to be 34 mb. The charm production cross section at mid rapidity $\left. \frac{d\sigma_{c\bar{c}}}{dy} \right|_{y=0}$ is $170 \pm 45(\text{stat.})_{-51}^{+37}(\text{sys.}) \mu\text{b}$ at $\sqrt{s} = 200$ GeV and is $217 \pm 86(\text{stat.}) \pm 73(\text{sys.}) \mu\text{b}$ at $\sqrt{s} = 500$ GeV. Fixed-order Next-to-leading Logarithm (FONLL) predictions for p_T spectra [8] shown in Fig. 2.

In order to compare STAR results with other experiments, we extrapolated $\left. \frac{d\sigma_{c\bar{c}}}{dy} \right|_{y=0}$ to $\sigma_{c\bar{c}}^{\text{NN}}$ using PYTHIA simulations with various parameter tunings giving extrapolation factors 4.7 ± 0.7 for 200 GeV and 5.6 ± 0.1 for 500 GeV collisions. The results are shown in Figure 2.

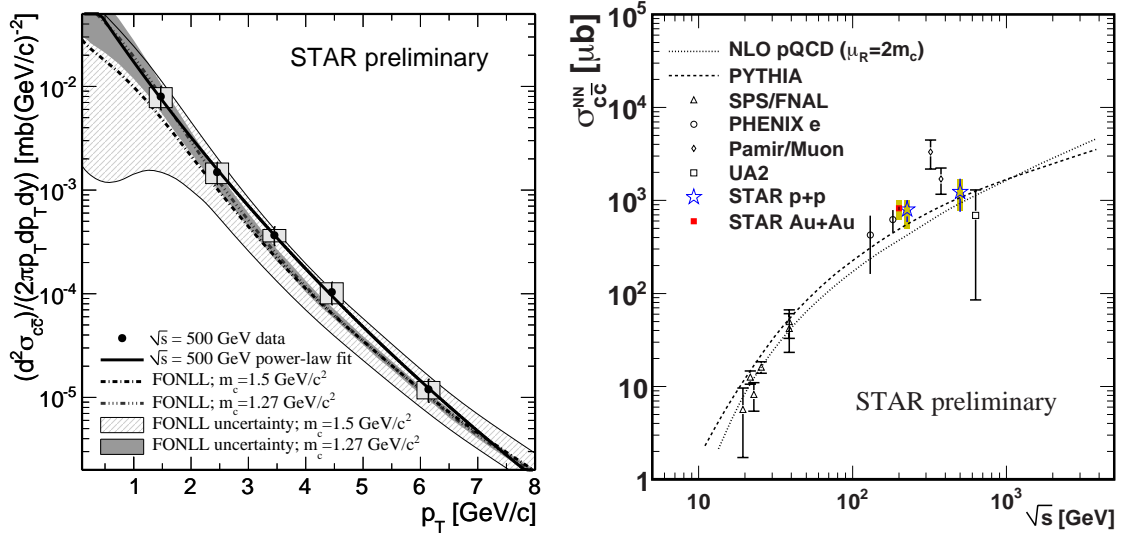


Figure 2: Left Panel: Charm quark production invariant cross section as a function of D meson p_T in 500 GeV p+p collisions with two FONLL predictions [8] using normalization and factorization scale equal to charm quark mass m_c . Right Panel: Total charm cross section as a function of \sqrt{s}

3.2 D^0 production in Au+Au collisions

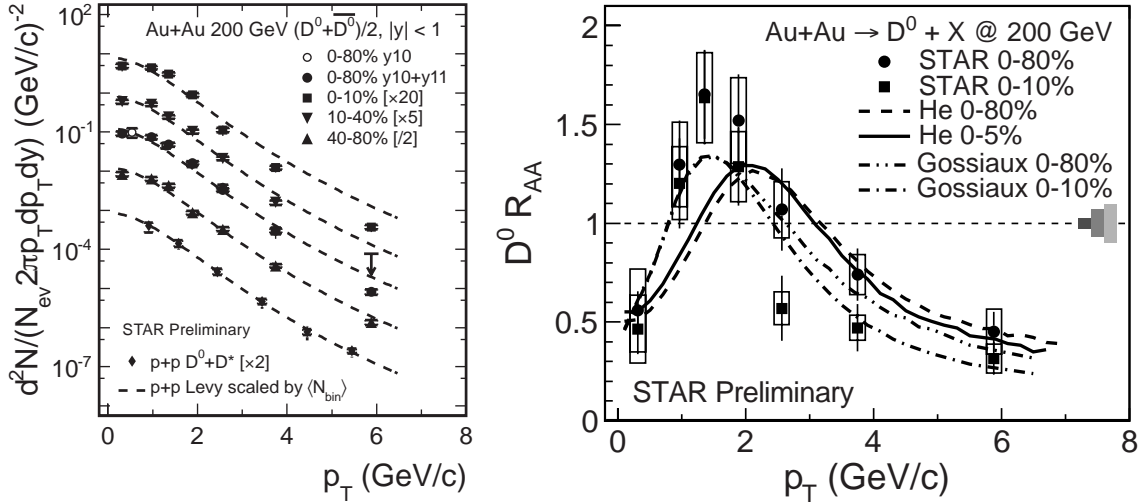


Figure 3: Left Panel: D^0 Invariant Yield spectra for various centralities, The last four p_T bins in $p + p$ collisions are from D^{+*} . Right panel: D^0 nuclear modification factor R_{AA} as a function of p_T for most central (blue) and minimum-bias (red) Au+Au collisions with theoretical predictions from two models [11, 12]. Gray rectangles around unity represent systematic uncertainties, from left to right, N_{bin} definition uncertainty for the most central (2.8%), N_{bin} definition uncertainty for all Au+Au (7%), and $p + p$ normalization error (8.1%).

Yields $Y(p_T, y)$ were calculated in eight p_T and three centrality bins. $d\sigma_{cc}^{NN}/dy$ was obtained from the integral of

$$d^2\sigma_{cc}^{NN}/(2\pi p_T dp_T dy) = \text{Inv}Y \cdot \sigma^{\text{inel}}/N_{bin} \quad (3.1)$$

over p_T and is measured to be $\left. \frac{d\sigma_{c\bar{c}}}{dy} \right|_{y=0} = 175 \pm 13(\text{stat.}) \pm 23(\text{sys.}) \mu\text{b}$. InvY is obtained from (2.1) and $\sigma^{\text{inel}} = 42 \text{ mb}$ is the total inelastic cross section [9]. To calculate the D^0 nuclear modification factor R_{AA} in various centrality bins, we scaled the Levy function [10]

$$\frac{1}{2\pi p_T} \frac{d^2\sigma_{c\bar{c}}}{dp_T dy} = \frac{d\sigma_{c\bar{c}}}{dy} \frac{(n-1)(n-2)}{2\pi n C [nC + m_0(n-2)]} \left(1 + \frac{\sqrt{p_T^2 + m_0^2} - m_0}{nC} \right)^{-n}$$

fit to $p + p$ data by N_{bin} , as shown in the left panel of Fig. 3, and follow the same process for the original power-law function as discussed in section 3.1. Since enhanced statistics allow more p_T bins in Au+Au collisions, we rely on the extrapolation from the two fits to estimate one source of systematic uncertainty. The $p + p$ baseline for R_{AA} calculation is the arithmetic average of the Levy and the power-law fit results. The measurement, shown in the right panel of Fig. 3, reveals strong suppression in the most central collisions for $p_T > 2 \text{ GeV/c}$ consistent with the prediction of the SUBATECH group (Gossiaux) model [12] and exhibits the maximum of the R_{AA} around $p_T \simeq 1.5 \text{ GeV/c}$. This agreement with [12] might indicate that the maximum is induced by the transverse flow picked up from the expanding medium through coalescence with light-quarks.

$d\sigma_{c\bar{c}}^{\text{NN}}/dy|_{y=0}$ as a function of N_{bin} is shown in the right panel of Fig. 4. Within errors, the results are in agreement and follow the number-of-binary-collisions scaling, which indicates that charm quark is produced via initial hard scatterings at early stage of the collisions at RHIC. The FONLL (darker band) and NLO [13] (gradient band) uncertainties are also shown here for comparison.

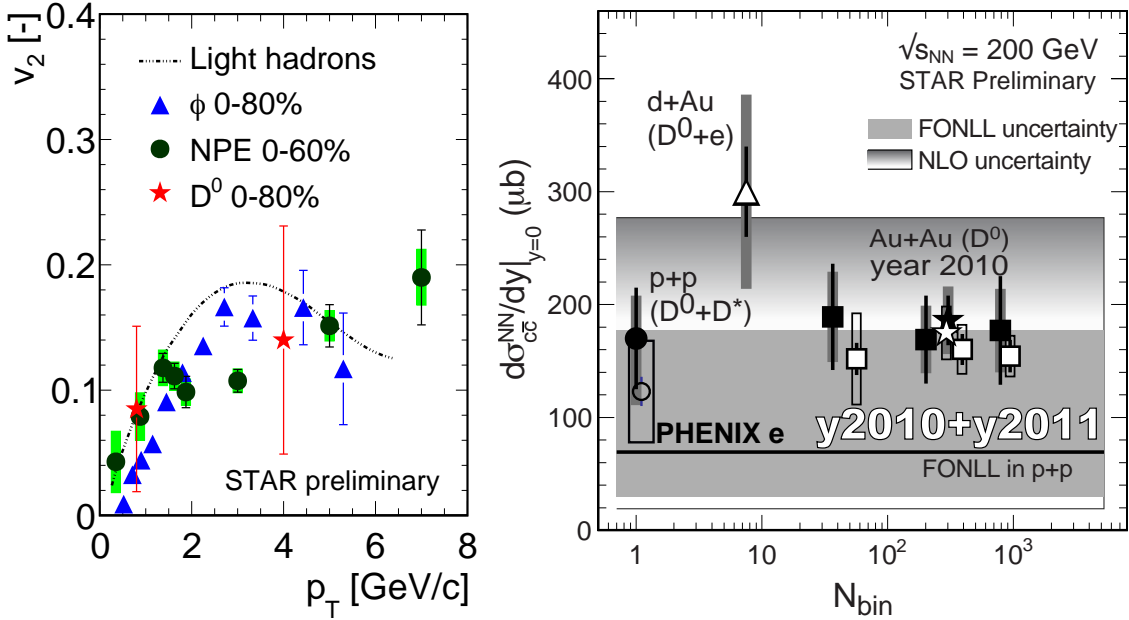


Figure 4: Left Panel: Elliptic flow as a function of p_T . Right panel: The charm production cross section per N_{bin} as a function of N_{bin} .

In the Left panel of Fig. 4, the measurement of D^0 elliptic flow v_2 is shown. Within large statistical error bars, D^0 v_2 is consistent with the STAR Non-photonic electrons v_2 .

4. Conclusions

New open charm hadrons (D^0, D^{*+}) measurements in $p + p$ and Au+Au minimum bias collisions at $\sqrt{s_{\text{NN}}} = 200$ GeV from STAR shows the N_{bin} scaling of the charm quark production cross section at mid rapidity. The differential invariant open charm cross section at mid rapidity is measured as $170 \pm 45(\text{stat.})_{-51}^{+37}(\text{sys.}) \mu\text{b}$ in $p + p$, $175 \pm 13(\text{stat.}) \pm 23(\text{sys.}) \mu\text{b}$ in Au+Au collisions at 200 GeV and $217 \pm 86(\text{stat.}) \pm 73(\text{sys.}) \mu\text{b}$ in $p + p$ collisions at 500 GeV. Results of the total charm cross section are within statistical and systematic uncertainties consistent with both PYTHIA and NLO pQCD predictions.

The new D^0 nuclear modification factor R_{AA} measurement reveals strong suppression in the most central collisions for $p_T > 2$ GeV/c consistent with the prediction of the model [12] and exhibits the maximum of the R_{AA} around $p_T \simeq 1.5$ GeV/c.

References

- [1] M. Cacciari, P. Nason and R. Vogt, Phys. Rev. Lett. **95**, 122001 (2005).
- [2] X. Zhu, *et al.*, PLB **647**, 366 (2007).
- [3] L. Adamczyk *et al.* [STAR Collaboration], Phys. Rev. D **86**, 072013 (2012).
- [4] B. I. Abelev *et al.*, Phys. Rev. Lett. **98**, 192301 (2007).
- [5] M. Shao *et al.*, Nucl. Instrum. Methods A **499**, 624 (2003).
- [6] J. Adams *et al.*, Phys. Rev. Lett. **94**, 062301 (2005).
- [7] J. Adams *et al.* [STAR Collaboration], Phys. Rev. Lett. **91**, 172302 (2003).
- [8] R. Vogt, private communication, (2012).
- [9] M. Honda *et al.*, Phys. Rev. Lett. **70**, 525 (1993).
- [10] G. Wilk and Z. Włodarczyk, Phys. Rev. Lett. **84**, 2770 (2000).
- [11] M. He, R. J. Fries, R. Rapp, arXiv: 1204.4442.
- [12] P. B. Gossiaux, J. Aichelin, M. Bluhm, T. Gousset, M. Nahrgang, S. Vogel, K. Werner, arXiv: 1207.5445.
- [13] R. Vogt, Eur.Phys.J.ST **155** 213 (2008).

Acknowledgments

This work has been supported by the grant 13-02841S of the Czech Science Foundation (GACR) and by the Grant Agency of the Czech Technical University in Prague, grant No. SGS13/215/OHK4/3T/14.

Open charm hadron production via hadronic decays at STAR

David Tlusty for the STAR Collaboration¹

Nuclear Physics Institute, Academy of Sciences and Czech Technical University, Prague, Czech Republic

Abstract

In this article, we report on the STAR results of open charm hadron production at mid-rapidity in $p + p$ and Au+Au collisions at $\sqrt{s_{NN}} = 200$ GeV and $p + p$ collisions at $\sqrt{s} = 500$ GeV. The measurements cover transverse momentum range from 0.6 to 6 GeV/c for $p + p$ 200 GeV collisions, from 1 to 6 GeV/c for $p + p$ 500 GeV collisions and from 0 to 6 GeV/c for Au+Au 200 GeV collisions. D^0 nuclear modification factor and elliptic flow in Au+Au collisions at $\sqrt{s_{NN}} = 200$ GeV are presented.

1. Introduction

The heavy quark production at RHIC is dominated by initial gluon fusion at initial hard partonic collisions and can be described by perturbative QCD (pQCD) due to their large mass [1]. One expects therefore that charm production total cross section $\sigma_{c\bar{c}}^{NN}$ should scale as a function of number-of-binary-collisions N_{bin} . In addition, if charm quarks participate in the collective expansion of the medium, there must have been enough interactions to easily thermalize light quarks. Hence, charm quark is an ideal probe to study early dynamics in high-energy nuclear collisions.

2. Analysis Method and Datasets

Invariant yield of charm quark production $InvY$ is calculated as

$$InvY \equiv \frac{d^2 N_{c\bar{c}}}{2\pi p_T dp_T dy} = \frac{1}{N_{trig}} \frac{Y(p_T, y)}{2\pi p_T \Delta p_T \Delta y} \frac{f_{trg}}{BR f_{frag} \epsilon_{rec}} \quad (1)$$

where N_{trig} is the total number of triggered events used for the analysis. $Y(p_T, y)$ is the raw charm hadron signal in each p_T bin within a rapidity window $\Delta y = 2$. BR is the hadronic decay branching ratio for the channel of interest. ϵ_{rec} is the reconstruction efficiency including geometric acceptance, track selection efficiency, PID efficiency, and analysis cut efficiency. f_{frag} represents the the ratio of charm quarks hadronized to open charm mesons. And f_{trg} is the correction factor to account for the bias between the minimum-bias sample used in this analysis and the total NSD sample [2]. f_{trg} is found to be unity in Au+Au, 0.65 in $p + p$ collisions at $\sqrt{s} = 200$ GeV and 0.58 in $p + p$ collisions at $\sqrt{s} = 500$ GeV.

¹A list of members of the STAR Collaboration and acknowledgements can be found at the end of this issue.

$Y(p_T, y)$ is obtained from fitting the reconstructed invariant mass spectrum (Fig. 1) of open charm mesons through hadronic decays: $D^0(\bar{D}^0) \rightarrow K^\mp \pi^\pm$ (BR = 3.89%) and $D^{*\pm} \rightarrow D^0(\bar{D}^0) \pi^\pm$ (BR = 67.7%) $\rightarrow K^- \pi^+ \pi^\pm$ (total BR = 2.63%)

The identification of daughter particles is done in the STAR experiment [4] at mid-rapidity $|y| < 1$ at $\sqrt{s_{NN}} = 200$ and 500 GeV. The analysis presented herein is done using three datasets; the first one collected in year 2009 ($N_{\text{trig}} \sim 105$ million 200 GeV p+p collisions), the second one collected in 2010 and 2011 ($N_{\text{trig}} \sim 800$ million Au+Au 200 GeV collisions), and the third one in 2011 ($N_{\text{MB}} \sim 50$ million 500 GeV p+p collisions).

At present, STAR does not have the capability to reconstruct the secondary vertex of D^0 decay; one must calculate the invariant mass of all $K\pi$ pairs coming from the vicinity of the primary vertex. This results in a large combinatorial background which was reconstructed via the mixed-event method (Au+Au dataset), same-charge-sign, and kaon momentum-rotation ($p + p$ dataset) and subtracted from invariant mass spectra of all particle pairs [5]. To reconstruct D^* , one may exploit the softness of $D^* \rightarrow D^0 \pi$ decay; combine low momentum pions with D^0 candidates, i.e. pairs with $1.82 < M(K\pi) < 1.9$ GeV/c², and plot difference $M(K\pi\pi) - M(K\pi)$ whose resolution is determined by mostly the soft pion high momentum resolution. The combinatorial background is reconstructed by side-band (picking $K\pi$ pair outside the D^0 mass region) and wrong-sign (picking soft pion with opposite charge) methods. The dominant source of systematic uncertainties for both D^0 and D^* analyses is the difference between yields obtained from subtractions of combinatorial background from all particle combinations.

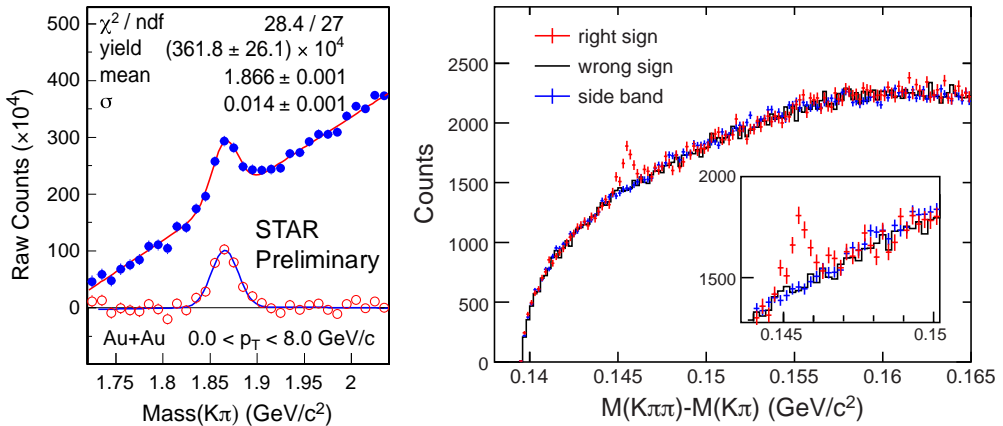


Figure 1: Left panel: D^0 signal in Au+Au 200 GeV collisions after mixed-event background subtraction. Right panel: D^* signal in $p + p$ 200 GeV collisions with comb. background reproduced by wrong-sign and side-band methods [2].

3. Results

3.1. D meson production in $p + p$ collisions

Yields $Y(p_T, y)$ are calculated in six p_T bins (first two for D^0 , the next four for D^*) in $p + p$ 200 GeV and five p_T bins (first for D^0 , the next four for D^*) in $p + p$ 500 GeV. The charm cross section at mid-rapidity $d\sigma^{c\bar{c}}/dy$ was obtained from the power-law function fit [2] to $d^2\sigma^{c\bar{c}}/(2\pi p_T dp_T dy) = \text{Inv}Y \cdot \sigma_{\text{NSD}}$, where $\text{Inv}Y$ is obtained from (1). σ^{NSD} is the total Non-single Diffractive (NSD) cross section, which is measured at STAR to be 30.0 ± 2.4 mb at $\sqrt{s} = 200$

GeV [6]. In the case of $\sqrt{s} = 500$ GeV, there's no STAR measurement yet; σ^{NSD} is extrapolated from 200 GeV measurement with the help of PYTHIA simulation to be 34 mb. The charm pro-

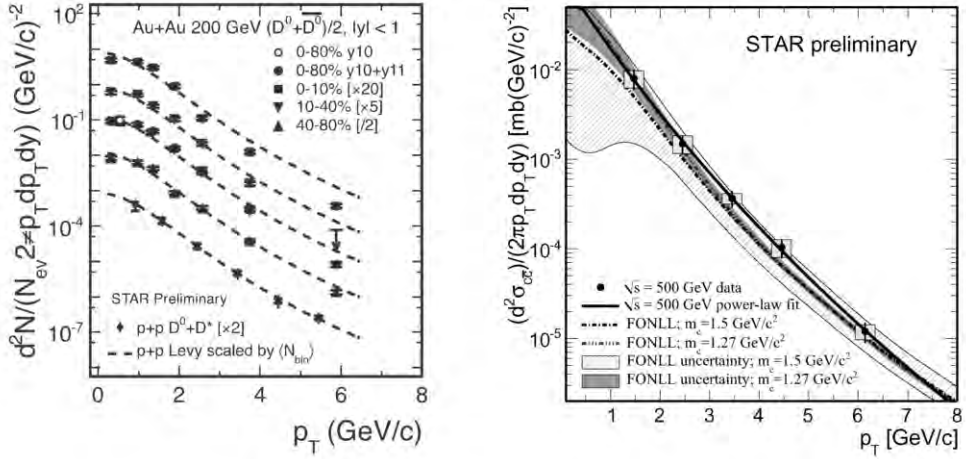


Figure 2: Left Panel: D^0 InvY spectra for various centralities, The last four p_T bins in $p + p$ collisions are from D^{*+} . Right Panel: Charm quark production invariant cross section as a function of D meson p_T in 500 GeV $p+p$ collisions with two FONLL predictions [7] using normalization and factorization scale equal to charm quark mass m_c .

duction cross section at mid rapidity $\frac{d\sigma_{cc}}{dy} \Big|_{y=0}$ is $170 \pm 45(\text{stat.})_{-51}^{+37}(\text{sys.}) \mu\text{b}$ at $\sqrt{s} = 200$ GeV and is $217 \pm 86(\text{stat.}) \pm 73(\text{sys.}) \mu\text{b}$ at $\sqrt{s} = 500$ GeV. FONLL predictions for p_T spectra [7] shown in Fig. 2.

3.2. D^0 production in Au+Au collisions

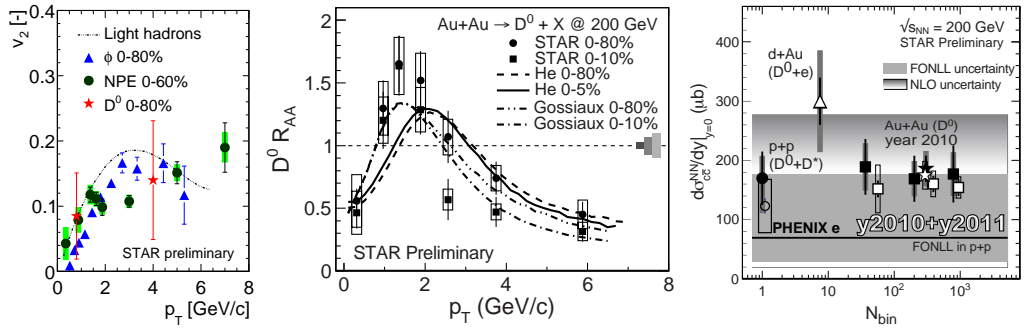


Figure 3: Left Panel: Elliptic flow as a function of p_T . Middle panel: D^0 nuclear modification factor R_{AA} as a function of p_T for most central (blue) and minimum-bias (red) Au+Au collisions with theoretical predictions from two models [10, 11]. Green rectangles around unity represent systematic uncertainties, from left to right, N_{bin} definition uncertainty for the most central (2.8%), N_{bin} definition uncertainty for all Au+Au (7%), and $p + p$ normalization error (8.1%). Right panel: The charm production cross section per N_{bin} as a function of N_{bin} .

Yields $Y(p_T, y)$ were calculated in eight p_T and three centrality bins. $d\sigma_{cc}^{\text{NN}}/dy$ was obtained from the integral of

$$d^2\sigma_{cc}^{\text{NN}}/(2\pi p_T dp_T dy) = \text{InvY} \cdot \sigma^{\text{inel}}/N_{\text{bin}} \quad (2)$$

over p_T and is measured to be $\left. \frac{d\sigma_{c\bar{c}}}{dy} \right|_{y=0} = 175 \pm 13(\text{stat.}) \pm 23(\text{sys.}) \mu\text{b}$. $\text{Inv}Y$ is obtained from (1) and $\sigma^{\text{inel}} = 42 \text{ mb}$ is the total inelastic cross section [8]. To calculate the D^0 nuclear modification factor R_{AA} in various centrality bins, we scaled the Levy function [9] fit to $p + p$ data by N_{bin} , as shown in the left panel of Fig. 2, and follow the same process for the original power-law function as discussed in section 3.1. Since enhanced statistics allow more p_T bins in Au+Au collisions, we rely on the extrapolation from the two fits to estimate one source of systematic uncertainty. The $p + p$ baseline for R_{AA} calculation is the arithmetic average of the Levy and the power-law fit results. The measurement, shown in the middle panel of Fig. 3, reveals strong suppression in the most central collisions for $p_T > 2 \text{ GeV/c}$ consistent with the prediction of the SUBATECH group (Gossiaux) model [11] and exhibits the maximum of the R_{AA} around $p_T \simeq 1.5 \text{ GeV/c}$. This agreement with [11] might indicate that the maximum is induced by the transverse flow picked up from the expanding medium through coalescence with light-quarks.

$d\sigma_{c\bar{c}}^{\text{NN}}/dy|_{y=0}$ as a function of N_{bin} is shown in the right panel of Fig. 3. Within errors, the results are in agreement and follow the number-of-binary-collisions scaling, which indicates that charm quark is produced via initial hard scatterings at early stage of the collisions at RHIC. The FONLL (darker band) and NLO [12] (gradient band) uncertainties are also shown here for comparison.

In the Left panel of Fig. 3, the measurement of D^0 elliptic flow v_2 is shown. Within large statistical error bars, $D^0 v_2$ is consistent with the STAR Non-photonic electrons v_2 indicating non zero elliptic flow of D^0 mesons in Au+Au collisions at $\sqrt{s_{\text{NN}}} = 200 \text{ GeV}$.

4. Conclusions

New open charm hadrons (D^0, D^{*+}) measurements in $p + p$ and Au+Au minimum bias collisions at $\sqrt{s_{\text{NN}}} = 200 \text{ GeV}$ from STAR shows the N_{coll} scaling of the charm quark production cross section at mid rapidity. $d\sigma_{c\bar{c}}^{\text{NN}}/dy|_{y=0} = 170 \pm 45(\text{stat.})_{-51}^{+37}(\text{sys.}) \mu\text{b}$ in $p + p$, $175 \pm 13(\text{stat.}) \pm 23(\text{sys.}) \mu\text{b}$ in Au+Au collisions at 200 GeV and $217 \pm 86(\text{stat.}) \pm 73(\text{sys.}) \mu\text{b}$ in $p + p$ collisions at 500 GeV.

The new D^0 nuclear modification factor R_{AA} measurement reveals strong suppression in the most central collisions for $p_T > 2 \text{ GeV/c}$ consistent with the prediction of the model [11] and exhibits the maximum of the R_{AA} around $p_T \simeq 1.5 \text{ GeV/c}$.

This work was supported by grants INGO LA09013 and SGS10/292/OHK4/3T/14.

References

- [1] M. Cacciari, P. Nason and R. Vogt, Phys. Rev. Lett. **95**, 122001 (2005).
- [2] L. Adamczyk *et al.* [STAR Collaboration], Phys. Rev. D **86**, 072013 (2012).
- [3] B. I. Abelev *et al.*, Phys. Rev. Lett. **98**, 192301 (2007).
- [4] M. Shao *et al.*, Nucl. Instrum. Methods A **499**, 624 (2003).
- [5] J. Adams *et al.*, Phys. Rev. Lett. **94**, 062301 (2005).
- [6] J. Adams *et al.* [STAR Collaboration], Phys. Rev. Lett. **91**, 172302 (2003).
- [7] R. Vogt, private communication, (2012).
- [8] M. Honda *et al.*, Phys. Rev. Lett. **70**, 525 (1993).
- [9] G. Wilk and Z. Włodarczyk, Phys. Rev. Lett. **84**, 2770 (2000).
- [10] M. He, R. J. Fries, R. Rapp, arXiv: 1204.4442.
- [11] P. B. Gossiaux, J. Aichelin, M. Bluhm, T. Gousset, M. Nahrgang, S. Vogel, K. Werner, arXiv: 1207.5445.
- [12] R. Vogt, Eur.Phys.J.ST **155** 213 (2008).

Open charm hadron production via hadronic decays at STAR

David Tlustý for the STAR collaboration

^aNuclear Physics Institute, Academy of Sciences Czech Republic, Na Truhlářce 39/64, 180 86 Praha 8, Czech Republic

^bCzech Technical University in Prague, Faculty of Nuclear Sciences and Physical Engineering, Břehová 7, 11519, Prague 1, Czech Republic

Abstract

Heavy quarks are a unique probe to study the medium produced in ultra-relativistic heavy ion collisions. The dominant process of charm quark production at RHIC is believed to be initial gluon fusion which can be calculated in perturbative QCD. The upper limit of FONLL calculation seems to be in good agreement with charm cross section measurements at mid-rapidity in $p + p$ collisions at $\sqrt{s_{NN}} = 200$ GeV provided by STAR. The same measurement in Au+Au collisions at equal energy reveals the number-of-binary-collisions scaling of the charm cross section indicating that charm production is dominated by initial hard scatterings. In this article, we report the measurements of D^0 , D^+ in $p + p$ at $0.6 \text{ GeV}/c < p_T < 6 \text{ GeV}/c$ and D^0 in Au+Au collisions at $0.2 \text{ GeV}/c < p_T < 5 \text{ GeV}/c$ via hadronic decays $D^0 \rightarrow K^-\pi^+$, $D^{*+} \rightarrow D^0\pi^+ \rightarrow K^-\pi^+\pi^+$ at mid-rapidity $|y| < 1$.

Keywords: STAR, QGP, Heavy Flavor, Open Charm

1. Introduction

The charm quark production is dominated by initial gluon fusion in initial hard partonic collisions and well described by perturbative QCD (pQCD) because of the large charm quark mass ($\sim 1.5 \text{ GeV}/c^2$) [1]. The mass is almost exclusively generated through its coupling to the Higgs field in the electroweak sector, while masses of (u, d, s) quarks are dominated by spontaneous breaking of chiral symmetry (CS) in QCD [2]. This means that charm quarks remain heavy even if CS is restored, as it likely is in a QGP. Since charm is produced mainly in initial hard scatterings, one expects that charm production total cross section σ_{cc}^{NN} should scale as a function of number-of-binary-collisions N_{bin} . In addition, if charm quarks participate in the collective expansion of the medium, there must have been enough interactions to easily thermalize light quarks. Hence, charm quarks are an ideal probe to study early dynamics in high-energy nuclear collisions.

2. Measurement

The charm cross section at mid-rapidity is calculated from the open charm hadron yields. These yields are obtained from the invariant mass reconstruction of open charm mesons through hadronic decays: $D^0(\overline{D}^0) \rightarrow K^\mp\pi^\pm$ (BR = 3.89%) and $D^{*+} \rightarrow D^0(\overline{D}^0)\pi^\pm$ (BR = 67.7%) $\rightarrow K^-\pi^+\pi^+$. The identification of daughter particles was done in the STAR experiment (see Fig. 1) at mid-rapidity $|y| < 1$ in $p + p$ and Au+Au collisions at $\sqrt{s_{NN}} = 200$ GeV.

Email address: tlustdav@fjfi.cvut.cz (David Tlustý for the STAR collaboration)

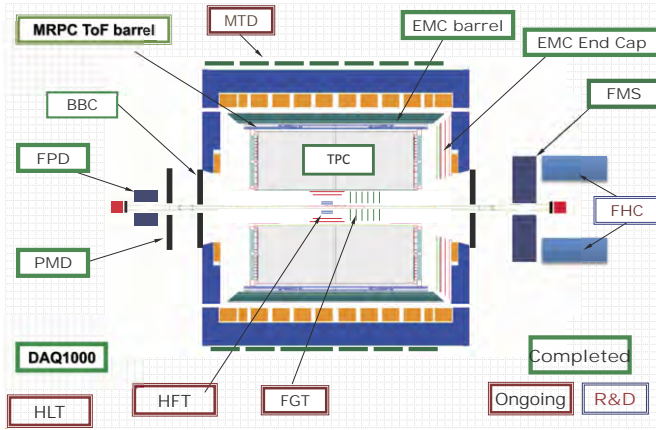


Figure 1: The STAR detector. TPC (Time Projection Chamber) is main detector for tracking and PID (providing dE/dx , \vec{p}), TOF (Time Of Flight) for PID improvement, and pile-up tracks removal and BEMC (Barrel Electromagnetic Calorimeter) in this analysis for pile-up tracks removal if TOF is not available.

The analysis presented herein was done using two datasets; the first one collected in 2009 with minimum bias trigger defined as a coincidence in Vertex Position Detectors East and West (105 million events total) and the second one collected in 2010 with minimum bias trigger defined as a signal in Zero Degree Calorimeter (280 million events total).

The subdetectors used in this analysis were:

- Time Projection Chamber (TPC) providing 3D image of a particle track and ionization energy loss (dE/dx) and covering a large acceptance with full 2π azimuthal angle at $|\eta| < 1$. The track momentum is calculated from its curvature in the uniform magnetic field.
- Time-Of-Flight (TOF) detector providing the time of the particle's flight from primary vertex to a channel pad and covering 72% in 2009 and 100% in 2010 of the whole barrel ($|\eta| < 1$). When combined with the momentum measurement from the TPC, this allows to separate pions from kaons up to 1.6 GeV/c [4].

STAR doesn't have any subsystem being able to reconstruct secondary the vertex of D^0 or D^* decay; one must calculate the invariant mass of all $K\pi$ pair coming from the vicinity of the primary vertex. This results in a large combinatorial background which was reconstructed via the event-mixing method (Au+Au dataset), same-charge-sign, and kaon momentum-rotation (in a kaon-pion pair in the $p + p$ dataset) and subtracted from the invariant mass distributions from all particle pairs [5]. To reconstruct D^* , one may exploit the low Q -value of the $D^* \rightarrow D^0\pi$ decay and combine low momentum pions with D^0 candidates, i.e. pairs with $1.82 < M(K\pi) < 1.9$ GeV/c, and plot difference $M(K\pi\pi) - M(K\pi)$. Such value occupies the beginning of the phase space; hence it does not suffer from large combinatorial background making the D^* direct observation possible. The combinatorial background was reconstructed by side-band (picking D^0 candidates outside the D^0 mass region) and wrong-sign (picking soft pion with opposite charge) methods. The difference between these methods is the dominant source of systematic uncertainties for both D^0 and D^* analyses.

Open charm hadrons yields Y_{D^0, D^*} were calculated as Gaussian function areas from the invariant mass peaks fits shown in Figure 2. Raw counts were corrected with the reconstruction efficiency in used sub-detectors to obtain the corrected yields Y_{D^0, D^*} .

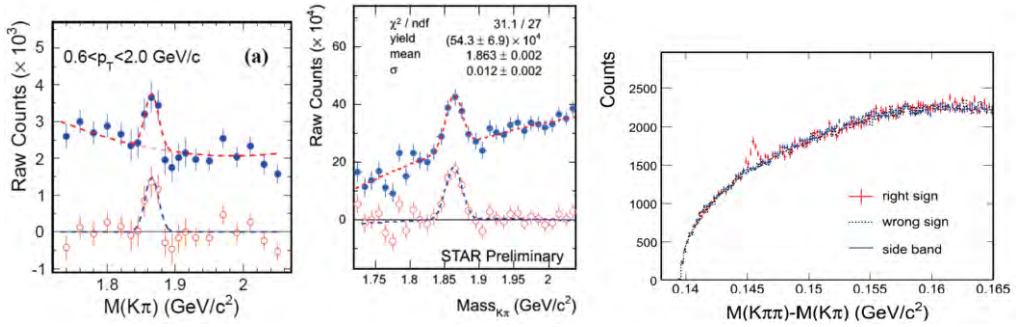


Figure 2: Left panel: D^0 signal in p+p 200 GeV collisions after same-sign background subtraction [6]. Middle panel: D^0 signal in Au+Au 200 GeV collisions after mixed-event background subtraction. Right panel: D^* signal in p+p 200 GeV collisions. Combinatorial background is reproduced by the distributions from the wrong-sign (black dotted) and side-band (blue solid) methods [6].

3. RESULTS

Yields were calculated in 6 p_T bins (2 for D^0 , 4 for D^*) in the $p+p$ dataset and 5 p_T bins (all for D^0) in the Au+Au dataset. Then the invariant charm cross section $d^2\sigma_{p+p}^{c\bar{c}}/(2\pi p_T dp_T dy)$ was calculated as

$$\frac{d^2\sigma_{p+p}^{c\bar{c}}}{2\pi p_T dp_T dy} = \frac{Y\sigma^{\text{NSD}}}{2\pi p_T \Delta p_T \Delta y \text{BR}} \frac{f_T}{N f_{\text{frag.}}} \quad (1)$$

in each p_T bin within a rapidity window $\Delta y = 2$. (σ^{NSD} is non-single diffractive p+p inelastic cross section, $f_{\text{frag.}} = 0.565$ is the ratio of charm quarks hadronized to open charm mesons [7] and f_T is the trigger bias correction). The charm cross section at mid rapidity $d\sigma^{c\bar{c}}/dy$ was obtained from a power-law function fit to $d\sigma^{c\bar{c}}/(2\pi p_T dp_T dy)$ points (see Fig. 3) as $170 \pm 45(\text{stat.})^{+37}_{-51}(\text{sys.}) \mu\text{b}$. In Au+Au collisions, the cross section per a nucleon-nucleon (NN) collision at mid rapidity is calculated from the Au+Au invariant yield dN/dy by dividing by the number of binary collisions N_{bin} ; no trigger bias is preset in this case and σ^{NSD} has to be replaced by total inelastic cross section $\sigma^{\text{inel}} = 42 \text{ mb}$.

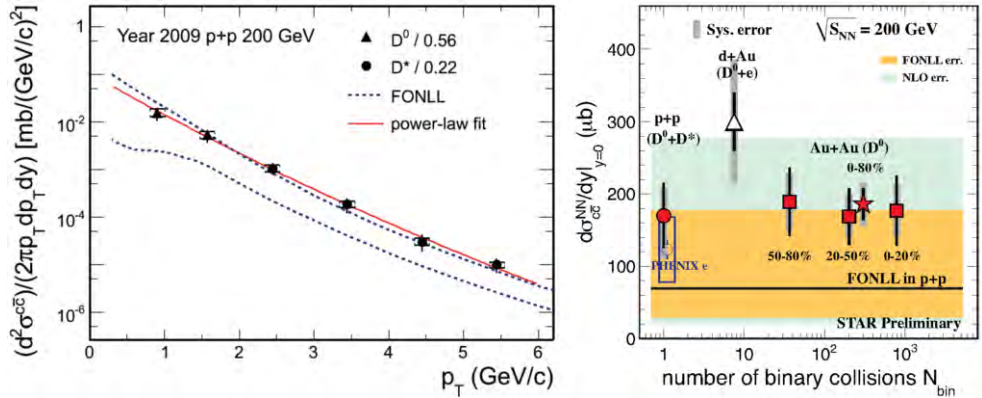


Figure 3: Left Panel: $c\bar{c}$ pair production cross section (symbols) as a function of p_T in 200 GeV p+p collisions [6]. Right Panel: The charm production cross section per nucleon-nucleon collision at mid-rapidity as a function of N_{bin} .

The $d\sigma^{c\bar{c}}/dy$ at mid-rapidity in Au+Au collisions was extracted, from a power-law fit as $186 \pm 22(\text{stat.}) \pm 30(\text{sys.}) \pm 18(\text{norm.}) \mu\text{b}$ assuming that the $f_{\text{frag.}}$ does not change from p+p to Au+Au collisions. The charm cross section for three centrality bins, 0-20%, 20-50% and 50-80%, is obtained according to the integrated yields. The charm production cross section per nucleon-nucleon collision at mid-rapidity as a function of N_{bin} is shown in the right panel of Fig. 3. Within errors, the results are in agreement and follow the number of binary collisions scaling, which indicates that charm quark is produced via initial hard scatterings at early stage of the collisions at RHIC. The FONLL (orange band) and NLO [8] (light-blue band) uncertainties are also shown here for comparison.

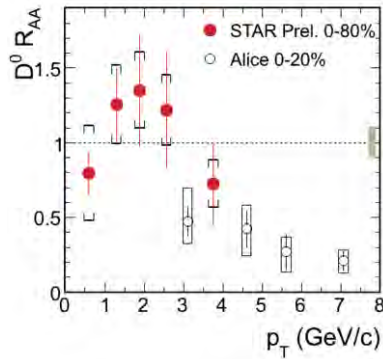


Figure 4: D^0 nuclear modification factor R_{AA} as a function of p_T . ALICE preliminary data taken from [9]

The $R_{AA}^{D^0}$ depicted in Figure 4 was obtained via dividing D^0 yields in Au+Au 0-80% minbias collisions by the power-law fit to p+p yields scaled by N_{bin} . The uncertainty of the p+p power-law shape is taken into account as systematic error. No suppression is observed at $p_T < 4$ GeV/c.

4. CONCLUSIONS

Open charm hadrons (D^0, D^{*+}) are measured in p+p and Au+Au collisions at $\sqrt{s_{NN}} = 200$ GeV at STAR. The charm cross section per nucleon-nucleon collision at mid-rapidity follows the number of binary collisions scaling. The charm pair production cross sections per nucleon-nucleon collision at mid-rapidity are measured to be $d\sigma^{c\bar{c}}/dy = 170 \pm 45(\text{stat.})^{+37}_{-51}(\text{sys.}) \mu\text{b}$ in p+p and $186 \pm 22(\text{stat.}) \pm 30(\text{sys.}) \pm 18(\text{norm.}) \mu\text{b}$ in Au+Au minimum bias collisions. In the near future the STAR Heavy Flavor Tracker [10] will provide the necessary resolution to reconstruct secondary vertices of charm mesons, which will increase the precision of the charm measurements.

Acknowledgments

This work was supported by grant INGO LA09013 of the Ministry of Education, Youth and Sports of the Czech Republic, and by the Grant Agency of the Czech Technical University in Prague, grant No. SGS10/292/OHK4/3T/14.

References

- [1] M. Cacciari, P. Nason and R. Vogt, Phys. Rev. Lett. 95 (2005) 122001.
- [2] X. Zhu, et al., PLB 647 (2007) 366.
- [3] B. I. Abelev et al., Phys. Rev. Lett. 98 (2007) 192301.
- [4] M. Shao et al., Nucl. Instrum. Methods A 499 (2003) 624.
- [5] J. Adams et al., Phys. Rev. Lett. 94 (2005) 062301.
- [6] L. Adamczyk et al. [STAR Collaboration], arXiv:1204.4244 (2011).
- [7] C. Amsler et al., Phys. Lett. B 667 (2008) 1.
- [8] R. Vogt, Eur. Phys. J. ST 155 (2008) 213.
- [9] A. Grelli et al., SQM 2011 Conference Proceedings, arXiv:1201.2262.
- [10] Z. Xu et al., J. Phys. G 32 (2006) S571.

Measurements of Open Heavy Flavor Production in STAR

David Tlustý for STAR collaboration

Nuclear Physics Institute, Academy of Sciences Czech Republic, Na Truhlářce 39/64, 180 86 Praha 8, Czech Republic
Czech Technical University in Prague, Faculty of Nuclear Sciences and Physical Engineering, Břehová 7, 11519, Prague 1, Czech Republic

E-mail: tlustdav@fjfi.cvut.cz

Abstract. In this article, we report the measurements of D^0 , D^* in $p + p$ at $0.6 \text{ GeV}/c < p_T < 6 \text{ GeV}/c$ and D^0 in Au+Au collisions at $0.2 \text{ GeV}/c < p_T < 5 \text{ GeV}/c$ via hadronic decays $D^0 \rightarrow K^- \pi^+$, $D^{*+} \rightarrow D^0 \pi^+ \rightarrow K^- \pi^+ \pi^+$ and non-photonic electrons spectra at $3 \text{ GeV}/c < p_T < 10 \text{ GeV}/c$ reconstruction in $\sqrt{s_{NN}} = 200 \text{ GeV}$ $p + p$ collisions at mid-rapidity.

1. INTRODUCTION

Heavy quark production is dominated by initial gluon fusion and can be described by perturbative QCD (pQCD) due to their large mass [1]. The measurement of heavy quark production total cross section in $p + p$ and Au+Au collisions is important to understand both open heavy flavor and heavy quarkonia production mechanisms in the nuclear matter. The study of heavy quark production in relativistic nuclear collisions follows two different approaches: (i) the direct reconstruction of heavy flavor mesons and (ii) the identification of electrons from semi-leptonic decays of such mesons.

The data presented in this paper were collected with the Solenoidal Tracker at RHIC (STAR) detector [2] (Figure 1). Main detector subsystems used for these analyses are the large cylindrical time projection chamber (TPC), which is able to track charged particles in the pseudo-rapidity range $|\eta| < 1.8$ with full azimuthal coverage [3], time of flight (TOF) significantly improving charged hadrons identification [4] and barrel electromagnetic calorimeter (BEMC) being able to trigger on high- p_T particles and improving electron-hadron separation [5]. Both TOF and BEMC subsystems provide full azimuthal coverage as TPC, but slightly reduces pseudo-rapidity range $|\eta| < 1.0$. A uniform magnetic field of 0.5 T is applied along the beamline by the surrounding solenoidal coils, allowing the p_T of charged particles to be determined.

2. DATA ANALYSES

2.1. Direct reconstruction

Direct reconstruction of open charm mesons is being performed by the STAR collaboration using decay channels $D^0 \rightarrow K^- \pi^+$ with branching ratio of 3.83%, $D^* \rightarrow D^0 \pi^+$ with branching ratio of 67.7% in $p+p$ collisions, and former in Au+Au

Solenoidal Tracker At RHIC : $-1 < \eta < 1, 0 < \phi < 2\pi$

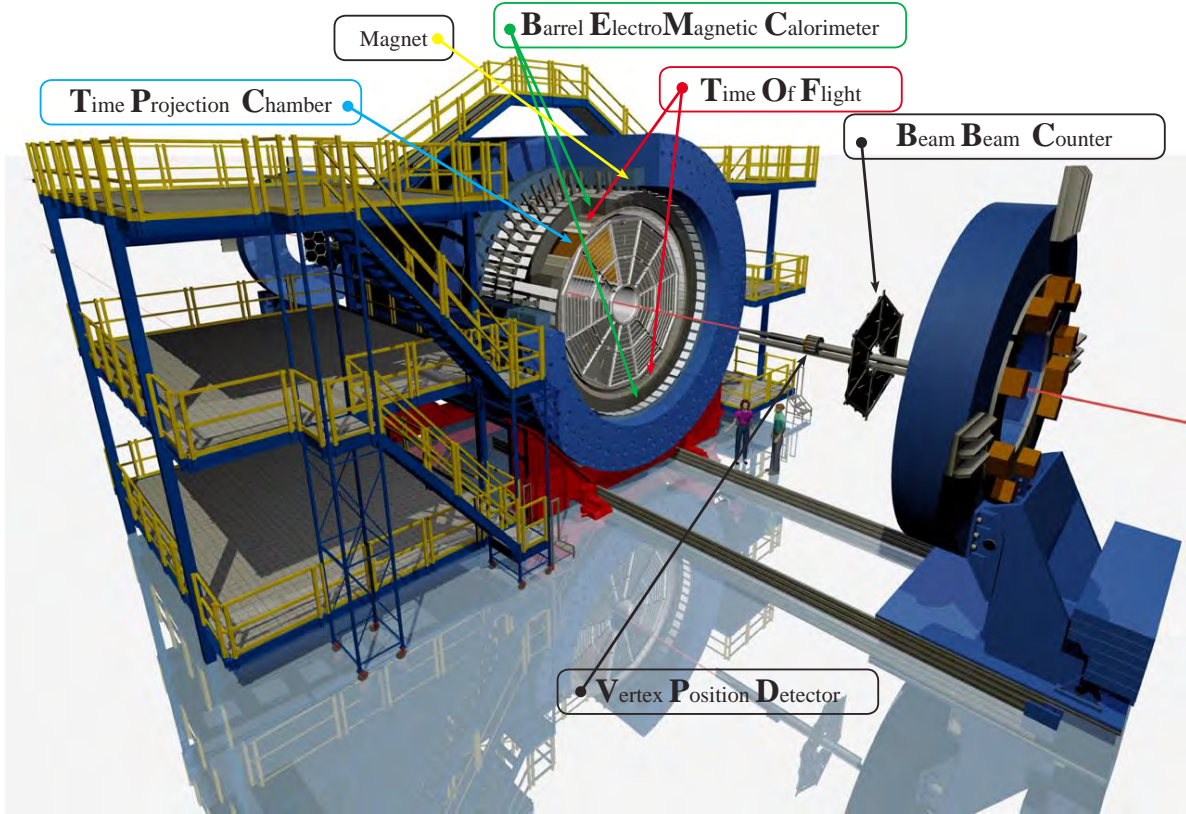


Figure 1. The STAR detector. TPC (Time Projection Chamber) is main detector for tracking and PID (provides $dE/dx, \vec{p}$), TOF (Time Of Flight) is used for PID improvement and pileup tracks removal, BEMC (Barrel Electromagnetic Calorimeter) used for electron identification improvement and pile-up tracks removal.

collisions at $\sqrt{s_{NN}} = 200$ GeV. Because of the small branching ratio and the lack of dedicated detector determining decay vertices, the direct reconstruction of D-mesons requires the analysis of a large amount of data. The available statistics limits the study of such mesons to the p_T region ($0.6 < p_T < 6$ GeV and $0.2 < p_T < 8$ GeV). Kaons and pions are identified using the TPC dE/dx and TOF $1/\beta$. The resulting invariant mass spectrum of kaon-pion pairs contains a substantial amount of background from random combinatorics that can be subtracted using various independent methods:

- (i) **Mixed-Event:** Events are categorized according to the event multiplicity. Pions from one event are paired with kaons from other random events from an event pool with similar global features.
- (ii) **Track-Rotation:** Each π is paired with K with reversed 3-momenta (within same event).
- (iii) **Same-Sign:** pions are paired with same charged kaons (within same event). The geometric mean for positive N_{++} and negative N_{--} pair is calculated as $2\sqrt{N_{++}N_{--}}$.

We used Mixed-Event for Au+Au collisions and an average of Track-Rotation and Same-Sign for $p + p$ collision where difference between raw signals obtained by subtraction of background was the main source of systematic uncertainties. Figure 2 left and center panels show raw D^0 signals after combinatorial background reconstruction. A second-order polynomial function is used to fit the residual background. The background fitting with a first-order polynomial function gives negligible difference. A Gaussian function is used to fit the signal. The raw yield of the D^0 is obtained by fitting the data (blue solid circles) with a fit function representing the sum of signal and background (red dashed curve) in the mass region of $1.72 < M_{K\pi} < 2.05 \text{ GeV}/c^2$. The signal after the residual background subtraction is shown as the red open circles. The Gaussian function used to describe the signal is shown as the blue dashed curve.

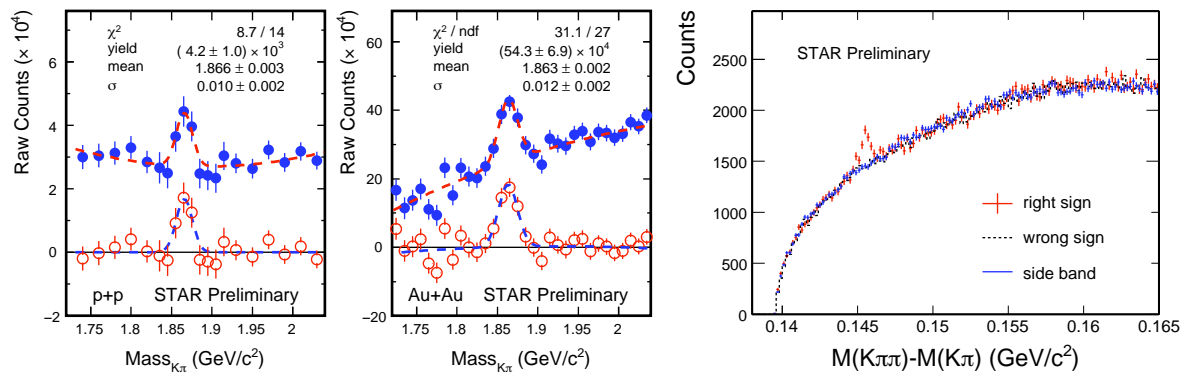


Figure 2. Left and center panels: D^0 signals in p+p and Au+Au 0-80% minbias collisions after same-sign and mix-event background subtraction, respectively. Right panel: D^* signal in p+p collisions. Combinatorial background is reproduced by the distributions from the wrong-sign (black dotted) and side-band (blue solid) methods.

In the case of D^* , we followed the same analysis technique as described in [6]. Compared to the cuts used in [6], the p_T threshold cut for the π^+ (from D^* decays), denoted as π_s^+ , was lowered to 0.15 GeV/c. The ratio, r , of transverse momenta from the D^0 and π_s^+ was required to be $7 < r < 20$. These two changes were implemented to improve the statistics near the lower bound in p_T . The invariant mass difference $\Delta M = M(K\pi\pi) - M(K\pi)$ was calculated in reconstructing the D^* signal to take advantage of the partial cancellation in the detector resolution in measured mass distributions. The ΔM distributions are shown in the right panel of Fig. 2. The right-sign combinations $K^\mp \pi^\pm \pi_s^\pm$ were used to select the $D^{*\pm}$ candidates. Two independent methods - wrong-sign combinations (opposite sign of π_s) and D^0 side-band combinations - were used for combinatorial background reconstruction. The plot illustrates that both methods reproduce the combinatorial background very well.

2.2. Identification of electrons from semi-leptonic decays

The analysis of non-photonic electrons consists of three main steps: selection of a clean electron sample; subtraction of electron background arising from interactions in material and decays; and residual corrections of the signal yield. The inclusive electron

identification was done using TPC dE/dx + BEMC information (matching of track momentum and electromagnetic energy) + Shower Max Detector (SMD) information (the shape of the electro magnetic shower, that is much wider for electrons). The analysis details and a discussion of the sources of uncertainty can be found in [9]. The main background in this analysis is the substantial flux of photonic electrons from photon conversion in the detector material and Dalitz decay of π^0 and η mesons. These contributions need to be subtracted in order to extract the non-photonic electron yield according to formula

$$N(\text{npe}) = N(\text{inc}) \cdot \varepsilon_{\text{purity}} - \frac{N(\text{pho})}{\varepsilon_{\text{pho}}}, \quad (1)$$

where $N(\text{npe})$ is the non-photonic electron yield, $N(\text{inc})$ is the inclusive electron yield, $N(\text{pho})$ is the photonic electron yield, ε_{pho} is the photonic electron reconstruction efficiency defined as the fraction of the photonic electrons identified through invariant mass reconstruction, and $\varepsilon_{\text{purity}}$ is the purity reflecting hadron contamination in the inclusive electron sample.

3. RESULTS

3.1. Direct reconstruction

Raw Yields $N_{\text{raw}}^{D \text{ mesons}}$ were calculated in 7 p_T bins (3 for D^0 , 4 for D^*) for p+p data and 5 p_T bins for Au+Au data. Then the invariant charm cross section $d\sigma_{\text{p+p}}^{\bar{c}c}/(2\pi p_T dp_T dy)$ was calculated by formula

$$\frac{d\sigma^{\bar{c}c}}{2\pi p_T dp_T dy} = \frac{N_{\text{raw}}^{D \text{ mesons}} \sigma^{\text{NSD}}}{2\pi p_T \Delta p_T \Delta y \text{BR}} \frac{\epsilon_T}{N f_{\text{frag.}}} \quad (2)$$

in each p_T bin (σ^{NSD} is non-single diffractive p+p inelastic cross section, $f_{\text{frag.}}$ is the ratio of charm quarks hadronized to open charm mesons and ϵ_T represents the trigger bias correction including the vertex reconstruction efficiency in the measurement). The charm cross section at mid rapidity $d\sigma^{\bar{c}c}/dy$ was obtained from power-law function fit to $d\sigma^{\bar{c}c}/(2\pi p_T dp_T dy)$ points (see Fig. 3) as $202 \pm 56(\text{stat.}) \pm 40(\text{sys.}) \pm 20(\text{norm.}) \mu\text{b}$. In Au+Au collisions we calculate invariant yield $d^2N/(N_{\text{ev}} p_T dp_T dy)$.

The $d\sigma^{\bar{c}c}/dy$ at mid-rapidity in Au+Au collisions was extracted, from the average of a power-law(dot-dashed curve) and a blast-wave (dashed curve) fit (Fig. 4) as $186 \pm 22(\text{stat.}) \pm 30(\text{sys.}) \pm 18(\text{norm.}) \mu\text{b}$ assuming that the $f_{\text{frag.}}$ does not change from p+p to Au+Au collisions. The power-law fit to p+p scaled by the average number of binary collisions (N_{bin}) is shown as solid curve. The charm cross section for three centrality bins, 0-20%, 20-50% and 50-80%, is obtained according to the integrated yields. The charm production cross section per nucleon-nucleon collision at mid-rapidity as a function of N_{bin} is shown in the right panel of Fig. 3. Within errors, the results are in agreement and follow the number of binary collisions scaling, which indicates that charm quark is produced via initial hard scatterings at early stage of the collisions at RHIC. The FONLL(orange band)and NLO [7] (light-blue band) uncertainties are also shown here for comparison.

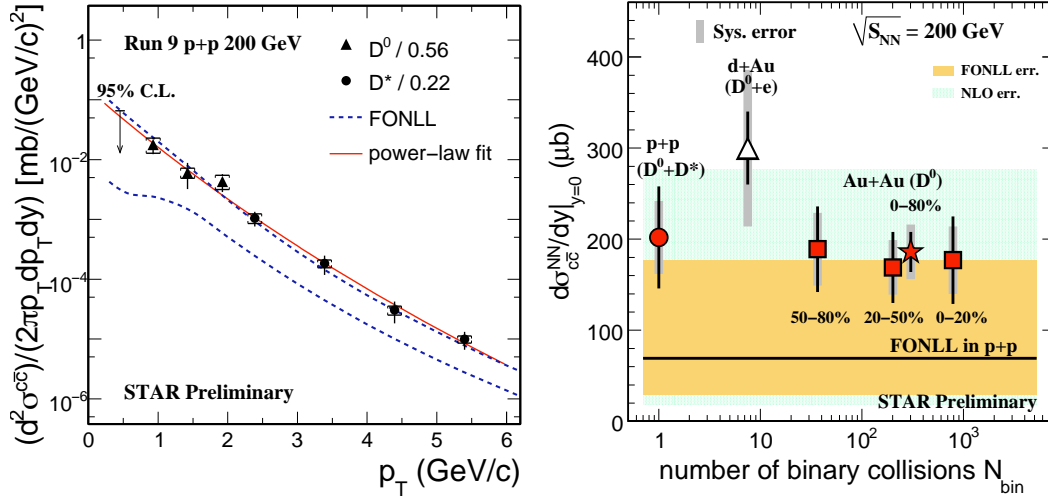


Figure 3. Left Panel: $c\bar{c}$ pair production cross sections (symbols) as a function of p_T in 200 GeV p+p collisions. Right Panel: The charm production cross section per nucleon-nucleon collision at mid-rapidity as a function of N_{bin} .

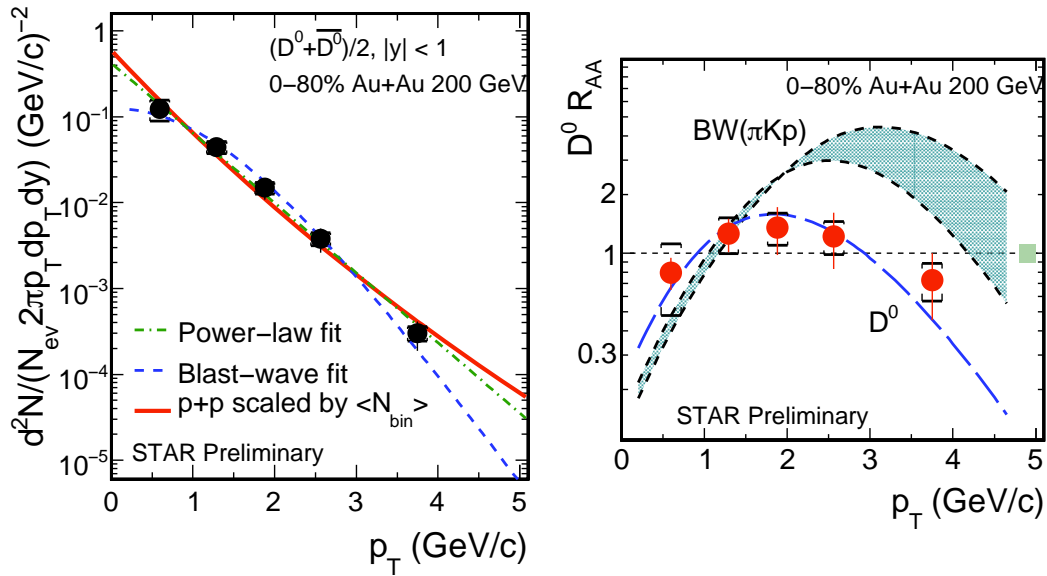


Figure 4. Left Panel: D^0 p_T spectrum in 200 GeV 0-80% Au+Au collisions. Right Panel: D^0 nuclear modification factor R_{AA} as a function of p_T .

The $R_{AA}^{D^0}$ was obtained via dividing D^0 yields in Au+Au 0-80% minbias collisions by the power-law fit to p+p yields scaled by N_{bin} , shown in right panel of Fig. 4. The uncertainty of the p+p power-law shape is taken into account as systematic error. No suppression is observed at $p_T < 3$ GeV/c. The dashed curve shows the blast-wave fit. The shaded band is the predicted $R_{AA}^{D^0}$ blast-wave parameters from light-quark hadrons [8], which is different from data. This might indicate that D^0 mesons freeze out earlier than light flavor hadrons or has less radial flow.

3.2. Identification of electrons from semi-leptonic decays

The invariant cross section for non-photonic electron production is calculated according to

$$E \frac{d^3\sigma}{dp^3} = \frac{1}{\mathcal{L}} \frac{1}{2\pi p_T \Delta p_T \delta y} \frac{N_{\text{npe}}}{\varepsilon_{\text{rec}} \varepsilon_{\text{trig}} \varepsilon_{\text{eid}} \varepsilon_{\text{BBC}}}, \quad (3)$$

where N_{npe} is the nonphoton electron raw yield, ε_{rec} is the product of the single electron reconstruction efficiency and the correction factor for momentum resolution and finite spectrum bin width, $\varepsilon_{\text{trig}}$ is the high-tower trigger efficiency, ε_{eid} is the electron identification efficiency, \mathcal{L} is the integrated luminosity with the z-position of vertex cuts, and $\varepsilon_{\text{BBC}} = 0.87 \pm 0.08$ is the BBC trigger efficiency.

Figure 5(a) shows the non-photon electron $\left(\frac{e^+ + e^-}{2}\right)$ invariant cross section obtained by combining the Run2008 and the Run2005 results using the "best linear unbiased estimate" [10]. The corrected result of our early published measurement using year 2003 data [11] is shown in the plot as well. Fig. 5(b) shows the ratio of each individual measurement, including PHENIX results, to the FONLL calculation. One can see that all measurements at RHIC on non-photon electron production in $p+p$ collisions are now consistent with each other. The corrected run 2003 data points have large uncertainties because of the small integrated luminosity (100nb^{-1}) in that run. FONLL is able to describe the RHIC measurements within its theoretical uncertainties.

Electrons from bottom and charm meson decays are the two dominant components of the non-photon electrons. Mostly due to the decay kinematics, the azimuthal

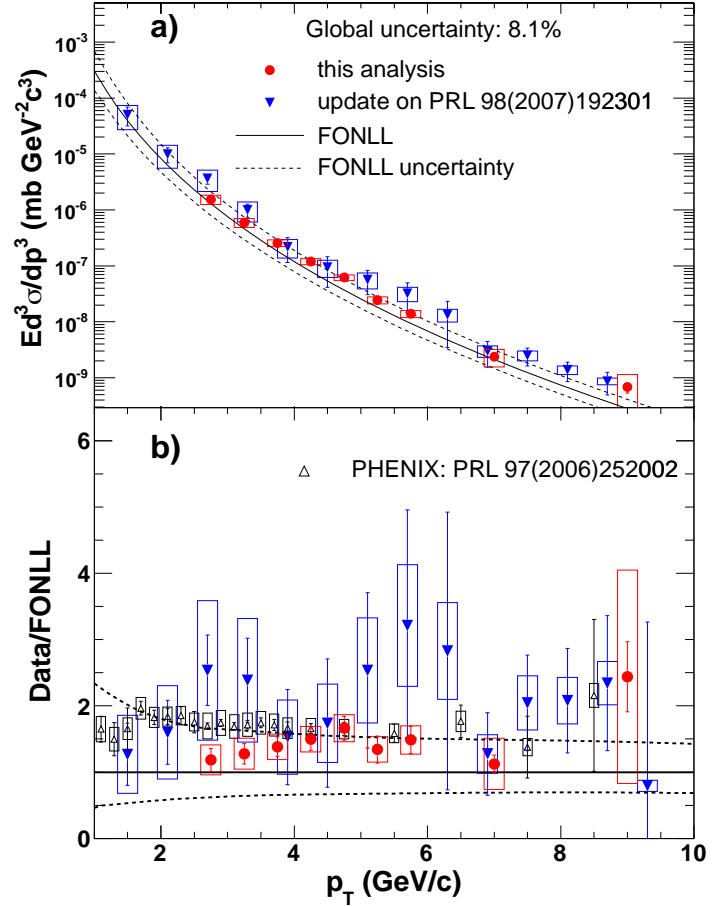


Figure 5. (a) Invariant cross section of non-photon electron production $\left(\frac{e^+ + e^-}{2}\right)$ in $p + p$ collisions from [9] analysis (closed circles) after combining results from Run2005 and Run2008. The published STAR result [11] (closed triangles) is also shown. (b) Ratio of data over FONLL [1] from all measurements at RHIC including PHENIX results [12] (open triangles).

correlations between the daughter electron and daughter hadron are different for bottom meson decays and charm meson decays. A study of these azimuthal correlations has been carried out on STAR data and is compared with a PYTHIA simulation to obtain the ratio of the bottom electron yield to the heavy-flavor decay electron yield $\frac{e_b}{e_b+e_c}$ [13], where PYTHIA was tuned to reproduce STAR measurements of D mesons p_T spectra [14]. Using the measured $e_b/(e_b + e_c)$ together with the measured non-photonic electron cross section with the electrons from J/Ψ , Υ decay and Drell-Yan processes subtracted, we are able to disentangle these two components. Figure 6 shows the invariant cross section of electrons $\left(\frac{e^+ + e^-}{2}\right)$ from bottom (upper left) and charm (upper right) mesons as a function of p_T and the corresponding FONLL predictions, along with the ratio of each measurement to the FONLL calculations (lower panels).

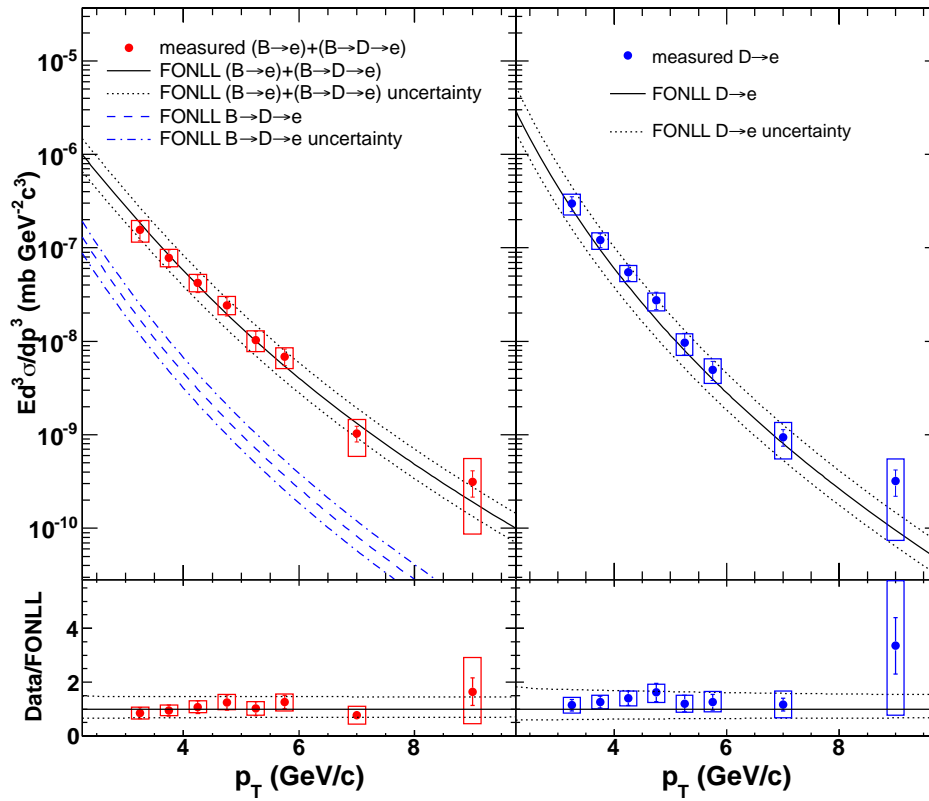


Figure 6. Invariant cross section of electrons $\left(\frac{e_b}{e_b+e_c}\right)$ from bottom (upper left) and charm meson (upper right) decay, together with the ratio of the corresponding measurements to the FONLL predictions for bottom (lower left) and charm electrons (lower right). The solid circles are experimental measurements. The error bars and the boxes are, respectively, the statistical and systematic uncertainties. The solid and dotted curves are the FONLL predictions and their uncertainties. The dashed and dot-dashed curves are the FONLL prediction for $B \rightarrow D \rightarrow e$.

From the measured spectrum, we determine the integrated cross section of electrons $\left(\frac{e^+ + e^-}{2}\right)$ at $3 \text{ GeV}/c < p_T < 10 \text{ GeV}/c$ from bottom and charm meson decays to be,

respectively,

$$\left. \frac{d\sigma_{(B \rightarrow e) + (B \rightarrow D \rightarrow e)}}{dy} \right|_{y_e=0} = 4.0 \pm 0.5(\text{stat}) \pm 1.1(\text{syst}) \text{ nb}$$

$$\left. \frac{d\sigma_{D \rightarrow e}}{dy} \right|_{y_e=0} = 6.2 \pm 0.7(\text{stat}) \pm 1.5(\text{syst}) \text{ nb}$$

4. CONCLUSIONS

Open charm mesons (D^0, D^{*+}) are measured in p+p and Au+Au collisions at $\sqrt{s_{\text{NN}}} = 200$ GeV at STAR. Charm cross sections per nucleon-nucleon collision at mid-rapidity follow the number of binary collisions scaling. The charm pair production cross sections per nucleon-nucleon collision at mid-rapidity are measured to be $d\sigma^{c\bar{c}}/(2\pi p_T dp_T dy) = 202 \pm 56(\text{stat.}) \pm 40(\text{sys.}) \pm 20(\text{norm.}) \mu\text{b}$ in p+p and $186 \pm 22(\text{stat.}) \pm 30(\text{sys.}) \pm 18(\text{norm.}) \mu\text{b}$ in Au+Au minimum bias collisions. Blast-wave predictions with light-quark hadron parameters are different from data, which might indicate that D^0 mesons freeze out earlier than light flavor hadrons or have less radial flow.

STAR measurements of high p_T non-photonic electron production in $p+p$ collisions at $\sqrt{s} = 200$ GeV using data from Run2005 and Run2008 and PHENIX result are consistent with each other. We are able to disentangle the electrons from bottom and charm meson decays in the non-photonic electron spectrum using the measured ratio of $e_B/(e_B + e_D)$ and the measured non-photonic cross section.

In the near future the STAR Heavy Flavor Tracker [15] will provide the necessary resolution to reconstruct secondary vertices of charm mesons, which will increase the precision of charm measurements.

REFERENCES

- [1] M. Cacciari, P. Nason and R. Vogt, *Phys. Rev. Lett.* **95**, 122001 (2005).
- [2] K. H. Ackermann *et al.* (STAR Collaboration), *Nucl. Instrum. Methods A* **499**, 624 (2003).
- [3] M. Anderson *et al.*, *Nucl. Instrum. Methods A* **499**, 659 (2003).
- [4] M. Shao *et al.*, *Nucl. Instrum. Methods A* **558**, 419 (2006).
- [5] M. Beddo *et al.*, *Nucl. Instrum. Methods A* **499**, 725 (2003).
- [6] B.I. Abelev *et al.* [STAR Collaboration], *Phys. Rev. D* **79**, 112006 (2009).
- [7] R. Vogt, *Eur.Phys.J.ST* **155** 213, (2008).
- [8] B. I. Abelev *et al.*, *Phys. Rev. C* **79**, 34909 (2009).
- [9] B.I. Agakishiev *et al.* [STAR Collaboration], *Phys. Rev. D* **83**, 052006 (2011).
- [10] A. Valassi, *Nucl. Instrum. Methods Phys. Res., Sect. A* **500**, 391 (2003).
- [11] B. I. Abelev *et al.* (STAR Collaboration), *Phys. Rev. Lett.* **98**, 192301 (2007); B.I. Abelev *et al.* (STAR Collaboration), arXiv:nucl-ex/0607012v3
- [12] A. Adare *et al.* (PHENIX Collaboration), *Phys. Rev. Lett.* **97**, 252002 (2006).
- [13] M. M. Aggarwal *et al.* (STAR Collaboration), *Phys. Rev. Lett.* **105**, 202301 (2010).
- [14] X. Lin, arXiv:hep-ph/0602067.
- [15] Z. Xu *et al.*, *J. Phys. G* **32**, S571(2006).

This work was supported by grant INGO LA09013 of the Ministry of Education, Youth and Sports of the Czech Republic, and by the Grant Agency of the Czech Technical University in Prague, grant No. SGS10/292/OHK4/3T/14.